

# **Predictions and Measurements of Film-Cooling on the Endwall of a First Stage Vane**

Daniel G. Knost

Thesis submitted to the Faculty of the  
Virginia Polytechnic Institute and State University  
in partial fulfillment of the requirements for the degree of

Master of Science  
in  
Mechanical Engineering

Dr. K. A. Thole, Chair  
Dr. W. F. Ng  
Dr. B. Vick

September 12, 2003  
Blacksburg, VA

Keywords: endwall, gas turbine,  
gas turbine heat transfer

© 2003, Daniel G. Knost

# **PREDICTIONS AND MEASUREMENTS OF FILM-COOLING ON THE ENDWALL OF A FIRST STAGE VANE**

**Daniel G. Knost**

## **Abstract**

In gas turbine development, the direction has been toward higher turbine inlet temperatures to increase the work output and thermal efficiency. This extreme environment can significantly impact component life. One means of preventing component burnout in the turbine is to effectively use film-cooling whereby coolant is extracted from the compressor and injected through component surfaces. One such surface is the endwall of the first stage nozzle guide vane.

This thesis details the design, prediction, and testing of two endwall film-cooling hole patterns provided by leading gas turbine engine companies. In addition a flush, two-dimensional slot was included to simulate leakage flow from the combustor-turbine interface.

The slot coolant was found to exit in a non-uniform manner leaving a large, uncooled ring around the vane. Film-cooling holes were effective at distributing coolant throughout much of the passage, but at low blowing rates were unable to provide any benefit to the critical vane-endwall junction both at the leading edge and along the pressure side. At high blowing ratios, the increased momentum of the jets induced separation at the leading edge and in the upstream portion of the passage along the pressure side, while the jets near the passage exit remained attached and penetrated completely to the vane surface.

Computational fluid dynamics (CFD) was successful at predicting coolant trajectory, but tended to under-predict thermal spreading and jet separation. Superposition was shown to be inaccurate, over-predicting effectiveness levels and thus component life, because the flow field was altered by the coolant injection.

## Acknowledgments

I would like to briefly acknowledge those who have provided guidance and assistance in this study as well as those who have been deeply involved in my personal and professional development. First I would like to thank the United States Department of Energy for providing the funding for this project as well as those at General Electric, Pratt & Whitney, and Rolls Royce who provided input during the developmental phase of the project.

I must also extend my sincerest gratitude to my advisor Dr. Karen Thole for bringing me into her lab and providing support and guidance to me as I wandered through this process. I would also like to thank Dr. Brian Vick and Dr. Wing Ng for sitting on my committee and reviewing this thesis. I must acknowledge my fellow students at VTE<sub>x</sub>CCL (the Virginia Tech Experimental and Computational Convection Lab): Andy, Andrew, Chris, Eric, Erik, Erin, Evan, Jeff, Jesse, Joe, Mike, Severin, Sachin, Will, and William, who have provided both ideas and friendship during our two years together. Special recognition is also due to Andy Lethander, Lyle Sewall and John Hatchet who assisted in building the test section, and both a shout out and big ups are owed to Jeff Prausa who was instrumental in helping me collect and analyze my data. I would like to thank all of my professors both at North Carolina State University and at Virginia Tech and give mention to Dr. Manoel Gonzalez, my advisor at N.C. State, who encouraged me to take a risk and do something that I wasn't sure that I was capable of. I would also like to extend special recognition to all of my teachers at Providence Day School in Charlotte who gave me 13 years of guidance and encouragement and challenged me to realize my potential. I never realized what a special environment existed there until I was out of it. I also had the pleasure of working two summers at Duke Energy and would like to thank all of those who took me under their wing and worked to maximize my learning experience and enjoyment there.

On a personal level I would like to thank my mom, dad, and sister, Melissa, for their love and support. I know I don't say it frequently, but I love you all. I would also like to thank Nicole for her love, support, encouragement, and the occasional kick in the pants when appropriate. I know without doubt that I would not have achieved many of my successes without you. Finally, I would like to thank Chuck Amato, head football coach of the N.C. State Wolfpack, for taking our team to a level of national prominence, instilling a sense of confidence in the program, and making it fun to be passionate about N.C. State. You are an inspiring man, and it is wonderful to have a leader who has a great sense of Pack Pride. Once again, thank you to you all and GO PACK !!!

## Table of Contents

Abstract .....	ii
Acknowledgements .....	iii
Table of Contents .....	iv
Nomenclature .....	vi
List of Tables .....	viii
List of Figures .....	ix
1. Introduction.....	1
2. Summary of Past Literature .....	13
3. Design of Cooling Configurations and Test Matrix .....	17
3.1 Vane Description.....	17
3.2 Endwall Cooling Configuration Design.....	18
3.3 Test Matrix Development .....	21
4. Computational Methods .....	31
4.1 Construction and Meshing of Model .....	31
4.2 Boundary Conditions .....	33
4.3 Governing Equations and Solution Methods .....	34
4.4 Turbulence and Near-wall Modeling .....	36
4.5 Convergence, Grid Adaption, and Independence .....	37
4.6 Data Post-Processing .....	39
5. Experimental Facility and Methods .....	54
5.1 Wind Tunnel Overview.....	54
5.2 Thermal Conditioning System .....	56
5.3 Construction of Endwall Test Plate .....	57
5.4 Coolant Plenums .....	58
5.5 Instrumentation .....	59
5.6 Setting Flow Conditions .....	63
5.7 Endwall Image, Collection, Calibration, and Assembly.....	66

5.8 Repeatability .....	70
5.9 Uncertainty Analysis .....	70
6. Computational Results .....	99
6.1 Predictions of Adiabatic Effectiveness .....	100
6.2 Superposition of Results .....	105
6.3 Secondary Flow Field Analysis .....	106
6.4 Summary .....	108
7. Experimental Results .....	119
7.1 Measurements of Adiabatic Effectiveness for an Isothermal Inlet Profile .....	120
7.2 Momentum Ratio at the Leading Edge and Along the Pressure Side .....	129
7.3 Area-Averaged Effectiveness Levels .....	131
7.4 Effects of a Steep Temperature Gradient on Film-Cooling .....	133
7.5 Streamline Analysis of Film-Coolant Trajectory .....	134
7.6 Spatial Superposition Analysis .....	138
7.7 Thermal Field Analysis .....	140
7.8 Summary .....	141
8. Comparison of Predictions and Measurements .....	167
8.1 Adiabatic Effectiveness Contours .....	167
8.2 Area-Averaged Adiabatic Effectiveness .....	179
8.3 Summary .....	180
9. Conclusions and Recommendations for Future Study .....	193
9.1 Analysis of Predictions .....	193
9.2 Analysis of Measurements .....	194
9.3 Comparison of Predictions and Measurements .....	195
9.4 Recommendations for Future Study .....	196
References .....	198
Appendix A: Sample Experimental Data Sheet .....	201
Appendix B: Code for Program Used to Align Images in Global Coordinates .....	204
Appendix C: Visual Basic Code for Secondary Flow Calculations .....	219
Vita .....	239

## Nomenclature

C	=	true chord of stator vane
$C_a$	=	axial chord of stator vane
$C_D$	=	discharge coefficient
$C_L$	=	lift coefficient
$C_p$	=	pressure coefficient
d	=	hole diameter
I	=	momentum flux ratio, $I = \rho_j u_j^2 / \rho_u$
h	=	convection heat transfer coefficient
l	=	hole length
m	=	mass flowrate
M	=	mass flux ratio, $m = \rho_j u_j / \rho_u$
Ma	=	Mach Number
$q''$	=	heat flux
P, p	=	vane pitch; hole pitch
$P_o, p$	=	total and static pressures
Re	=	Reynolds number defined as $Re = C U_\infty / \nu$
s	=	distance along vane from flow stagnation
S	=	span of stator vane
T	=	temperature
x, y, z	=	local coordinates
X, Y, Z	=	global coordinates
u, v, w	=	local velocity
$\underline{U}, \underline{V}, \underline{W}$	=	velocity in global frame
$\bar{\phantom{x}}$	=	lateral average
$\overline{\phantom{x}}$	=	area average
Greek		
$\alpha$	=	flow angle leaving vane
$\epsilon$	=	turbulence kinetic energy
$\eta$	=	adiabatic effectiveness, $\eta \equiv (T_\infty - T_{aw}) / (T_\infty - T_c)$
$\theta$	=	dimensionless temperature, $\theta \equiv (T_\infty - T) / (T_\infty - T_c)$
$\kappa$	=	turbulence dissipation rate
$\nu$	=	kinematic viscosity
$\rho$	=	density
$\phi$	=	deviation from axial direction
$\psi$	=	streamline
Subscripts		
1	=	combustor/contraction exit
ave	=	average
aw	=	adiabatic wall

c	=	coolant conditions
dyn	=	dynamic
G	=	global
h	=	hot
in	=	inlet conditions
$\infty$	=	freestream conditions
j	=	jet
loc	=	local
ms	=	midspan
n	=	normal
plen	=	plenum
s	=	streamline
sup	=	superposition
w	=	wall
z	=	spanwise

## List of Tables

<b>Table 3.1</b>	Parameters for Stator Vane Operating at Altitude and Wind Tunnel Conditions .	22
<b>Table 3.2</b>	Summary of Geometric Cooling Parameters for Both Cooling Configurations ...	23
<b>Table 3.3</b>	Comparison of Features at Engine and Study Scales .....	23
<b>Table 3.4</b>	Hole Center Locations and Angle from Axial Direction for Hole Pattern #1 .....	24
<b>Table 3.5</b>	Hole Center Locations and Angle from Axial Direction for Hole Pattern #2 .....	25
<b>Table 3.6</b>	Experimental and Computational Test Matrix .....	26
<b>Table 4.1</b>	Cell Edge Length in Regions of Constant Cell Size .....	42
<b>Table 4.2</b>	Beginning and Ending Cell Edge Length in Regions of Graduated Mesh Size ....	42
<b>Table 4.3</b>	Various Settings for Under Relaxation Factors .....	42
<b>Table 5.1</b>	Typical Experimental Operating Conditions .....	71
<b>Table 5.2</b>	Experimental Pressure Ratios and Film-cooling Discharge Coefficients .....	71
<b>Table 5.3</b>	Global Locations of Markers Used to Align Images .....	72
<b>Table 5.4</b>	Global Locations of Endwall Thermocouples Used for Image Calibration.....	73
<b>Table 6.1</b>	Computational Test Matrix and Hole Discharge Coefficients .....	110
<b>Table 6.2a</b>	Film-Cooling Blowing Ratios for Selected Holes in Pattern #1 .....	110
<b>Table 6.2b</b>	Film-Cooling Blowing Ratios for Selected Holes in Pattern #2 .....	110
<b>Table 7.1</b>	Experimental Test Matrix .....	143
<b>Table 7.2</b>	Local Blowing and Momentum Ratio of Selected Holes for Various Cases .....	144
<b>Table 8.1</b>	Test Matrix of Cases with Both Predictions and Measurements .....	182
<b>Table A.1</b>	Steady State Check .....	202

## List of Figures

<b>Figure 1.1</b> Schematic of an aeolipile, invented by Hero in 150 A.D ( <a href="http://www.aviation-history.com/engines/theory.htm">http://www.aviation-history.com/engines/theory.htm</a> ) .....	7
<b>Figure 1.2</b> The Wright brothers achieved the first powered flight on December 17, 1903 at Kill Devel Hills, North Carolina. This photo was taken just after the Wright flyer took off (Library of Congress). .....	7
<b>Figure 1.3</b> The W-1 flight demonstration engine designed by Sir Frank Whittle in 1939 .8	
<b>Figure 1.4</b> Pratt & Whitney’s F-119 turbo fan engine used to power the F-22 fighter.....8	
<b>Figure 1.5</b> GE MS7001EA power turbine producing 85 MW. This engine is used in both simple and combined cycle applications. ( <a href="http://www.gepower.com/corporate/en_us/assets/gasturbines_heavy/prod/pdf/gasturbine_2002.pdf">http://www.gepower.com/corporate/en_us/assets/gasturbines_heavy/prod/pdf/gasturbine_2002.pdf</a> ) .....	9
<b>Figure 1.6a-c</b> The Brayton cycle defining the combustion turbine in its simplest form is illustrated. (a) The system, (b) p-v diagram, and (c) T-s diagram are illustrated. ....	10
<b>Figure 1.7</b> Endwall secondary flow model for a turbulent boundary layer presented by Langston (1980). The horseshoe vortex develops as the leading edge and the passage vortex results from strong cross-passage flows along the endwall. ....	11
<b>Figure 1.8</b> A heat damaged first stage stator vane is shown. At the time of removal this part was still considered a servicable part. ....	11
<b>Figure 1.9</b> Film-cooling holes are shown both on the vane surface and along the vane endwall. Film-cooling holes use cool fluid bled from the compressor to create a cool film blanket over the metal surfaces of the hardware (Friedrichs, 1997). ....	12
<b>Figure 2.1a-c</b> Friedrichs et al. originally studied a conventional circumferential film-cooling pattern shown in (a). Based on flow visualization they then identified (b) four regions with varying cooling requirements and designed a new pattern (c) to meet the individual needs of the regions. ....	16
<b>Figure 2.2</b> Harasgama and Burton studied film-cooling holes along an iso-velocity contour. Their row of holes lay on contour F corresponding to $Ma = 0.25$ . ....	16
<b>Figure 3.1</b> Characteristic lengths used to define airfoil geometry .....	27
<b>Figure 3.2a</b> The two film-cooling patterns that were designed for this study (Pattern #1 and #2) and labels for several specific film cooling holes. In addition, a secondary flow plane is identified that was used to evaluate the flow field. ....	28

**Figure 3.2b** Shown are the directions of the coolant hole injection along with iso-velocity contours ( $U/U_1$ ) and the gutter location for mating two turbine vane platforms. 28

**Figure 3.3** Critical dimensions of the slot and film-cooling holes at model scale (9X) . Note that the figure is not drawn to scale.....29

**Figure 3.4** A turbine disc is shown with the gutter(s) marked. The stators shown are singlets, but stators are often grouped as doublets.....30

**Figure 3.5** Nozzle guide vane doublet shown with vane and endwall film-cooling holes. Gutters would be formed by adjoining another doublet to each side. Slot leakage would come from the upstream edge (Friedrichs, 1997). .....30

**Figure 4.1a-b** (a) Top and (b) side views of the computational domain are shown along with the boundary conditions. Symmetry and periodic boundary conditions were used to reduce the size of the model. ....43

**Figure 4.2a-b** Models for the slot combined with (a) film pattern #1 and (b) film pattern #2 are shown with one periodic repeat. Models were also developed for each film-pattern without the slot and for the slot without film-cooling. ....44

**Figure 4.3a-c** The face mesh on the endwall for (a) pattern #1 and (b) pattern #2 is shown. (c) The film-cooling holes and the film-cooling plenum were individually meshed. The reduction of cell size near the holes to maintain a conformal mesh is clearly visible. ....45

**Figure 4.4** The volume mesh for the entire domain is shown. The mesh is graduated so that larger cells exist near inlet and outlet where the flow field is less complex with smaller cells in the passage. The mesh is also graduated from the wall, where viscous effects are present, to the midspan where the flow is inviscid.....46

**Figure 4.5a-b** (a) While a uniform temperature and velocity profile are specified at the inlet to the vane, (b) at the combustor exit the approaching velocity field is distorted by the vane downstream. ....47

**Figure 4.6** The two methods for modeling the viscous boundary layer are illustrated. In the wall function approach, semi-empirical relations are used to predict the boundary layer while thin elements are used to compute the boundary layer in the near-wall modeling approach (Fluent 2002). ....48

**Figure 4.7a-b** (a) Convergence of residuals in initial computations are shown to go unstable beginning with the energy equation. (b) By reducing the under relaxation factors to the values shown in the “Partially Modified” column of Table 4.3 the solution

converged smoothly. The large jumps correspond to resumption of calculation after adapting the grid.....49

**Figure 4.8a-c** A hanging node adaption is shown in (a) where all nodes are not shared with a neighboring cell. Adaption of simple two-dimensional cells is shown in (b) while a more complex tetrahedral cell is divided into eight tetrahedrons in (c).....50

**Figure 4.9** The endwall grid is shown before and after adaption. Cells were added near the throat and along the vane surfaces to capture the accelerating flow. ....51

**Figure 4.10** The lift coefficient and area-averaged endwall temperature were used to evaluate grid independence of the results. The lift coefficient and average endwall temperature were not significantly altered despite adapting the grid after 1000 and 2000 iterations.....52

**Figure 4.11** Multiple coordinate systems are used to define the secondary flow vectors.53

**Figure 5.1** Illustration of wind tunnel facility. The flow is split into the primary channel and secondary channels before passing through the combustor simulator section and the vane cascade.....74

**Figure 5.2** The flow is driven by a Joy Technologies 50 hp 0-60 Hz fan.....74

**Figure 5.3** A perforated plate with 24.6% open area is used to achieve the proper pressure drop through the core flow channel. ....75

**Figure 5.4** Plenums in the combustor bypass feed film-cooling and dilution holes in the combustor simulator. The plenums were closed off and liner holes covered over because no combustor flows were simulated. ....75

**Figure 5.5** Cooling air from the bypass channel passes into the supply plenums through holes at the end of the combustor bypass. The cooling air is then injected into the passage through the slot or the holes where it interacts with the hot mainstream gases. ..76

**Figure 5.6** A three zone heater bank is used to generate various combustor exit temperature profiles. ....76

**Figure 5.7** Watlow Series 988 controller used to specify percentage of full power to the heater banks.....77

**Figure 5.8** Each of the three heater sub-banks is wired in a three phase delta with each leg consisting of two elements in parallel (Vakil 2002). ....77

**Figure 5.9** Film-cooling holes were cut with a water jet. (a) Passage 1 and (b) the leading edge region are shown. ....78

<b>Figure 5.10</b> The upstream slot was constructed from balsa wood to provide improved stiffness. ....	78
<b>Figure 5.11a-b</b> Schematics of balsa wood slot. Extent of the slot is shown in (a) while locations of the endwall static pressure taps are shown in (b). ....	79
<b>Figure 5.12</b> The rear plenum provides coolant flow through the film-cooling holes. ....	80
<b>Figure 5.13</b> A division was added to separate the front plenum which fed the slot flow. ....	80
<b>Figure 5.14a-b</b> Coolant flow passes from the combustor bypass into the plenums through two feed slots. ....	81
<b>Figure 5.15</b> A typical shutter control is shown. Panes connected to a pushrod slide past stationary panes to open and close the flow area. ....	81
<b>Figure 5.16</b> The plenum control devices are shown along with a splash plate to aid in mixing the slot flow. ....	82
<b>Figure 5.17</b> The gate was raised and lowered to control flow into the hole plenum. ....	82
<b>Figure 5.18</b> Three Scani- Valve wafers were used to scan pressure measurements (Vakil 2002). ....	83
<b>Figure 5.19</b> Eight pressure transducers converted pressure readings into voltages for the data acquisition system (Vakil 2002). ....	84
<b>Figure 5.20a-b</b> A pitot tube measures the difference between the total pressure and static pressure yielding the dynamic pressure and thus the velocity. ....	85
<b>Figure 5.21</b> Seven pitchwise velocity measurements were averaged to determine the cascade inlet velocity. The inlet profile exhibits periodicity. ....	85
<b>Figure 5.22a-c</b> A thermocouple rake was used to document the thermal field at a plane within the passage. ....	86
<b>Figure 5.23a-c</b> (a) The thermocouple rake was suspended from a boom and (b) moved by a computer controlled traverse. (c) The rake is shown in the passage. ....	87
<b>Figure 5.24a-d</b> The data acquisition (DAQ) system is depicted. (a) Voltage outputs from the thermocouples and transducers are connected to a SCXI-1303 terminal block. The terminal block plugs into one of (b) three SCXI-1100 modules which are housed in the (c) SCXI-1000 chassis. The signal is output to (d) the DAQ card where it is digitized for processing on the computer (Vakil 2002). ....	88

**Figure 5.25** A Flir P20 infra-red camera was used to thermally image the endwall surface and record endwall temperature data. ....89

**Figure 5.26** A flexible wall allows the passage flows to be adjusted in order to achieve the proper pressure distribution. The wall is adjusted with various knobs. ....90

**Figure 5.27** The pressure coefficient was verified at multiple locations along the vane. The pressure coefficient was verified at multiple locations along the vane. ....90

**Figure 5.28** A linear fit was used to calculate the global discharge scaling parameter for each passage based upon computational predictions. ....91

**Figure 5.29a-d** The bisection method used to calculate the experimental pressure difference is illustrated. (a) The mid-point of the possible pressure range is calculated and slightly higher and lower pressure are selected (points a and b). The discharge coefficient and corresponding mass flow of each search point are calculated. (b) The error of each search point is calculated. The search point with the greater error along with the range between that pressure and the limit are discarded. (c) The new mid-point is calculated and errors are again compared. (d) Bisection continues until the error between the points is less than the specified tolerance. ....92

**Figure 5.30** When setting experimental cooling flows, four pressure measurements were recorded for both the slot flow and the film-cooling for the pattern of interest as shown by the wiring diagram. The pressure measurements were averaged to determine the coolant flow rates. ....93

**Figure 5.31** Images were collected at 13 different locations to entirely map the endwall thermal contours. ....94

**Figure 5.32** Small markers were embedded in the endwall to provide global reference points and thermocouples were used to post calibrate the infra-red images. ....95

**Figure 5.33** The multiple images were combined using know global locations to form a mosaic of the endwall thermal contours. ....96

**Figure 5.34a-e** The image transformation process is illustrated. (a) an image in space has two markers at know global locations. (b) The transition matrix from a pixel aligned coordinate system to the marker aligned system is developed by projecting the pixel basis onto the marker basis. (c) The vector from the left to right marker in the global frame is found by a vector subtraction of the vectors to the markers. (d) The transition matrix from the marker frame to the global frame is found by projecting the marker basis onto the global basis. (e) The offset vector to one of the markers positions the image globally. ....97

**Figure 5.35a-d** Both endwall contour data (a and b) and thermal field data (c and d) showed excellent repeatability. ....98

<b>Figure 6.1a-b</b> Predicted contours of adiabatic effectiveness for (a) 0.5% slot flow alone, case 1S0F0 and (b) 1.0% slot flow alone, case 3S0F0. ....	111
<b>Figure 6.2</b> Pitchwise-averaged adiabatic effectiveness levels through the vane passage for slot flow alone. ....	111
<b>Figure 6.3a-b</b> The film-cooling patterns are shown with (a) several featured holes used for comparisons between passages. A secondary flow plane is also indicated where the flow field was examined. (b) Iso-velocity contours as well as the gutter location and arrows indicating the direction of hole injection are shown. ....	112
<b>Figure 6.4a-b</b> Predicted contours of adiabatic effectiveness for the baseline film cooling cases without slot flow (a) pattern #1, 0.5% film alone, case 0S1F1 and (b) pattern #2 0.5% film alone, case 0S1F2.....	113
<b>Figure 6.5a-b</b> Predicted adiabatic effectiveness levels for pattern #1 at 0.5% slot flow combined with (a) the low 0.5% film flow rate, case 1S1F1 and (b) the high 0.75% film flow rate, case 1S2F1. ....	114
<b>Figure 6.6a-b</b> Predicted adiabatic effectiveness levels for pattern #2 at 0.5% slot flow combined with (a) the low 0.5% film flow rate, case 1S1F2 and (b) the high 0.75% film flow rate, case 1S2F2. ....	114
<b>Figure 6.7</b> Pitchwise-averaged adiabatic effectiveness levels through the vane passage for the combined slot and film-cooling cases. ....	115
<b>Figure 6.8</b> Summary of area-averaged effectiveness values for all of the computational cases studied. It can be seen that including film-cooling leads to higher averaged effectiveness levels than slot flow alone. ....	116
<b>Figure 6.9</b> Comparison of predicted pitchwise-averaged effectiveness levels as compared with those calculated using the superposition for the 0.5% slot and 0.5% film-cooling flow cases with hole pattern #2. ....	117
<b>Figure 6.10a-d</b> Secondary flow and thermal fields for the (a) slot cooling alone, case 1S0F0 (b) film-cooling alone, case 0S1F2 (c) combined slot flow-and low film flow rate, case 1S1F2 (d) combined film-cooling and slot flow at the higher film blowing ratio, case 1S2F2. Cooling hole pattern #2 was used for these results. ....	118
<b>Figure 7.1</b> Measured inlet temperature profiles for the cases investigated. These temperature profiles were measured just upstream of the contraction of the wind tunnel. ....	145
<b>Figure 7.2a-c</b> Contours of adiabatic effectiveness for the cases of slot flow without film-cooling (a) 0.5%, case 1S0F0, (b) 0.75%, case 2S0F0, and (c) 1.0% case 3S0F0. ....	146

<b>Figure 7.3</b> Laterally averaged effectiveness levels for the three cases of slot flow injection without film-cooling. ....	147
<b>Figure 7.4a-d</b> Contours of adiabatic effectiveness for the baseline film-cooling only cases: (a) pattern #1, 0.5% film, case 0S1F1, (b) pattern #1, 0.75% film, case 0S2F1, (c) pattern #2, 0.5% film, case 0S1F1, and (d) pattern #2, 0.75% film, case 0S2F2. ....	148
<b>Figure 7.5</b> Laterally averaged effectiveness levels for the four cases of film-cooling injection without slot injection. ....	149
<b>Figure 7.6a-d</b> Contours of adiabatic effectiveness for pattern #1 at the various combined slot and film-cooling cases (a) 0.5% slot 0.5% film, case 1S1F1, (b) 0.5% slot 0.75% film, case 1S2F1, (c) 0.75% slot 0.5% film, case 2S1F1, and (d) 0.75% slot 0.75% film, case 2S2F1. ....	150
<b>Figure 7.7</b> Laterally averaged adiabatic effectiveness levels for pattern #1 at four cooling combinations of slot and film-coolant injection. ....	151
<b>Figure 7.8a-d</b> Contours of adiabatic effectiveness for pattern #2 at the various combined slot and film-cooling cases (a) 0.5% slot 0.5% film, case 1S1F2, (b) 0.5% slot 0.75% film, case 1S2F2, (c) 0.75% slot 0.5% film, case 2S1F2, and (d) 0.75% slot 0.75% film, case 2S2F2. ....	152
<b>Figure 7.9</b> Laterally averaged adiabatic effectiveness levels for pattern #2 at four cooling combinations of slot and film-coolant injection. ....	153
<b>Figure 7.10a-b</b> Momentum flux ratios for holes indicated by the dashed lines are shown in (a) the leading edge region and (b) the upstream and downstream pressure side regions. Adiabatic effectiveness levels of neighboring holes are also pictured for reference. ....	154
<b>Figure 7.11</b> Area-averaged effectiveness levels are shown for the 15 experimental cases with a uniform inlet profile. The cases are grouped by cumulative coolant flow rate providing a quantifiable method of assessing the effects of distributing coolant between the slot and film-cooling holes. ....	155
<b>Figure 7.12a-d</b> Adiabatic effectiveness contours are shown for case 1S1F2 with both an (a) endwall-peaked and (b) center-peaked inlet profile. Contours were normalized by the maximum temperature in the profile. The same cases are shown in (c) and (d) with the adiabatic wall temperature normalized by the spatially averaged temperature from the profile. ....	156
<b>Figure 7.12e</b> Adiabatic effectiveness contours are shown for case 1S1F2 with a near-wall peaked profile. The contours are normalized by the average near-wall temperature (0%-5% span) to illustrate that when properly scaled, the results from all three temperature profiles for case 1S1F2 appear the same. ....	157

**Figure 7.13a-d** Contours of flow angle,  $\phi$  measured in degrees as deviation from the downstream axial direction are shown along with streamlines for (a) the midspan corresponding to inviscid predictions (b) 2% span with a low 0.5% slot coolant flow rate and (c) 2% span with a high 0.75% slot coolant flow rate. The streamlines for all three cases are superimposed in (d) to illustrate the strengthened cross flow because of the slot. 158

**Figure 7.14a-b** Predicted streamlines at 2% span for both the low and mid-level slot flow rates are presented with the hole locations of pattern #1 (a) and pattern #2 (b) shown for reference. ....159

**Figure 7.15a-d** Predicted streamlines at 2% span for 0.5% slot flow without film-cooling are superimposed on (a) pattern #1 with 0.5% slot flow and 0.5% film-cooling and (b) pattern #2 with 0.5% slot flow and 0.5% film-cooling. The two cases are shown with predicted streamlines at the midspan superimposed in (c) and (d). ....160

**Figure 7.16a-d** Predicted streamlines at 2% span for 1% slot flow without film-cooling are superimposed on (a) pattern #1 with 1% slot flow and 0.5% film-cooling and (b) pattern #2 with 1% slot flow and 0.5% film-cooling. The same two cases are shown with predicted streamlines at the midspan superimposed in (c) and (d). ....161

**Figure 7.17a-d** Contours of the difference between the predicted flow angles at 2% span and midspan are shown for the low 0.5% slot flow case (a) and (b) and the mid-level 0.75% slot flow case (c) and (d). The hole locations of pattern #1 and pattern #2 are shown for reference. ....162

**Figure 7.18a-d** Contours of adiabatic effectiveness are shown for (a) case 1S0F0, 0.5% slot flow and (b) case 0S1F2, 0.75% film. Contours of adiabatic effectiveness for case 1S1F2, 0.5% slot 0.5% film, are shown from both (c) superposition and (d) measurements. ....163

**Figure 7.19a-b** (a) Superposition predicted and (b) measured contours of adiabatic effectiveness are shown for case 1S2F2, 0.5% slot 0.75% film. ....164

**Figure 7.20a-b** (a) Superposition predicted and (b) measured contours of adiabatic effectiveness are shown for case 2S1F2, 0.75% slot 0.5% film. ....164

**Figure 7.21a-b** (a) Superposition predicted and (b) measured contours of adiabatic effectiveness are shown for case 2S2F2, 0.75% slot 0.75% film. ....165

**Figure 7.22a-d** Thermal field data was acquired in (a) a plane normal to the pressure surface at  $x/Ca = -0.77$ . Contours of non-dimensional temperature are shown for (b) 0.5% slot flow without film-cooling, case 1S0F0, (c) 0.5% slot flow with 0.5% film-cooling, case 1S1F2, and (d) 0.5% slot flow with 0.75% film-cooling, case 1S2F2. ....166

**Figure 8.1a-b** (a) Predictions and (b) measurements of adiabatic effectiveness are shown for the low 0.5% slot flow rate, case 1S0F0. ....183

<b>Figure 8.2a-b</b> (a) Predictions and (b) measurements of the non-dimensional thermal field for case 1S0F0.....	183
<b>Figure 8.3a-b</b> (a) Predictions and (b) measurements of adiabatic effectiveness are shown for the high 1.0% slot flow rate, case 3S0F0. ....	184
<b>Figure 8.4</b> Comparison of laterally-averaged adiabatic effectiveness for predicted and measured cases of slot flow alone.....	184
<b>Figure 8.5a-b</b> (a) Predictions and (b) measurements of adiabatic effectiveness for pattern #1 at 0.5% film-cooling without slot flow, case 0S1F1.....	185
<b>Figure 8.6a-b</b> (a) Predictions and (b) measurements of adiabatic effectiveness for pattern #2 at 0.5% film-cooling without slot flow, case 0S1F2.....	185
<b>Figure 8.7</b> Comparison of laterally-averaged adiabatic effectiveness for predicted and measured cases of film-cooling flow alone.....	186
<b>Figure 8.8a-b</b> (a) Predictions and (b) measurements of adiabatic effectiveness for pattern #1 at 0.5% slot with the low 0.5% film-cooling flow rate, case 1S1F1.....	187
<b>Figure 8.9a-b</b> (a) Predictions and (b) measurements of adiabatic effectiveness for pattern #1 at 0.5% slot with the high 0.75% film-cooling flow rate, case 1S2F1. ....	187
<b>Figure 8.10</b> Comparison of laterally-averaged adiabatic effectiveness from predictions and measurements for 0.5% slot flow with film cooling from pattern #1 at 0.5% and 0.75%. ....	188
<b>Figure 8.11a-b</b> (a) Predictions and (b) measurements of adiabatic effectiveness for pattern #2 at 0.5% slot flow with the low 0.5% film-cooling flow rate, case 1S1F2. ....	189
<b>Figure 8.12a-b</b> (a) Predictions and (b) measurements of the non-dimensional thermal field for case 1S1F2. ....	189
<b>Figure 8.13a-b</b> (a) Predictions and (b) measurements of adiabatic effectiveness for pattern #2 at 0.5% slot flow with the high 0.75% film-cooling flow rate, case 1S2F2. ...	190
<b>Figure 8.14a-b</b> (a) Predictions and (b) measurements of the non-dimensional thermal field for case 1S2F2. ....	190
<b>Figure 8.15</b> Comparison of laterally-averaged adiabatic effectiveness from predictions and measurements for 0.5% slot flow with film cooling from pattern #2 at 0.5% and 0.75%. ....	191

<b>Figure 8.16</b> Area-averaged adiabatic effectiveness levels from predictions and measurements grouped by cumulative coolant flow rate.....	192
<b>Figure B.1</b> Graphical User Interface to Program for Image Alignment .....	204
<b>Figure C.1</b> The “Enter Parameters” button opens a GUI to input plane data to the spreadsheet. ....	219
<b>Figure C.2</b> The “Import Data” button runs the Text File Import Wizard. ....	219
<b>Figure C.3</b> After importing the data all rows with text are deleted. ....	220
<b>Figure C.4</b> The “Manipulate Data” button sorts the data, performs the flow plane calculations, and formats the output.....	220

# Chapter 1

## Introduction

As we move into the new millennium, combustion turbine engines have become an integral part of our daily lives. Gas turbines are used to propel aircraft, tanks, and large naval ships. They also provide pumping power to large pipelines and are used for peaking power on the electrical grid. In some parts of the world where cooling water for steam cycle plants is in short supply, combustion turbines have also been implemented for base load power supply. As research is pursued, the technology of the combustion turbine will continue to grow providing more power at a higher efficiency in today's more environmentally conscious, yet energy thirsty, world.

The principles of propulsion were first demonstrated by Hero in 150 A.D. (Hill and Peterson, 1992). Hero's engine, consisting of a heated sphere with two vent ports is shown in Figure 1.1. An understanding of the physics driving Hero's engine was not developed until the period of Newton, though. Around the turn of the 20<sup>th</sup> century the steam turbine entered service and today has become the primary source of electrical generation around the world.

At the same time Wilbur and Orville Wright achieved the first powered flight on December 17, 1903 on the dunes of Kill Devil Hills, North Carolina. The first flight covered 120 feet and lasted 12 seconds with Wilbur piloting the flyer. The historic moment captured just after take-off is shown in Figure 1.2. By the end of the day, the brothers were learning to control their flyer and on the final flight of the day Wilbur was able to cover 852 feet in 59 seconds. The Wright flyer was powered by a home-made four-cylinder internal combustion engine making 12 hp.

As flight technology developed the demand quickly arose for more powerful engines. The steam turbine was a proven power plant with good efficiency, but was not practical for flight applications because of the bulky equipment necessary for steam generation. As metallurgical technology improved, the possibilities of a new working fluid, air, began to be realized. In 1939 Sir Frank Whittle introduced the first gas turbine demonstration engine, shown in Figure 1.3. The gas turbine had advantages over the

reciprocating engines because there were no reciprocating parts, leading to less wear, and a much larger percentage of the machine could contain the working fluid leading to a significantly better power to weight ratio. While initial efforts were geared toward generating shaft power, the developmental focus quickly shifted toward the turbojet engine which propels the aircraft by thrust. By the 1950s the gas turbine had become the engine of choice for aviation and was beginning to make an impact in other applications as well.

Today two primary applications of combustion turbines are aero propulsion and power generation. A modern turbofan engine, the Pratt & Whitney F-119, is illustrated in Figure 1.4. Turbofan engines typically use a dual spool configuration consisting of a high-pressure turbine coupled with a high-pressure compressor and a low-pressure turbine coupled with a fan. The bypass ratio, or the ratio of fluid bypassing the core to fluid passing through the core, is varied to accommodate efficiency and performance needs. Thrust is developed by the momentum of the fluid exiting the engine. Commercial airliners typically use high bypass ratios, generating thrust by moving large quantities of air, because this is more efficient. Military engines put a premium on performance and often use low bypass ratios and high jet velocities sacrificing some efficiency.

The second wide spread application of combustion turbine technology is power generation. Power turbines are much larger than aero turbines because weight and space are not an issue. They are frequently as large as a school bus and place a premium on efficiency. Units range in size from output measured in kW to 500 MW. A GE MS7001EA power turbine is shown in Figure 1.5. Combustion turbines are ideal for peaking power (meeting maximum power needs) because they can be started and provide power to the grid in minutes. In contrast, a nuclear power plant, which is used for base load power, must go through multiple modes and testing at startup and may take up to three days to reach full power. Combustion turbines have also found wide spread use in the power industry as merchant plants. Merchant plants are stationed in areas of high power demand, such as California, and when the local utility has a shortage of power or a plant off-line, the owner of the merchant plant can fire the plant and sell to the utility to meet their needs. Merchant plants have boomed because they are relatively inexpensive

(in the millions) and can be erected in a few months. Once again, the nuclear power plant would take more than ten years to be operational and the cost would be well in excess of \$10 billion dollars. In arid environments such as the Middle East, combustion turbines have become part of the base load power supply as well. This is because fossil and nuclear plants that use steam cycles require a large water supply for condensing purposes. In areas where water is limited, large steam plants are not practical.

One of the newest, and perhaps most promising, applications of power turbines is the combined cycle unit. Combined cycle plants employ a gas turbine combined with a power turbine to turn a generator just as a conventional cycle unit would. The waste heat from the turbine is then used to generate steam which drives a steam turbine. Thermal efficiency of combined cycle plants has approached 60%.

The thermodynamics of a combustion turbine are described in simplest form by the Brayton cycle illustrated in Figures 1.6a-c. The basic components of the combustion turbine are labeled in Figure 1.4. Air enters the machine from the atmosphere through the intake and absorbs work from the compressor which raises both the pressure and temperature of the fluid. The air then passes through the combustor where heat energy is added in the form of fuel. The combustion gases are then expanded through the turbine, extracting useful work, and finally exhausted to the atmosphere out of the nozzle.

The turbine is coupled with the compressor and this unit together with the combustor is known as the gas generator. The turbine extracts only enough work to continue driving the compressor. In turbojet and turbofan applications, the relatively high enthalpy fluid leaving the turbine is then accelerated through the exit nozzle creating a high momentum jet which delivers thrust. In other applications where thrust is not desirable, such as power plants or helicopter engines, the fluid is then further expanded through a second turbine known as the power turbine. The power turbine is coupled to a generator, propeller, or some other shaft driven device.

Two parameters are used to measure the performance of non-aero engines. They are thermal efficiency,  $\eta_{th}$ , and specific work. These parameters are defined as:

$$\eta_{th} = \frac{W_T}{Q_{in}} = 1 - \frac{T_4}{T_3} \quad (1.1)$$

$$\frac{W_T}{C_p T_1} = \frac{T_3}{T_1} \left( 1 - \frac{T_4}{T_3} \right) - \left( \frac{T_3}{T_4} - 1 \right) \quad (1.2)$$

Thermal efficiency quantifies how effectively the input energy is converted to useful output energy in the form of work, and specific work is the amount of work that a plant of a given size is capable of producing.

As seen in equations 1.1 and 1.2 both performance parameters are dependent upon the  $T_3$ , the temperature of the fluid entering the turbine. The direction of turbine development has been to increase the temperature exiting the combustor to improve performance. As turbine inlet temperatures continue to rise the metallurgical limits of the machine have been pushed and frequently exceeded. Modern turbines have inlet temperatures of approximately 1650° C (3000° F) while the melting point of the turbine materials is approximately 1205° C (2200° F) (Mattingly, 1996).

As the fluid approaches the first stage stator, used to accelerate and direct the flow into the first stage rotor, secondary flows develop. A classic secondary flow model for a turbulent boundary layer, presented by Langston (1980), is shown in Figure 1.7. A vortex develops at the vane leading edge with legs extending into the passage around both the pressure and suction sides. This vortex is called the horseshoe vortex. Another vortex, known as the passage vortex, also develops because of strong cross-passage currents generated by the sharp pressure gradient across the passage. These secondary flows can entrain the hot mainstream gases convecting them down onto the metal surfaces and leading to component burnout. An example of this is shown in the heat damaged first stage stator vane of Figure 1.8. If the surface temperature can be lowered even by only 28° C (50° F) this can have a dramatic impacting on component life increasing by as much as a factor of two (Cohen, 2001).

One method of combating this overheating problem is through the use of film-cooling holes whereby cooler air 675° C (1250° F) is extracted from the compressor, bypasses the combustor, and is injected through discrete holes in the vane and endwall surfaces. A vane with film-cooling holes is shown in Figure 1.9. Film-cooling hole placement has traditionally been based upon designer experience. If an area of the vane has been troublesome a film-cooling hole is placed there.

In addition to film-cooling, most turbines have a slot at the combustor-turbine interface where bypass gases leak through. Depending on the design the slot may have a forward or backward facing step or flush configuration. If designed properly, the leakage flow from the slot may be relied upon as source of coolant for the endwall.

The goal of this research was to develop an understanding of the trajectory of slot and film-coolant as well as effectiveness levels achieved by each of these cooling methods. A test matrix was developed to evaluate the effectiveness and distribution of both slot flow and film-coolant from two original endwall film-cooling designs at various blowing and momentum flux ratios. The patterns were based on different design philosophies allowing a comparison of the design methods. Areas requiring special consideration were identified. The slot and film-cooling patterns were also combined to evaluate the influence that each cooling mechanism had on the other. The coolant distribution and effectiveness levels were both predicted using computational fluid dynamics (CFD) and measured in a large scale, low speed wind tunnel. The effects of coolant injection on the flow field and thermal field were also examined. The accuracy of the predictions was evaluated to determine if CFD was a viable tool to aid a designer in the development of a cooling scheme.

Chapter 2 provides a summary of the past studies on endwall film-cooling. The relevance and uniqueness of this study is explained. Chapter 3 lends insight into the development of the cooling schemes as well as the test matrix. Chapter 4 provides a detailed account of the computational modeling process. The options available to the computationalist are discussed as well as reasoning for the modeling techniques that were used. Chapter 5 details the test facility as well as experimental setup, instrumentation, and data acquisition and analysis techniques. Chapter 6 provides analysis of the predictions. Both adiabatic effectiveness levels and flow and thermal field phenomena are examined. A laterally-averaged superposition of results is also evaluated. Chapter 7 provides analysis of the measurements. Endwall adiabatic effectiveness levels are examined as well as the effect of blowing ratio on jet separation in critical areas. Spatial superposition of measurements is evaluated and a method for identifying hard to cool areas based on streamline predictions is developed. Chapter 8 provides a comparison of

the predictions and measurements, and finally, chapter 9 discusses conclusions drawn from this research and suggests areas for further investigation.



**Figure 1.1** Schematic of an aeolipile, invented by Hero in 150 A.D (<http://www.aviation-history.com/engines/theory.htm>)

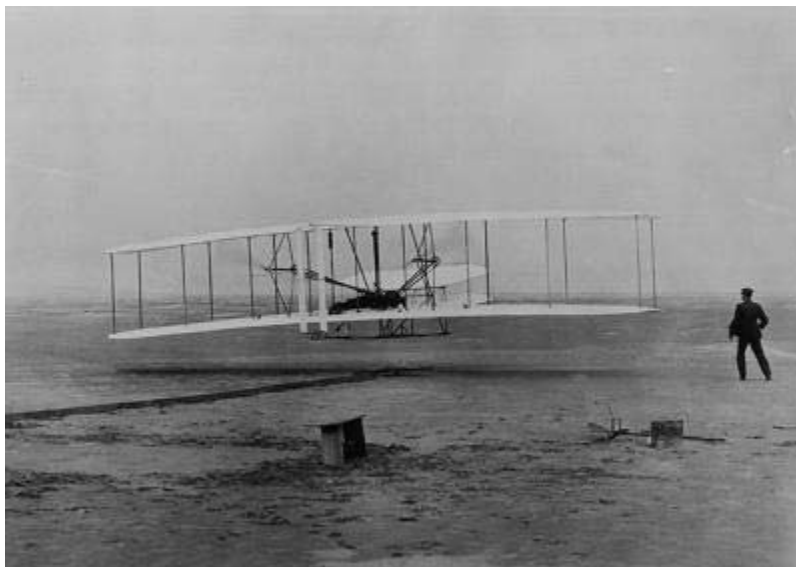


**Figure 1.2** The Wright brothers achieved the first powered flight on December 17, 1903 at Kill Devel Hills, North Carolina. This photo was taken just after the Wright flyer took off (Library of Congress).

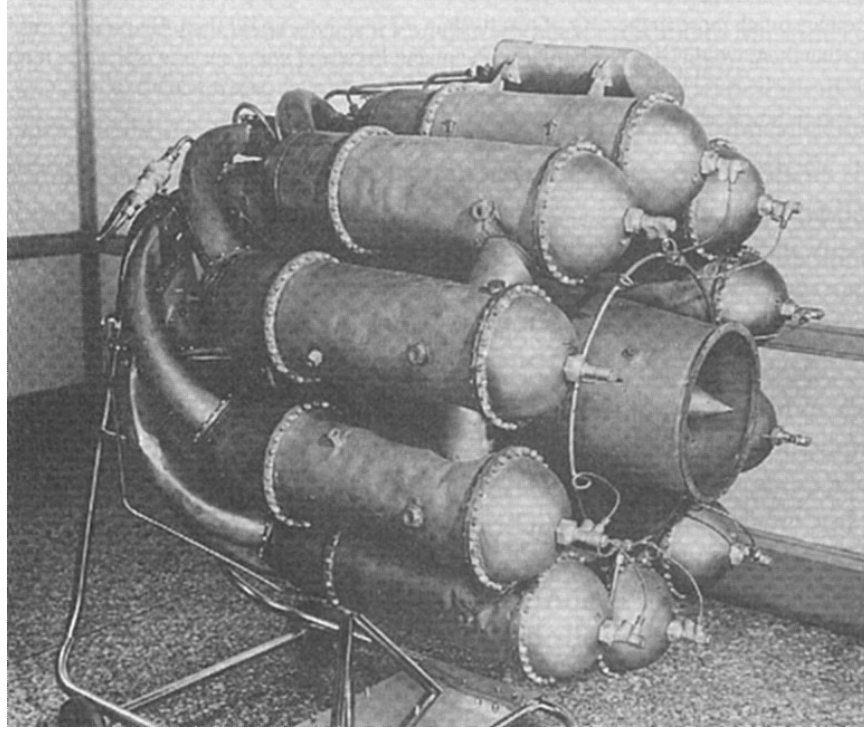


**Figure 1.3** The W-1 flight demonstration engine designed by Sir Frank Whittle in 1939

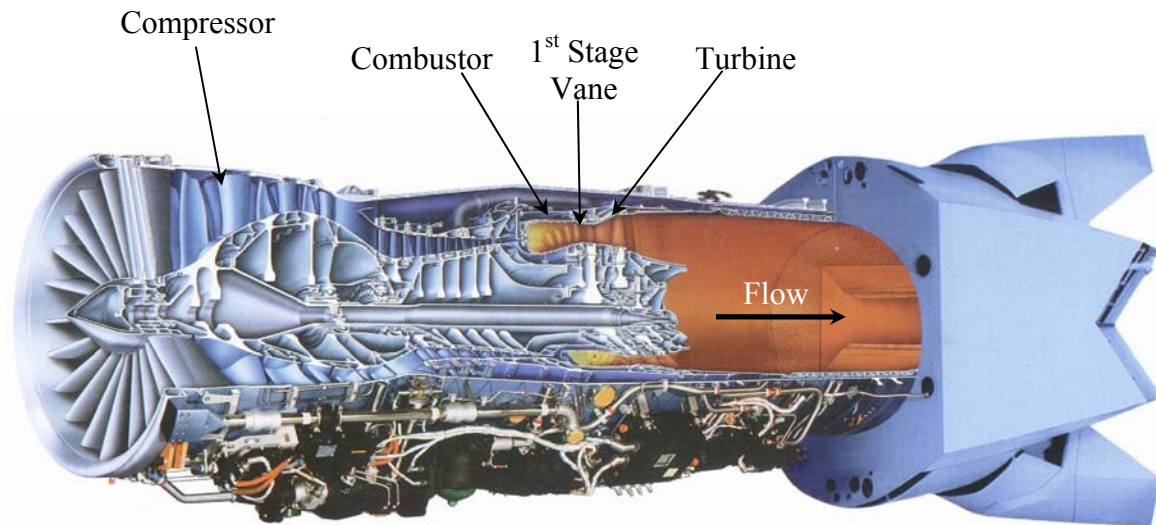


**Figure 1.4** Pratt & Whitney's F-119 turbo fan engine used to power the F-22 fighter (Courtesy of Pratt & Whitney).



**Figure 1.5** GE MS7001EA power turbine producing 85 MW. This engine is used in both simple and combined cycle applications. ([http://www.gepower.com/corporate/en\\_us/assets/gasturbines\\_heavy/prod/pdf/gasturbine\\_2002.pdf](http://www.gepower.com/corporate/en_us/assets/gasturbines_heavy/prod/pdf/gasturbine_2002.pdf))

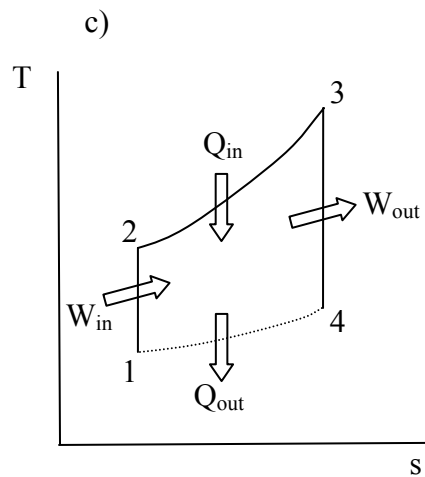
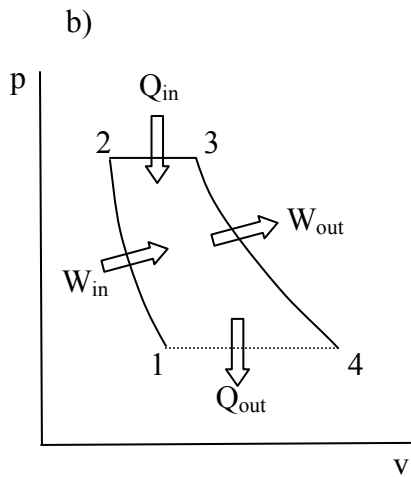
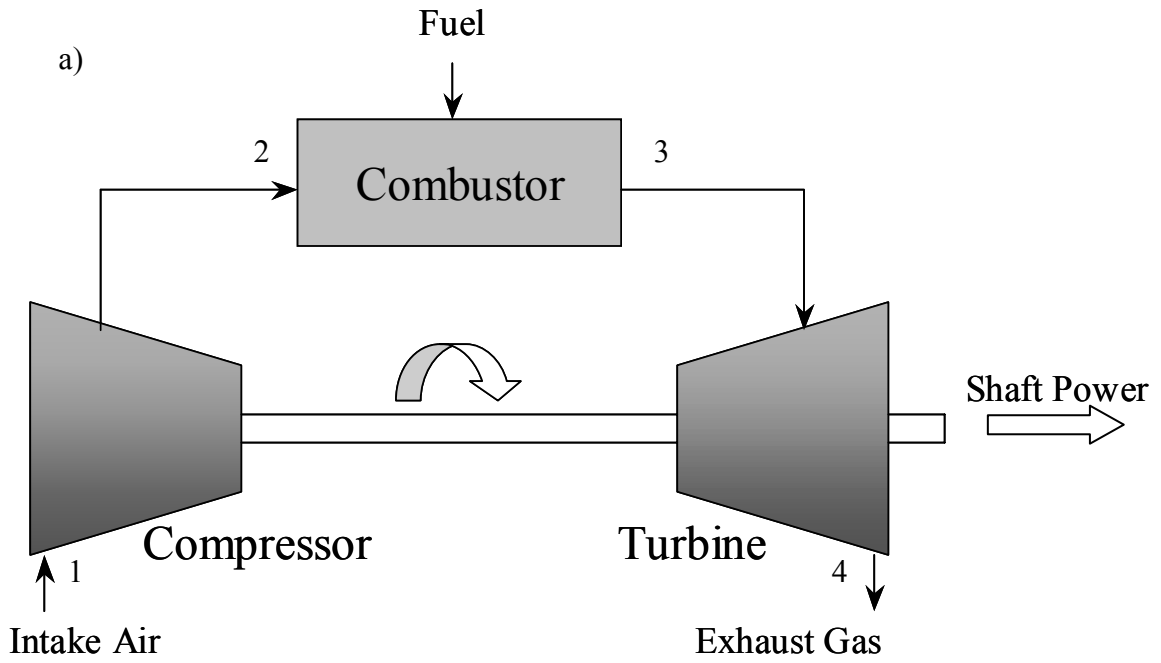


**Figure 1.6a-c** The Brayton cycle defining the combustion turbine in its simplest form is illustrated. (a) The system, (b)  $p$ - $v$  diagram, and (c)  $T$ - $s$  diagram are illustrated.

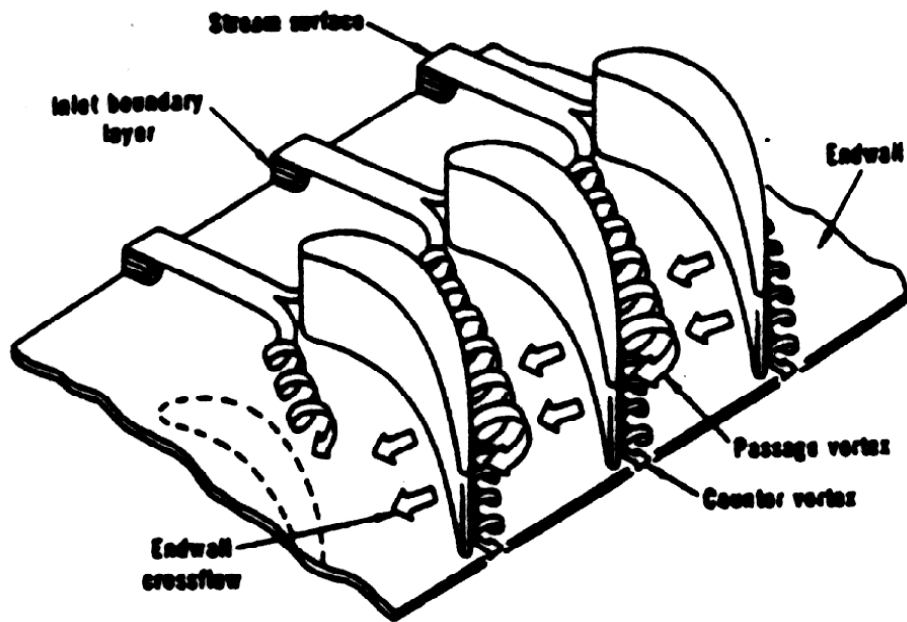


**Figure 1.7** Endwall secondary flow model for a turbulent boundary layer presented by Langston (1980). The horseshoe vortex develops as the leading edge and the passage vortex results from strong cross-passage flows along the endwall.



**Figure 1.8** A heat damaged first stage stator vane is shown. At the time of removal this part was still considered a serviceable part.

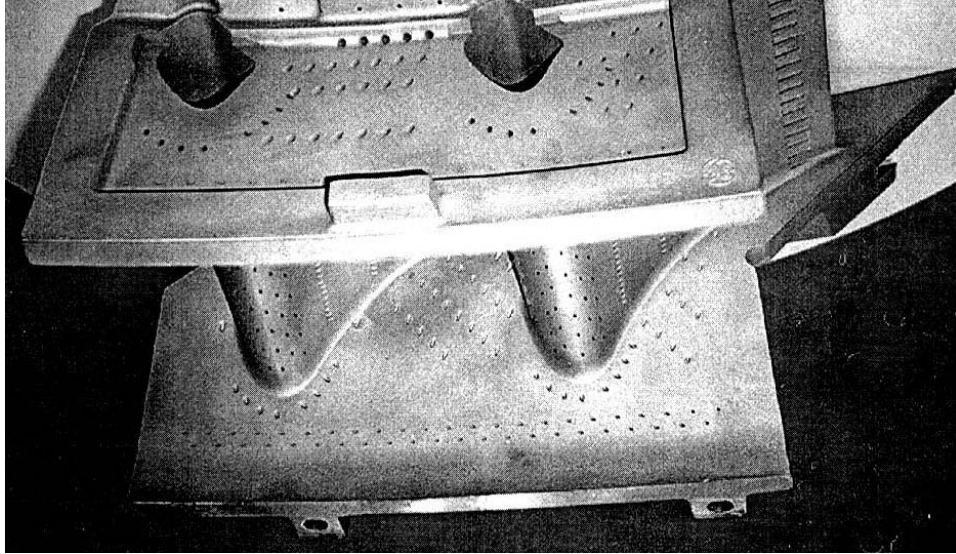


**Figure 1.9** Film-cooling holes are shown both on the vane surface and along the vane endwall. Film-cooling holes use cool fluid bled from the compressor to create a cool film blanket over the metal surfaces of the hardware (Friedrichs, 1997).

## Chapter 2

### Summary of Past Literature

There have been a number of studies documenting endwall film-cooling and a number of studies documenting cooling from the turbine-combustor junction. As will also be discussed in this summary, there has been only one study presented in the literature that has combined endwall film-cooling with coolant leakage from an upstream slot.

The most recent studies of detailed endwall film cooling have been those conducted by Friedrichs et al. (1996, 1997, and 1999). The endwall patterns studied by Friedrichs et al. are shown in Figures 2.1a-c. The results of their first study (1996) which were all surface measurements or visualization, indicated a strong influence of the secondary flows on the film cooling and an influence of the film-cooling on the secondary flows. Quite counter-intuitive to most, their data showed that the angle at which the coolant leaves the hole did not dictate the coolant trajectory except near the hole exit. Furthermore the endwall cross-flow was altered so that the cross-flow was turned toward the inviscid streamlines, which was due to the film-cooling injection.

Harrasgama and Burton (1992) suggested that locating film-cooling holes along iso-Mach lines would provide more uniform blowing ratios and help to prevent jet lift off. The iso-Mach lines of their passage are shown in Figure 2.2. There have been a few studies that have measured endwall heat transfer as a result of injection from a two-dimensional, flush slot just upstream of the vane. Blair (1974) measured adiabatic effectiveness levels and heat transfer coefficients for a range of blowing ratios through a flush slot placed just upstream of the leading edges of his single passage channel. One of the key findings was that the endwall adiabatic effectiveness distributions showed extreme variations across the vane gap. Much of the coolant was swept across the endwall toward the suction side corner resulting in reduced coolant near the pressure side. As the blowing ratio was increased, he found that the extent of the coolant coverage also increased. Measured heat transfer coefficients were similar between no slot and slot injection cases. In a later study by Granser and Schulenberg (1990), similar adiabatic

effectiveness results were reported with higher values occurring near the suction side of the vane.

A series of experiments have been reported for various injection schemes upstream of a nozzle guide vane with a contoured endwall by Burd and Simon (2000); Burd et al. (2000); Oke, et al. (2000); and Oke et al. (2001). In the studies presented by Burd and Simon (2000), Burd et al. (2000) and Oke, et al. (2000) coolant was injected from an interrupted, flush slot that was inclined at  $45^\circ$  just upstream of their vane. Similar to others, they found that most of the slot coolant was directed toward the suction side at low slot flow conditions. As they increased the percentage of slot flow to 3.2% of the exit flow, however, their measurements indicated better coverage occurred between the airfoils. In contrast, the study by Oke et al. (2001) used a double row of filmcooling holes that were aligned with the flow direction and inclined at  $45^\circ$  with respect to the surface while maintaining nearly the same optimum 3% bleed flow of their previously described studies. They found that the jets lifted off the surface producing more mixing thereby resulting in a poorer thermal performance than the single slot.

Roy et al. (2000) compared their experimental measurements and computational predictions for a flush cooling slot that extended over only a portion of the pitch directly in front of the vane stagnation. Contrary to the previously discussed studies, their adiabatic effectiveness measurements indicated that the coolant migrated toward the pressure side of the vane. Their measurements indicated reduced values of local heat transfer coefficients at the leading edge when slot cooling was present relative to no slot cooling.

Colban et al. (2002, 2002) reported flow field and endwall effectiveness contours for a backward-facing slot with several different coolant exit conditions. Their results indicated the presence of a tertiary vortex that developed in the vane passage due to a peaked total pressure profile in the near-wall region. For all of the conditions simulated, the effectiveness contours indicated the coolant from the slot was swept towards the suction surface. While this study was completed for the same vane geometry as that reported in our paper, the slot geometry has been altered to be flush with the endwall surface.

The only studies to have combined an upstream slot with film-cooling holes in the downstream endwall vane passage were those of Kost and Nicklas (2001) and Nicklas (2001). One of the most interesting results from this study was that they found for the slot flow alone, which was 1.3% of the passage mass flow, the horseshoe vortex became more intense. This increase in intensity resulted in the slot coolant being moved off of the endwall surface and heat transfer coefficients that were over three times that measured for no slot flow injection. They attributed the strengthening of the horseshoe vortex to the fact that for the no slot injection the boundary layer was already separated with fluid being turned away from the endwall at the injection location. Given that the slot had a normal component of velocity, injection at this location promoted the separation and enhanced the vortex. Their adiabatic effectiveness measurements indicated higher values near the suction side of the vane due to the slot coolant migration.

Zhang and Moon (2003) tested a two row film-cooling configuration upstream of a contoured endwall. Both a flush transition and a backward facing step were examined. For the flush transition, the film effectiveness levels on the endwall increased in a non-linear fashion indicating interference by the secondary flows. At low mass flows the secondary flows dominated the film-cooling jets resulting in low effectiveness levels. At the high mass flow rates the jet momentum was sufficient to overcome the secondary flows and provide improved cooling. The effectiveness levels were considerably lower for the backward-facing step configuration indicating that the secondary flows were exacerbated by the step.

Clearly there is a need for further study on the cooling problems associated with the endwall of a turbine platform. This study focuses on the interaction between the coolant leaving a two-dimensional slot at the combustor-turbine interface and the endwall film-cooling injection. It is unique in combining slot coolant with two full endwall cooling patterns. This study also uses a non-unity density ratio, different from the other full cooling pattern studies by Friedrichs, and was performed at a large scale to provide improved measurement resolution.

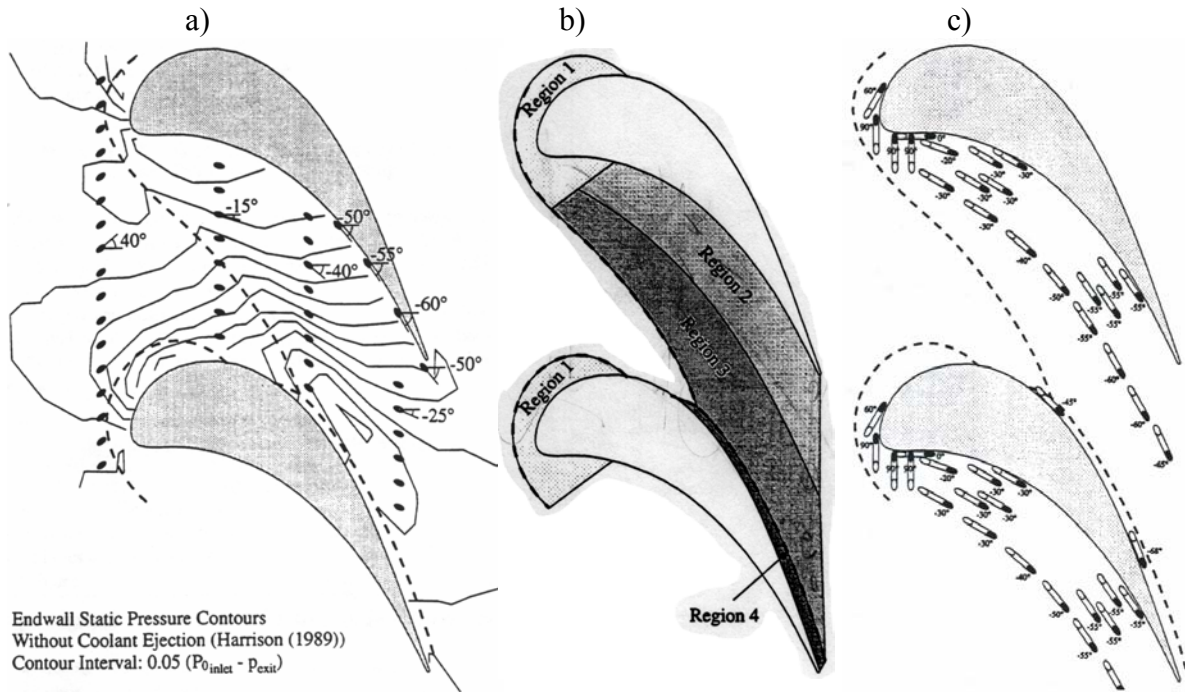


**Figure 2.1a-c** Friedrichs et al. (1995, 1998) originally studied a conventional circumferential film-cooling pattern shown in (a). Based on flow visualization they then identified (b) four regions with varying cooling requirements and designed a new pattern (c) to meet the individual needs of the regions.

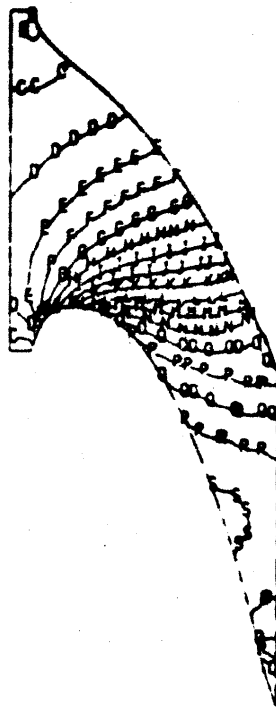


**Figure 2.2** Harasgama and Burton (1991) studied film-cooling holes along an iso-velocity contour. Their row of holes lay on contour F corresponding to  $Ma = 0.25$ .

## Chapter 3

### Design of Cooling Configurations and Test Matrix

Two original vane endwall cooling configurations were developed for this study based upon industrial input. The endwall requires cooling because of the extreme environment that it is exposed to as hot combustion gases move through the passage and are transported to the endwall by secondary flows. It is the goal of this chapter to describe the airfoil geometry and to describe the different cooling mechanisms that were studied as well as to explain the sizing and location of the various cooling mechanisms.

Section 3.1 will detail the geometry of the turbine vane in the wind tunnel cascade. Section 3.2 will discuss the design philosophy behind each cooling configuration that was studied. The specific cooling mechanisms, or features of the design, will be detailed as well as the methodology used in determining the physical characteristics and location of the features. Section 3.3 will present the test matrix and discuss the reasoning and goals behind the various test cases.

#### 3.1 Vane Description

The vane used in the study was a first stage stator guide vane from the Pratt & Whitney 6000 series engine. The vane was originally described in a number of publications such as Radomsky and Thole (2000). The vane was two-dimensional with the midspan geometry modeled along the entire span. The vane was geometrically scaled up by a factor of nine in order to achieve good measurement resolution. Several characteristic lengths, which may be seen in Figure 3.1, are used to describe the vane cascade. The chord is the maximum extent of the vane, while the axial chord is the distance from the vane leading edge to the trailing edge in the axial direction. The span is the radial extent of the vane, and the pitch is the circumferential distance between adjacent vanes. The characteristic lengths for both the engine and the scaled up cascade are presented in Table 3.1. The absolute flow angle,  $\alpha_2$ , leaving the pressure side of the blade was  $72^\circ$ . Radomsky (2000) showed surface heat transfer to be a strong function of the Reynolds number but only a weak function of Mach number which could not be

matched at large scale. Therefore the inlet Reynolds number based on inlet velocity and vane chord was matched. In addition, the dimensionless pressure coefficient distribution

$$C_p = \frac{P_{s,loc} - P_{s,in}}{P_{dyn,in}} \quad (3.1)$$

was matched to the 2-D, low speed, inviscid prediction presented by Kang et al.(1999) along the vane midspan.

### 3.2 Endwall Cooling Configuration Design

As was stated in the literature review, there is very little public documentation of leakage slot flow combined with endwall film-cooling. As such, two unique cooling configurations, designated pattern #1 and pattern #2, were designed based upon industry input for the purpose of examining the relationship between these two cooling mechanisms. The two cooling schemes may be seen in Figures 3.2a-b. Several individual holes are numbered for the purpose of analyses to follow. Iso-velocity contours and the direction of hole injection are shown in Figure 3.2b. Iso-velocity lines are normalized by the mass averaged inlet velocity. An upstream slot as well as the location of where a “gutter” would be are also illustrated. A gutter is a gap between two mating vane platforms on a turbine disc. A gutter is a potential source of leakage flow but was not simulated in the current study. Tables 3.2 and 3.3 provide a summary of data relevant to the cooling schemes.

The first cooling mechanism, which was common to both pattern #1 and pattern #2, was a flush, two-dimensional slot. The upstream edge of the slot was located  $0.31C_a$  upstream of the dynamic stagnation point on the vane. Due to geometric constraints of the test facility, the slot had to be moved 1.27 cm upstream to  $-0.35C_a$  for the experiments. The slot location is indicated in Figure 3.2a. The slot was designed to simulate the junction between the combustor and turbine sections. One would expect to have bypass leakage flow through this junction resulting in some thermal benefit to the endwall. The slot injected in the inlet direction at an angle of  $45^\circ$  with respect to the endwall with a length (flow path length) to width (cross-sectional width) ratio of 1.8 as is shown in Figure 3.3.

Downstream of the slot, two different film-cooling patterns were employed based upon different design philosophies. All film-cooling holes injected at an angle of  $30^\circ$  with respect to the endwall and had a length (flow path length) to diameter (cross-sectional) ratio of 8.3.

Each of the two film-cooling patterns could be divided into two distinct zones: the leading edge zone and the zone within the passage between the vanes as shown in Figure 3.2a. The leading edge region could be further sub-divided into the group of holes directly upstream of the vane and the holes between the vanes. The holes directly upstream of the leading edge were termed “leading edge blockers”. The leading edge blockers injected in the inlet direction and had a pitch (center-to-center spacing) to diameter ratio of three. These holes were intended to blanket the vane-endwall junction of the leading edge where temperatures rise due to stagnating flow. The leading row holes between the vanes were rotated to inject perpendicular to the inlet flow in the direction of the vane turning. The holes in this region were spaced with  $p/d = 4$ . The leading row of holes was identical for each of the two film-cooling patterns with the exception of a discontinuity in the perpendicular holes in pattern #2 as compared to a continuous row for pattern #1. This gap for hole pattern #2 is present to allow for the gutter design which was previously discussed.

Harasgama and Burton (1992) suggested that locating film-cooling holes along iso-Mach lines would help to insure a uniform blowing ratio and momentum flux helping to prevent jet lift-off. Hole pattern #1 was designed such that the film-cooling holes were located along straight lines approximating iso-velocity lines predicted by Radomsky (2000). Iso-velocity contours were used because experimentation was performed in a large-scale, low-speed facility with little variation in Mach number. The hole closest to the pressure side was positioned allowing space for a 0.127 cm (0.050 inch) extent manufacturing fillet at engine scale, which was not simulated. The rows of holes were then extended with  $p/d = 3$  along the approximate iso-velocity contours allowing for a manufacturing fillet on the suction side as well. Two rows of holes were extended across the entire width of the passage, while the remaining rows were limited to three holes nearer to the pressure side. It was thought that the cross passage rows would provide some cooling to the endwall near the suction side, while the cross passage secondary

flows would be relied upon to transport the coolant from the truncated rows. Three holes were placed across the passage at the trailing edge in order to provide cooling downstream of the vanes. This row was oriented at an angle of  $135^\circ$  from the inlet direction. The locations of the 65 holes in pattern #1 are presented in Table 3.4. All holes within the passage injected downstream in the axial direction.

The second cooling configuration, also shown in Figures 3.2a-b, was designed around a feature known as the gutter. Examples of gutters may be seen in Figures 3.4 and 3.5. The design gutter was 0.127 cm (0.050 inches) wide at engine scale and extended through the passage at an angle of forty-five degrees with respect to the axial direction. Ordinarily, one may expect to achieve some cooling benefit from leakage flow through the gutter. However, because of the preliminary nature of the current film-cooling study, the gutter was not simulated in this study. Nonetheless, the gutter dramatically impacted the location of film-cooling holes in passage #2. The hole nearest to the pressure surface in each row was placed in the same manner as in passage #1. Each hole was located along the same iso-velocity contours as were used in passage #1 while allowing for a 0.127 cm extent manufacturing fillet. Each row was then extended upstream through the passage along axial lines with  $p/d = 3$ . Three short rows of three holes each were located along the pressure surface in the upstream portion of the passage. Two extended rows were used to provide cooling near the shoulder of the suction side. If a hole intersected the gutter the hole was omitted. Upstream of the gutter the row was continued with the first hole located along the axial row with the hole center three hole diameters upstream of the gutter. The row was then extended upstream until the hole inlets would interfere with the leading row of holes. Two holes were located near trailing edge. These holes were rotated by forty-five degrees with the turning in order to avoid interference from the gutter and still provide cooling to the region just downstream of the trailing edge. All other holes within the passage of pattern #2 injected downstream in the axial direction. Pattern #2 had 51 cooling holes equating to only 78% of the cooling area of pattern #1. The locations of the holes in pattern #2 are presented in Table 3.5.

### 3.3 Test Matrix Development

The test matrix, consisting of 17 different coolant combinations, was developed with the goal of examining the relationship between the slot flow and film-cooling flow from an adiabatic endwall effectiveness perspective. The test matrix may be seen in Table 3.6. Based upon industry input, two coolant flow rates were established to test low and high flow rates. The lower limit was set at 0.5% of the core flow and the upper limit was set at 0.75% of the core flow. This limited the cumulative coolant flow rate for any single platform to 1.5% of the core flow. As was stated previously, it is desirable to limit coolant flow because the coolant must be bled off of the compressor bypassing the combustor. This leads to a lower enthalpy thereby decreasing the work potential of the fluid.

It was desirable to test all flow rates in both cooling configurations as a means of comparing the effectiveness of the two different design philosophies. Each cooling mechanism was also tested independently in order to assess the validity of a superposition solution of the individual results. Coolant was distributed between the two cooling mechanisms at varying rates while maintaining cumulative coolant flow rates of 0.5, 1.0, 1.25, and 1.5% of the core flow, in order to assess the effects of varying the coolant distribution. Nine of the cases were also computed in an attempt to predict the coolant distribution and effectiveness levels. Thermal fields were documented for three cases for the purpose of comparison with computed solutions. Finally, three different temperature profiles were studied in order to analyze the effects of temperature gradients at the combustor exit/turbine inlet. A flat temperature profile was used as a baseline case, with center peaked and near wall peaked profiles as the perturbation cases.

**Table 3.1** Parameters for Stator Vane Operating at Altitude and Wind Tunnel Conditions

	Engine	Wind Tunnel
True chord length (cm)	6.6	59.4
Axial chord length (cm)	3.3	29.3
Span (cm)	6.1	54.9
Pitch (cm)	5.1	45.7
Aspect ratio (true chord length to span)	1.08	1.08
Solidity ratio (true chord length to vane spacing)	1.30	1.30
Inlet velocity (m/s)	92.9	6.3
Inlet Mach number	0.12	0.012
Exit Mach number	0.90	0.085
Inlet Reynolds number, $Re_{in}=(\rho U_{in}C/\mu)$	$2.25 \times 10^5$	$2.25 \times 10^5$
Exit Reynolds number, $Re_{ex}=(\rho U_{ex}C/\mu)$	$1.2 \times 10^6$	$1.06 \times 10^6$
Stagnation temperature (K)	1666	293
Stagnation pressure (Pa)	$10.34 \times 10^5$	$98.4 \times 10^4$
Flow inlet angle (degrees)	0	0
Trailing edge metal angle (degrees)	72	72
Inlet absolute viscosity (Pa·s)	$5.86 \times 10^{-5}$	$17.9 \times 10^{-6}$
Inlet density ( $kg/m^3$ )	2.123	1.16

Radomsky (2000)

**Table 3.2** Summary of Geometric Cooling Parameters for Both Cooling Configurations

Parameter	Value
Cooling hole l/d	8.3
Hole injection angle	30°
p/d for leading edge holes	4 / 3
p/d for passage holes	3
Slot length to width	1.8
Upstream slot location of vane	-0.31C <sub>a</sub>
Slot injection angle	45°

**Table 3.3** Comparison of Features at Engine and Study Scales

Feature	Engine	Study
Scale	1	9
Slot width, cm (in)	0.165 (0.065)	1.485 (0.585)
Slot length, cm (in)	0.299 (0.118)	2.694 (1.061)
Cooling hole diameter, cm (in)	0.051 (0.020)	0.457 (0.180)
Cooling hole length, cm (in)	0.508 (0.200)	3.810 (1.500)
Gutter width, cm (in)	0.127 (0.050)	1.143 (0.450)
Cooling hole l/d	10	8.3

**Table 3.4** Hole Center Locations and Angle from Axial Direction for Hole Pattern #1

Hole #	X [m]	Y [m]	$\phi$	Hole #	X [m]	Y [m]	$\phi$
1	0.0248	-0.3555	0	34	0.1540	-0.1050	0
2	0.0134	-0.3479	0	35	0.1404	-0.1058	0
3	0.0020	-0.3404	0	36	0.1268	-0.1069	0
4	0.0705	-0.2926	0	37	0.2476	-0.0211	0
5	0.0600	-0.2838	0	38	0.2351	-0.0154	0
6	0.0495	-0.2750	0	39	0.2226	-0.0098	0
7	0.1112	-0.2426	0	40	-0.0253	-0.4570	0
8	0.1004	-0.2341	0	41	-0.0253	-0.4433	0
9	0.0896	-0.2257	0	42	-0.0418	-0.4069	90
10	0.0788	-0.2173	0	43	-0.0418	-0.3886	90
11	0.0679	-0.2089	0	44	-0.0418	-0.3703	90
12	0.0573	-0.2002	0	45	-0.0418	-0.3520	90
13	0.0482	-0.1899	0	46	-0.0418	-0.3338	90
14	0.0391	-0.1797	0	47	-0.0418	-0.3155	90
15	0.0300	-0.1694	0	48	-0.0418	-0.2972	90
16	0.0209	-0.1591	0	49	-0.0418	-0.2789	90
17	0.0144	-0.1471	0	50	-0.0418	-0.2606	90
18	0.0111	-0.1338	0	51	-0.0418	-0.2423	90
19	0.0078	-0.1204	0	52	-0.0418	-0.2240	90
20	0.0045	-0.1071	0	53	-0.0418	-0.2057	90
21	0.1422	-0.2033	0	54	-0.0418	-0.1875	90
22	0.1301	-0.1968	0	55	-0.0418	-0.1692	90
23	0.1180	-0.1903	0	56	-0.0418	-0.1509	90
24	0.1669	-0.1693	0	57	-0.0418	-0.1326	90
25	0.1537	-0.1656	0	58	-0.0418	-0.1143	90
26	0.1405	-0.1619	0	59	-0.0253	-0.0960	0
27	0.1902	-0.1340	0	60	-0.0253	-0.0823	0
28	0.1765	-0.1332	0	61	-0.0253	-0.0686	0
29	0.1628	-0.1324	0	62	-0.0253	-0.0549	0
30	0.2086	-0.1026	0	63	-0.0253	-0.0411	0
31	0.1949	-0.1032	0	64	-0.0253	-0.0274	0
32	0.1812	-0.1038	0	65	-0.0253	-0.0137	0
33	0.1676	-0.1044	0				

Note – (0,0) is at dynamic stagnation point of center vane in three vane cascade

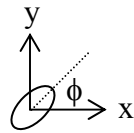


**Table 3.5** Hole Center Locations and Angle from Axial Direction for Hole Pattern #2

Hole #	X [m]	Y [m]	$\phi$	Hole #	X [m]	Y [m]	$\phi$
1	0.0701	0.1606	0	27	0.2375	0.4121	45
2	0.0564	0.1606	0	28	0.2238	0.4121	45
3	0.0427	0.1606	0	29	-0.0253	0.0000	0
4	0.1108	0.2107	0	30	-0.0253	0.0137	0
5	0.0971	0.2107	0	31	-0.0418	0.0564	90
6	0.0834	0.2107	0	32	-0.0418	0.0746	90
7	0.1419	0.2505	0	33	-0.0418	0.0929	90
8	0.1282	0.2505	0	34	-0.0418	0.1112	90
9	0.1144	0.2505	0	35	-0.0418	0.1295	90
10	0.1673	0.2863	0	36	-0.0418	0.1478	90
11	0.1536	0.2863	0	37	-0.0418	0.2147	90
12	0.1398	0.2863	0	38	-0.0418	0.2330	90
13	0.0623	0.2863	0	39	-0.0418	0.2513	90
14	0.0485	0.2863	0	40	-0.0418	0.2695	90
15	0.0348	0.2863	0	41	-0.0418	0.2878	90
16	0.0211	0.2863	0	42	-0.0418	0.3061	90
17	0.1902	0.3227	0	43	-0.0418	0.3244	90
18	0.1765	0.3227	0	44	-0.0418	0.3427	90
19	0.0986	0.3227	0	45	-0.0253	0.3610	0
20	0.0849	0.3227	0	46	-0.0253	0.3747	0
21	0.0712	0.3227	0	47	-0.0253	0.3884	0
22	0.0574	0.3227	0	48	-0.0253	0.4021	0
23	0.0437	0.3227	0	49	-0.0253	0.4159	0
24	0.0300	0.3227	0	50	-0.0253	0.4296	0
25	0.0163	0.3227	0	51	-0.0253	0.4433	0
26	0.2086	0.3548	0				

Note – (0,0) is at dynamic stagnation point of center vane in three vane cascade

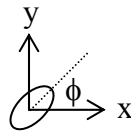
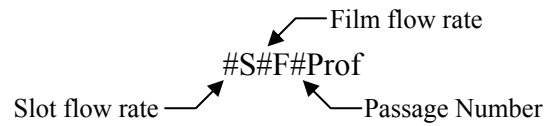


**Table 3.6** Experimental and Computational Test Matrix

Case	Slot Flow %m <sub>in</sub>	Film Flow %m <sub>in</sub>	Inlet Temp Profile	CFD	Thermal Field
1S0F0	0.50	---	Flat	Y	Y
2S0F0	0.75	---	Flat	N	N
3S0F0	1.00	---	Flat	Y	N
0S1F1	---	0.50	Flat	Y	N
0S1F2	---	0.50	Flat	Y	N
0S2F1	---	0.75	Flat	N	N
0S2F2	---	0.75	Flat	N	N
1S1F1	0.50	0.50	Flat	Y	N
1S1F2	0.50	0.50	Flat	Y	Y
1S1F2Bot	0.50	0.50	Bot	N	N
1S1F2Mid	0.50	0.50	Mid	N	N
2S1F1	0.75	0.50	Flat	N	N
2S1F2	0.75	0.50	Flat	N	N
1S2F1	0.50	0.75	Flat	Y	N
1S2F2	0.50	0.75	Flat	Y	Y
2S2F1	0.75	0.75	Flat	N	N
2S2F2	0.75	0.75	Flat	N	N

Key:



Number	Passage Number	Flow Rate %m <sub>in</sub>
0	No Film-Cooling	No Cooling
1	1	0.50
2	2	0.75
3	---	1.00

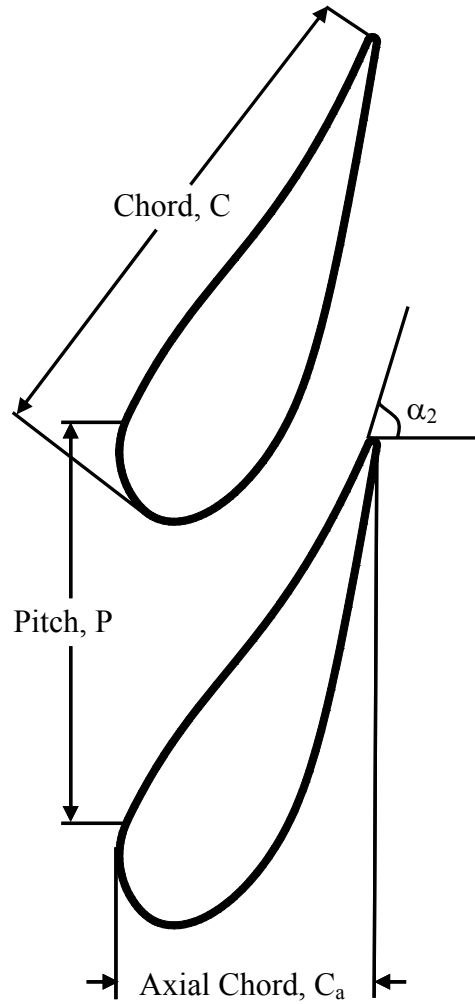


**Figure 3.1** Characteristic lengths used to define airfoil geometry

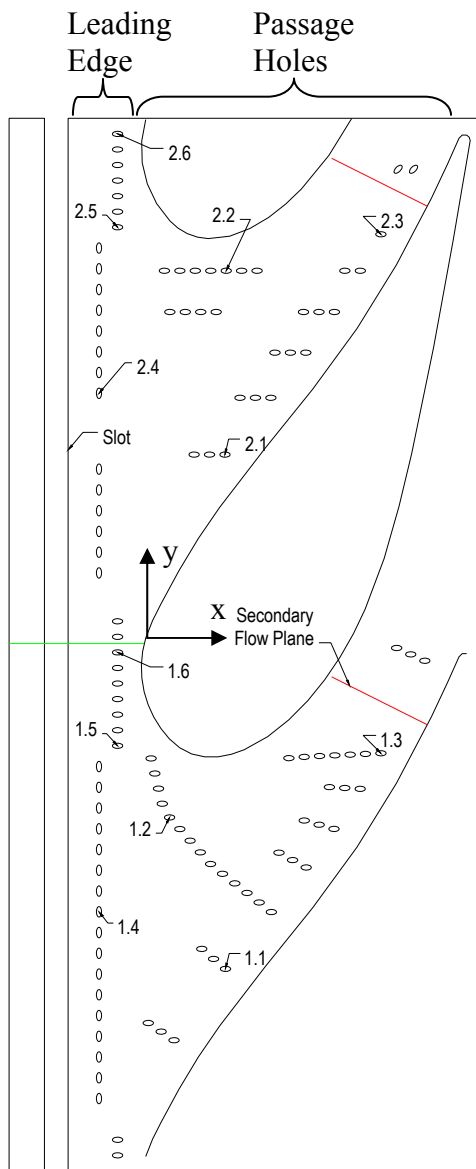


**Figure 3.2a** The two film-cooling patterns that were designed for this study (Pattern #1 and #2) and labels for several specific film cooling holes. In addition, a secondary flow plane is identified that was used to evaluate the flow field.

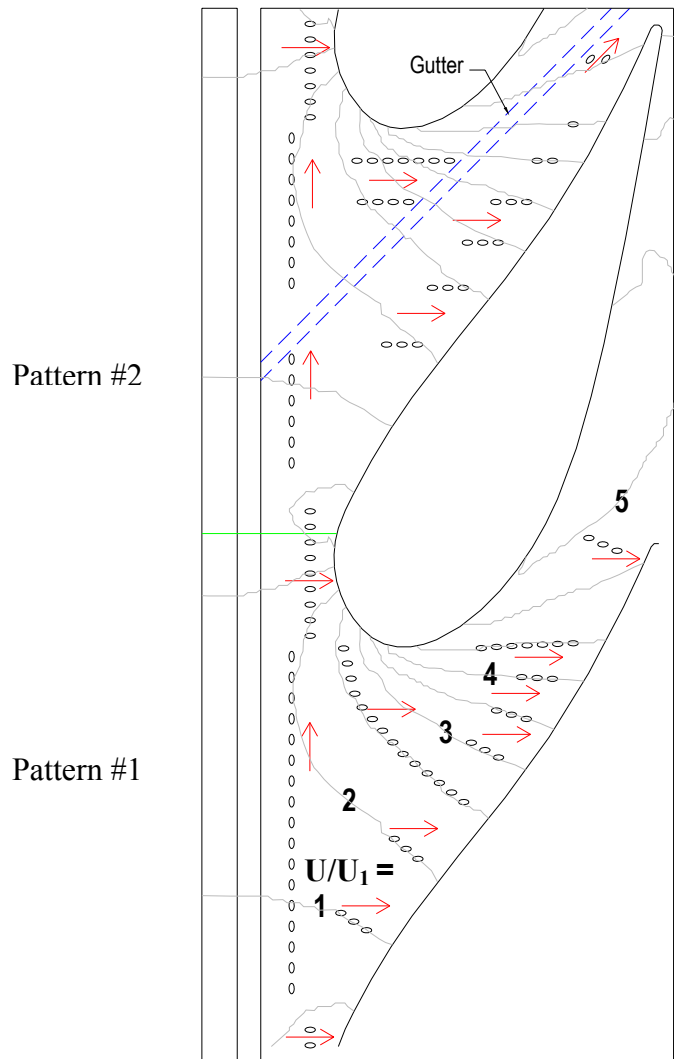


**Figure 3.2b** Shown are the directions of the coolant hole injection along with iso-velocity contours ( $U/U_1$ ) and the gutter location for mating two turbine vane platforms.

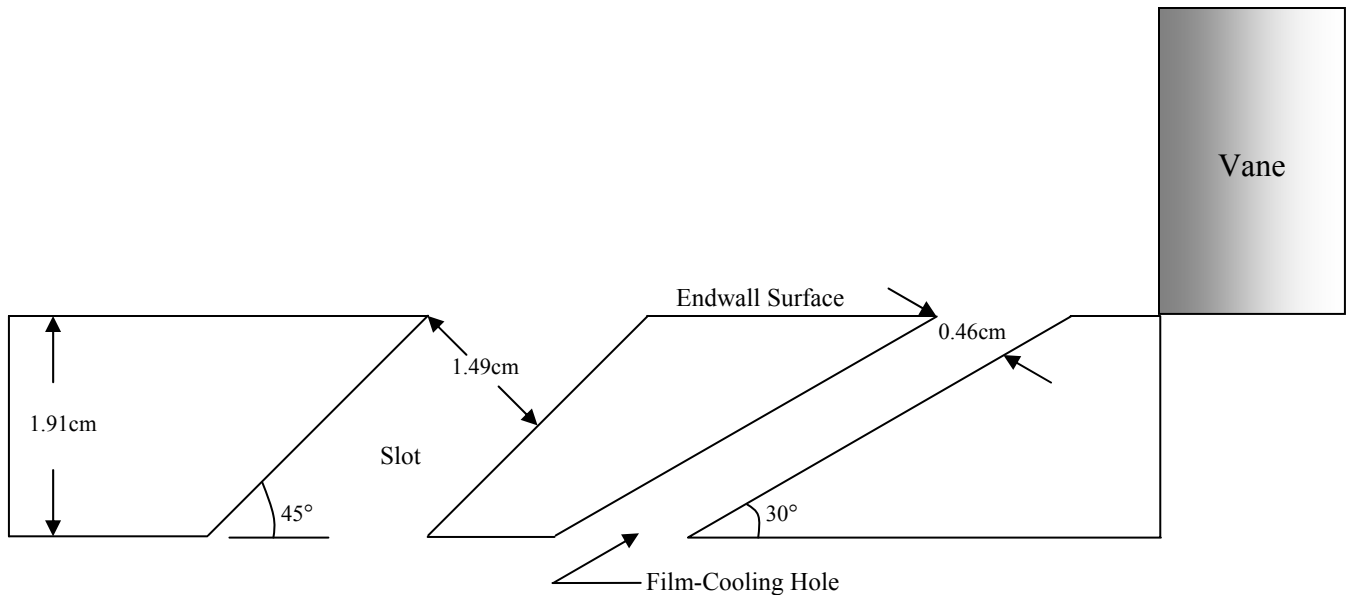


**Figure 3.3** Critical dimensions of the slot and film-cooling holes at model scale (9X) .  
 Note that the figure is not drawn to scale.

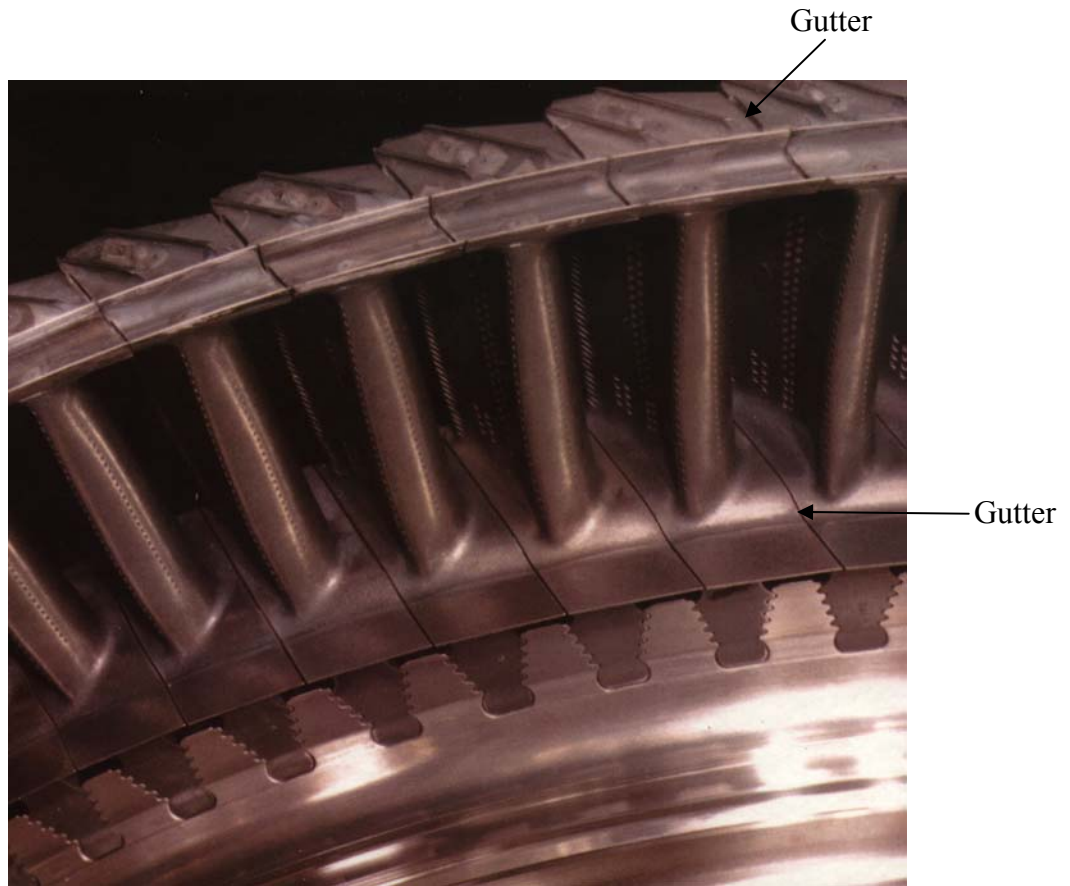


**Figure 3.4** A turbine disc is shown with the gutter(s) marked. The stators shown are singlets, but stators are often grouped as doublets (Cohen, 2001).

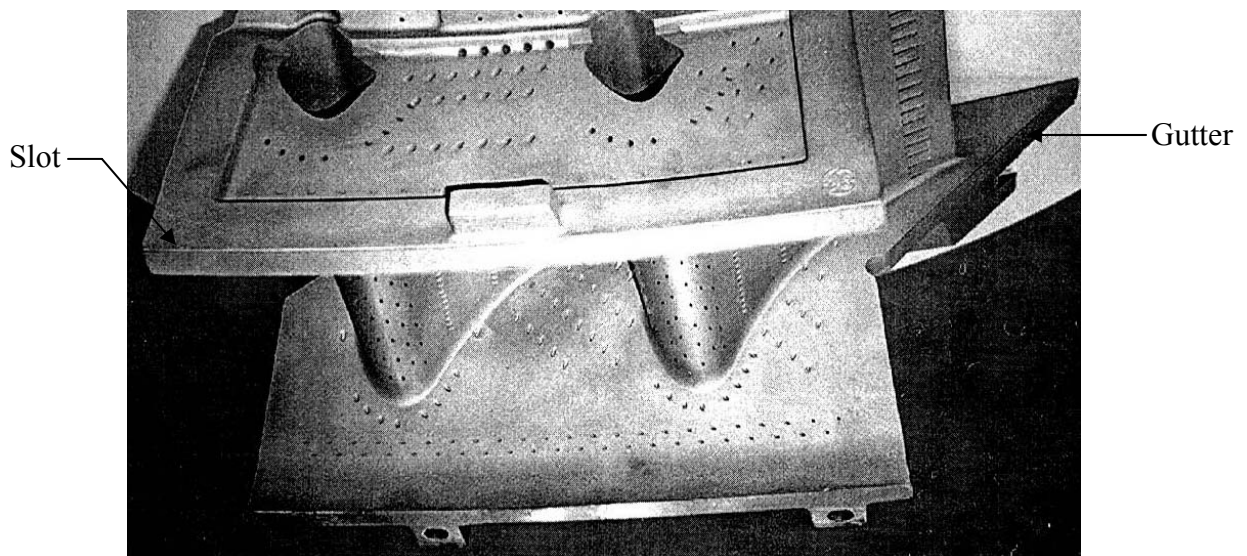


**Figure 3.5** Nozzle guide vane doublet shown with vane and endwall film-cooling holes. Gutters would be formed by adjoining another doublet to each side. Slot leakage would come from the upstream edge (Friedrichs, 1997).

## **Chapter 4**

### **Computational Methods**

Computational fluid dynamics (CFD) is a powerful tool which has become invaluable in the modern design process of fluid machinery. CFD easily facilitates parametric studies and allows a designer to test multiple design configurations at low expense and in a brief time frame. Many choices must be made during the modeling process, however, that automatically constrain the solution set before computation has begun. Some decisions may not have an adverse effect on the results. The domain is generally modeled in a geometrically correct fashion, but if a feature is unimportant to the solution it may be altered without consequence. For example, a hexagonal bolt head may be modeled as a cylinder if it is not in a region of interest. Other decisions may have far more significant impacts, though. Are the boundary conditions appropriate? Is the flow incompressible or should a variable density model be considered? Is transient behavior important?

The focus of this chapter is to explain the modeling procedures and choices that were made in this study. Section 4.1 describes the construction and meshing of the model. Section 4.2 presents the applied boundary conditions. Section 4.3 discusses the governing equations and the methods used to solve them. The turbulence model is discussed in section 4.4. Much of the discussion in sections 4.3 and 4.4 was excerpted from the thesis of Erik Hohlfeld. The convergence requirements as well as grid adaption and the characterization of grid independence of results are presented in section 4.5. Finally, section 4.6 describes the methods used to process the data from the computational results.

#### **4.1 Construction and Meshing of Model**

The first step in the computational process is constructing the model. The model was developed in Gambit, which is the modeling and meshing companion to the solver Fluent. Five permutations of the model were constructed: (1) slot only; (2) film-cooling pattern #1 without the slot; (3) film-cooling pattern #2 without the slot; (4) film-cooling pattern #1 with the slot; and (5) film-cooling pattern #2 with the slot. Included in the

models were: the vane (modeled to midspan) with the pressure and suction surfaces forming one passage, endwall, film-cooling holes, slot, and a  $15.6^\circ$  contraction which was part of the combustor simulator section of the wind tunnel where experimental data was acquired. Two views of the computational domain are shown in Figures 4.1a-b. The combined slot and film-cooling models for each of the two patterns are shown in Figures 4.2a-b. The only differences are the location and number of film-cooling holes. The coolant for the slot and film-cooling holes was supplied through two plenums allowing individual control of the flow through both of the cooling features.

The model was built by starting with vertices defining all features. The vertices were then connected forming lines and the lines were connected to form faces. Finally the faces were stitched together to form the volumes. The main passage, as well as the film-cooling holes and the film plenum were modeled as individual volumes to allow greater control when meshing. The volumes were merged together to form a single volume and the holes and plenum were then re-divided using split planes at the endwall level and at the plenum level to regain the individual volumes. This step was necessary to establish connections between the volumes so that the mesh would be conformal at the volume interfaces.

Meshing proceeded in the same fashion. First the periodic faces, which will be discussed in section 4.2, were linked so that the mesh on each matching face would be identical. Next the edges were meshed to control the cell size. Features within the passage were given uniform node spacing. The node spacing for each of these features is given in Table 4.1. Edges upstream and downstream of the passage were graduated so that the cell size would expand further away from the passage to avoid wasting cells in areas where the flow was inviscid with few gradients. Table 4.2 lists the cell edge length near the passage and the larger cell edge length away from the passage for these edges.

Next the faces were meshed with a tri-pave routine using the maximum node spacing for the given feature. For example, the nodes within the passage were spaced 8 mm apart while the nodes in the holes were spaced only 2 mm apart. When meshing the endwall, which is part of the passage but has the holes in it, the face mesh cell size was specified as 8 mm. Therefore the maximum cell size was 8 mm, but near the holes the cell size was reduced to 2 mm because of the conformal meshing routine. The mesh on

the endwall of each pattern is shown in Figures 4.3a-b. Finally the volumes were meshed once again using the maximum desired cell edge length within the particular volume. An unstructured mesh consisting of tetrahedral elements was generated. The holes were meshed first with a cell edge length of 2 mm resulting in approximately 500 cells per film-cooling hole. Then the hole plenum was meshed. The mesh in the holes and hole plenum of pattern #2 is shown in Figure 4.3c. The reduced size of the cells near the holes are clearly visible in this figure. Finally the main passage was meshed as shown in Figure 4.4 resulting in approximately  $7 \times 10^5$  cells in the model. It is seen that the mesh is graduated so that larger cells exist near the inlet and outlet where the flow field is less complex with smaller cells in the passage. The mesh is also graduated from the wall, where viscous effects, are present to the midspan where the flow is inviscid.

## 4.2 Boundary Conditions

After meshing, the entire domain was specified as a continuum and boundary conditions were applied as shown in Figures 4.1a-b. The vane was divided at the dynamic stagnation point and trailing edge, and a single passage was modeled with periodic boundaries specified in both the leading and trailing planes to reduce the size of the model. The model size was further reduced by imposing a symmetry condition at midspan. No-slip was imposed at the combustor wall, endwall, and vane surfaces. The inlet to the domain was specified as a velocity inlet and located one chord upstream of the contraction. Hermanson and Thole (2000) showed that a velocity inlet located at least one chord upstream of the vane would exhibit no effects from the vane. The velocity inlet gives the option to model various profiles as inlet conditions. For the cases presented, however, only a uniform velocity of approximately  $U_{in} = 3.6$  m/s and a uniform temperature of  $T_{in} = 333.15$  K were specified. Figures 4.5a-b show that at the exit of the combustor, though, the inlet velocity is no longer uniform as a result of pressure distortion by the vane immediately downstream. Also, a reference pressure of 101,325 Pa was specified at midspan in the center of the velocity inlet. An outflow boundary was located 1.5C downstream of the trailing edge. In addition, a 0.5C extension was added to the exit of the domain to avoid highly skewed cells at the domain exit. As stated previously, the coolant was supplied through two plenums. Mass flow

inlets were imposed at the entrances of the plenums and the appropriate flow rate (kg/s) at  $T_c = 291.15$  K was specified for each computation.

### 4.3 Governing equations and solution methods

Computations were performed for incompressible, viscous, low-speed conditions with an exit Reynolds number of  $Re_{ex} = 1.2 \times 10^6$  based on the vane chord. The simulations were performed using the FLUENT commercial software package (Fluent 2002). FLUENT/UNS is a pressure-based, incompressible flow solver for unstructured meshes. FLUENT/UNS allows for unstructured meshing capability and also allows solution-adaptive mesh refinement in order to resolve regions of high gradients. Solutions were computed on one of two UNIX computer systems: the SGI Origin 2100, located in the VTeXCCL computer laboratory and the ICAM SGI Origin 2000, located at the Interdisciplinary Center for Applied Mathematics on the Virginia Tech campus. The Origin 2100 is a four processor machine while the Origin 2000 has 32 processors. Solution times varied substantially based on the mesh size and the number of processors over which the model was distributed. Generally, a solution could be obtained within 48 hours when divided over 3-4 processors.

The Reynolds Averaged Navier Stokes (RANS) equations as well as the energy and turbulence equations were solved using a control volume technique. Fluent offers two solver options: a segregated solution algorithm (FLUENT/UNS) using a control volume based technique or a coupled solver (RAMPANT) also employing a control volume technique. The basic premise behind the segregated solver, which was used exclusively in this study, involves the integration of the mass, momentum, energy and turbulence equations for each unknown variable. The discretized equations are then linearized with a solution of the resulting system of linear equations providing updated results to the unknown variables.

The governing equations were solved sequentially employing an implicit form of linearization where, for each variable, the value of interest in each cell was computed through the use of equations that used both known and unknown values from various neighboring cells. Ultimately each unknown appeared in a series of equations that must

be solved simultaneously. A converged solution requires multiple iterations and included the following general process:

- (1) fluid properties are updated with the current solution,
- (2) the u, v, w momentum equations are each solved with current values for pressure and mass fluxes to update the velocity field,
- (3) the velocities from step one may not locally satisfy the continuity equation so adjustments are made by correction equations so that continuity is satisfied,
- (4) scalar equations are solved for such things as turbulence and energy with the previously updated values from other variables, and
- (5) a convergence check is made of the equations.

Fluent offers several discretization techniques for the convective terms of each governing equation. Using the segregated solver, the operator may choose to have either first or second order discretization of terms. The first order method computes the solution at the center of each cell while the second order method computes the solution at the center of each face (Fluent 2002). The first order discretization is generally acceptable for simple flows when the grid is aligned with the flow and a quadrilateral or hexahedral grid is in place. A second order discretization method reduces errors over the first order methods, while generally increasing the difficulty of obtaining a converged solution. For triangular and tetrahedral grids when the flow is not aligned with the grid, a second order method is recommended for superior results. The second order discretization was used for all simulations in this study.

Pressure and velocity were coupled with the Semi-Implicit Method for Pressure Linked Equations (SIMPLE) algorithm. SIMPLE uses a relationship between velocity and pressure corrections to obtain mass conservation and a pressure field. The pressure discretization scheme was the default value, Standard.

Before beginning computation, the flow within the model must be initialized based on some condition within the model. This initialization process acts as an initial guess at the solution of the flow field. The flow field was initialized by the inlet conditions to the model for all simulations.

#### 4.4 Turbulence and near-wall modeling

Because of the numerous cooling jets injecting through the endwall, the boundary layer was assumed turbulent. All simulations employed the RNG k- $\epsilon$  turbulence model with non-equilibrium wall functions. Past studies by Hermanson (1999) and Radomsky (2000) have shown this method to adequately model secondary flows within a turbine passage. The RNG k- $\epsilon$  model was derived from the instantaneous Navier-Stokes equations. The analytical derivation results in a model with constants that are different from those used with the standard k- $\epsilon$  models. Additional terms and functions are also present in the transport equations for k and  $\epsilon$ .

An RNG k- $\epsilon$  turbulence model is generally very similar in form to the k- $\epsilon$  model, with the following refinements:

- (1) the RNG model has an additional term in its  $\epsilon$  equation that significantly improves the accuracy for rapidly strained flows (such as that seen in a blade passage),
- (2) the effect of swirl on turbulence is included in the RNG model, enhancing accuracy for swirling flows,
- (3) the RNG theory provides an analytical formula for turbulent Prandtl numbers, while the standard k- $\epsilon$  model uses user-specified, constant values, and
- (4) while the standard k- $\epsilon$  model is a high-Reynolds-number model, the RNG theory provides an analytically-derived differential formula for effective viscosity that accounts for low-Reynolds-number effects. Note that effective use of this feature does depend on an appropriate treatment of the near-wall region.

Two approaches to predicting the near-wall region are illustrated in Figure 4.6. The near-wall flow can be predicted through near-wall modeling or the use of wall functions. The near-wall modeling approach involves a very fine mesh near the wall that must transition to a larger mesh in the free stream. The near-wall model permits the viscosity-affected region to be fully resolved all the way to the wall. Wall functions do

not fully resolve the viscous sub-layer and buffer layer, leaving semi-empirical formulas to bridge the viscosity-affected region between the wall and the mainstream turbulent flow. Within the figure notice that the wall functions method maintains a relatively large mesh from the free stream down to the wall where the wall models take over.

The wall-function approach offers a significant savings in computational resources over near wall modeling by using a collection of formulas and empirical data to approximate laws-of-the-wall for mean velocity and temperature and formulas for near-wall turbulent quantities. There are some instances when wall functions may not always be accurate because of a departure from ideal conditions that include strong body forces, severe pressure gradients which may lead to boundary layer separation, highly three-dimensional effects near the wall, and large blowing and suction around the wall.

Fluent offers two types of wall functions: standard wall functions and non-equilibrium wall functions, both of which require the non-dimensionalized  $y^+$  values of turbulence to be resolved to levels between 30 and 60. The standard wall functions are based on proposals by Launder and Spalding (1974) while the non-equilibrium wall functions offer several modifications to the standard function. Included in these modifications is a log-law that is sensitized to pressure-gradient effects and the two-layer-based concept that computes turbulent kinetic energy in neighboring cells. Generally, non-equilibrium wall functions are considered more robust and accurate than the standard wall function. Because of limited computing power, non-equilibrium wall functions were used in all computations in this study to approximate the viscous near-wall layer.

The free stream turbulence intensity was set at 1% with a dissipation length scale of 0.1m. This low turbulence was set because an industrial application was being simulated where large dilution jets are not used in the combustor to mix the flow.

#### **4.5 Convergence, Grid Adaption and Independence**

The basic method employed in this study to judge the convergence of a solution involved monitoring the normalized residuals of the continuity, x-, y- and z- momentum, energy, k and  $\epsilon$  after each iteration. The normalized residuals are calculated by first finding the unscaled residuals. The unscaled residuals are the result of computations that have some numerical errors and as these solutions run through many iterations the

numerical errors become smaller and smaller, normally dropping several orders of magnitude. In order to judge convergence it is most convenient to monitor the scaled (normalized) residuals. Taking the largest residual values from the initial iterations and dividing each subsequent residual value by this number will provide a scaled residual. Most models experience significant noise in the residual values during the initial iterations followed by a smooth decaying slope of these quantities.

There is no exact rule for determining when a solution is complete. Fluent has default residual values of convergence set to  $10^{-3}$  for all quantities except energy, which is set to  $10^{-6}$ . For this study the residual levels for convergence were lowered to values of  $10^{-4}$  with the exception of energy which was required to reach  $10^{-7}$ .

During initial computations the residuals would decline for approximately 200 iterations before going unstable as shown in Figure 4.7a. To prevent this problem, the under relaxation factors were reduced to the values listed in Table 4.3. When computing a solution the value of interest,  $\phi$ , is computed at each step by:

$$\phi_{\text{new}} = \phi_{\text{old}} + \alpha\Delta\phi \quad (4.1)$$

where  $0 \leq \alpha \leq 1$  is called the under relaxation factor. Reducing the under relaxation factors acts as a numerical brake to slow and control the computation. Originally all under relaxation factors were reduced to the values suggested in the Fluent manual to prevent instability. This was effective, but the convergence of the solution was quite slow. Then, because the instability originated in the energy equation and a constant ideal gas density model was used, only the energy and density under relaxation factors were reduced. As seen in Figure 4.7b, this was effective in controlling the convergence of the solution while still converging at a reasonable rate.

For this study a solution was computed for 1000 iterations after which the residuals had not reduced to the convergence limits of  $10^{-7}$  for energy and  $10^{-4}$  for everything else, but the solution was unchanging. The grid was then adapted based upon  $y^+$  values and temperature and velocity gradients. All cells where  $30 \leq y^+ \leq 60$  was not true were marked for adaption. Then the maximum temperature and velocity gradients were calculated and any cells with gradients higher than half of the maximum were marked for adaption. The gradient marking technique generally only resulted in a few thousand marked cells most of which had already been marked because of  $y^+$  values. The

grid was then adapted using the hanging node method illustrated in Figures 4.8a-c. Each cell is subdivided along each leg resulting in eight tetrahedrons from a single tetrahedron shown in Figure 4.8c. The method is called hanging node because, as shown in Figure 4.8a, adapted cells will have nodes that are not shared with a neighboring cell. This results in a non-conformal grid at these locations. The adapted grid on the endwall is shown in Figures 4.9a-b. It is important for the user to note that cells may only be expanded (combined) in a 2-D grid and then the combination of cells is limited to the original grid (original cells may not be combined to generate super cells). Therefore, it is preferable to start with larger cells and adapt in the necessary areas rather than starting with a grid that is too fine. After adaptation the computation was continued for another 1000 iterations. The adaptation results in a large increase in the residuals during the first few iterations as seen in Figure 4.7b. Another adaptation was performed resulting in a mesh with approximately  $1.3 \times 10^6$  cells, and finally 1000 more iterations were computed.

To evaluate whether results were grid independent, the lift coefficient and area-averaged endwall temperature were also monitored after each iteration. As seen in Figures 4.10a-b, these values are relatively constant even after the two grid adaptations. After adapting from a mesh size of  $8.5 \times 10^5$  to  $1.3 \times 10^6$  cells the area-averaged effectiveness predictions on the endwall were found to vary by only  $\Delta\eta = \pm 0.005$  at a level of  $\eta = 0.11$  indicating that the solution was converged and grid independent despite failing to reach the specified residual levels. In order to use these additional monitors, a solution was first computed for five iterations to get the solution started and then the monitors were activated.

#### **4.6 Data Post-Processing**

To visualize the secondary flow patterns throughout the passage a method was developed by Hermanson and Thole (2000) where secondary flow vectors are presented as in plane deviations from the midspan streamlines. The calculation procedure is given in equations 4.2 through 4.12 and illustrated in Figure 4.11. Fluid flow at the mid-span is assumed as the reference condition because no viscous effects are present. Variations from this reference flow path are plotted as secondary flows within the turbine passage. The general methodology employed for this visualization technique involves a

transformation from the global  $-X, -Y, -Z, -U, -V, -W$  system to a local  $-x, -y, -z, -u, -v, -w$  system. The entire transformation is based on the rotation,  $\phi$ , of a plane normal to the vane surface from the axial direction. The in plane calculations are as follows:

$$x = X \cos \phi + Y \sin \phi \quad (4.2)$$

$$y = -X \sin \phi + Y \cos \phi \quad (4.3)$$

$$z = Z \quad (4.4)$$

$$u = U \cos \phi + V \sin \phi \quad (4.4)$$

$$v = -U \sin \phi + V \cos \phi \quad (4.6)$$

$$w = W \quad (4.7)$$

Phi was calculated from known points along the vane surface on either side of the plane

$$\phi = \tan^{-1} \frac{\Delta Y}{\Delta X} \quad (4.8)$$

The flow angle of the inviscid flow at the midspan was calculated from:

$$\Psi_{ms} = \tan^{-1} \frac{V_{ms}}{u_{ms}} \quad (4.9)$$

After obtaining an angle for  $\Psi_{ms}$ , a translation from the local coordinate system consisting of  $-x, -y, -z$  and  $-u, -v, -w$  to a coordinate system in the form of a tangential and normal component to the inviscid streamline was necessary. The equations used for this transformation consisted of the following:

$$V_s = u \cos \Psi_{ms} + v \sin \Psi_{ms} \quad (4.10)$$

$$V_n = -u \sin \Psi_{ms} + v \cos \Psi_{ms} \quad (4.11)$$

$$V_z = w \quad (4.12)$$

This concluded the transformation. Plots were then constructed with the components  $V_n$  and  $V_z$  illustrating the off-axis flow phenomena (secondary flows).

Two dimensionless thermal values were also computed. The adiabatic effectiveness level,  $\eta$ , and the dimensionless temperature,  $\theta$ , represent surface and fluid temperatures respectively. They are calculated in the same fashion:

$$\eta = \frac{T_{aw} - T_\infty}{T_c - T_\infty} \quad (4.13)$$

$$\theta = \frac{T - T_\infty}{T_c - T_\infty} \quad (4.14)$$

Once adiabatic effectiveness is known the temperature at the wall is simply a function of the coolant and mainstream flow. This is obtained experimentally by using a wall material of low thermal conductivity while computationally a wall boundary condition is set as adiabatic. For a value of  $\eta = 1$ , the wall would have the same temperature as the coolant and we would say the coolant effectiveness is at a maximum. For a value of  $\eta = 0$ , the coolant would have no effect on the wall temperature since it would be the same temperature as the mainstream flow. Simply put, surface adiabatic effectiveness measures the local fluid temperature. When measuring heat transfer within an engine often times the adiabatic wall temperature,  $T_{aw}$ , is used as shown in equation 4.15.

$$q_w'' = h(T_w - T_{aw}) \quad (4.15)$$

So, if the adiabatic wall temperature and heat transfer coefficient,  $h$ , are known then the metal temperature,  $T_w$ , can be predicted for any maximum and coolant temperatures and a given heat flux, or the heat flux can be determined from surface temperature measurements.

Non-dimensional fluid temperature is presented as  $\theta$  and similar to adiabatic effectiveness varies from zero to one. A value of zero corresponds to a fluid temperature of the mainstream gas,  $T_\infty$ , while a value of one corresponds to the temperature of the coolant,  $T_c$ . Normalizing the thermal field in this fashion allows for a direct comparison between the thermal field temperatures and the surface temperatures.

With all of the computational methods laid out and presented within this chapter, along with a general understanding of the data analysis techniques, the results from the computations are presented in chapter 6.

**Table 4.1** Cell Edge Length in Regions of Constant Cell Size

Feature	Cell Size (mm)
Holes	2
Hole Plenum	8
Slot	8
Slot Plenum	8
Endwall	8
Outflow	20

**Table 4.2** Beginning and Ending Cell Edge Length in Regions of Graduated Mesh Size

Edge	Start Cell Size (mm)	End Cell Size (mm)
Contraction Entrance to Contraction Exit	14	8
Velocity Inlet to Contraction Entrance	24	14
Inlet at Endwall to Inlet Midspan	24	30
Inlet at Midspan to Contraction Exit	30	8
Trailing Edge to OutFlow	8	20

**Table 4.3** Various Settings for Under Relaxation Factors

Variable	Default	Fluent Modified	Partially Modified
Pressure	0.3	0.2	0.3
Density, $\rho$	1	0.8	0.7
Body Force	1	0.8	1
Momentum	0.7	0.5	0.7
Turbulence Kinetic Energy, $\epsilon$	0.8	0.5	0.8
Turbulence Dissipation Rate, $\kappa$	0.8	0.5	0.8
Turbulent Viscosity	1	0.8	1
Energy	1	0.8	0.7

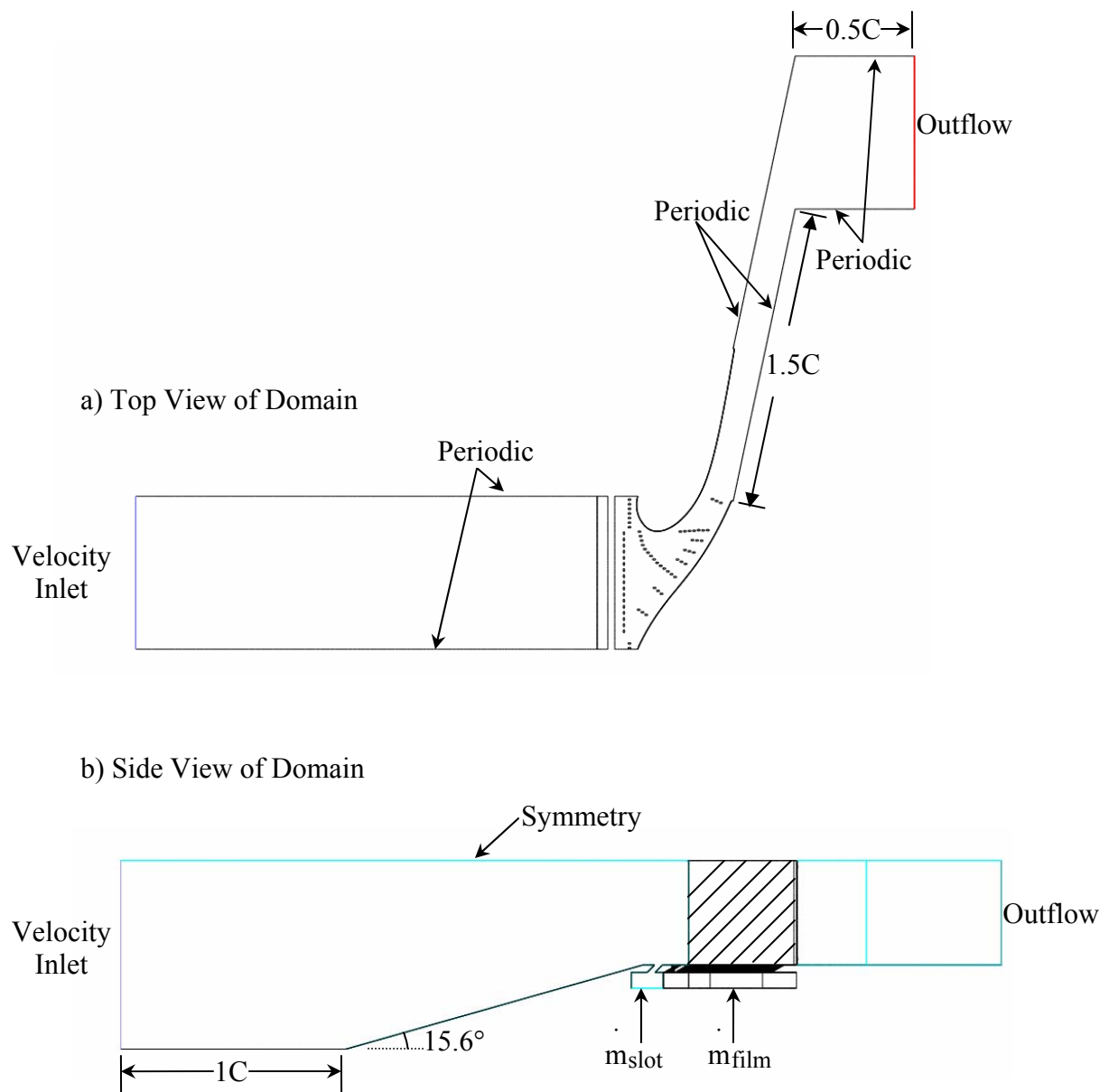


**Figure 4.1a-b** (a) Top and (b) side views of the computational domain are shown along with the boundary conditions. Symmetry and periodic boundary conditions were used to reduce the size of the model.

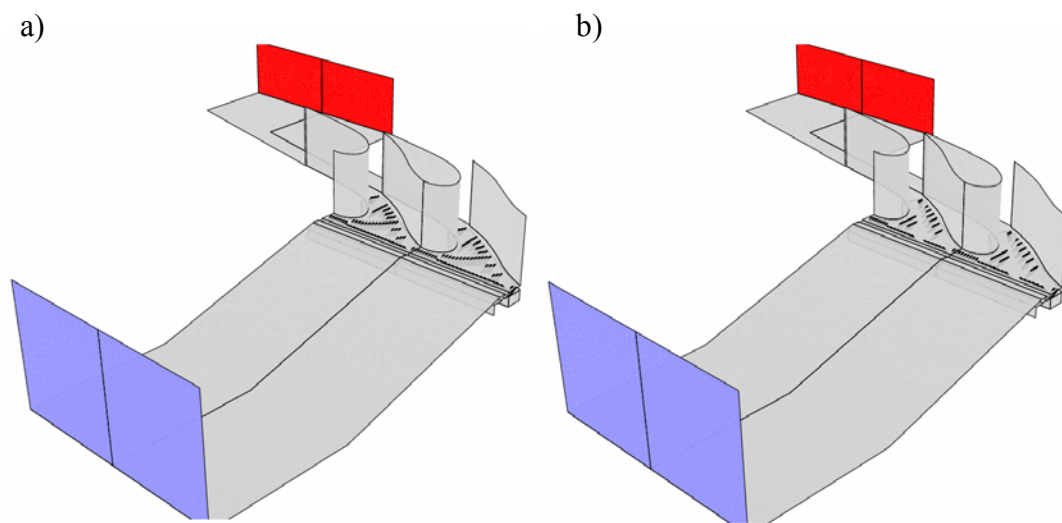


**Figure 4.2a-b** Models for the slot combined with (a) film pattern #1 and (b) film pattern #2 are shown with one periodic repeat. Models were also developed for each film-pattern without the slot and for the slot without film-cooling.

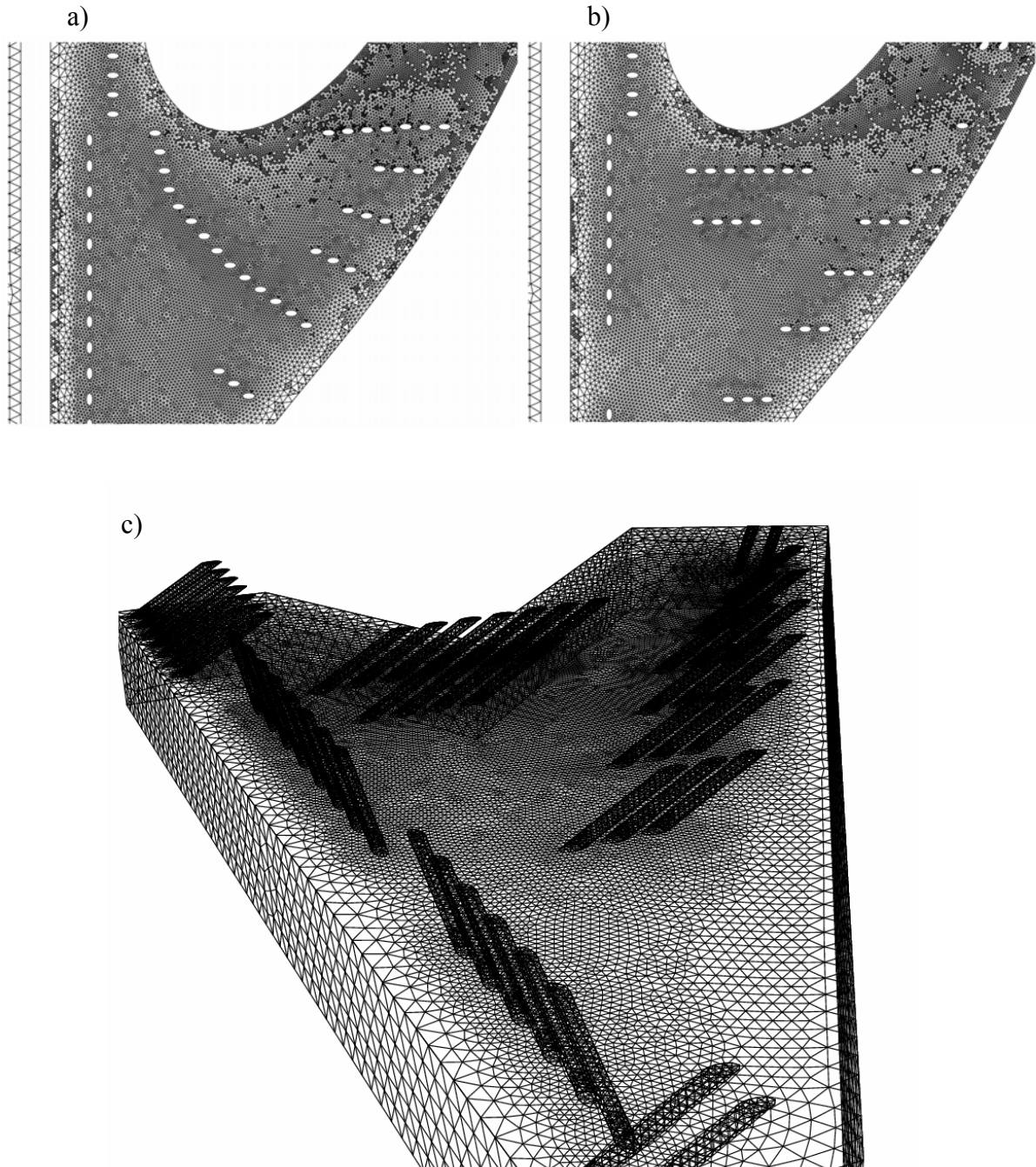


**Figure 4.3a-c** The face mesh on the endwall for (a) pattern #1 and (b) pattern #2 is shown. (c) The film-cooling holes and the film-cooling plenum were individually meshed. The reduction of cell size near the holes to maintain a conformal mesh is clearly visible.

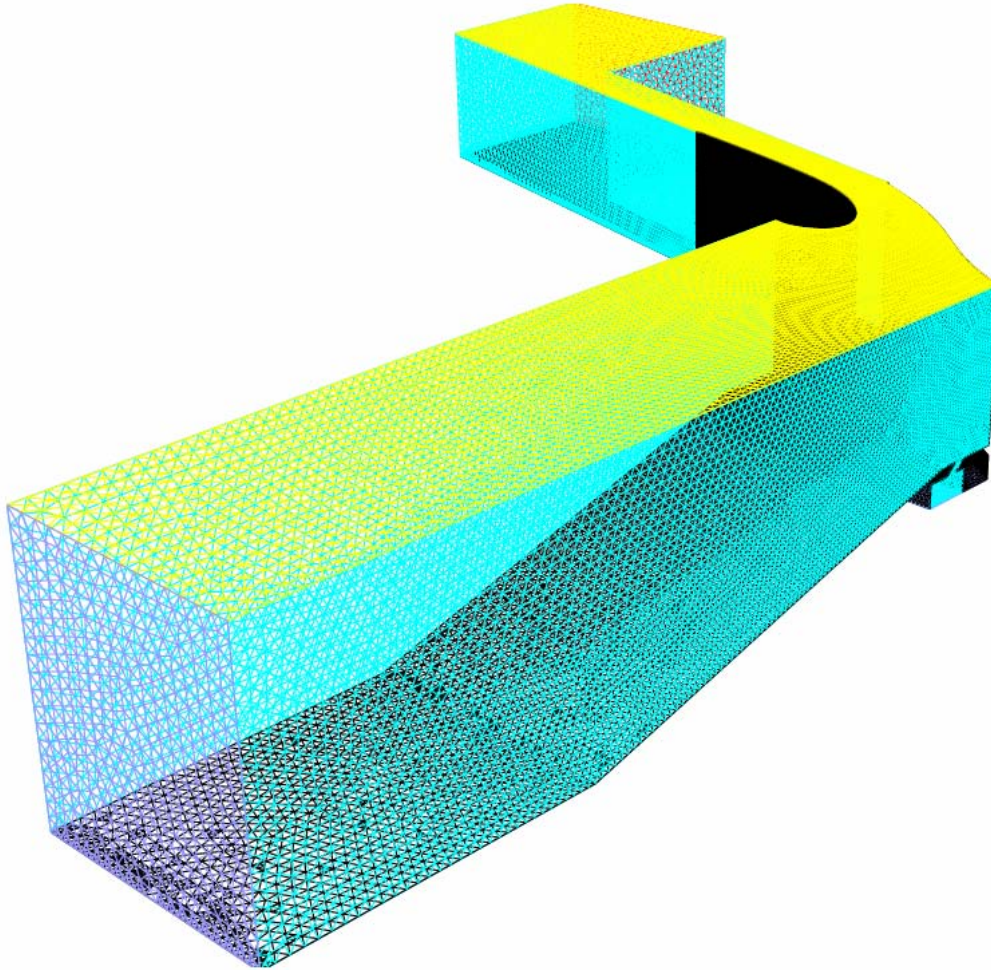


**Figure 4.4** The volume mesh for the entire domain is shown. The mesh is graduated so that larger cells exist near inlet and outlet where the flow field is less complex with smaller cells in the passage. The mesh is also graduated from the wall, where viscous effects are present, to the midspan where the flow is inviscid.

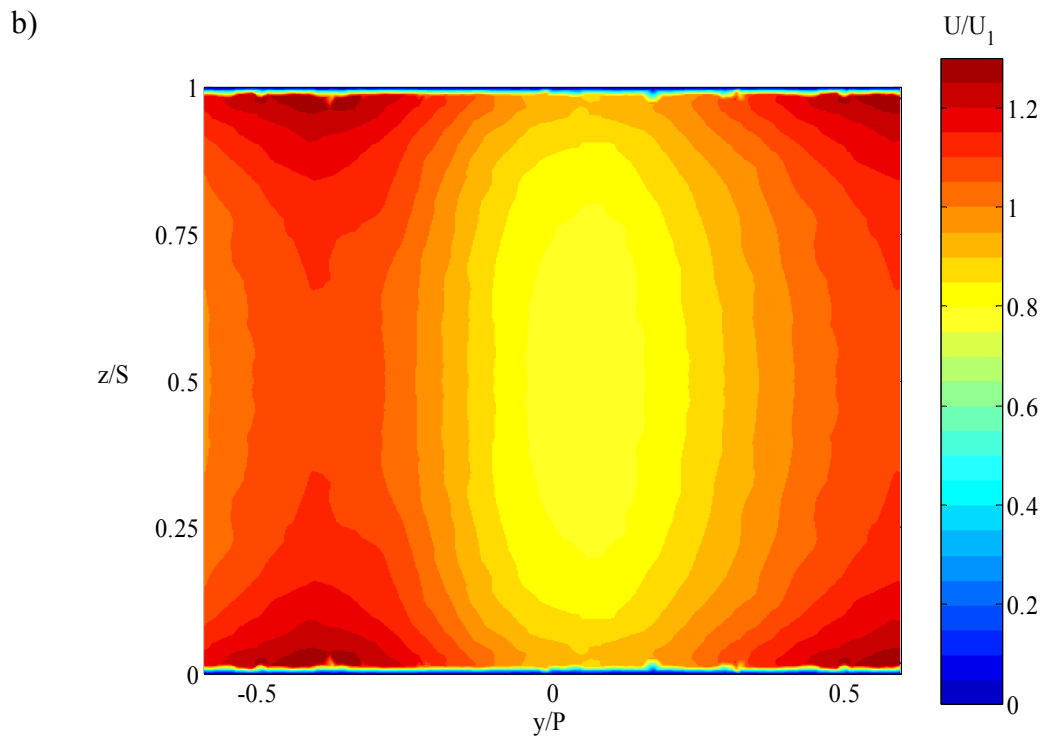
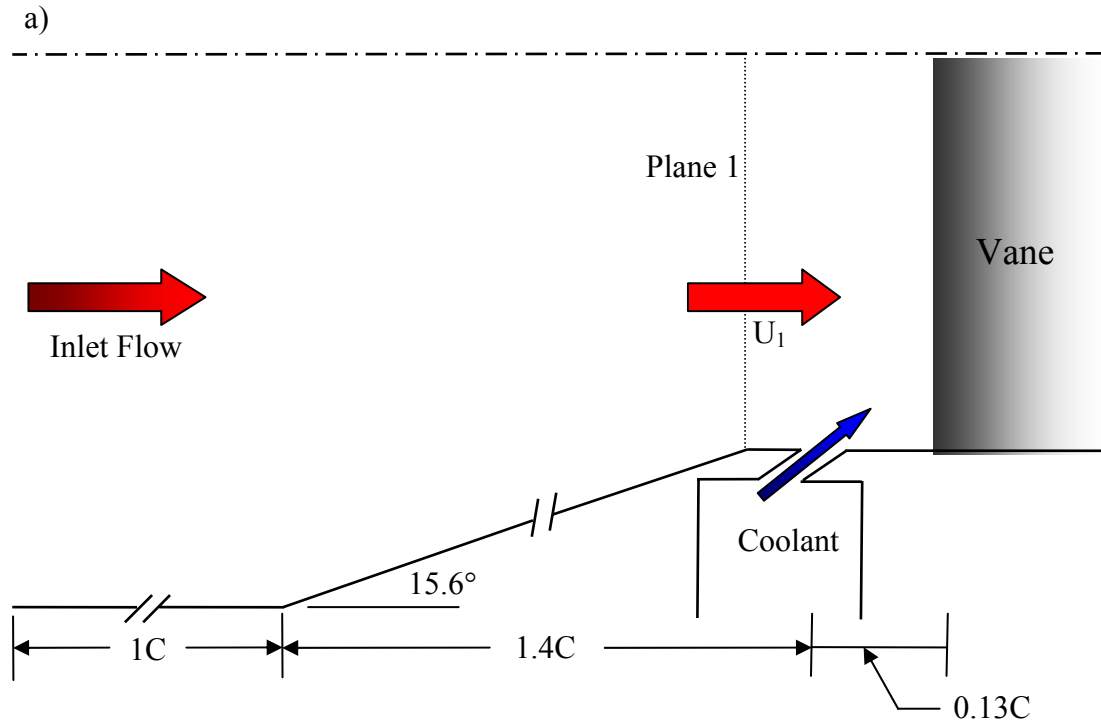


**Figure 4.5a-b** (a) While a uniform temperature and velocity profile are specified at the inlet to the vane, (b) at the combustor exit the approaching velocity field is distorted by the vane downstream.

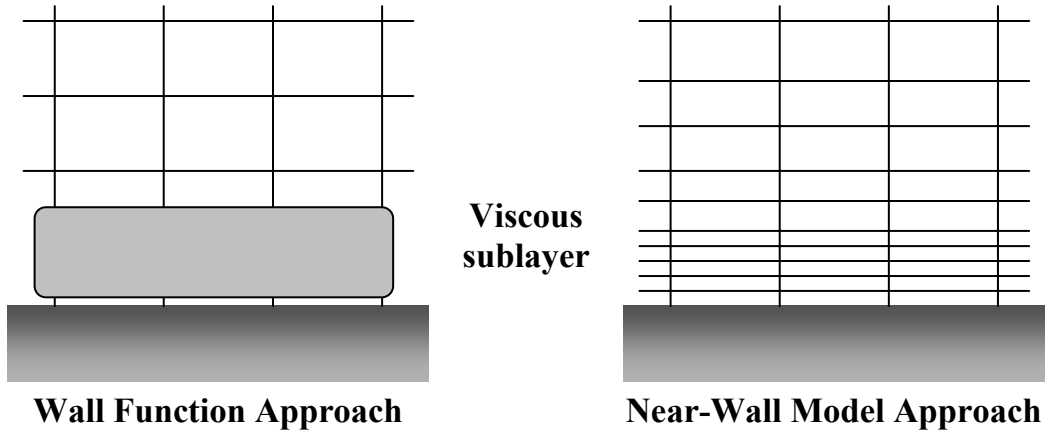


**Figure 4.6** The two methods for modeling the viscous boundary layer are illustrated. In the wall function approach, semi-empirical relations are used to predict the boundary layer while thin elements are used to compute the boundary layer in the near-wall modeling approach (Fluent 2002).

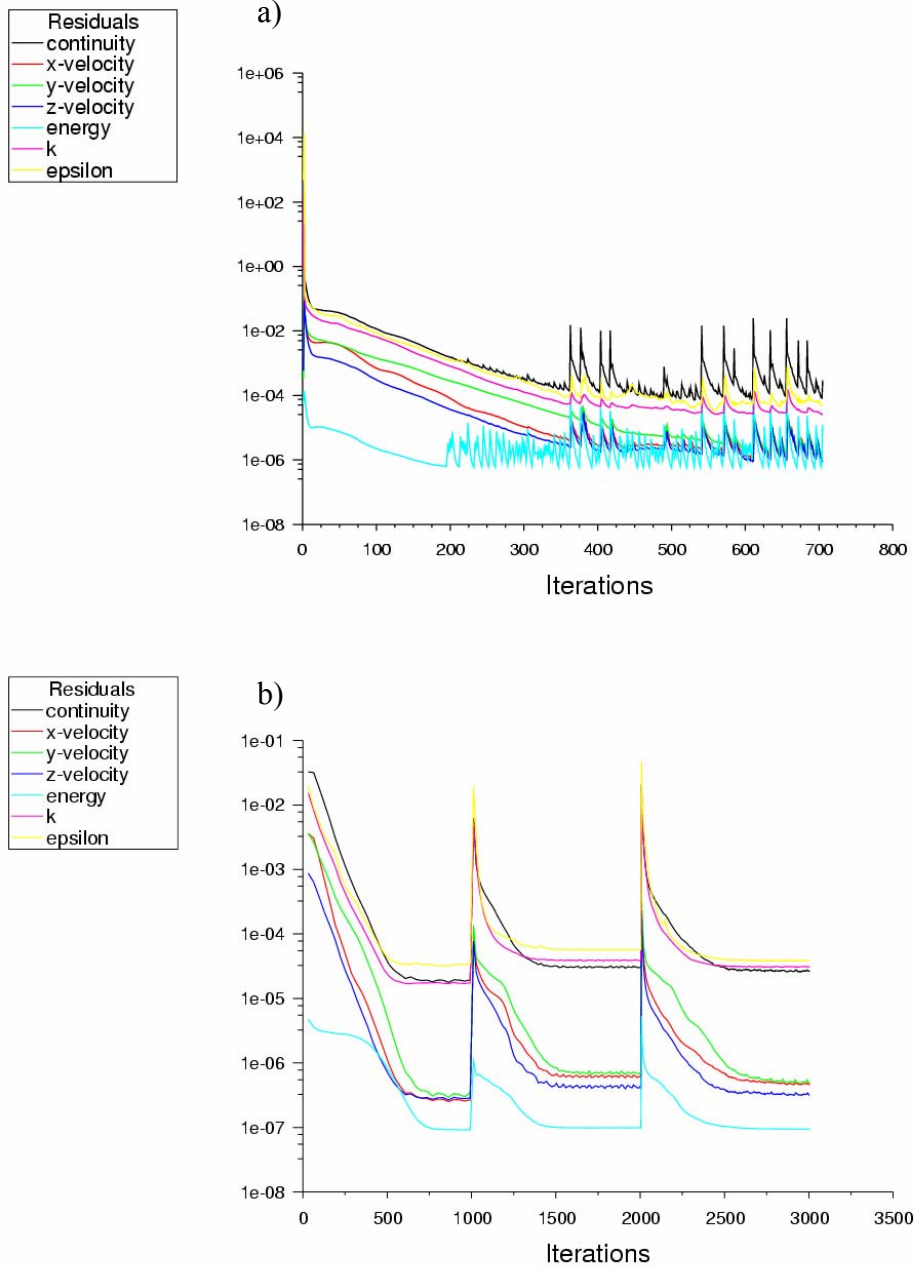


**Figure 4.7a-b** (a) Convergence of residuals in initial computations are shown to go unstable beginning with the energy equation. (b) By reducing the under relaxation factors to the values shown in the “Partially Modified” column of Table 4.3 the solution converged smoothly. The large jumps correspond to resumption of calculation after adapting the grid.

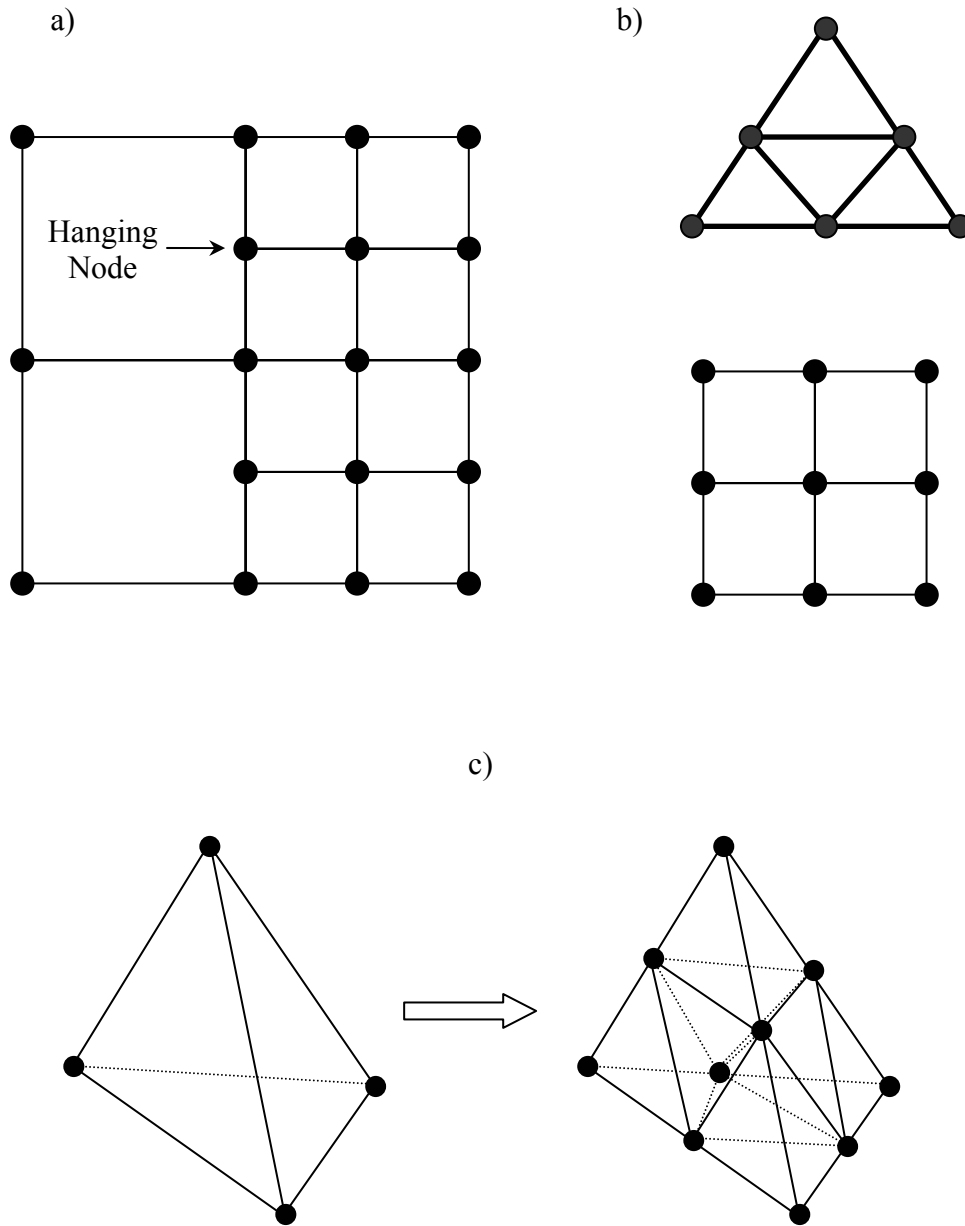


**Figure 4.8a-c** A hanging node adaption is shown in (a) where all nodes are not shared with a neighboring cell. Adaption of simple two-dimensional cells is shown in (b) while a more complex tetrahedral cell is divided into eight tetrahedrons in (c).

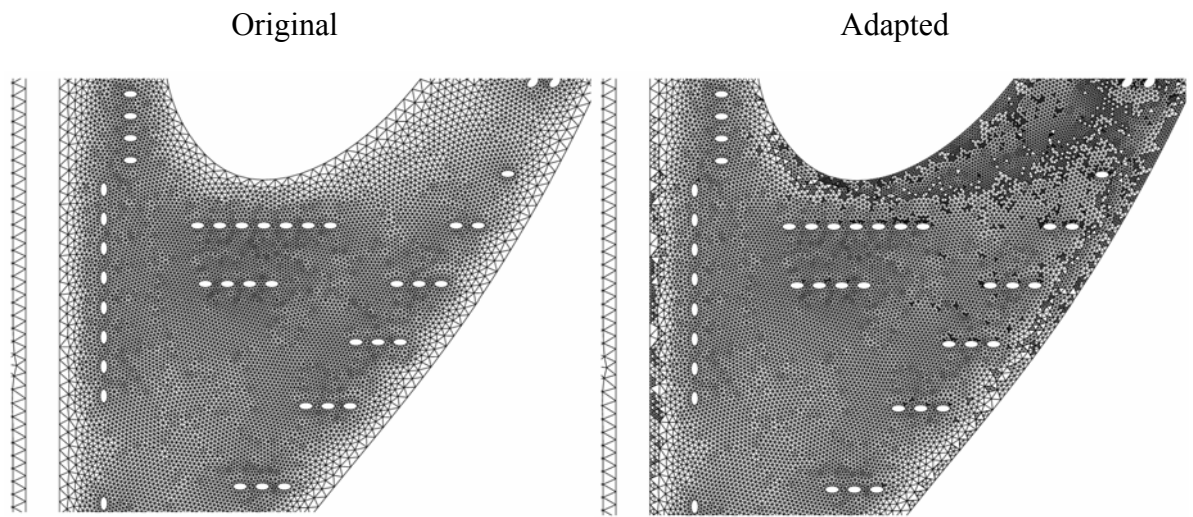


**Figure 4.9** The endwall grid is shown before and after adaption. Cells were added near the throat and along the vane surfaces to capture the accelerating flow.

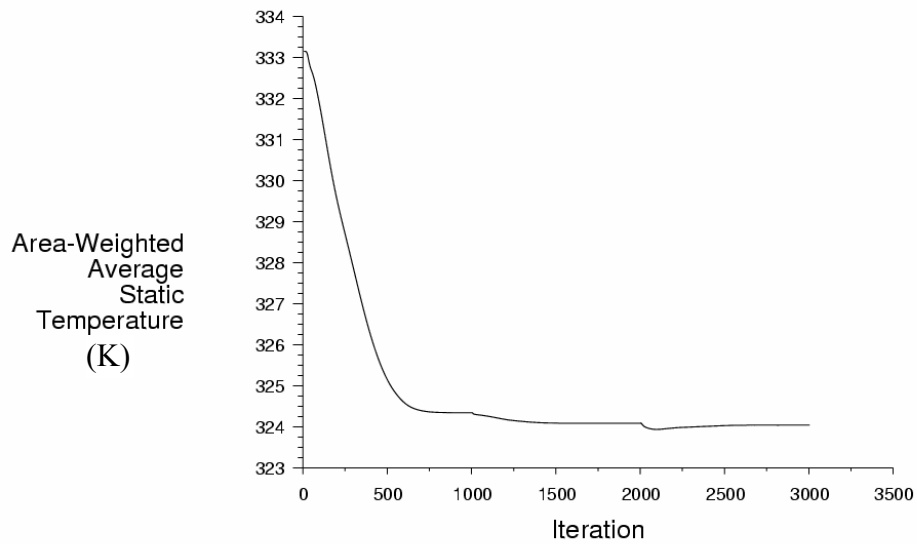
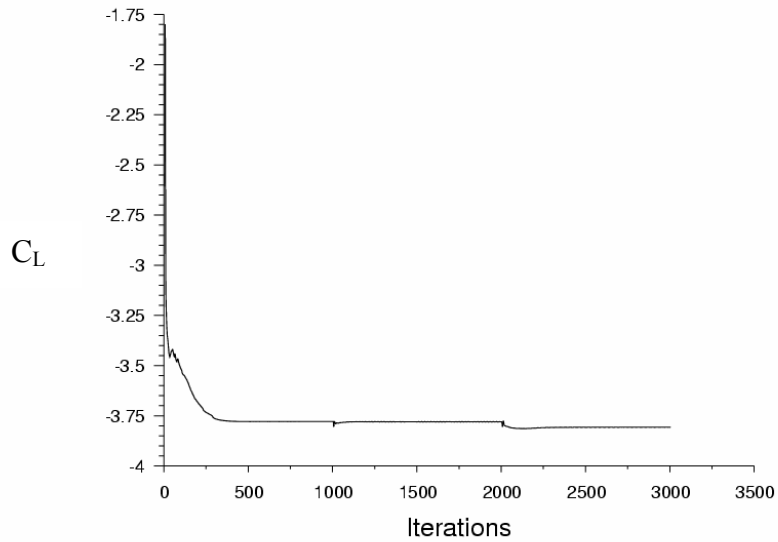


**Figure 4.10** The lift coefficient and area-averaged endwall temperature were used to evaluate grid independence of the results. The lift coefficient and average endwall temperature were not significantly altered despite adapting the grid after 1000 and 2000 iterations.

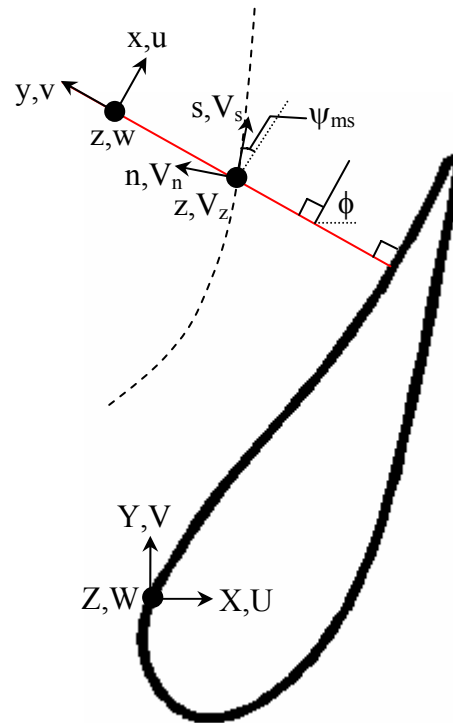


**Figure 4.11** Multiple coordinate systems are used to define the secondary flow vectors.

## Chapter 5

### Experimental Facility and Methods

Before presenting experimental results it is necessary to discuss the facility in which data was acquired. It is also important to detail data collection methods, measurement tools, and to explain the development of any data processing techniques. This chapter is dedicated to providing an overview of the facility and its capabilities. The chapter is also intended to elaborate on all instrumentation used in data collection and to explain the methods of setting up experiments and collecting and post processing data.

Section 5.1 provides an overview of the entire wind tunnel facility. The capabilities of the facility and the main components encountered by the flow are briefly discussed. Section 5.2 provides a more thorough discussion of the flow conditioning elements in the facility. Specific settings for this study are also presented. Section 5.3 details the construction of the slot and film-cooling test plate. Section 5.4 presents a general discussion of plenums and their usage as well as discussing the plenums and flow controllers used in this study. Section 5.5 details the instrumentation used for data collection in this study. The pressure taps and transducers, pitot tube, thermocouples, data acquisition system, and infra-red camera are discussed. Section 5.6 details the methods of setting experimental flows. The development of a global discharge coefficient to quantify mass flow through the film-cooling holes is discussed. Section 5.7 explains the collection, calibration, and mapping of endwall thermal images. The transition matrix method used to locate images in the global frame is explained. Section 5.8 briefly discusses the repeatability of experimental results. Finally, Section 5.9 quantifies the uncertainty of experimental results.

#### 5.1 Wind Tunnel Overview

All experimental data presented in this study was collected in a large scale, low speed, closed loop, non-rotating wind tunnel facility owned and operated by the Virginia Tech Experimental and Computational Convection Lab (VTECCCL). The laboratory is located in Randolph Hall on the main campus of Virginia Tech in Blacksburg, Virginia. A diagram of the facility is shown in Figure 5.1. The flow in the wind tunnel is driven by

a 50 hp, 0-60 Hz Joy Technologies axial vane fan, seen in Figure 5.2, which is controlled by a Toshiba variable frequency inverter. Downstream of the fan, the flow is turned by a 90° elbow and passes through the primary flow, finned-tube heat exchanger used to cool the bulk flow. After being turned by another 90° elbow, the flow encounters a three-way flow split. Flow passing through the upper or lower passage, which are shown in blue in Figure 5.1, is used as coolant while flow passing through the center passage simulates heated primary or core flow.

Downstream of the flow split, the primary flow passes through a perforated plate with 24.6% open area (0.269 m<sup>2</sup>), shown in Figure 5.3, to obtain the proper pressure drop in the main gas path and force some of the air into the bypass legs. The core flow then passes through a heater bank, a series of screens used for flow straightening, and into the combustor simulator. The combustor simulator has a fixed span segment and then a 2-D, 15.6° contraction in the vertical direction leading to the vane cascade. In the cascade two full passages are modeled with three vanes. A bleed is positioned on either side of the two-passage cascade to remove edge effects from the side walls of the combustor simulator and to balance the flow through each passage insuring periodicity of the inlet flow. Periodicity of the facility has been documented by Kang et al. (1999).

The flow passing through the upper and lower bypass channels is used to simulate coolant flow. Only the lower bypass channel was used for this study. The bypass flow in each channel passes through a secondary finned-tube heat exchanger, where it is cooled below the bulk flow temperature, and into the combustor simulator bypass. At this point, the flow encounters a series of plenums below the combustor liner panels as seen in Figure 5.4. No combustor cooling was simulated in this study because an industrial application was being simulated where methods other than film-cooling are used for combustor liner cooling. Therefore, the plenums were closed off and the combustor liner panels were covered over with thin Lexan sheets. The coolant flow instead passes through the end wall of the combustor simulator into two separate plenums as shown in Figure 5.5. One plenum is used for slot coolant and the second plenum is used for endwall film-cooling.

The coolant is injected into the cascade through either the slot or the film-cooling holes and travels through the passage along with the core flow. The flow from the bleed

channels is reintroduced beyond the passage, and the bulk flow exits the modular test section. The flow is then turned by another 90° elbow and returned to the fan.

## 5.2 Thermal Conditioning System

Actual engine operating conditions could not be simulated due to many factors including: size of the facility, equipment limitations, required power, and thermal limitations of wind tunnel materials. It was, however, desirable to obtain as large of a temperature difference as possible within these constraints. As was briefly discussed in the previous section, the flow passes through a series of flow conditioning elements in order to simulate hot core flow gases and cooler bypass gases. A temperature difference of 35 °C - 42 °C was achieved between the mainstream and coolant flows as a result of this thermal conditioning. Typical operating conditions for the thermal conditioning elements are shown in Table 5.1.

The primary flow, finned-tube heat exchanger is located downstream of the fan, and two smaller finned-tube heat exchangers are located in the bypass legs of the combustor simulator section. These heat exchangers can be run with either chiller or tap water. The primary heat exchanger is used to cool the bulk flow after the fan, while the secondary heat exchanger is used to further cool the bypass air in the combustor simulator.

A 40 kW Freeze Co. Systems chiller is available to supply cooling water to the heat exchangers. The compressor is programmed to shut off once the outgoing cooling water reaches 7.2 °C in order to prevent pipe freeze. Unfortunately, because the airflow rate was so low in the secondary channel, the heat load was not large enough to prevent the chiller from cycling on and off. Because of this cycling problem, tap water was used as a coolant supply rather than chilled water. Both the primary and secondary heat exchanger were typically run at 26.5 lpm. The bypass air was cooled to 12-18 °C using tap water in the heat exchangers.

Downstream of the perforated plate, the core flow passes through a section of finned, electric heating elements, shown in Figure 5.6, which are used to simulate hot combustion gases in a turbine engine. The heater section contains three parallel heater banks with each having six Watlow heating elements. The heating elements have a

resistance of 75 ohms each and are stacked vertically and perpendicular to the flow stream. Each bank of heaters is independently controlled by a Watlow Series 988 controller, shown in Figure 5.7, allowing different inlet temperature profiles to be generated. The user must specify the percentage of total available power supplied to each of the three banks. The heaters are powered by an industrial 3-phase, 480 volt line.

The banks are wired in a 3-Phase Delta configuration, shown in Figure 5.8, where each leg consists of two elements wired in parallel with an effective leg resistance of 37.5 ohms. The total available heating power for each bank can be calculated from:

$$P_{\text{Delta}} = \frac{3 \cdot V_L^2}{R} = \frac{3(480\text{V})^2}{37.5\Omega} = 18,432 \frac{\text{W}}{\text{bank}} \quad (5.1)$$

The delta configuration provides an available power of 18,432 W to the lower, middle, and upper heater banks resulting in a total of 55,296 W of available heating power. In order to counter buoyancy effects and maintain a uniform temperature profile, the lower, middle, and upper heater banks were typically run at 80, 82, and 50 percent of full power respectively resulting in an 11 °C temperature increase across the heater section. Representative temperature profiles that were generated will be presented in chapter 7.

### 5.3 Construction of Endwall Test Plate

When designing the endwall test surface, two goals were to achieve the proper flow length for the cooling holes and to limit conduction through the surface as much as possible. The engine scale design called for  $l/d = 10$  for the film-cooling holes. A test plate thickness of 1.9 cm (0.75 in) was selected because it most closely approximated the design length scale yielding  $l/d = 8.3$ . Last-A-Foam FR6708 was selected as the endwall material because of its extremely low 0.033 W/m·K thermal conductivity. Last-A-Foam is a closed cell foam manufactured by General Plastics Manufacturing Co. of Tacoma, Washington. To insure the precision and integrity of the cooling hole pattern, the holes were cut with a five-axis water jet cutting machine by Springfield Manufacturing in York, South Carolina. Portions of the hole patterns are shown in Figures 5.9a-b. A 1.27 cm thick sheet of Lexan was attached to the underside of the foam to provide stiffness to the structure during the water jetting process. The Lexan backing was retained for

stiffness purposes when the endwall test plate was constructed. Large holes were cut in the Lexan beneath the film-cooling holes, to insure that the Lexan did not alter airflow into the holes and to maintain the proper  $p/d$  for the holes. Five hole diameters were left between the holes and the Lexan backing. Finally, the endwall surface was painted black to enhance the radiative emissivity of the surface. This was because an infra-red camera, which measures radiation, was used to image the test surface.

The slot, shown in Figure 5.10, was constructed from balsa wood which had the same thermal conductivity as the FR6708 foam but was stiffer. Stiffness was important because the slot had a 1.18 m unsupported span. The balsa wood extended 0.32 cm downstream of the slot and 11.4 cm upstream of the slot to the contraction exit as shown in Figures 5.11a-b. The downstream edge of the slot was  $0.35C_a$  upstream of the dynamic stagnation point.

#### 5.4 Coolant Plenums

Coolant air for the slot and the film-cooling holes was provided from two separate plenums. A plenum is a supply chamber where the fluid is stagnant. In general fluid energy can be stored in three basic forms: static pressure, dynamic pressure, and elevation head, as shown by the Bernoulli equation.

$$\underbrace{P_o}_{\text{total}} = \underbrace{p_s}_{\text{static}} + \underbrace{\frac{1}{2}\rho V^2}_{\text{dynamic}} + \underbrace{\rho g z}_{\text{elevation}} \quad (5.2)$$

In the plenum, there is no velocity and elevation head is negligible if the datum is at plenum level, so all the energy is stored in the pressure head. Therefore, the total pressure is equal to the static pressure. Energy is a conserved quantity, so if one head is increased, the others will decrease accordingly. Because air has relatively low density, the elevation head may be neglected except for drastic changes in altitude. Therefore, if the coolant is fed from a plenum one can deduce the coolant flow rate by measuring the difference between the pressure in the plenum, and the pressure at the location where the coolant exits.

Two supply plenums, seen in Figures 5.12 and 5.13, were constructed to provide independent control of the slot and film-cooling flow rates. The front plenum supplied

the slot flow, and the rear plenum supplied the film-cooling. Flow into the plenums was fed through two slots from the combustor bypass flow shown in Figures 5.14a-b. The slot flow was controlled by a window shutter mechanism, where a rod is connected to several short covers in a track. When the rod is pushed or pulled the window covers slide back and forth in the track to expose or cover an open section behind them. A typical shutter mechanism is shown in Figure 5.15. A splash plate was positioned just above the shutter, as shown in Figure 5.16, to aid in mixing the slot coolant.

Flow into the film-cooling plenum was controlled by a lift gate. The gate was connected to a threaded rod by two arms attached to nuts. When the crank on the threaded rod was turned the nuts would move down the rod and pull the arms thereby lifting the gate. The threaded rod, rocker arms and gate, as well as the pushrod used to open and close the window shutters and the gate crank, may be seen in Figures 5.16 and 5.17.

## **5.5 Instrumentation**

Several different types of instrumentation were used to document the flow conditions and record data. Pressure taps were used to deduce coolant flow rates and document the flow conditions around the vane, and a pitot tube was used to measure the inlet flow velocity. Thermocouples measured the freestream temperature, coolant temperatures, and temperature at several locations on the endwall. Thermal fields were documented for three cases with a thermocouple rake. All pressure and temperature data was collected using LabVIEW virtual instruments and a National Instruments SCXI data acquisition (DAQ) system. The endwall thermal distribution was recorded with an infrared camera.

Static pressure measurements were taken using 0.156 cm diameter copper tubes connected to nylon hose made by Scani-Valve. The pressure taps were grouped by expected pressure reading and connected to one of three 24 channel Scani-Valve wafers, shown in Figure 5.18, allowing three simultaneous pressure measurements. Each of the three wafers had a single output channel which was connected to one of eight pressure transducers manufactured by Setra and Omega and housed in a box shown in Figure 5.19. The pressure transducers measure voltage and convert that to a corresponding pressure.

The transducers, which were wired in parallel, required between 9 and 30 volts each and were powered by two 12 volt lantern batteries wired in series. The voltage readings were output to the DAQ via BNC cables.

Thirty-one pressure taps were positioned along the vane to record the pressure distribution, and three pressure taps were located in each of the two plenums as well as three pressure taps 2.54 cm upstream of the slot on the endwall to document the coolant flows. The endwall pressure taps were spaced 22.86 cm (0.5P) apart to capture variations in static pressure from upstream of the leading edge to upstream of the passage centers. A variation of 5 Pa (2.7% to 23.8% of the driving pressure difference depending on the pattern and flow rate) was typically seen from the leading edge pressure tap to the taps located upstream of the passages and the static pressure upstream of pattern #2 was generally 0.5 Pa (0.27% to 2.27% of driving pressure difference) higher than upstream of pattern #1.

The inlet velocity was measured with a pitot tube, shown in Figures 5.20a and b. The pitot tube contains two concentric tubes. One tube has a small opening at the tip of the probe. Flow enters the hole and stagnates yielding the stagnation pressure of the flow stream. The second tube has four small holes around the perimeter of the pitot probe used to measure the static pressure of the flow stream. When the total pressure is measured against the static pressure, the dynamic pressure is recorded yielding the velocity and allowing the mass flow rate to be calculated. The inlet velocity was measured at seven different locations, as shown in Figure 5.21, and averaged to obtain the inlet flow velocity. Higher velocities were seen upstream of the passages and lower velocities upstream of the vanes with a typical range of approximately 1.27 m/s.

Type E thermocouples, consisting of chromel (+) and constantan (-), were used for all thermal measurements. An arc welder was used to fuse the positive and negative wires together forming a small, round bead. When exposed to a given temperature, each material heats up generating a current in the wire. The difference between the positive and negative wires creates a voltage drop, which is used to determine the temperature that the thermocouple is experiencing. Five thermocouple strips were also used consisting of chromel and constantan ribbons that were soldered together. The strip thermocouples, which lie flush on the surface, were to verify the temperatures that were being recorded

by the thermocouple beads and insure that surface temperatures, rather than air temperatures, were being reported. Agreement within 0.1°C or better was found between the strip and beaded thermocouples located within one inch of each other upstream of the cascade.

Two thermocouples were located on each of the three vanes at 5% span and 30% span. These thermocouples helped monitor variations along the vane in the span-wise direction as well as variations from passage to passage of the incoming flow. At high film-cooling rates the thermocouples near the endwall measured cooler temperatures than the free stream thermocouples as a result of coolant from the leading edge holes separating and impacting the vane. Variations in free stream temperature from passage to passage were generally less than 1.5 °C or  $\Delta\theta \leq 0.0375$ . When normalizing surface temperatures to adiabatic effectiveness, the average temperature from the thermocouple at 30% span on the center vane was always used as the maximum temperature. Three thermocouples were also located in both the slot and film-cooling plenums with one thermocouple beneath each of the passages and one beneath the center vane. These thermocouples allowed gradients in the coolant supply to be documented. Variation within the plenums was generally less than 0.3 °C or  $\Delta\theta \leq 0.0075$ . When normalizing surface temperatures to adiabatic effectiveness, the average temperatures from the thermocouple beneath the passage of interest and the thermocouple below the center vane were averaged to determine the coolant temperature.

The endwall, vane, and plenum thermocouples were also used to document when steady state was achieved. Six endwall thermocouples from various locations in the passages as well as the center vane, free stream thermocouple and a thermocouple from each of the two coolant plenums were documented at ten minute intervals. The range between the free stream thermocouple and the coolest plenum thermocouple was also calculated. Once the temperatures and temperature difference were stable for 30 minutes, a steady state was assumed. This was satisfactory because data collection could be completed in approximately 15 minutes. Typical time to steady state from a cold startup of the wind tunnel was 3 hours. If flows were adjusted for a second data set collection, steady state was generally re-achieved in 1 ½ hours.

A thermocouple rake, illustrated in Figures 5.22a-c was used to document the thermal field for several cases. The rake had 16 probes spaced 0.635 cm apart. The thermocouple wire diameter was 0.3 mm, and the bead diameter was approximately 0.8 mm. The beads were positioned 0.6 cm below the fingers to eliminate any conduction heating from the fingers that might alter the bead temperature. The rake was lowered into the passage from a boom, shown in Figure 5.23a-c, and moved by a computer controlled traverse. A single thermocouple moved by a computer controlled traverse was used to document the inlet temperature profile in the combustor simulator section.

Voltage outputs from the thermocouples and pressure transducers were handled by the National Instruments DAQ system shown in Figures 5.24a-d. Voltage outputs were connected to a 32 channel SCXI-1303 terminal block which was plugged into one of three SCXI-1100 modules. The modules serve as multiplexers and amplifiers. The modules switch between all 32 input channels and output all signals on a single line. The three modules were housed in a four slot SCXI-1000 chassis which powers the modules and orchestrates all timing, triggering, and signal routing between the modules and the DAQ card. The data was sent from the chassis via shielded cable to a National Instruments NI AT-MIO-16E-2 DAQ card. The DAQ card was capable of receiving up to 16 single-ended analog inputs from multiple SCXI chassis. The card performed 12-bit digitization sampling analog signals at up to 500 kHz. The user controlled the DAQ system using Virtual Instruments developed in LabView. When setting flows and recording temperature data for camera calibration, pressure and temperature measurements were collected from data blocks of 4096 samples collected at 1024 Hz. For thermal field measurements, block size was increased to 10,240 samples while still sampling at a frequency of 1024 Hz.

An Inframetrics P20 infrared camera, shown in Figures 5.25, was acquired specifically to achieve the spatial resolution needed to resolve the film cooling holes on the endwall. This camera was used to measure adiabatic wall temperatures on the endwall surface. The camera detects radiation with a Focal Plane Array (FPA), uncooled, microbolometer (FLIR 2002). The wall temperature is then back calculated from the measured radiation which is a function of temperature. Measurements were taken at thirteen different viewing locations to insure that the entire endwall surface was mapped.

From a camera distance of 55.23 cm, each picture covered an area that was 24 cm by 18 cm with the area being divided into 320 by 240 pixel locations. The spatial integration for the camera was 0.715 mm (0.16 hole diameters).

## 5.6 Setting Flow Conditions

The dimensionless pressure coefficient distribution was set to insure that the flows through the passages were properly balanced. The pressure coefficient is defined as:

$$C_p = \frac{P_{s,loc} - P_{s,in}}{P_{dyn,in}} \quad (5.3)$$

Pressure taps were located along the surface of the vane at midspan to document the static pressure distribution. Measurements were compared to the two-dimensional, inviscid prediction for periodic flow at low speed conditions presented by Kang et al. (1999). The pressure side wall of the outer passage, shown in Figure 5.26, was constructed of 0.32 cm thick Lexan. The flow through the passages could be altered by turning several adjustment knobs which were used to move the wall in and out and achieve the proper pressure distribution, shown in Figure 5.27. A bulb seal was used on the top and bottom of the flexible wall to prevent leakage flow from the atmosphere entering the passage.

Determining the film coolant flow rates proved challenging because the film-cooling holes were fed from a common plenum, but the local static pressure field varied greatly from hole to hole. Friedrichs (1996) suggested that the blowing ratio could be characterized by the blowing ratio of a single loss-free hole injecting into inlet conditions and calculated from:

$$M = \sqrt{\frac{P_{o,c} - P_{s,in}}{P_{o,in} - P_{s,in}}} \quad (5.4)$$

for the case of a unity coolant to freestream density ratio. The blowing ratio for a non-uniform density ratio can, therefore, be calculated from:

$$M_{ideal} = \sqrt{\frac{\rho_c}{\rho_{in}} \cdot \frac{P_{o,c} - P_{s,in}}{P_{o,in} - P_{s,in}}} \quad (5.5)$$

A modification of this approach was taken for this study. A global discharge coefficient,  $C_D$ , was desired so that the cumulative flow rate through either cooling pattern could be characterized based on the pressure difference between the plenum and the inlet static pressure. A  $C_D$  model was developed from the computational cases. The inlet mass flow rate, average inlet static pressure, coolant density, and plenum pressure were determined for each of the six film-cooling predictions. The total coolant flow rate as a fraction of inlet core flow was calculated from:

$$\frac{\dot{m}_c}{\dot{m}_{core}} = M_{ideal} \cdot C_D \cdot \frac{A_{hole} \cdot \#holes}{A_{in}} \quad (5.6)$$

where  $C_D$  was iterated using the Microsoft Excel Solver until the proper coolant fraction, which was known from the CFD, was achieved for each predicted case. The discharge coefficient for each prediction was then plotted against the square root of the pressure difference between the plenum and inlet static pressure.

$$C_D = f\left(\sqrt{P_{o,plen} - P_{s,in}}\right) \quad (5.7)$$

Even though there were three computational cases for both passage #1 and passage #2, two of the cases were very close together because the film flow rate was the same for the film-only cases and the low slot flow, low film flow cases. Therefore, a linear fit was developed in order to determine the discharge coefficient at a given pressure difference as shown in Figure 5.28. Regardless of the true shape of the  $\Delta P^{1/2}$  vs.  $C_D$  curve, the linear fit is sufficient because experimental operating points were very close to the calculated points. This is because the density ratio was similar between the predictions and experiments. Therefore, any error as a result of the linear approximation should be minimal. A different curve fit was used for each of the two cooling patterns, because the patterns had a different number of holes in different locations. Therefore, they were different orifice plates, which one would not expect to have the same flow coefficients.

When examining the computational data from passage #1 in Figure 5.28, one will notice that  $C_D > 1$  is necessary to properly match the flow rate to the computed pressure difference at the low coolant flow rates. One should consider  $C_D$  to be more of a scaling factor relative to the difference between plenum and inlet conditions rather than a viscous loss coefficient. If  $C_D > 1$  this simply means that the average film-cooling hole in the

pattern requires a greater pressure difference than what is measured between the plenum and the inlet to provide the proper amount of coolant. This is achieved by the accelerating flow through the passage which lowers the static pressure and creates a greater local pressure difference in the downstream portion of the passage as compared with the upstream region.

Once the  $C_D$  models were developed, the pressure difference between the plenum and the cascade inlet for a given experiment was determined using the bisection method illustrated in Figures 5.29a-d. First, the inlet flow rate was documented by averaging seven measurement locations at the cascade inlet, and the plenum and free stream temperatures were documented to determine the density ratio. Then the desired mass flow rate was specified as fraction of the core flow. A range of possible driving pressures was specified based upon knowledge of the system. For this study the initial range was  $0 \leq \Delta p \leq 250$  Pa. The midpoint of the pressure range was calculated, and a slightly lower (a) and slightly higher pressure (b) were selected as shown in Figure 5.29a. The discharge coefficient for each search pressure, a and b, was calculated from the curve fit corresponding to the passage of interest, and the mass fraction was calculated from equation 5.6. The specified mass fraction was subtracted from the calculated value at each search point to determine the error of the two search pressures. The errors were then compared, and the pressure with the larger error, along with all other pressures between that value and the range limit, were discarded as shown in Figure 5.29b. A new midpoint and search points were determined for the new interval, and the process was repeated as shown in Figures 5.29c-d. The process was repeated until the difference between the errors at each search point was less than a specified tolerance. Once the difference in the errors was less than the tolerance, the solution was converged and the midpoint pressure was selected as the operating point for the experiment.

The slot flow rate was calculated using the traditional Bernoulli equation method modified by a discharge coefficient. Once again equations 5.5 and 5.6 were used to calculate the pressure difference necessary to drive the slot flow. A constant discharge coefficient of  $C_D = 0.6$  was used because the local static pressure was measured from pressure taps just upstream of the slot, and there were no huge variations in pressure

dictating the need of a global discharge calculation in the manner of the film-cooling holes.

The plenum controls, which were discussed in section 5.4, were used to adjust the plenum pressures until the desired pressure was obtained. At the low slot flow rate, the shutter had to be completely closed to lower the coolant flow to the desired level. Three pressure taps were located with one in the outer passage region, one in the stagnation region, and one in the inner passage region in each of the slot plenum, the hole plenum, and 2.54 cm upstream of the slot on the endwall. The coolant flow rates were calculated using the average of four pressure difference measurements for both the slot and the film-cooling pattern of interest to verify the mass flows. The pressure combinations are shown in Figure 5.30. The discharge coefficient was recalculated based on the recorded pressure differences when computing the experimental mass flow rates. The pressure ratios and mass flow rates of the slot and film-cooling holes as well as the discharge coefficient for the film-cooling holes for each case are presented in Table 5.2. A sample experimental data sheet is available in Appendix A.

The multiple pressure measurements were also used to observe any pressure variations across the plenums and the cascade inlet. The static pressure was always observed to be approximately 5 Pa (2.7% to 23.8% of the driving pressure difference depending on the pattern and flow rate) higher in the center of the cascade inlet due to the presence of the downstream vane. Pressures were constant across the width of the supply plenums.

### **5.7 Endwall Image Collection, Calibration, and Assembly**

Endwall temperature data was collected using an infra-red camera. Because the image size was only 18 cm by 24 cm multiple pictures were needed in order to fully image the endwall surface. Images were acquired through 13 view ports positioned above the endwall. The locations are illustrated in Figure 5.31.

Copper tube segments of diameter 15.88 mm were embedded in the endwall surface to serve as global marker locations, and thermocouples were embedded in the endwall for image calibration purposes. The locations of the markers and thermocouples may be seen in Figure 5.32 and are listed in Tables 5.3 and 5.4. The origin is at the

dynamic stagnation point of the center vane. The film-cooling holes were also used as markers in the global coordinate system. Care was taken to insure that at least two markers were visible at each image location. Thermocouples were positioned based upon predictions of adiabatic effectiveness with an attempt to locate thermocouples in both high and low temperature, low gradient areas. Five images were acquired at each viewing port for averaging purposes.

The images were post calibrated using ThermaCam Researcher 2002, the companion software for the camera. Thermocouple data was continuously acquired during image collection. A typical thermocouple data set would consist of 350 measurements from each of the 30 thermocouples. Each measurement was sampled at 1024 Hz for four seconds. Measurements had a range of approximately 0.8 °C with a standard deviation of 0.17 °C during the image collection time. The thermocouple data was then averaged to determine the mean operating and endwall temperatures during data collection. The emissivity and background temperature were adjusted until the thermocouple data was within 1 °C of the corresponding image data location. The same emissivity was used to calibrate each image in a set, and the necessary background temperatures from the images were averaged to obtain a single background temperature for the set. Typical values were an emissivity of  $\epsilon = 0.89$  and a background temperature of 45 °C. Once the images were calibrated, the data was exported to a GUI-based Matlab program for image assembly. A sample image set for pattern #1 is shown in Figure 5.33.

The transition matrix method was used to position the images in the global coordinate system. The transition method is illustrated in Figure 5.34. The method involves projecting vectors from one coordinate system onto the basis vectors of another coordinate system. If given any coordinate vector  $\mathbf{x}_a$  with respect to the basis  $[\hat{x}_a, \hat{y}_a]$ , to find the corresponding coordinate vector  $\mathbf{x}_b$  with respect to basis  $[\hat{x}_b, \hat{y}_b]$ , one simply left multiplies the transition matrix,  $T$ , times  $\mathbf{x}_a$  (Leon 1998). The transition matrix from one system to another is simply the basis unit vectors of the original system expressed in terms of the basis unit vectors of the new system.

$$\begin{Bmatrix} x_b \\ y_b \end{Bmatrix}^T = T \begin{Bmatrix} x_a \\ y_a \end{Bmatrix}^T \quad (5.8)$$

where

$$T = \begin{bmatrix} \hat{x}_{a \rightarrow b}^T & \hat{y}_{a \rightarrow b}^T \end{bmatrix} \quad (5.9)$$

For the image alignment problem there are three coordinate systems: (1) aligned with the pixels of the image, (2) aligned along the markers in the image, and (G) the global coordinate system. First the image must be scaled into the proper dimensions. Each point in the image matrix, which can be uniquely identified by its index pair  $(x_{pix}, y_{pix})$ , corresponds to a pixel in the image. Using the pixel indices and the known global location of the markers, one can determine the scaling factor:

$$Scale = \frac{\sqrt{(x_{RMG} - x_{LMG})^2 + (y_{RMG} - y_{LMG})^2}}{\sqrt{(x_{RMPix} - x_{LMPix})^2 + (y_{RMPix} - y_{LMPix})^2}} \left[ \frac{inches}{pixel} \right] \quad (5.10)$$

where RMG is the global location of the right marker, LMG is the global location of the left marker, RMPix is the pixel number of the right marker, and LMPix is the pixel number of the left marker. The pixel index matrix was then shifted so that the origin (0,0) was at the pixel corresponding to the left marker. It is critical that the origin in each system be based at the left marker. This insures that all coordinate systems are right handed. The pixel coordinate matrix was then multiplied by the scaling factor to get the pixel aligned coordinate system into the same units as the marker aligned and global coordinate systems. This was done to make the transition matrix a projection of basis *unit* vectors which is more easily visualized because all basis vectors then have the same magnitude. Vectors may be projected, however, without normalizing to unit length first. Once the pixel frame of reference had been scaled and offset, a unit vector was constructed from the left marker to the right marker forming the x-dimension for the marker aligned coordinate system. The y-dimension unit vector for this system is not readily apparent, but because all images lie in the same plane, the z-dimension unit vector is known to be (0,0,1). The y-dimension unit vector can then be found from the cross product of the known vectors.

$$\hat{y}_2 = \hat{z}_2 \times \hat{x}_2 \quad (5.11)$$

The marker aligned system (2) can then be expressed in terms of the pixel aligned system (1), but in order to convert from the pixel aligned system to the marker aligned system, the basis for system 1 must be expressed in terms of system 2. The transition matrix from

system 1 to system 2 is obtained by simply inverting the transition matrix from system 2 to system 1.

$$T_{1 \rightarrow 2} = T_{2 \rightarrow 1}^{-1} \quad (5.12)$$

Once  $T_{1 \rightarrow 2}$  is known the image can be mapped into the marker aligned coordinate system as shown in Figure 5.34b. Although this computation is not performed, the step is necessary because the markers are the known locations corresponding to the global coordinate system.

Next the image must be transformed from the marker aligned system to the global system. First, the vector from the left marker to the right marker is determined in the global system by taking the vector difference of vectors from the global origin to each of the two markers, or the marker coordinates, as shown in Figure 5.34c.

$$\vec{M}_{(LM \rightarrow RM)G} = \vec{M}_{RMG} - \vec{M}_{LMG} \quad (5.13)$$

This vector must be normalized by its length to obtain the unit vector,  $\hat{x}_2$ , and once again the corresponding  $\hat{y}_2$  vector can be found from equation 5.11. The transition matrix from the marker aligned system to the global system is then:

$$T_{2 \rightarrow G} = \begin{bmatrix} \hat{x}_2^T \\ \hat{y}_2^T \end{bmatrix} \quad (5.14)$$

as illustrated in Figure 5.34d. For simplification, the transition matrix from the original pixel aligned system to the global system can then be found by left multiplying the transition matrix from 2 to G by the transition matrix from 1 to 2.

$$T_{1 \rightarrow G} = T_{2 \rightarrow G} \cdot T_{1 \rightarrow 2} = T_{2 \rightarrow G} \cdot T_{2 \rightarrow 1}^{-1} \quad (5.15)$$

Finally the image is offset in the global coordinate system by the vector from the origin one of the markers as shown in Figure 5.34e. The final image transition equation is of the form:

$$[x_G \ y_G] = T_{1 \rightarrow G} \cdot [x_1 \ y_1] + [x_{LMG} \ y_{LMG}] \quad (5.16)$$

After transforming each image, pixels corresponding to the marker location as well as any other user specified blemish points were discarded from the sample. The user could also apply a “data window” to sample only a subset of the image if extraneous data such as the vane was included in the image.

## 5.8 Repeatability

When collecting experimental data, it is important to show that results are independent of any local conditions, such as atmospheric pressure and temperature, absolute values of measured temperature, etc. To that end, a few test cases were repeated at different times and the results were compared. Figures 5.35a-d exhibit excellent repeatability of both adiabatic effectiveness and thermal field data. The adiabatic effectiveness data sets were taken on February 19, 2003 and March 14, 2003 respectively. The thermal field was taken on April 12, 2003 and repeated on April 15, 2003.

## 5.9 Uncertainty Analysis

An uncertainty analysis was performed on the measurements of adiabatic effectiveness using the partial derivative method described at length by Moffat (1988).

The precision uncertainty was determined by taking the standard deviation of six measurement sets of IR camera images, with each set consisting of five measurements. The standard deviation was then multiplied by the factor corresponding to a 95% confidence interval. The precision uncertainty of the measurements was  $\pm 0.0143$  °C. The bias uncertainty was  $\pm 1.02$  °C based on the calibration of the image. The bias uncertainty of the thermocouples was  $\pm 0.5$  °C. The total uncertainty was then calculated as  $\pm 1.02$  °C for the images and  $\pm 0.51$  °C for the thermocouples where total uncertainty is defined as:

$$\delta_{u_T} = \sqrt{\text{Pr}^2 + \text{Bi}^2} \quad (5.17)$$

The uncertainty in adiabatic effectiveness,  $\eta$ , was then found based on the partial derivative of  $\eta$  with respect to each temperature in the definition and the total uncertainty in the measurements. Uncertainty is calculated from the square root of the sum of the squares of each partial-uncertainty product.

$$\partial\eta = \sqrt{\left(\frac{\partial\eta}{\partial T_{aw}} \delta_{u_{T_{aw}}}\right)^2 + \left(\frac{\partial\eta}{\partial T_c} \delta_{u_{T_c}}\right)^2 + \left(\frac{\partial\eta}{\partial T_\infty} \delta_{u_{T_\infty}}\right)^2} \quad (5.18)$$

An uncertainty of  $\partial\eta = \pm 0.0825$  at  $\eta = 0.2$  and  $\partial\eta = \pm 0.0292$  at  $\eta = 0.9$  were calculated.

**Table 5.1** Typical Experimental Operating Conditions

Fan speed, Hz	38.5
Atmospheric pressure, kPa	94.5
Atmospheric temperature, C	24.0
Primary HX, lpm	26.5
Lower HX, lpm	26.5
Lower heater bank, % power	80
Middle heater bank, % power	82
Upper heater bank % power	50
$T_\infty - T_c$ , C	40
$\rho_c/\rho_\infty$	1.14
Turbulence intensity $Tu$ , %	1.35
Turbulent length scale $\Lambda_x$ , m	0.04

**Table 5.2** Experimental Pressure Ratios and Film-cooling Discharge Coefficients

Case	Slot		Film-cooling		
	$\Delta p_{o,c-\infty, in}/\Delta p_{in}$	$m_{dot}$	$\Delta p_{o,c-\infty, in}/\Delta p_{in}$	$C_D$	$m_{dot}$
1S0F0	0.198	0.5	---	---	---
2S0F0	0.449	0.75	---	---	---
3S0F0	0.794	1	---	---	---
0S1F1	---	---	1.156	1.093	0.5
0S2F1	---	---	4.428	0.835	0.751
0S1F2	---	---	3.27	0.809	0.494
0S2F2	---	---	9.705	0.71	0.755
1S1F1	0.229	0.528	1.095	1.1	0.493
1S1F1Bot	0.21	0.492	1.282	1.066	0.514
1S1F1Mid	0.229	0.53	1.119	1.099	0.497
1S2F1	0.223	0.518	4.424	0.839	0.744
2S1F1	0.478	0.762	1.184	1.095	0.494
2S2F1	0.465	0.75	4.822	0.837	0.75
1S1F2	0.197	0.492	3.382	0.805	0.504
1S2F2	0.218	0.512	9.698	0.708	0.742
2S1F2	0.461	0.75	3.871	0.804	0.507
2S2F2	0.458	0.746	10.945	0.707	0.749

**Table 5.3** Global Locations of Markers Used to Align Images

Marker #	X [cm]	Y [cm]
1	-5.715	-42.545
2	-5.715	-24.130
3	-5.715	5.715
4	-5.715	24.130
5	-5.715	27.940
6	-0.635	-6.350
7	2.540	8.890
8	1.905	26.670
9	3.810	34.290
10	13.970	23.495
11	20.955	33.655
12	22.225	49.530
13	36.830	57.150
14	31.115	45.085
15	33.020	28.575
16	25.400	14.605
17	28.575	8.890
18	20.955	-3.810
19	8.255	-13.335
20	5.715	-15.875
21	5.715	-33.020

**Table 5.4** Global Locations of Endwall Thermocouples Used for Image Calibration

Thermocouple #	X [cm]	Y [cm]
1	-5.715	-15.240
2	-5.715	3.810
3	-5.715	30.480
4	19.050	41.910
5	24.130	39.370
6	25.400	52.070
7	38.100	52.070
8	34.290	38.100
9	33.020	25.400
10	28.575	10.160

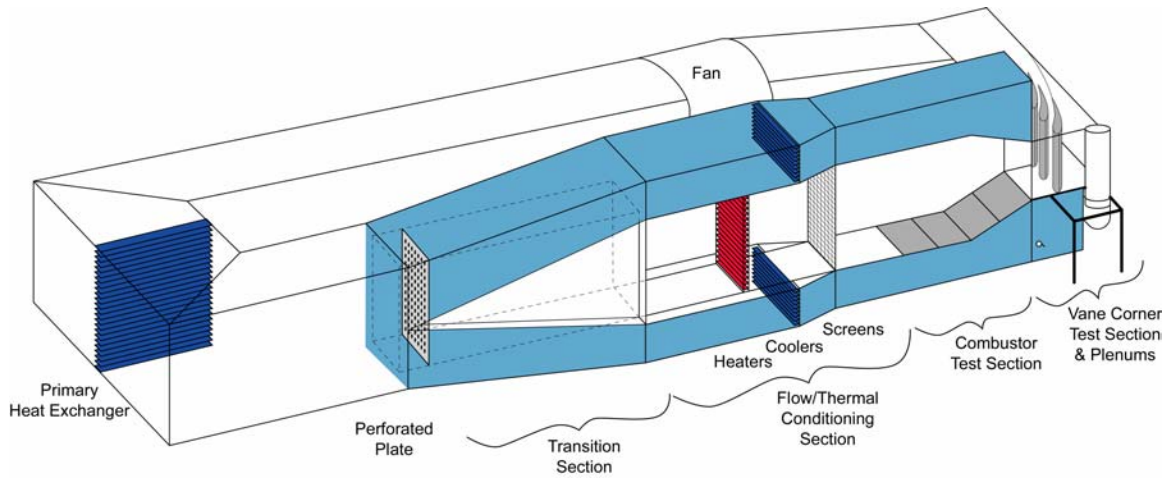


**Figure 5.1** Illustration of wind tunnel facility. The flow is split into the primary channel and secondary channels before passing through the combustor simulator section and the vane cascade.

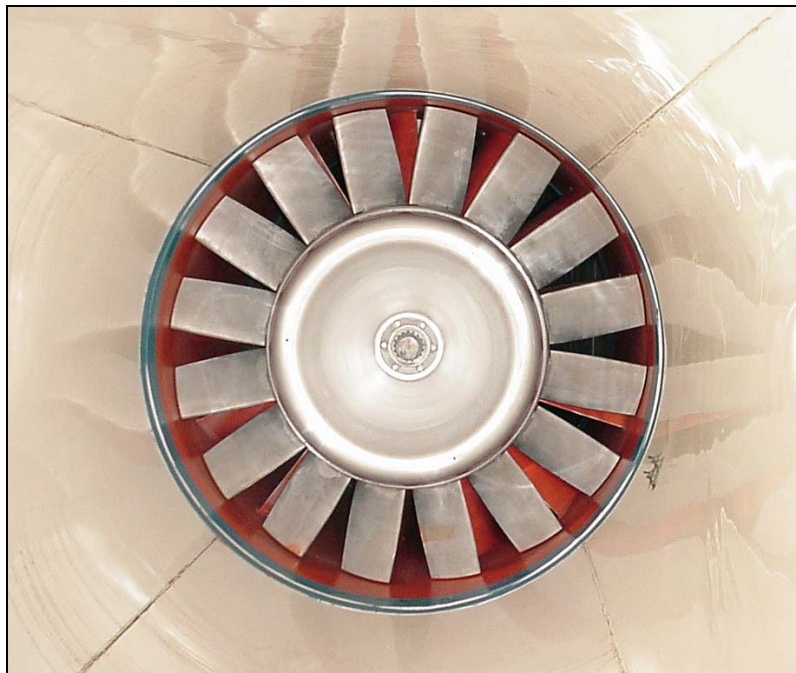


**Figure 5.2** The flow is driven by a Joy Technologies 50 hp 0-60 Hz fan.



**Figure 5.3** A perforated plate with 24.6% open area is used to achieve the proper pressure drop through the core flow channel.

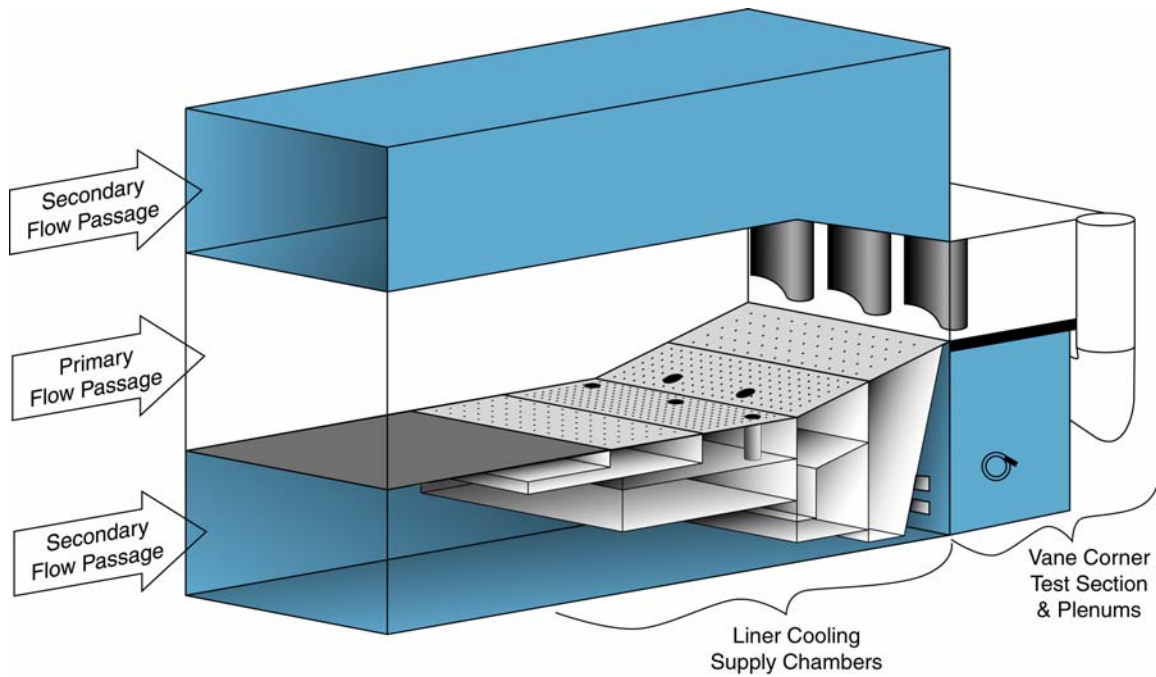


**Figure 5.4** Plenums in the combustor bypass feed film-cooling and dilution holes in the combustor simulator. The plenums were closed off and liner holes covered over because no combustor flows were simulated.

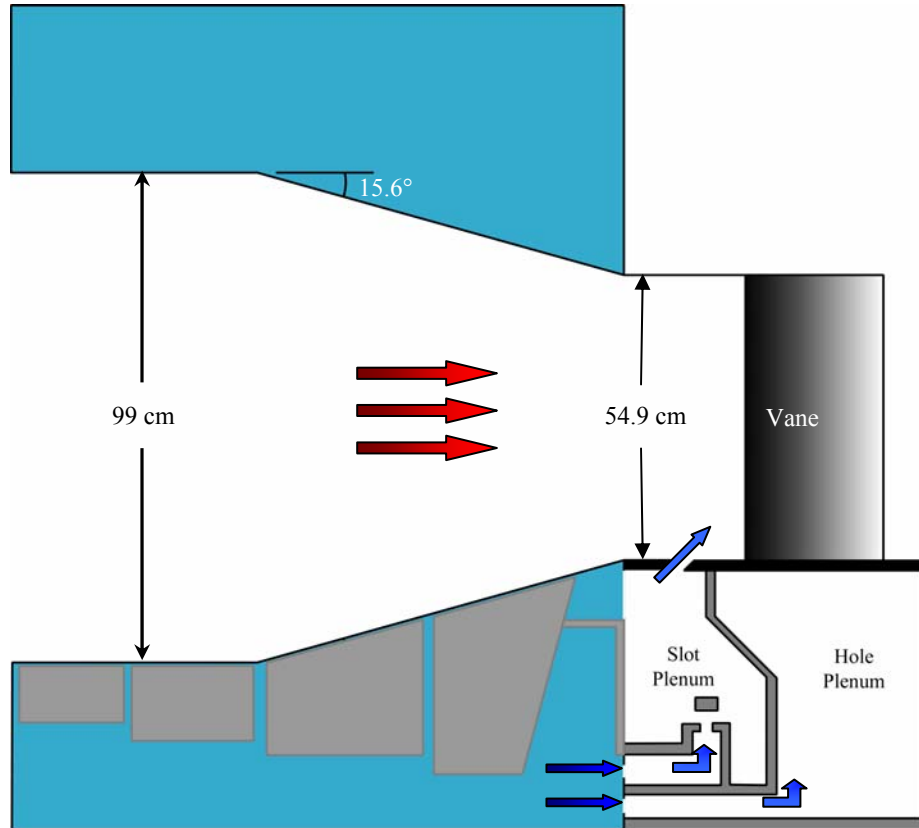


**Figure 5.5** Cooling air from the bypass channel passes into the supply plenums through holes at the end of the combustor bypass. The cooling air is then injected into the passage through the slot or the holes where it interacts with the hot mainstream gases.

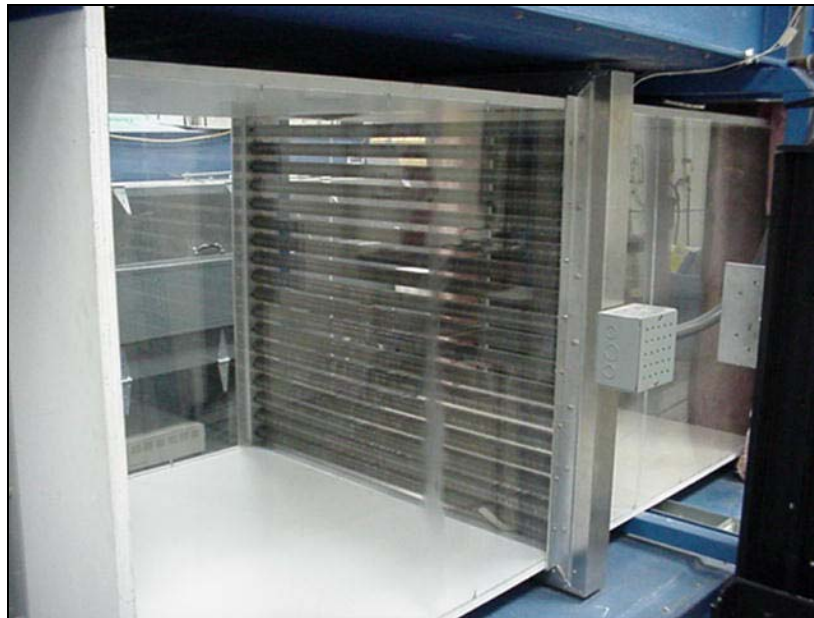


**Figure 5.6** A three zone heater bank is used to generate various combustor exit temperature profiles.



**Figure 5.7** Watlow Series 988 controller used to specify percentage of full power to the heater banks.

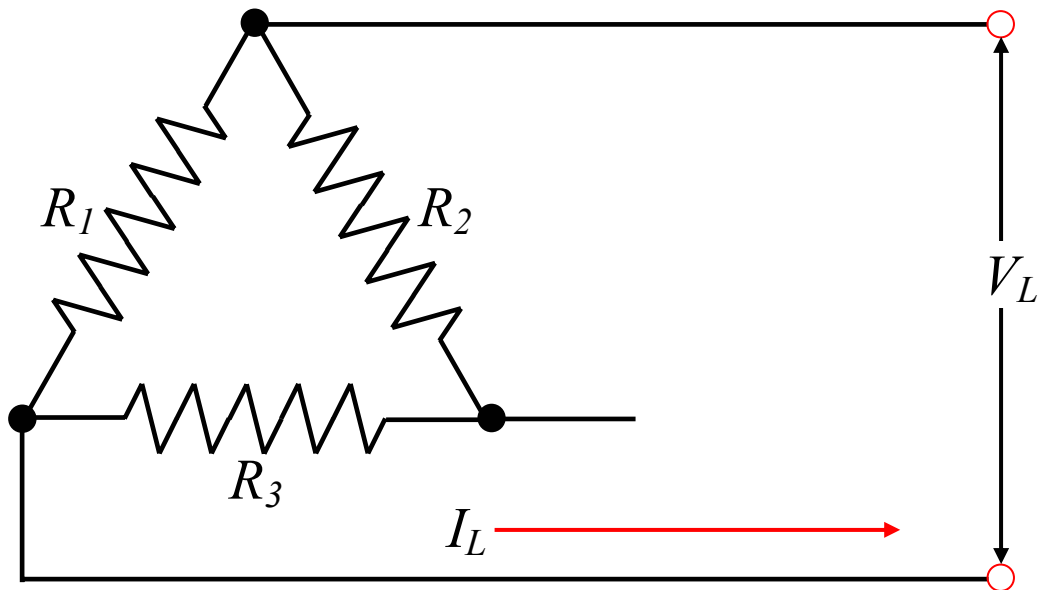


**Figure 5.8** Each of the three heater sub-banks is wired in a three phase delta with each leg consisting of two elements in parallel (Vakil 2002).

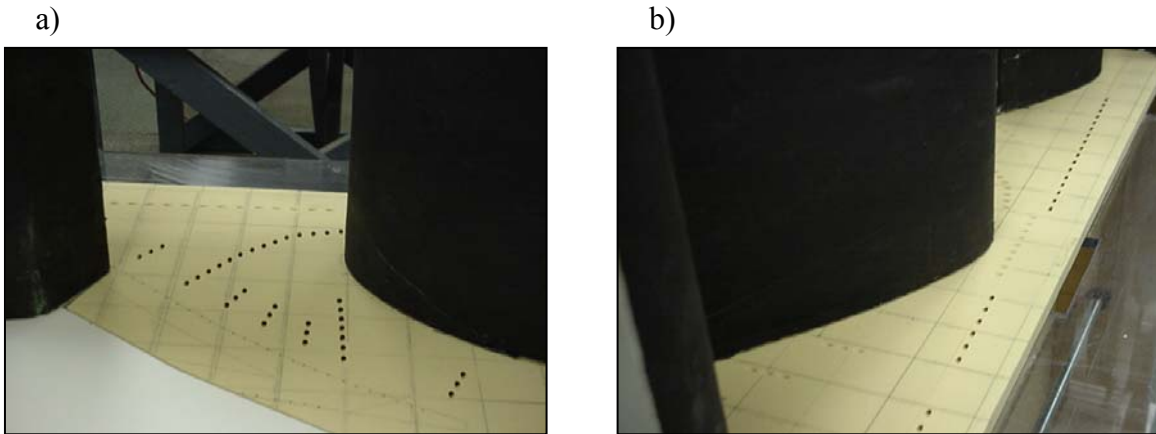


**Figure 5.9** Film-cooling holes were cut with a water jet. (a) Passage 1 and (b) the leading edge region are shown.

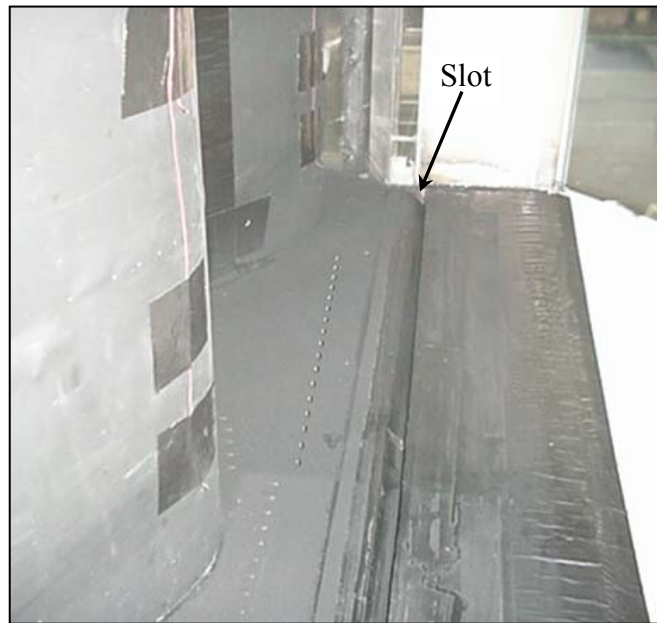


**Figure 5.10** The upstream slot was constructed from balsa wood to provide improved stiffness.

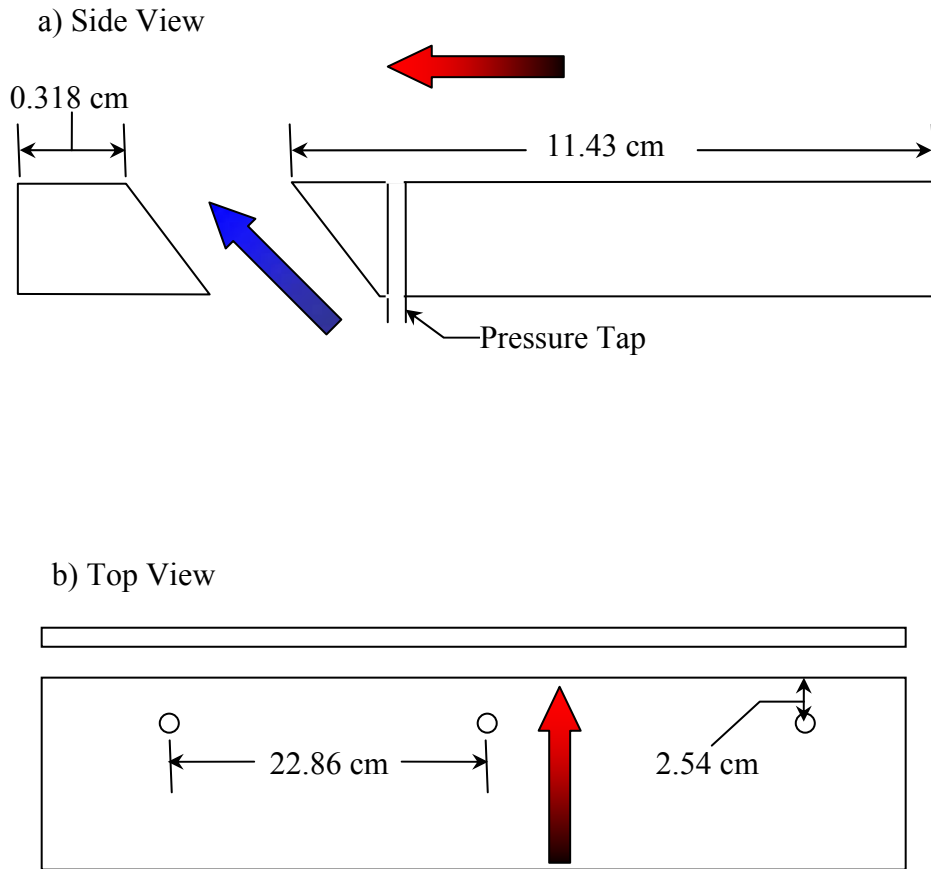


**Figure 5.11a-b** Schematics of balsa wood slot. Extent of the slot is shown in (a) while locations of the endwall static pressure taps are shown in (b).



**Figure 5.12** The rear plenum provides coolant flow through the film-cooling holes.



**Figure 5.13** A division was added to separate the front plenum which fed the slot flow.

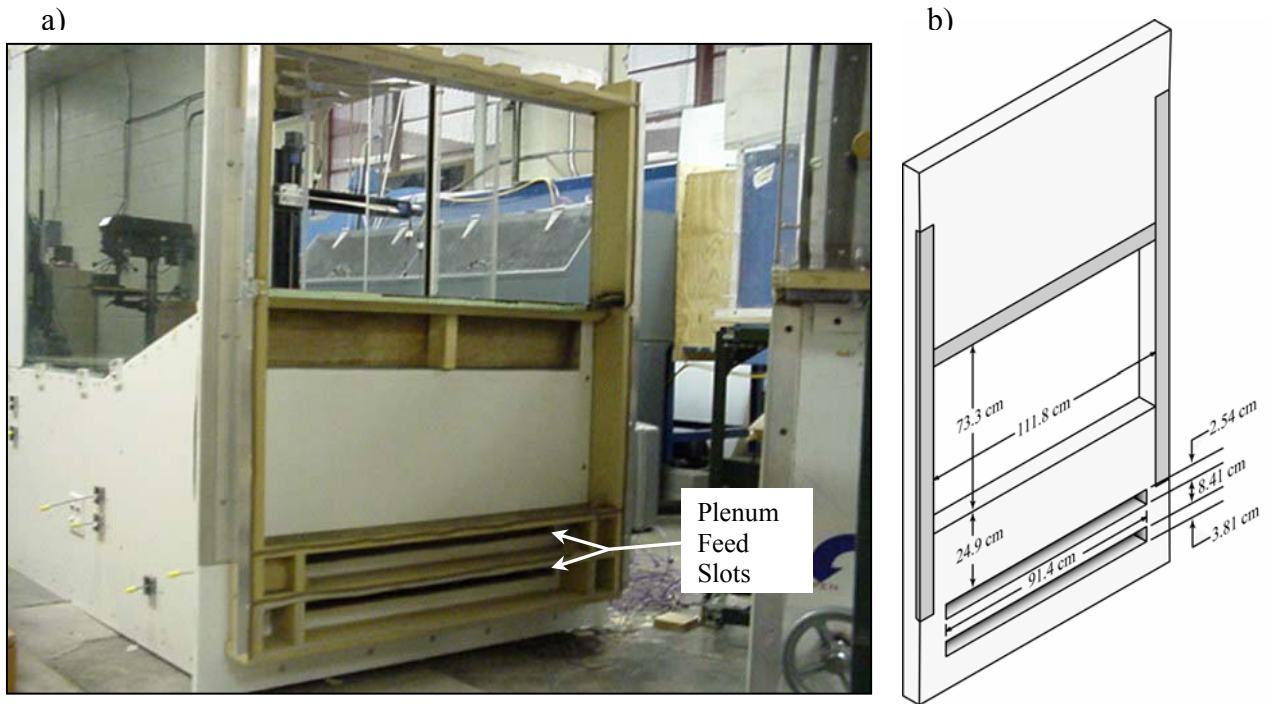


**Figure 5.14a-b** Coolant flow passes from the combustor bypass into the plenums through two feed slots.

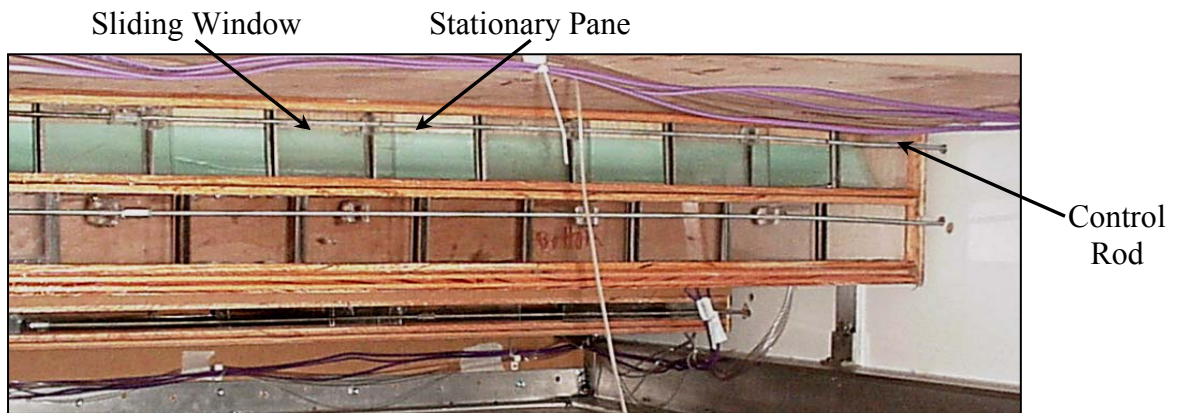


**Figure 5.15** A typical shutter control is shown. Panes connected to a pushrod slide past stationary panes to open and close the flow area.



**Figure 5.16** The plenum control devices are shown along with a splash plate to aid in mixing the slot flow.



**Figure 5.17** The gate was raised and lowered to control flow into the hole plenum.

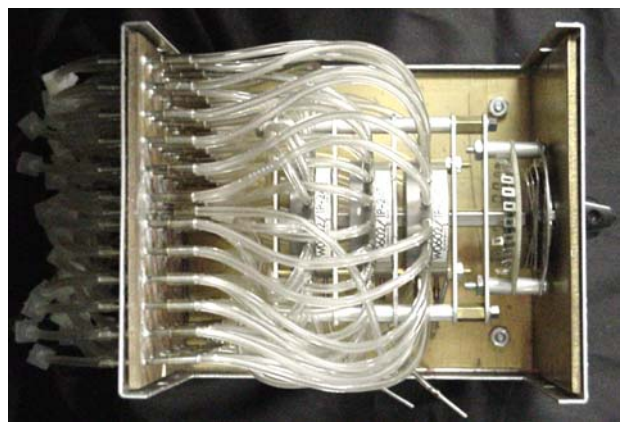
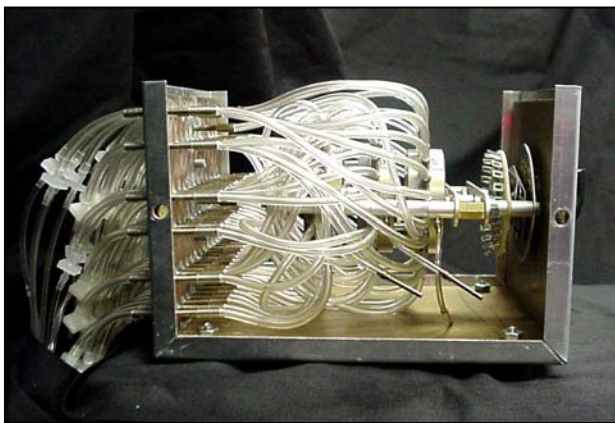


**Figure 5.18** Three Scani-Valve wafers were used to scan pressure measurements (Vakil 2002).

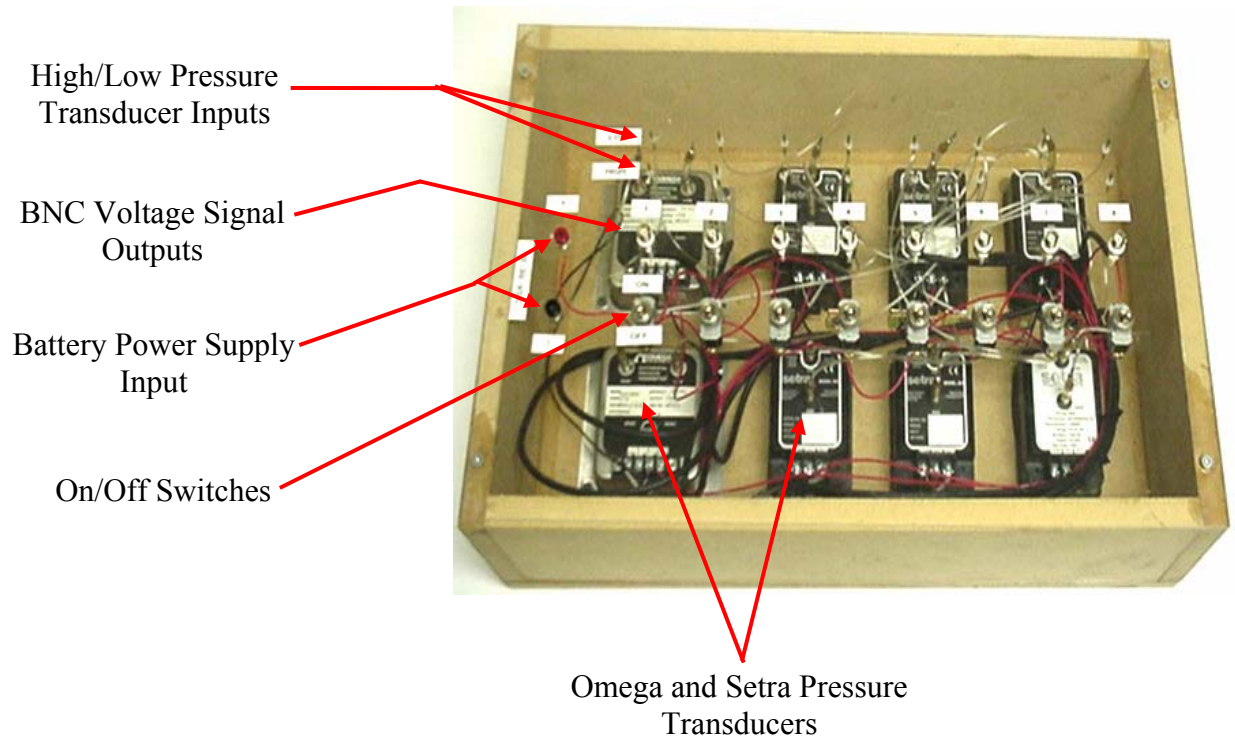


**Figure 5.19** Eight pressure transducers converted pressure readings into voltages for the data acquisition system (Vakil 2002).

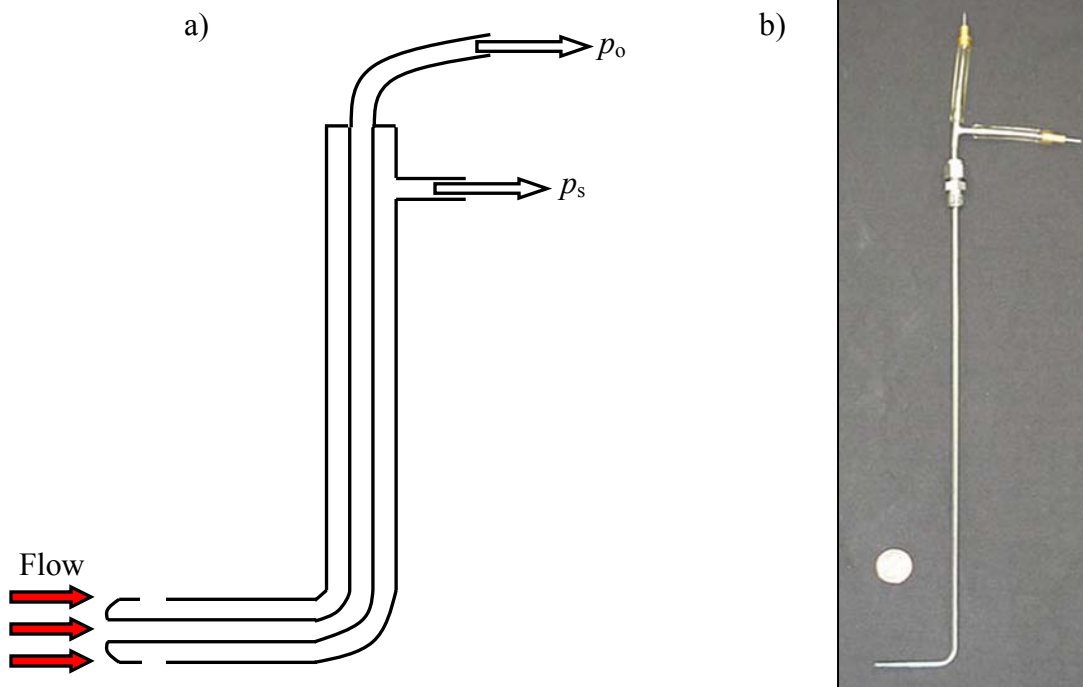


**Figure 5.20a-b** A pitot tube measures the difference between the total pressure and static pressure yielding the dynamic pressure and thus the velocity.

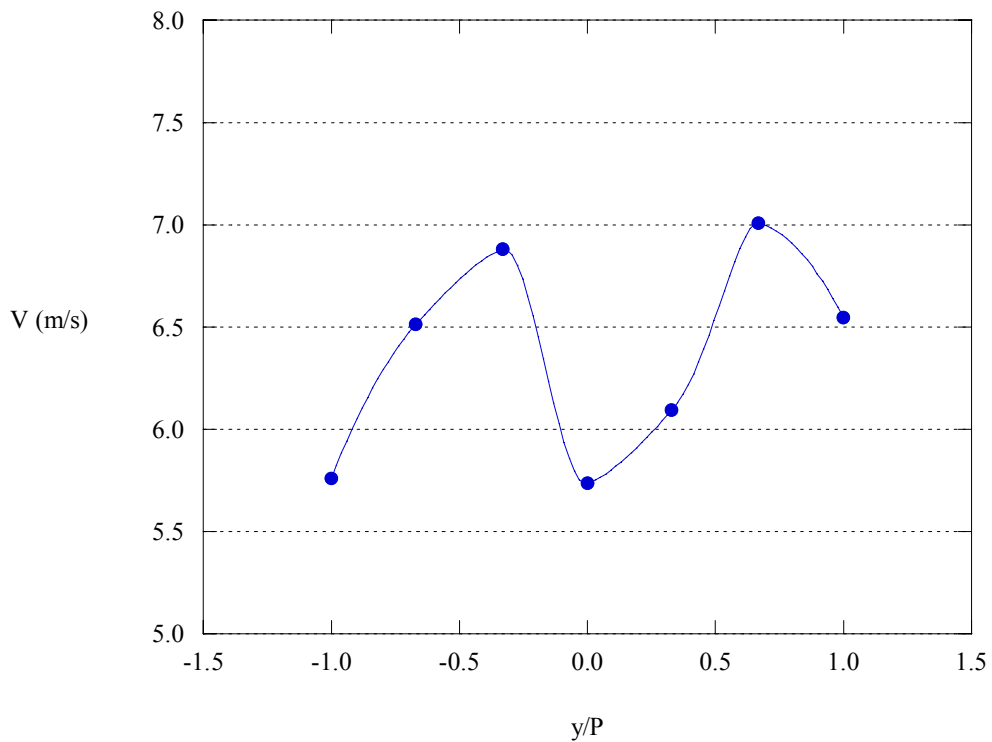


**Figure 5.21** Seven pitchwise velocity measurements were averaged to determine the cascade inlet velocity. The inlet profile exhibits periodicity.

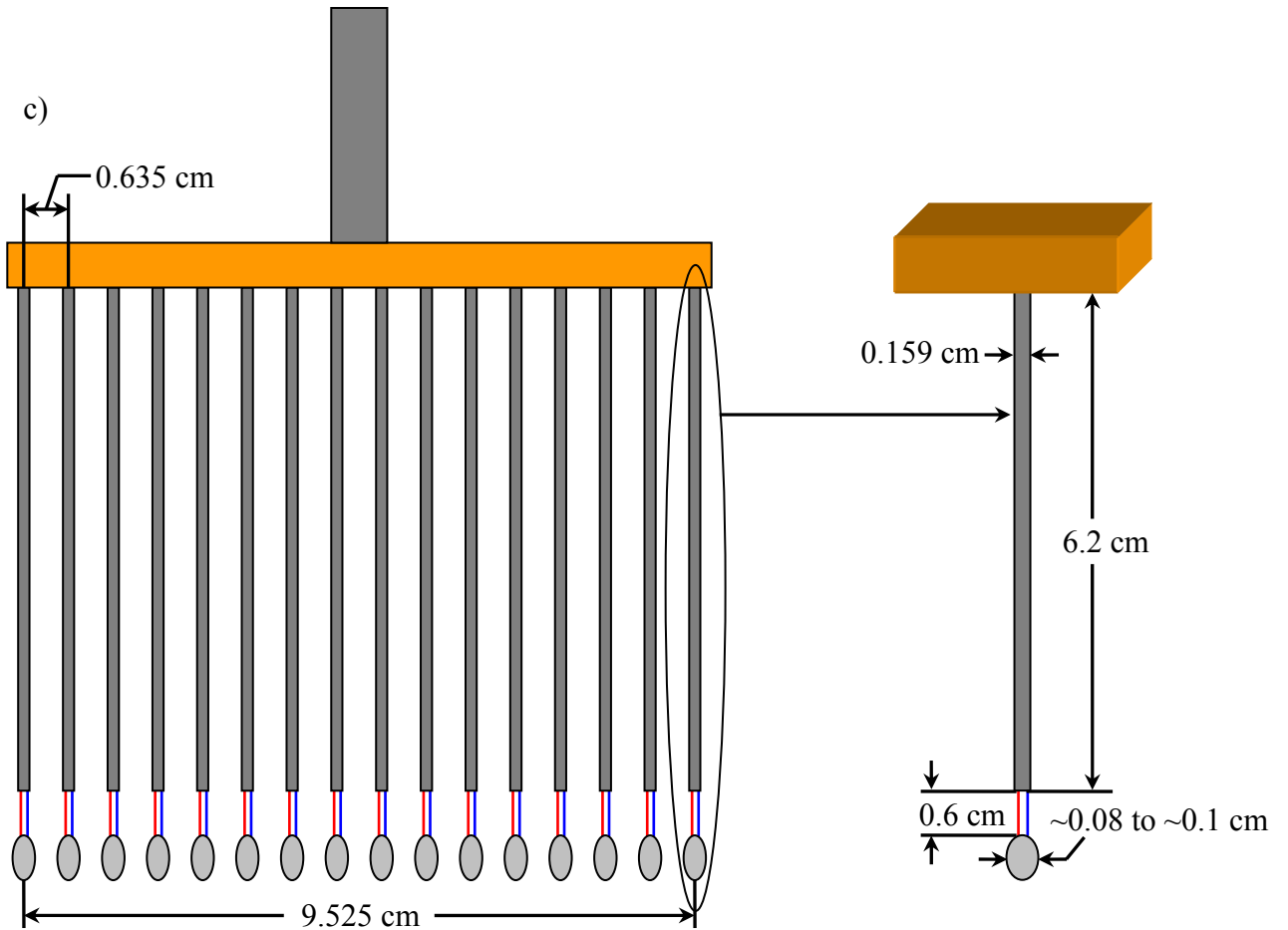
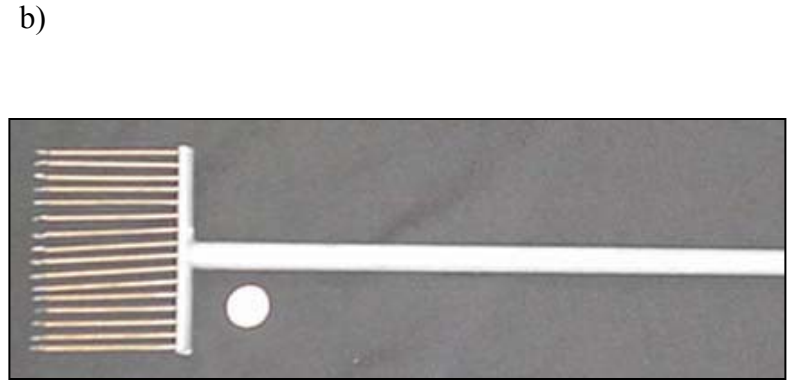
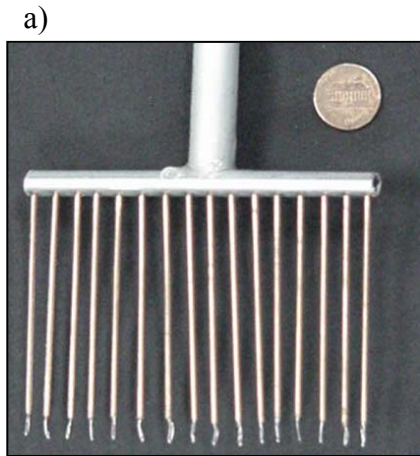


**Figure 5.22a-c** A thermocouple rake was used to document the thermal field at a plane within the passage.

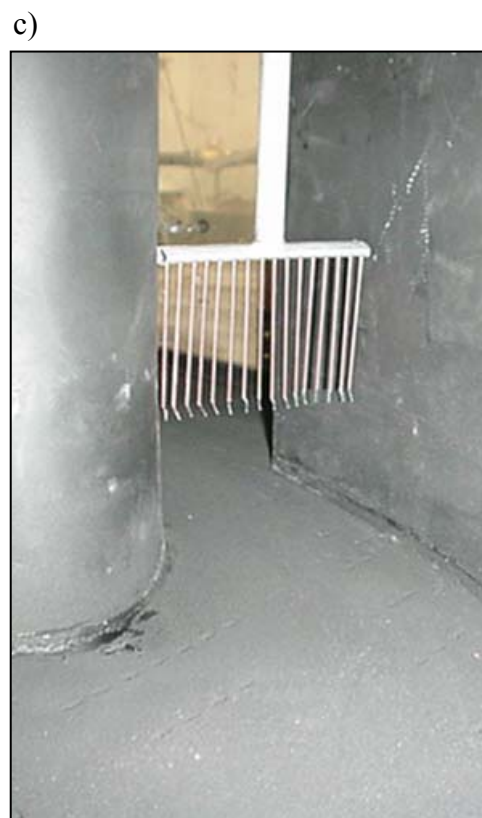
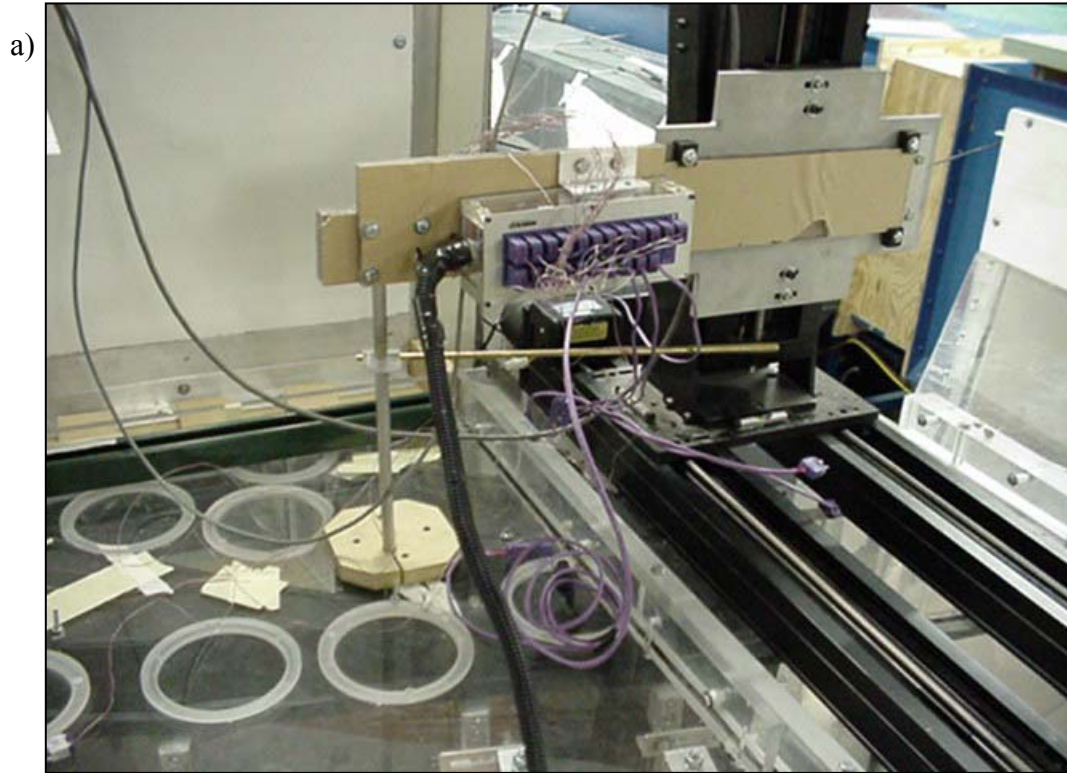


**Figure 5.23a-c** (a) The thermocouple rake was suspended from a boom and (b) moved by a computer controlled traverse. (c) The rake is shown in the passage.

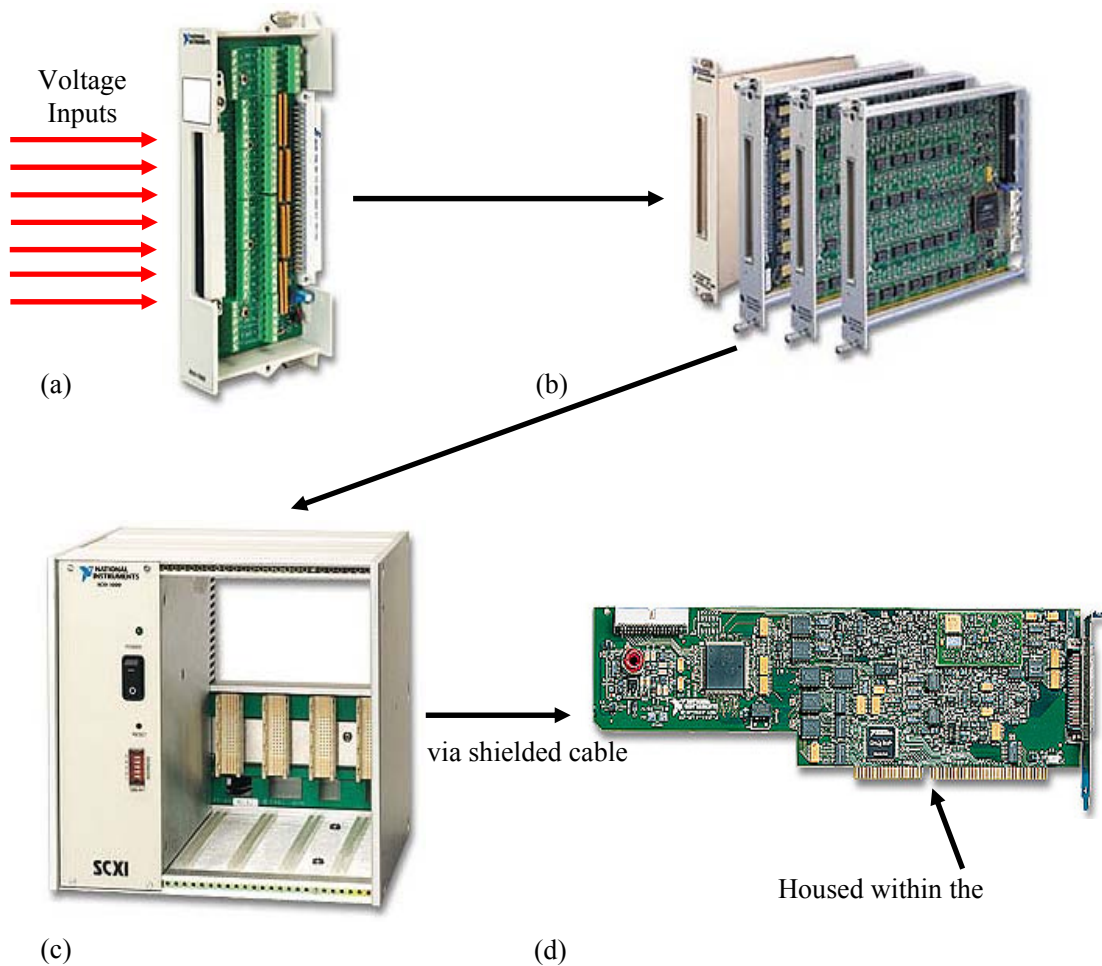


**Figure 5.24a-d** The data acquisition (DAQ) system is depicted. (a) Voltage outputs from the thermocouples and transducers are connected to a SCXI-1303 terminal block. The terminal block plugs into one of (b) three SCXI-1100 modules which are housed in the (c) SCXI-1000 chassis. The signal is output to (d) the DAQ card where it is digitized for processing on the computer (Vakil 2002).



**Figure 5.25** A Flir P20 infra-red camera was used to thermally image the endwall surface and record endwall temperature data.



**Figure 5.26** A flexible wall allows the passage flows to be adjusted in order to achieve the proper pressure distribution. The wall is adjusted with various knobs.

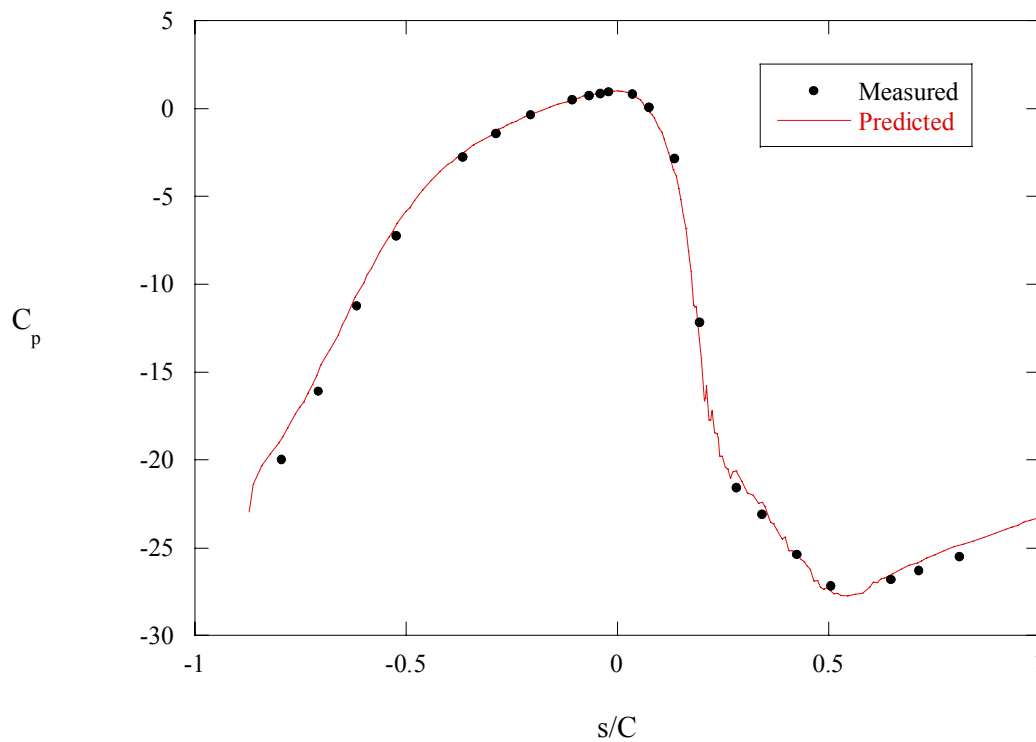


**Figure 5.27** The pressure coefficient was verified at multiple locations along the vane.

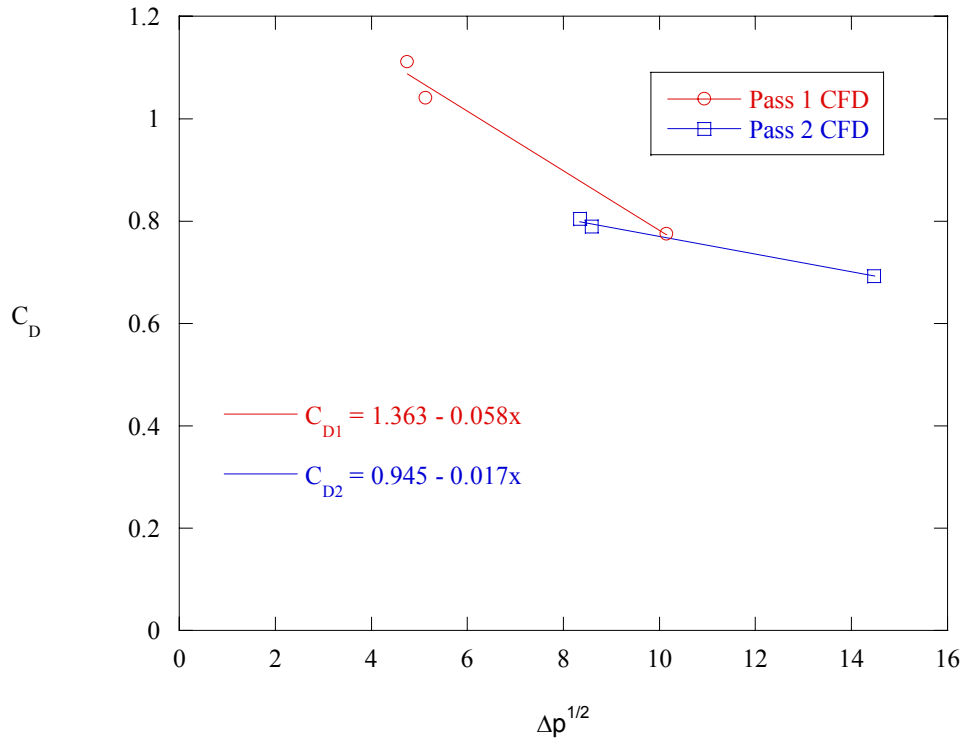


**Figure 5.28** A linear fit was used to calculate the global discharge scaling parameter for each passage based upon computational predictions.

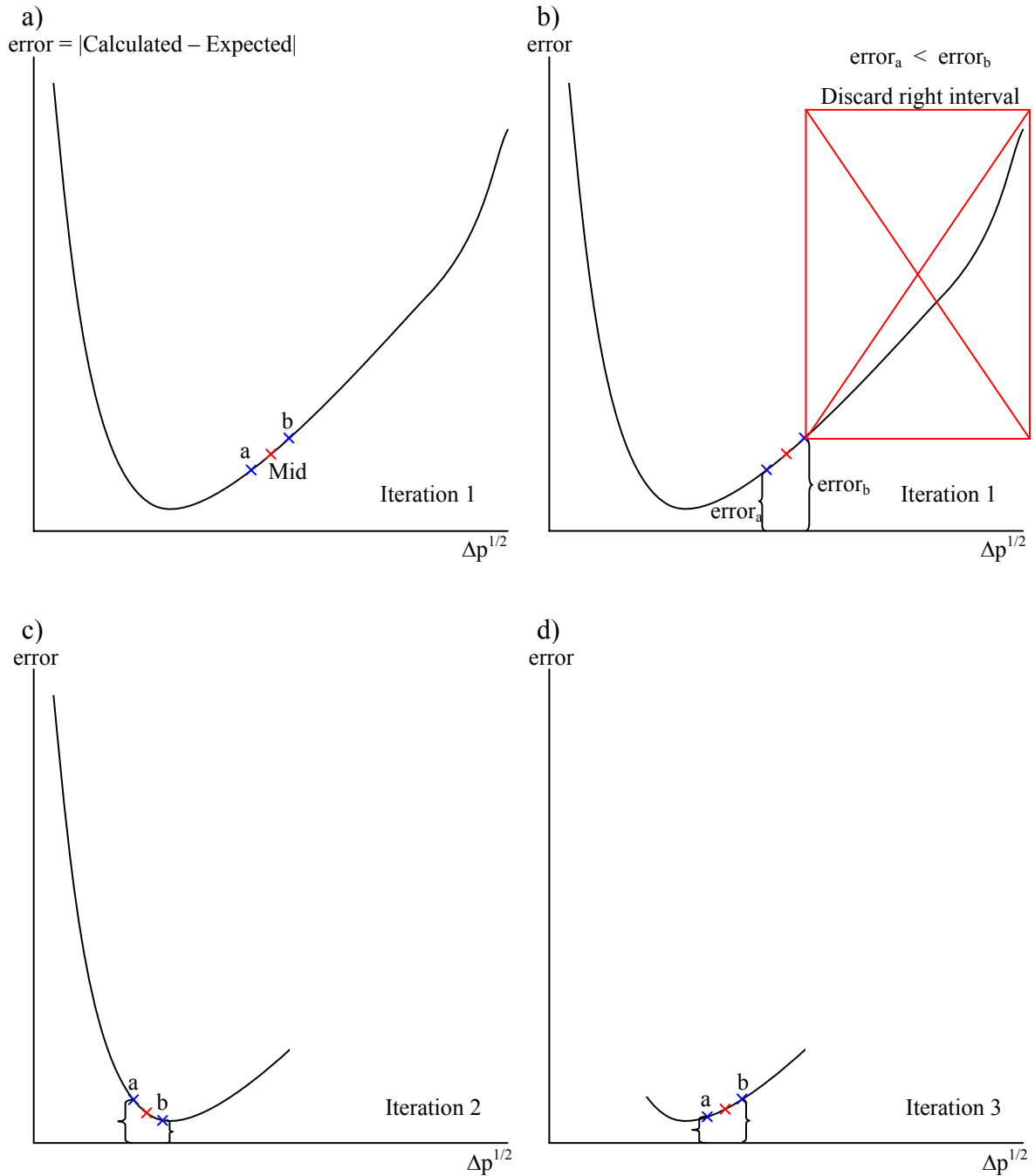


**Figure 5.29a-d** The bisection method used to calculate the experimental pressure difference is illustrated. (a) The mid-point of the possible pressure range is calculated and slightly higher and lower pressure are selected (points a and b). The discharge coefficient and corresponding mass flow of each search point are calculated. (b) The error of each search point is calculated. The search point with the greater error along with the range between that pressure and the limit are discarded. (c) The new mid-point is calculated and errors are again compared. (d) Bisection continues until the error between the points is less than the specified tolerance.

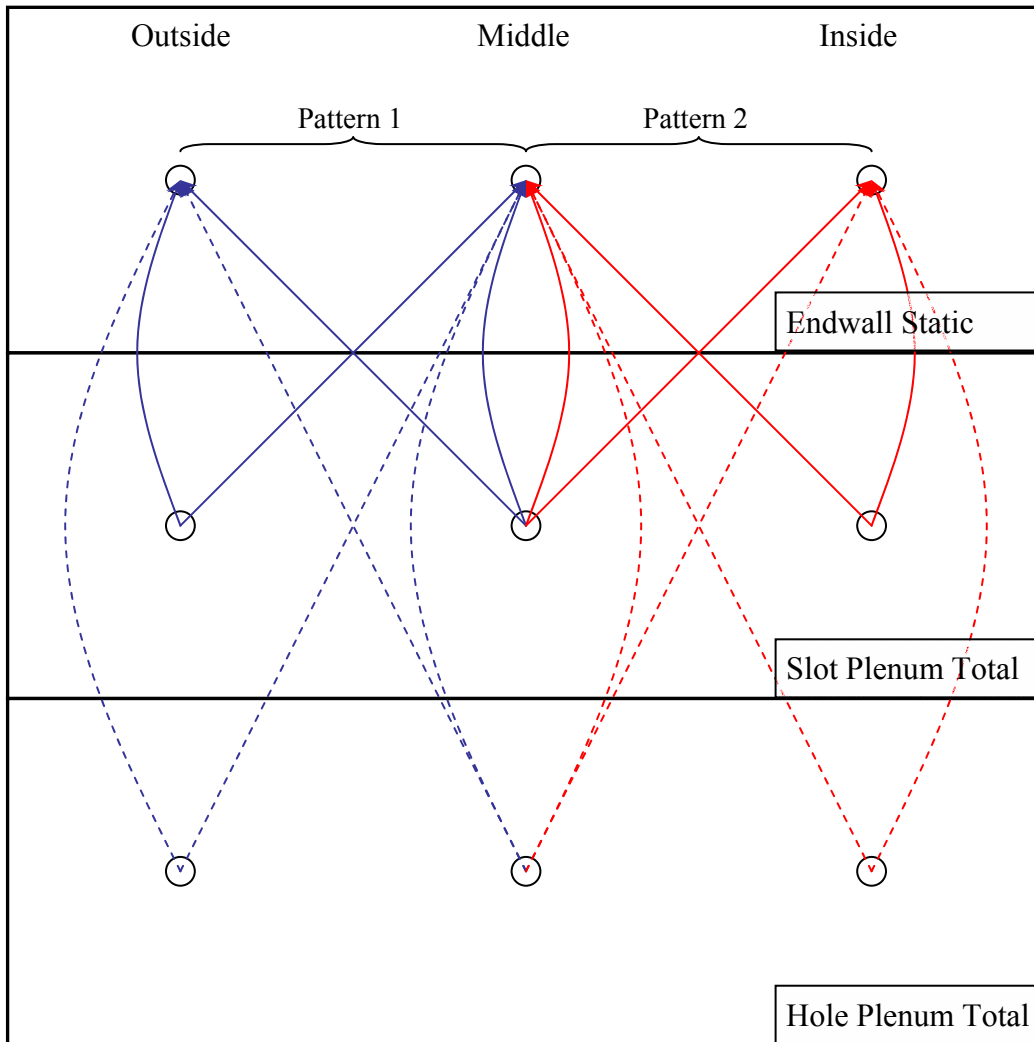


**Figure 5.30** When setting experimental cooling flows, four pressure measurements were recorded for both the slot flow and the film-cooling for the pattern of interest as shown by the wiring diagram. The pressure measurements were averaged to determine the coolant flow rates.

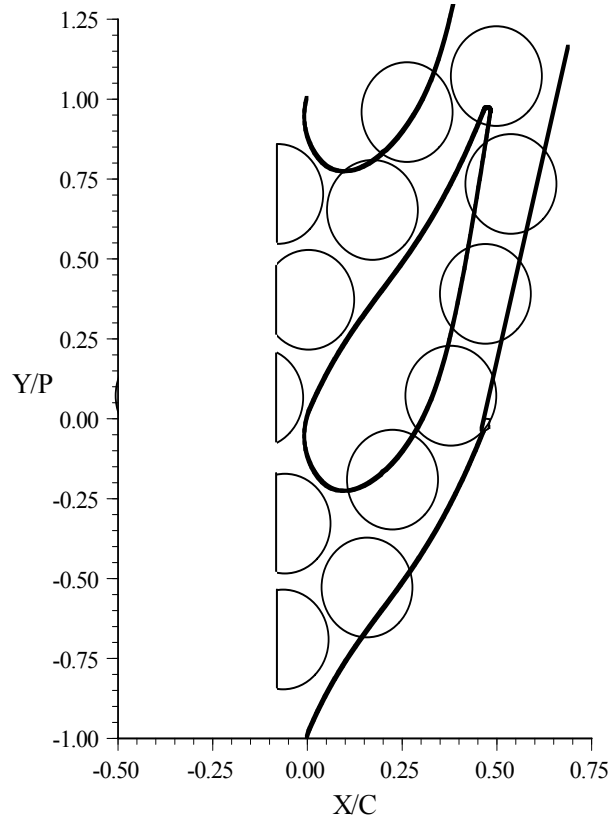


**Figure 5.31** Images were collected at 13 different locations to entirely map the endwall thermal contours.

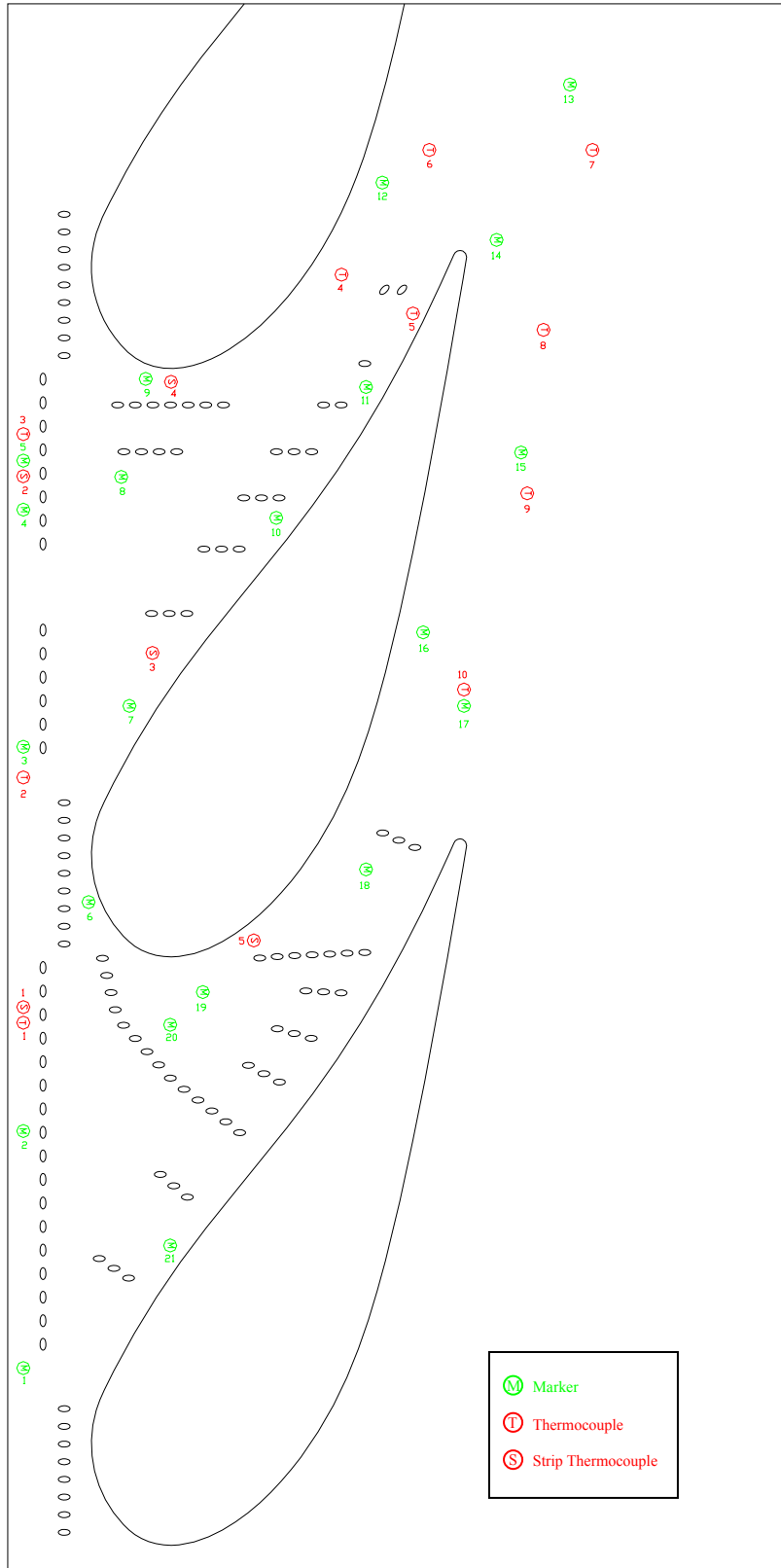


**Figure 5.32** Small markers were embedded in the endwall to provide global reference points and thermocouples were used to post calibrate the infra-red images.

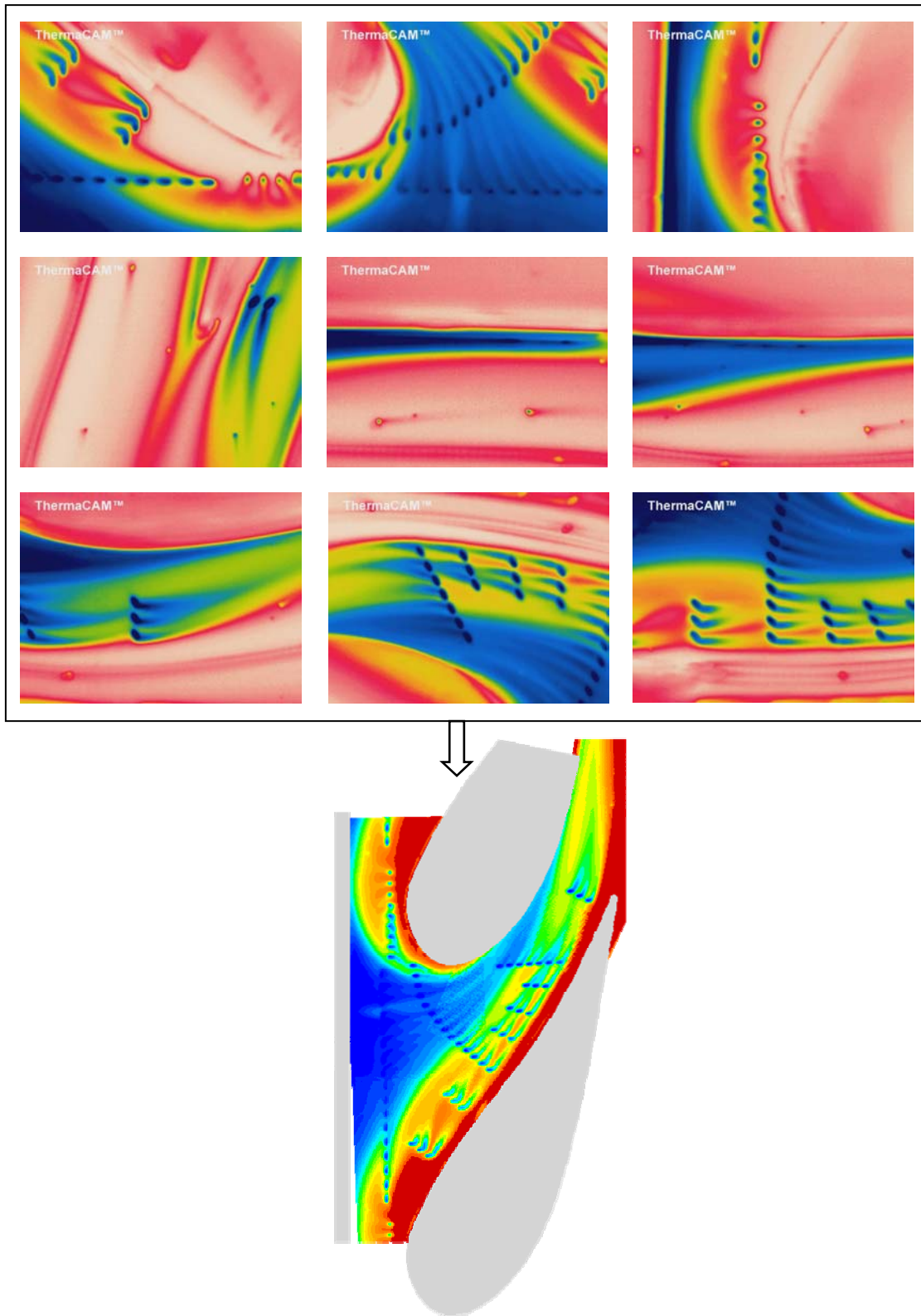


**Figure 5.33** The multiple images were combined using known global locations to form a mosaic of the endwall thermal contours.

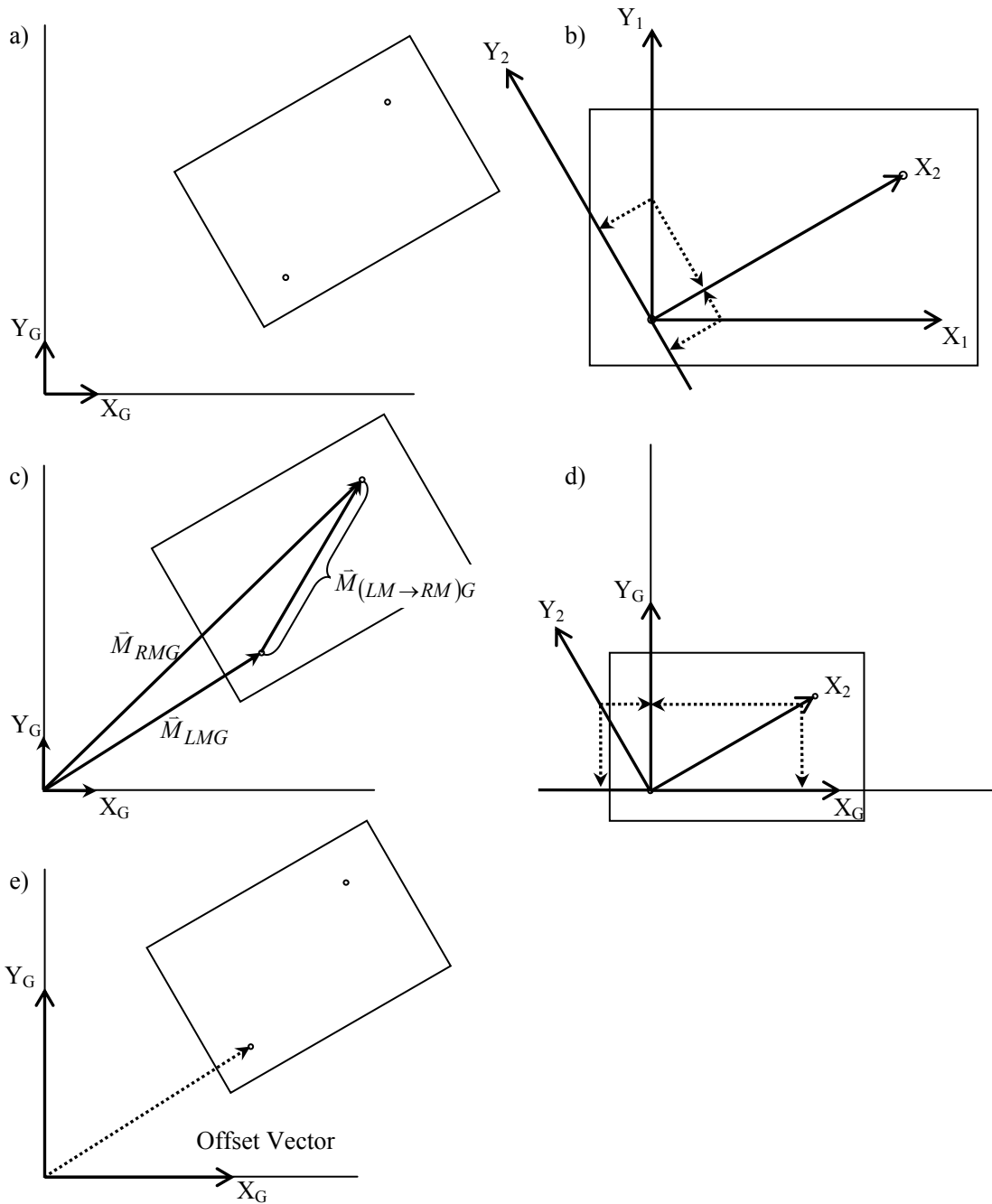


**Figure 5.34a-e** The image transformation process is illustrated. (a) an image in space has two markers at know global locations. (b) The transition matrix from a pixel aligned coordinate system to the marker aligned system is developed by projecting the pixel basis onto the marker basis. (c) The vector from the left to right marker in the global frame is found by a vector subtraction of the vectors to the markers. (d) The transition matrix from the marker frame to the global frame is found by projecting the marker basis onto the global basis. (e) The offset vector to one of the markers positions the image globally.

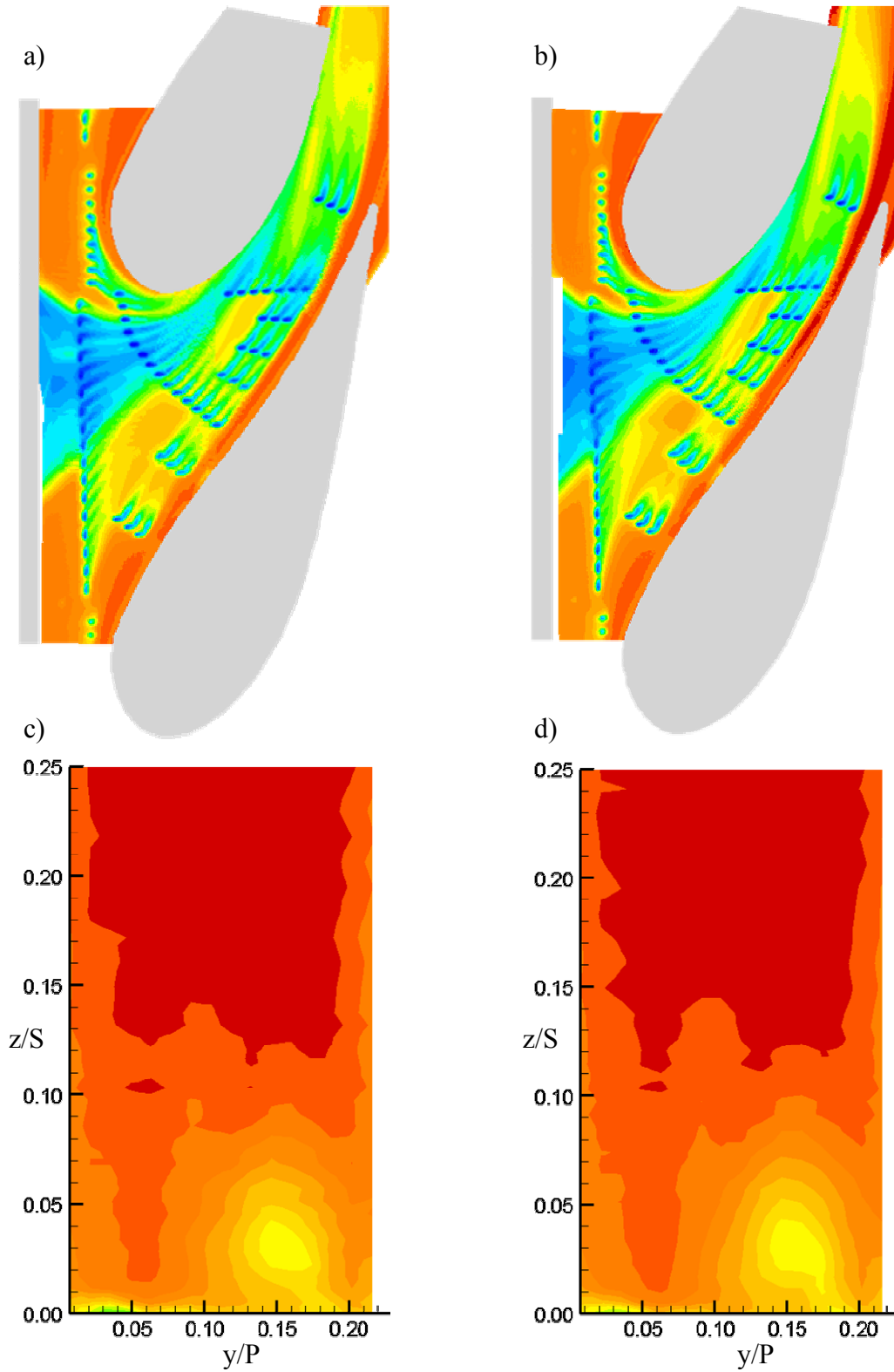


**Figure 5.35a-d** Both endwall contour data (a and b) and thermal field data (c and d) showed excellent repeatability.

## **Chapter 6**

### **Computational Results**

Computational modeling has revolutionized modern engineering. Designs can be quickly developed and evaluated without the expensive and time consuming process of prototyping and testing multiple design ideas. Computational Fluid Dynamics (CFD) has been integrated into the gas turbine design process to evaluate both the aerodynamic and thermal impacts of various airfoil geometries and cooling methods.

This study was focused on reducing heat transfer to the endwall surface of a first-stage vane through the implementation of slot leakage flow at the combustor-turbine interface and two unique endwall film-cooling patterns. A computational test matrix, shown in Table 6.1, was developed in order evaluate the performance of each cooling mechanism alone as well as the slot and film-cooling holes in concert at low and high flow rates to determine the effectiveness and interactions of the cooling mechanisms. Performance was evaluated based upon adiabatic film-cooling effectiveness levels which are the temperatures that the surface would see if no heat were conducted through the endwall surface. Experimental results will be presented in chapter 7 and the predictions from this chapter will be benchmarked against the experimental data in chapter 8. Note that for all of the calculations, the density ratio (jet-to-mainstream) was held fixed at 1.14 to allow for comparisons with experiments.

Much of the discussion in this chapter was taken from the conference paper by Knost and Thole (2003). The results from the predictions made for the test cases shown in Table 6.1 will be discussed in a logical progression of complexity in Section 6.1. First, the cooling provided from the leakage slot flow alone will be examined. Second, adiabatic effectiveness levels for the case with film-cooling alone for both endwall patterns will be discussed. Finally, the predictions for the combined slot and film-cooling configurations will be compared to the predictions for the slot alone and endwall film-cooling alone. In Section 6.2, the superposition method will be evaluated using the slot alone and endwall film-cooling alone as compared with the predictions for the combined slot and film-cooling configurations. Section 6.3 will present thermal and flow field

predictions from a plane intended to lend insight into the superposition evaluation. Finally, a summary of findings from the predictions will be given in Section 6.4.

## 6.1 Predictions of Adiabatic Effectiveness

### *Slot Injection at the Combustor-Turbine Interface*

As previously discussed several cases were computed for a two-dimensional flush slot upstream of the turbine vane (cases 1S0F0 and 3S0F0 in Table 6.1). Figure 6.1a shows the predicted contours for the 0.5% coolant flow (case 1S0F0). There is essentially no coolant exiting the slot directly upstream of the vane stagnation for case 1S0F0. In fact, a small amount of ingestion was predicted upstream of the leading edge. The slot coolant is swept across the passage toward the suction side-endwall junction leaving a large uncooled ring around the vane which is especially pronounced at the leading edge and along the pressure side. Cooling levels within the slot flow rapidly decrease to approximately  $\eta = 0.5$ .

The predicted adiabatic effectiveness levels for the slot cooling, with the coolant flow being 1% of the exit mass flow, are shown in Figure 6.1b. There is a definite increase in the predicted effectiveness levels for the 1% coolant flow as compared to the 0.5% coolant flow (case 1S0F0). The coolant exits across the entire width of the slot, but still in a non-uniform manner, and is again swept towards the suction side-endwall junction. Higher effectiveness levels are maintained throughout the slot affected region when compared to the low flow case. There is a warm ring around the airfoil that extends from the stagnation location and along the entire pressure side. A large portion of the suction side also has a warm ring along the endwall in the vane-endwall juncture. The computational results indicate that at  $s/C = 0.65$ , the coolant from the slot impacts the suction side of the vane which is upstream of the predicted impact location at the low slot flow rate. The warm ring is a result of the horseshoe vortex that is wrapping around the vane as well as the large passage vortex that is convected toward the suction side of the vane. The coolant is lifted from the endwall surface by the upward velocity vectors of the secondary flow thereby reducing the cooling effectiveness on the endwall.

Pitchwise averaged effectiveness levels predicted for the 0.5% and 1% cases are shown in Figure 6.2. These averages indicate improved cooling for the higher coolant

flow condition in the upstream endwall region. There is a large improvement in the leading edge region for the higher coolant flow condition. Progressing downstream, however, the two coolant flow conditions give approximately the same pitchwise-averaged effectiveness levels which is expected because coolant is no longer present across much of the passage.

### *Cooling Hole Injection Along the Vane Endwall*

Two cases were computed for the endwall cooling investigation, which included the two different endwall cooling hole patterns with each having 0.5% coolant injection. Note that there are 14 more cooling holes for the cooling hole configuration #1 as compared with #2, which was dictated by the designs given by industry (pattern #2 has 78% of the hole area of pattern #1). As a result of this disparity in the number of cooling holes, the coolant flow distribution is different for each of the hole patterns. The blowing ratios based on the inlet flow conditions ( $M_{in}$ ) for patterns #1 and #2 were 1.2 and 1.5, respectively as listed in Table 6.1.

As would be expected based on the iso-velocity contours, there is a large variation in the local flow rate through each of the holes given that all of the holes are fed from a common plenum supply. The blowing ratio ( $M_{in}$ ) based on the inlet mass flux of a number of representative holes is listed in Tables 6.2a and 6.2b for the two hole patterns. Of interest for this section of the discussion are cases 0S1F1 and 0S1F2 listed in Tables 6.2a and 6.2b. The locations of these holes, which are nearly paired between the two passages, are shown in Figure 6.3a. Tables 6.2a and 6.2b show that near the leading edge (holes 1.6 and 2.6) the blowing ratio is the lowest with a large discrepancy between the two cooling hole patterns. The large difference between the two hole patterns is attributed to the fact that there are fewer holes in pattern #2 as compared with pattern #1. One could predict the blowing ratio, and thus the mass flow rate, through any of the cooling holes using a known discharge coefficient and the total plenum to exit static pressure difference. Since the total flow through each of the holes is known from the CFD results, it was possible to deduce a representative discharge coefficient. These discharge coefficients are listed in Table 6.1 for the various cases. As the pressure ratio increases, so does the discharge coefficient.

Figures 6.4a and 6.4b present the predicted endwall effectiveness levels for the two cooling hole patterns at 0.5% coolant. The computational results indicate that the injection from the cooling holes in the first streamwise row of holes remain relatively discrete for pattern #1 (Figure 6.4a), particularly nearer to the suction side of the vane passage. Recall all of the holes in this first row are injecting towards the top of the picture, as was indicated in Figure 6.3b. Closer to the pressure side of the vane but still in the first row of holes, the jets are slightly more merged as a result of the sweeping motion of the passage vortex at this location. The endwall cooling along the pressure side of the airfoil is non-existent for pattern #1 as illustrated by the  $\eta = 0$  contours in this region. The coolant injected from holes in the vane passage located near the pressure side of the airfoil is primarily blowing in the same direction as the streamlines even though these holes are directed towards the pressure surface. Relatively good cooling along most of the endwall, with the exception of the band near the pressure surface, is predicted for pattern #1 at a film-cooling flow rate of 0.5%.

There are a number of noticeable differences in the effectiveness levels for hole pattern #2 relative to pattern #1. For the cooling holes located just upstream of the vane stagnation, it is clear that the cooling is much more effective for hole pattern #2 as compared with hole pattern #1 even though the hole configuration at this location is the same for the two patterns. The reason for this better cooling is because there is proportionally a higher flow rate through the set of holes at the leading edge for the pattern #2 as compared with pattern #1 (see holes 2.6 and 1.6 in Tables 6.2a and 6.2b). The effectiveness contours are much cooler in the stagnation area extending along the suction side of the vane for pattern #2 as compared to pattern #1.

In the passage itself, the most noticeable difference between the two cooling hole patterns is that while relatively uniform coverage in the passage existed for hole pattern #1 (with the exception of near the pressure surface), the effectiveness contours for hole pattern #2 indicate the presence of a hot streak that travels down the mid-passage of the vane. This hot streak is a result of the break in the cooling hole placement due to the gutter that would be present in the region where adjacent vane platforms meet (discussed previously). Coolant exiting from the gutter could potentially alleviate these high

temperatures, but if no coolant leaked out of the gutter region there would be damage to the endwall in this high temperature region.

Similar to pattern #1, the cooling from the first row of holes remains relatively discrete for the pitchwise row of holes injecting nearer to the suction side of the vane passage for pattern #2. For the first row holes in the mid-passage region of pattern #2, the coolant does not remain in discrete streaks, but rather merges into one large, cooler area. Also similar to pattern #1, there is no coolant present along the endwall close to the pressure side of the airfoil for pattern #2. In the case of hole pattern #2, the endwall cooling holes along the pressure side of the vane are injecting directly towards the vane. Although the coolant was not able to overcome the crossflows present resulting in a hot region along the pressure side, the overall cooling effectiveness levels downstream of the jet injection were higher than in the case for hole pattern #1 in this region.

#### *Combined Slot and Film-Cooling Injection*

Four cases were computed for the combined slot and film-cooling injection studies, which included the slot combined with the two hole patterns at two different film-cooling flow conditions. The slot flowrate remained fixed at 0.5% of the core flow while the film-cooling flowrates considered were 0.5% (cases 1S1F1 and 1S1F2) and 0.75% (cases 1S2F1 and 1S2F2). Note that the slot and the film-cooling flow rates were set independently through the use of two different supply plenums. Tables 6.2a and 6.2b give the local blowing ratios for the hole locations indicated in Figure 6.3a. Note that all of the blowing ratios slightly increased for the combined film-cooling/slot cases for both hole patterns. The reason for this slight increase is because the exit mass flow through the vane was held fixed and, as such, relatively more coolant was sent through the holes since the slot flow was taken out of the mainstream flow. Other than the slightly higher blowing ratios, the relative difference between the cooling holes was nominally the same. Figures 6.5a-b show the contour plots for the two flowrate conditions for the combined slot and cooling hole pattern #1. Figure 6.5a illustrates that the slot coolant contributes to the cooling effectiveness near the suction side of the airfoil and rather than discrete jets as was shown in Figure 5a, this region is relatively cooled uniformly. The trajectory of the cooling jets looks to be very similar for the endwall cooling alone as compared with the

combined slot/endwall cooling configuration. The exit slot flow is also not effected by the downstream cooling hole injection.

There is a definite increase in the adiabatic effectiveness levels for the increased film-cooling flow as shown by Figure 6.5b. The leading edge holes indicate a much better performance with continued increases in effectiveness along the pressure side of the airfoil. The pressure side region showed the most dramatic increases in effectiveness with the increased coolant flow from the film-cooling holes. The trajectory of the cooling jets has changed significantly for the higher cooling flow case, particularly along the pressure side. Rather than being swept in the streamwise direction, these jets have enough momentum to penetrate closer towards the pressure side of the vane. There is also a slight improvement in effectiveness along the suction side of the vane.

For cooling hole pattern #2, shown in Figures 6.6a-b at the two coolant flow conditions, the slot interaction with the cooling holes showed one noticeable effect. In the case with only endwall cooling, the jets exiting from the holes in the leading edge row near the mid-passage region were more directed toward the pressure side of the vane (Figure 6.4b) as compared to the predictions shown in Figure 6.6a. For the combined slot/hole configuration, Figure 6.6a shows that the leading edge jets in the mid-passage region are being entrained by the slot flow. This effect is even more dramatic at the higher cooling flow case shown in Figure 6.6b with the coolant from these jets being strongly turned toward the suction side of the adjacent vane.

For both coolant flow conditions in hole pattern #2, the hot streaks through mid-passage still remain for the combined slot/hole configuration. For the higher film-cooling flowrate shown in Figure 6.6b, there is a predicted increase in effectiveness levels as compared with the lower film-cooling flowrate shown in Figure 6.6a. The detriment at the higher blowing ratio for hole pattern #2 is that the hot streak becomes wider as shown in Figure 6.6b. The reason for this widening is because the jets are more directed towards the pressure surface. These results indicate that even with the presence of the gutter, it may not be possible to cool the entire hot streak region.

Figure 6.7 compares the pitchwise averaged effectiveness levels for the combined slot/hole configuration for hole patterns #1 and #2 at the two different film-cooling flowrates. For all of the cases, the averaged effectiveness levels agree just after the slot

to  $x/C_a = -0.15$ . The peak in effectiveness level occurs just downstream of the slot for all of the cases with a second peak occurring for hole pattern #1 at  $x/C_a = 0.6$ . Downstream of the slot, the averages indicate the highest predicted effectiveness averages occur for hole pattern #1 at the higher coolant flow condition. There is a distinct increase in the pitchwise-averaged effectiveness levels for hole pattern #1 at the higher coolant flow condition. This is not the case for hole pattern #2, which indicates nearly the same pitchwise averaged effectiveness levels for the two coolant flow conditions. The reason for the lack of improved performance is because of the large hot streak in the mid-passage for hole pattern #2, which occurs at both the low and high coolant flow conditions.

Figure 6.8 provides an overall summary of the area-averaged effectiveness levels for all of the cases evaluated. These area-averaged effectiveness levels can be used as a guide for designers in choosing whether coolant is more effectively used through the slot interface or through the cooling holes. Note that the areas for these cases were all computed based on the axial position located at the downstream edge of the slot. As a result of this fixed area, there is a large uncooled portion of the endwall upstream of the holes that brings down the area-averaged effectiveness levels for the two cases without slot flow. In all of the flow rates considered, pattern #1 was superior to pattern #2. It is also evident that increasing the flow rate from pattern #2 did not result in much benefit from an average endwall temperature perspective. Figure 6.8 also indicates that for the 0.5% coolant flow, it is beneficial from an average perspective to inject the coolant flow from the cooling holes alone rather than from the slot alone. One word of caution, however, is that the local variations without the slot cooling (such as upstream of the first row of holes) may be too great and, as such, the area averaged effectiveness values alone do not tell the entire story.

## 6.2 Superposition of Results

An analysis was made based on the predicted effectiveness levels as to whether superposition may be appropriate in which effectiveness predictions for the slot alone and for the film-cooling holes alone could be combined to give an indication of the effectiveness levels for a case with a combined slot and film-cooling holes. Figure 6.9

shows the predictions made for each cooling mechanism alone (slot or cooling holes), the two combined using superposition, and the directly predicted pattern #2 which was used for this exercise, the results are representative of what occurs for hole pattern #1 as well. The pitchwise-averaged effectiveness values in Figure 6.9 indicate that there is a slight effect of the downstream film-cooling on the exit slot flow as indicated by the slightly lower averaged effectiveness predicted by the superposition just downstream of the slot. Progressing downstream of the slot, the predicted averaged effectiveness values are slightly higher than the superimposed values until  $x/C_a = 0.15$ . Downstream of this location, the superposition solution indicates higher values. In general, these results indicate that a superposition analysis can not be simply applied for the combined film-cooling and slot flows. Recall that superposition theory presumes that the flow field remains constant for the two solutions used in the analysis. As such, one potential reason for the inability to accurately use superposition theory for the combined slot and film-cooling flows is that the flow field has significantly changed for the combined slot and film-cooling case as compared with the slot alone and the film-cooling alone.

### 6.3 Secondary Flow Field Analysis

Secondary flow fields were analyzed at a number of locations throughout the vane passage. Presented here is only one flow field plane, which is near the exit of the vane passage and is normal to the pressure side of the vane (indicated by the line shown in Figure 6.3b at the trailing edge of the pressure surface). The secondary flow fields are plotted using vectors of  $V_n$  and  $V_z$ , as defined in the nomenclature, thereby representing the deviation of the flow relative to that for the mid-span inviscid flow. The view taken for the plots is looking upstream. Figures 6.10a-d show the secondary flow vectors with superimposed thermal fields for the following cases: 0.5% slot flow alone (case 1S0F0), 0.5% film-cooling alone (case 0S1F2), 0.5% film-cooling (case 1S1F2) combined with 0.5% slot cooling, and 0.75% film-cooling combined with 0.5% slot cooling (case 1S2F2). Since the secondary flow field results are similar between hole patterns #1 and #2, representative results will only be presented for hole pattern #2. These plots are for 15% of the span ( $z/S = 0.15$ ) where  $y/P = 0$  is located on the pressure side of the vane.

Figure 6.10a shows the typical passage vortex that is expected to occur in most turbine vane flows with a low slot flow condition. The vortex center is located near 5% of the span near mid-passage ( $y/P = 0.1$ ). In contrast, Figure 6.10b indicates that with the film-cooling alone there is a strong cross-flow along the endwall, but the roll-up of the vortex is not as well-defined. The stronger cross-flow near the endwall is a result of the lower momentum fluid near the endwall that is present from the film-cooling injection as compared with the slot alone. The thermal fields in Figure 6.10b clearly show the existence of the gap in cooling along the endwall.

Figure 6.10c shows the secondary flow and thermal fields for the case with the low combined slot and film-cooling flows. The secondary flow pattern for the combined cooling flows is the strongest relative to the slot or film-cooling alone. The vortex pattern has shifted toward the suction side of the vane and is closer to the endwall than that shown in Figures 6.10a and 6.10b. The thermal fields in Figure 6.10c indicate the slot coolant has helped fill the gap along the endwall compared to Figure 6.10b.

The case with the higher film-cooling injection is shown in Figure 6.10d indicating a stronger secondary flow pattern than that shown in Figure 6.10c. As the film-cooling flow is further increased, more of the coolant is convected up the suction side of the vane. The other noticeable difference is the spreading apart of the two cool regions along the endwall. For the lower blowing case shown in Figure 6.10c, the peak effectiveness levels were located at  $y/P = 0.05$  and  $y/P = 0.18$  while for the higher blowing case shown in Figure 6.10d, the peak effectiveness levels were located at  $y/P = 0.03$  and  $y/P = 0.2$ . This difference in the location of the effectiveness peaks between the two blowing ratios occurs as a result of the higher momentum jets for the higher blowing ratio case. In addition to the difference in peak locations, there is a greater thermal spreading for the higher blowing ratio near the pressure side of the vane as indicated by comparing Figures 6.10c and 6.10d and coolant affects the pressure side up to 3% span.

Based on these secondary flow patterns and the thermal field contours, it is not surprising that the superposition method is not viable for predicting the coolant effectiveness along the endwall for the slot flow alone and film-cooling flow alone to give the cooling effectiveness for the combined cooling methods. As was shown in

Figure 6.9, an over-prediction of effectiveness results through the use of the superposition method as compared with the predicted effectiveness levels.

#### 6.4 Summary

The predictions presented in this chapter showed the effect of coolant injected from a two-dimensional slot at the combustor-turbine interface alone; endwall film-cooling alone; and combined slot and endwall film-cooling. The resulting endwall effectiveness from slot cooling alone showed a pattern that is quite non-uniform along the endwall with most of the coolant being swept toward the suction side of the vane. One could expect a burn-out near the vane-endwall juncture if only depending on the slot cooling from the combustor-turbine interface as a result of a warm ring extending most of the vane.

Placing film-cooling holes in the endwall is critical for increasing component life. The placement of these holes is difficult because the trajectory of the jets is not intuitive given the strong cross-flows that develop in the endwall region. The results of these predictions showed that the jet trajectory is highly dependent on the local blowing ratio for the cooling holes. One of the most significant findings was a lack of endwall film-cooling along the region where two turbine vanes are mated. While this region typically has a gutter with some leakage flow, it is particularly important that there is cooler leakage flow present since it provides cooling to the regions where the endwall film-cooling does not.

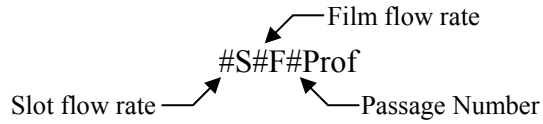
Combining the slot and film-cooling flows provided the best overall coverage for the endwall, but the warm ring around the vane was still present until a higher flow rate through the film-cooling flows was introduced. The higher flow rate provided a higher momentum for the pressure side film-cooling jets thereby allowing for a jet trajectory that approached the vane. One important finding was that there was a change in the secondary flows that developed for the combined film-cooling and slot flow studies as compared to the film-cooling alone and slot alone. This is important because this change in flow fields explained why the superposition method can not be used to predict the combined endwall film-cooling and slot cooling effectiveness levels. Moreover, using

the superposition method resulted in an over-prediction of cooling results thereby over-predicting component life.

**Table 6.1** Computational Test Matrix and Hole Discharge Coefficients

	Slot flow $\%m_{\text{exit}}/M_{\text{in}}$	Film flow $\%m_{\text{exit}}/M_{\text{in}}$	Discharge Coefficient
Case 1S0F0	0.5 / 0.18	---	---
Case 3S0F0	1.0 / 0.37	---	---
Case 0S1F1	---	0.5 / 1.2	0.49
Case 0S1F2	---	0.5 / 1.5	0.50
Case 1S1F1	0.5 / 0.17	0.5 / 1.2	0.57
Case 1S1F2	0.5 / 0.18	0.5 / 1.5	0.58
Case 1S2F1	0.5 / 0.17	0.75 / 1.8	0.59
Case 1S2F2	0.5 / 0.18	0.75 / 2.2	0.60

Key:



Number	Passage Number	Flow Rate $\%m_{\text{in}}$
0	No Film-Cooling	No Cooling
1	1	0.50
2	2	0.75
3	---	1.00

**Table 6.2a** Film-Cooling Blowing Ratios for Selected Holes in Pattern #1

Hole	Case 0S1F1	Case 1S1F1	Case 1S2F1
1.1	0.82	0.92	1.59
1.2	1.22	1.42	1.95
1.3	2.37	2.77	3.07
1.4	0.70	0.89	1.58
1.5	0.86	0.90	1.55
1.6	0.33	0.33	1.27

**Table 6.2b** Film-Cooling Blowing Ratios for Selected Holes in Pattern #2

Hole	Case 0S1F2	Case 1S1F2	Case 1S2F2
2.1	1.18	1.32	2.14
2.2	2.09	2.34	2.92
2.3	2.51	2.92	3.39
2.4	1.10	1.31	2.18
2.5	1.28	1.31	2.16
2.6	0.94	0.96	1.93

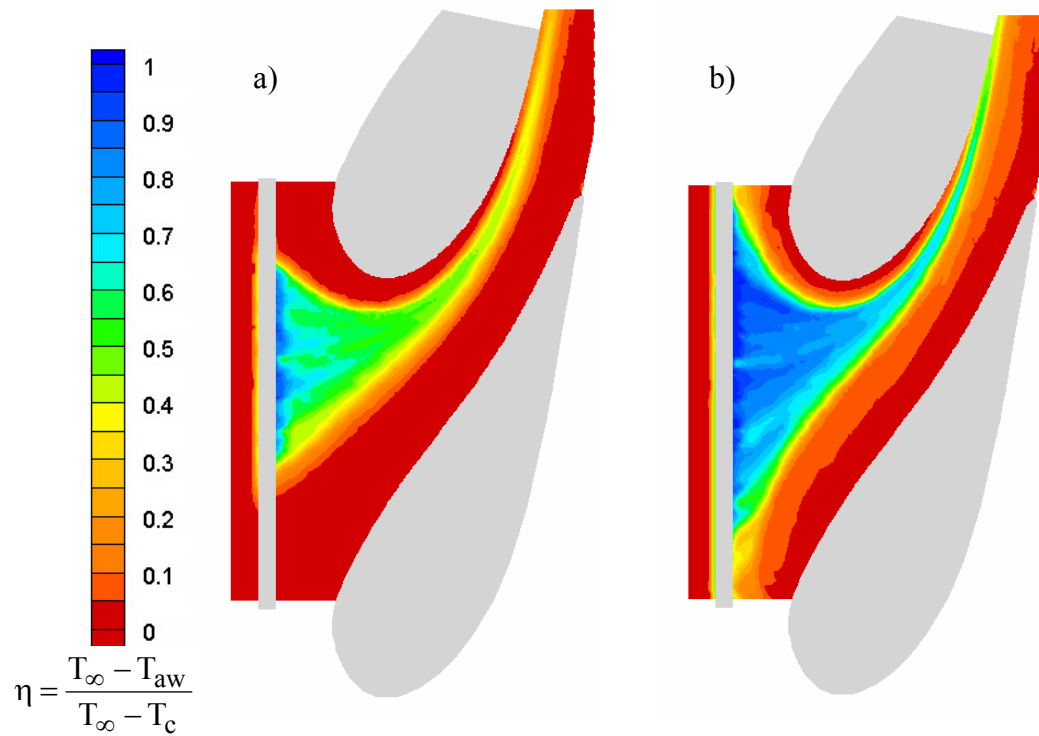


**Figure 6.1a-b** Predicted contours of adiabatic effectiveness for (a) 0.5% slot flow alone, case 1S0F0 and (b) 1.0% slot flow alone, case 3S0F0.

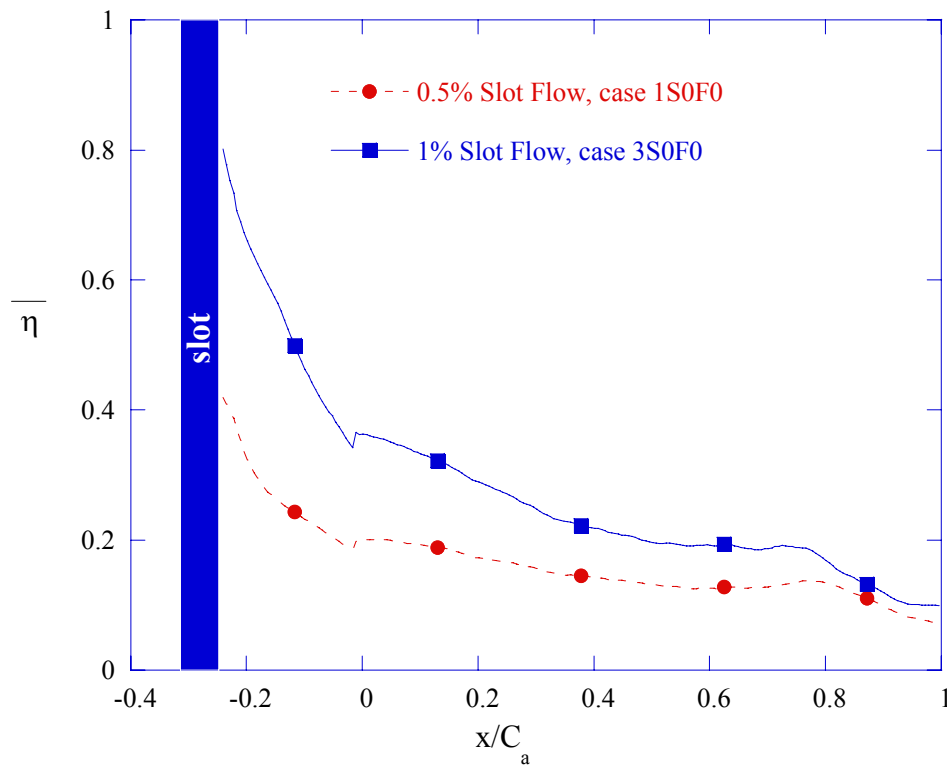


**Figure 6.2** Pitchwise-averaged adiabatic effectiveness levels through the vane passage for slot flow alone.

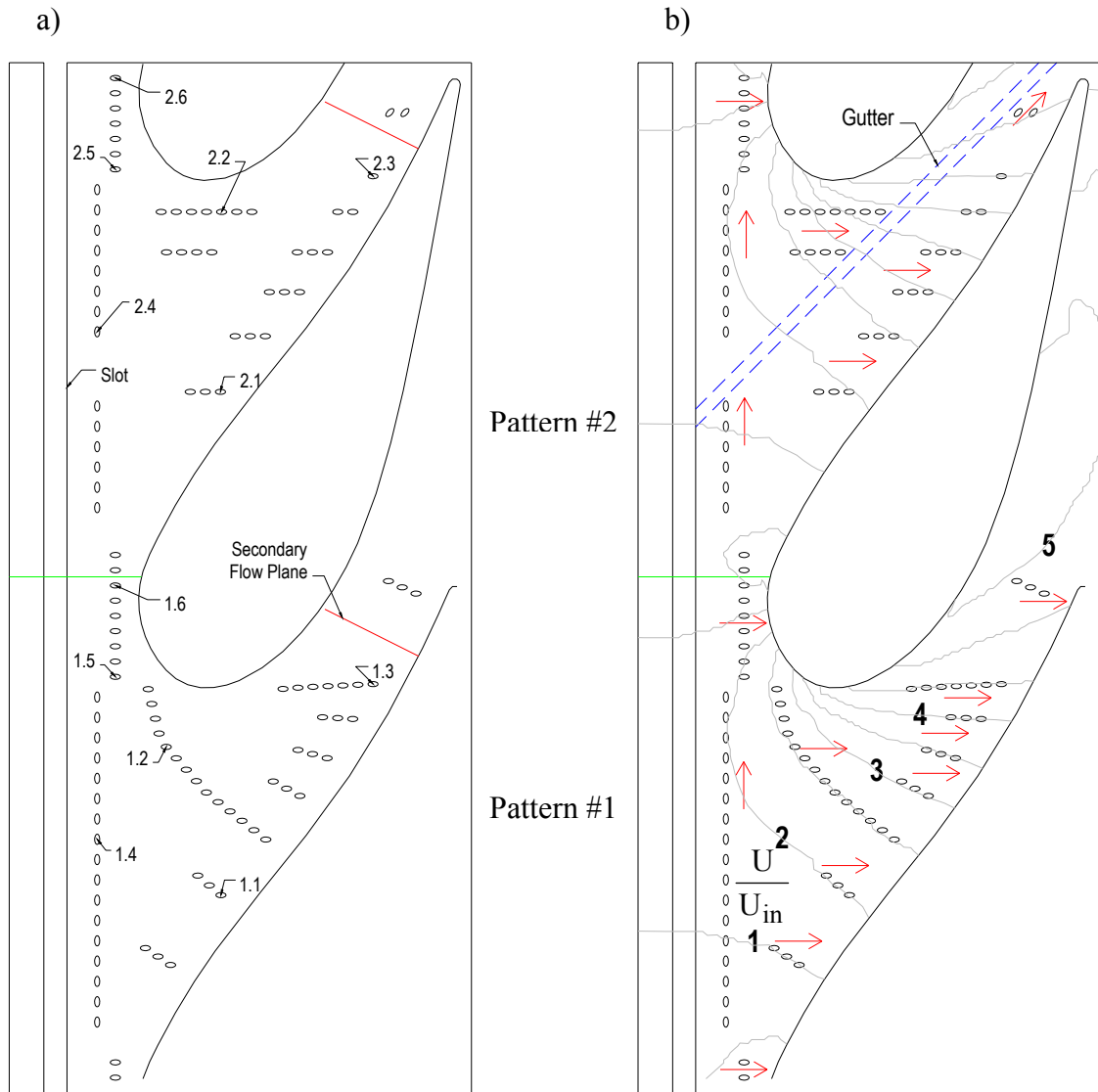


**Figure 6.3a-b** The film-cooling patterns are shown with (a) several featured holes used for comparisons between passages. A secondary flow plane is also indicated where the flow field was examined. (b) Iso-velocity contours as well as the gutter location and arrows indicating the direction of hole injection are shown.

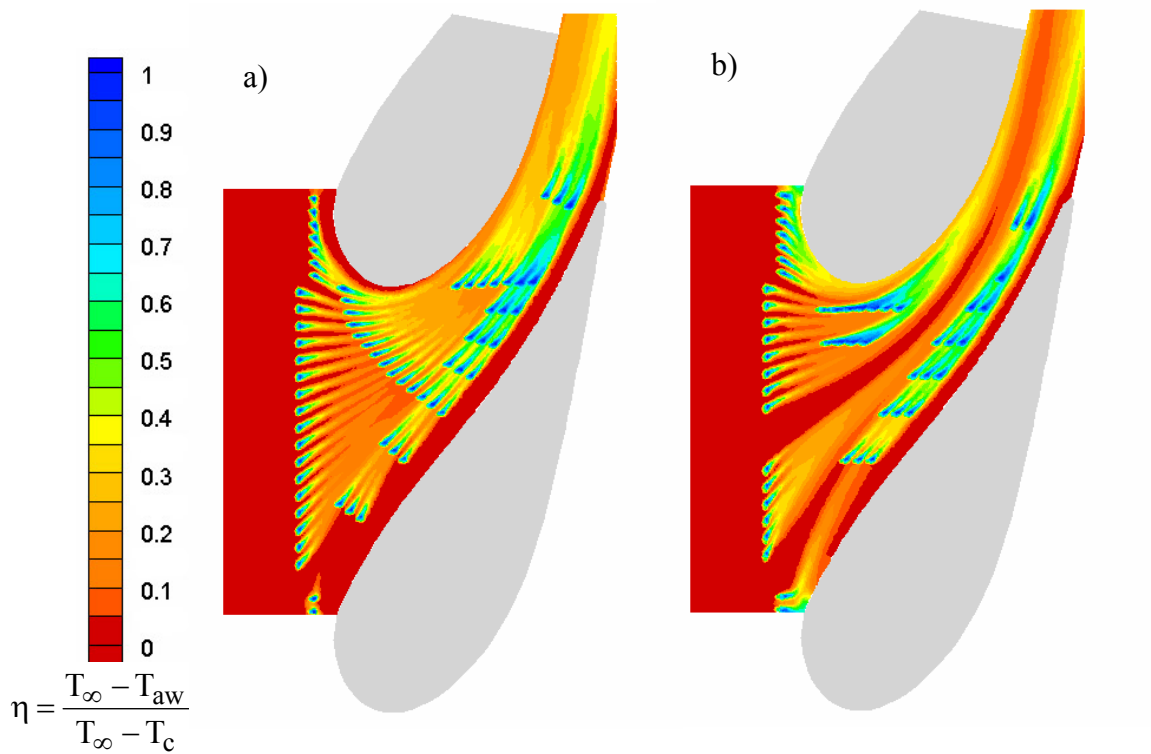


**Figure 6.4a-b** Predicted contours of adiabatic effectiveness for the baseline film cooling cases without slot flow (a) pattern #1, 0.5% film alone, case 0S1F1 and (b) pattern #2 0.5% film alone, case 0S1F2.

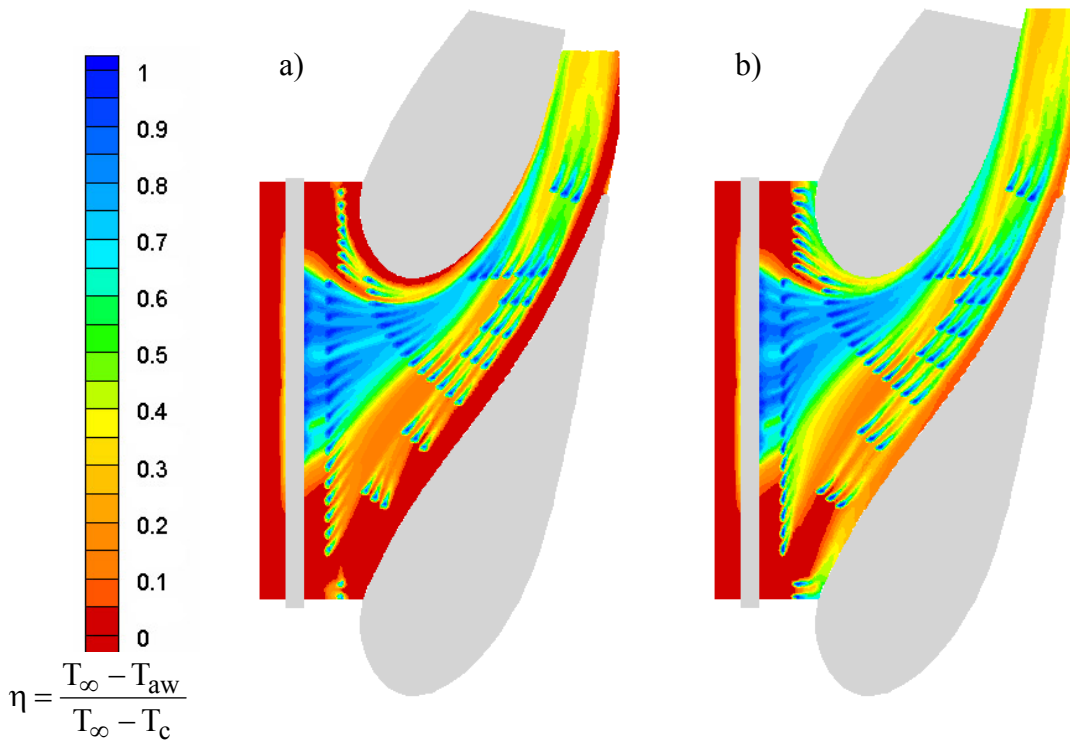


**Figure 6.5a-b** Predicted adiabatic effectiveness levels for pattern #1 at 0.5% slot flow combined with (a) the low 0.5% film flow rate, case 1S1F1 and (b) the high 0.75% film flow rate, case 1S2F1.

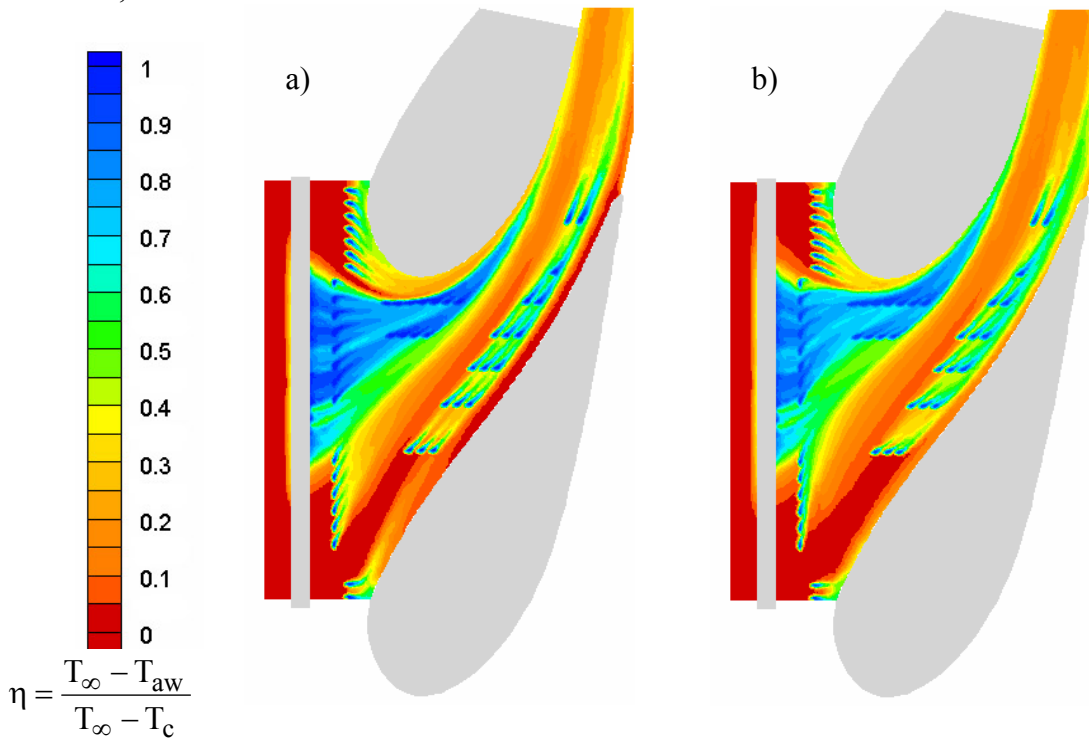


**Figure 6.6a-b** Predicted adiabatic effectiveness levels for pattern #2 at 0.5% slot flow combined with (a) the low 0.5% film flow rate, case 1S1F2 and (b) the high 0.75% film flow rate, case 1S2F2.

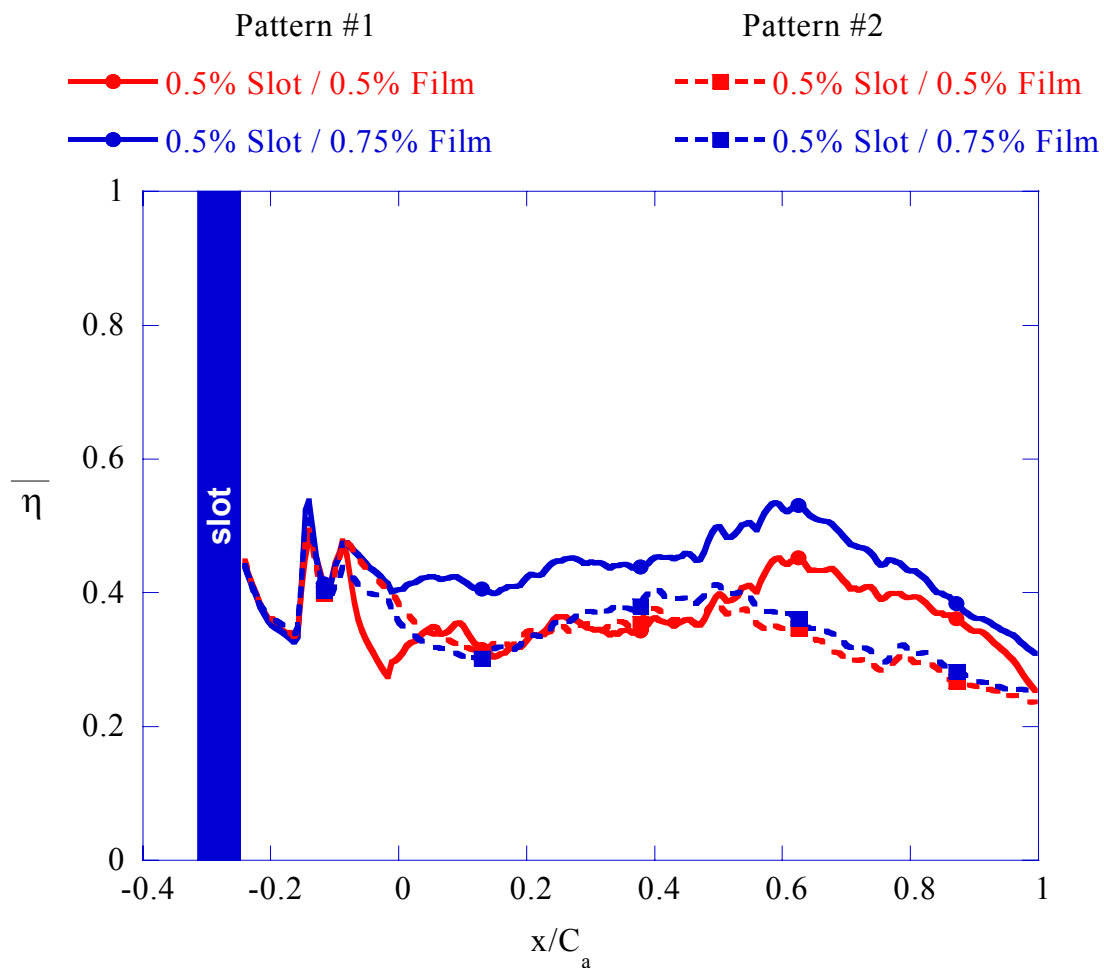


**Figure 6.7** Pitchwise-averaged adiabatic effectiveness levels through the vane passage for the combined slot and film-cooling cases.

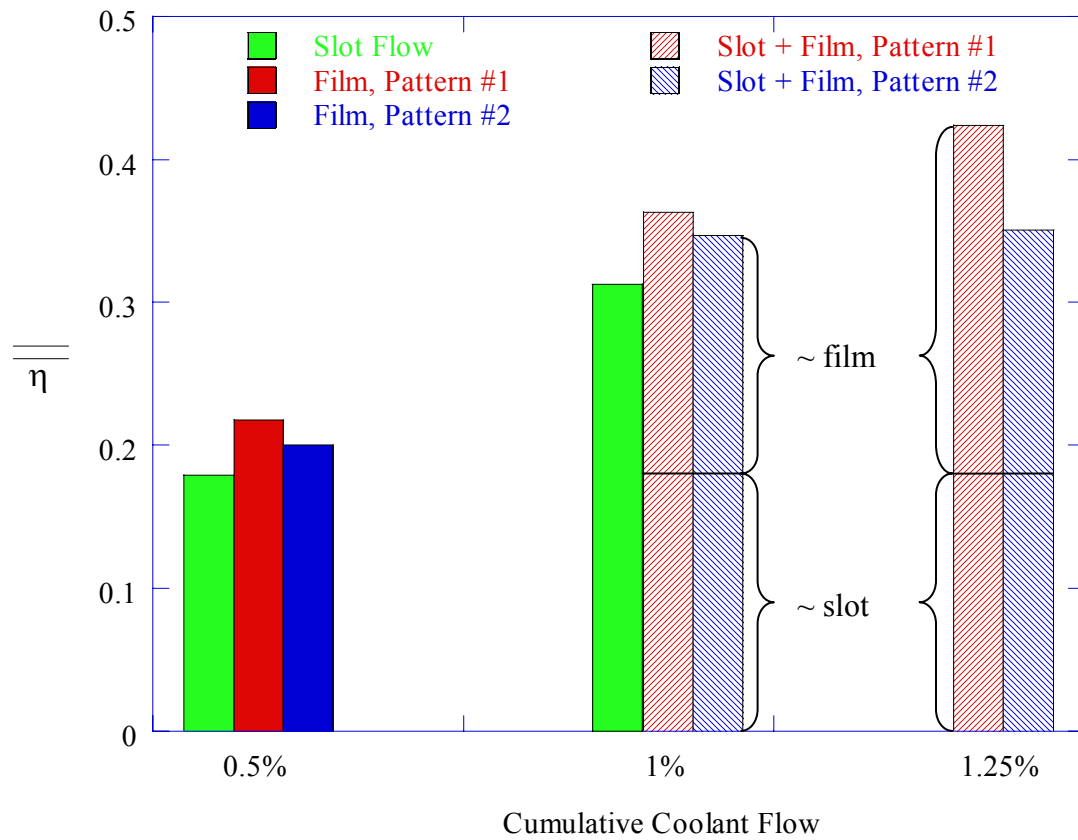


**Figure 6.8** Summary of area-averaged effectiveness values for all of the computational cases studied. It can be seen that including film-cooling leads to higher averaged effectiveness levels than slot flow alone.

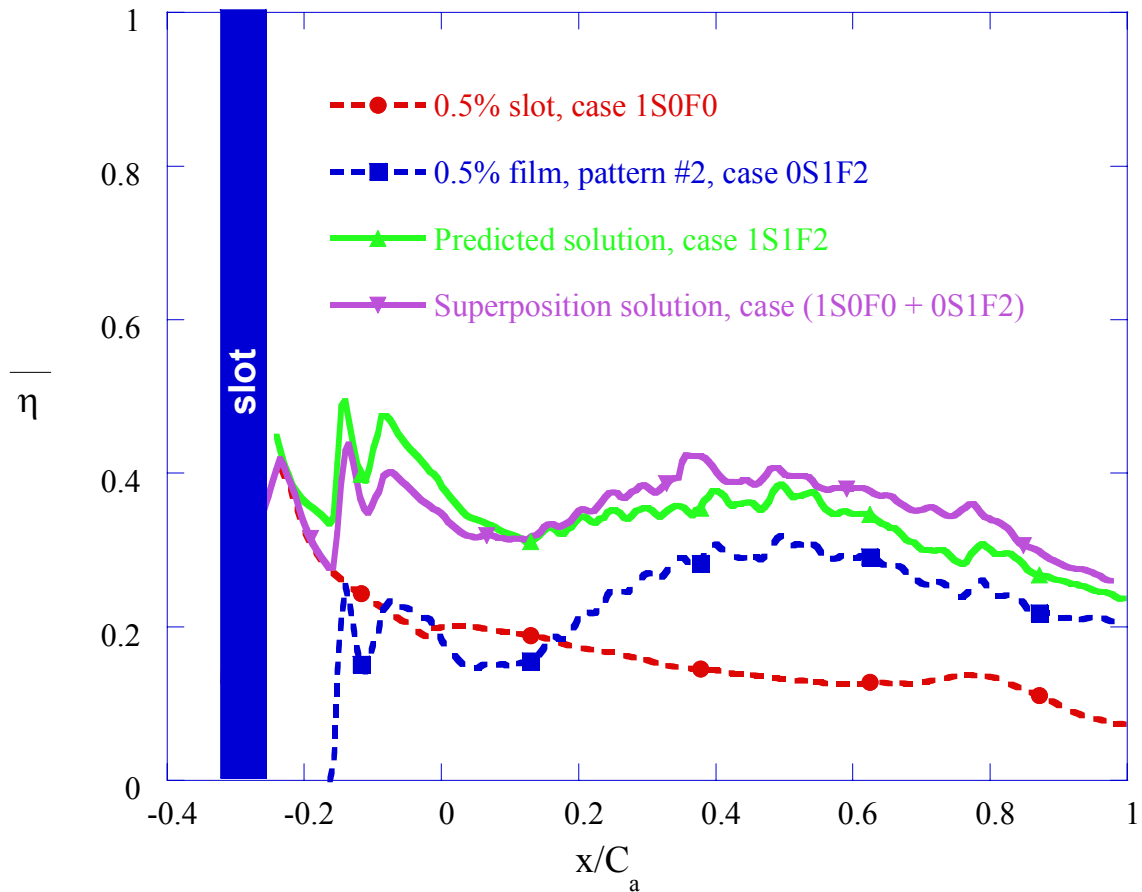


**Figure 6.9** Comparison of predicted pitchwise-averaged effectiveness levels as compared with those calculated using the superposition for the 0.5% slot and 0.5% film-cooling flow cases with hole pattern #2.

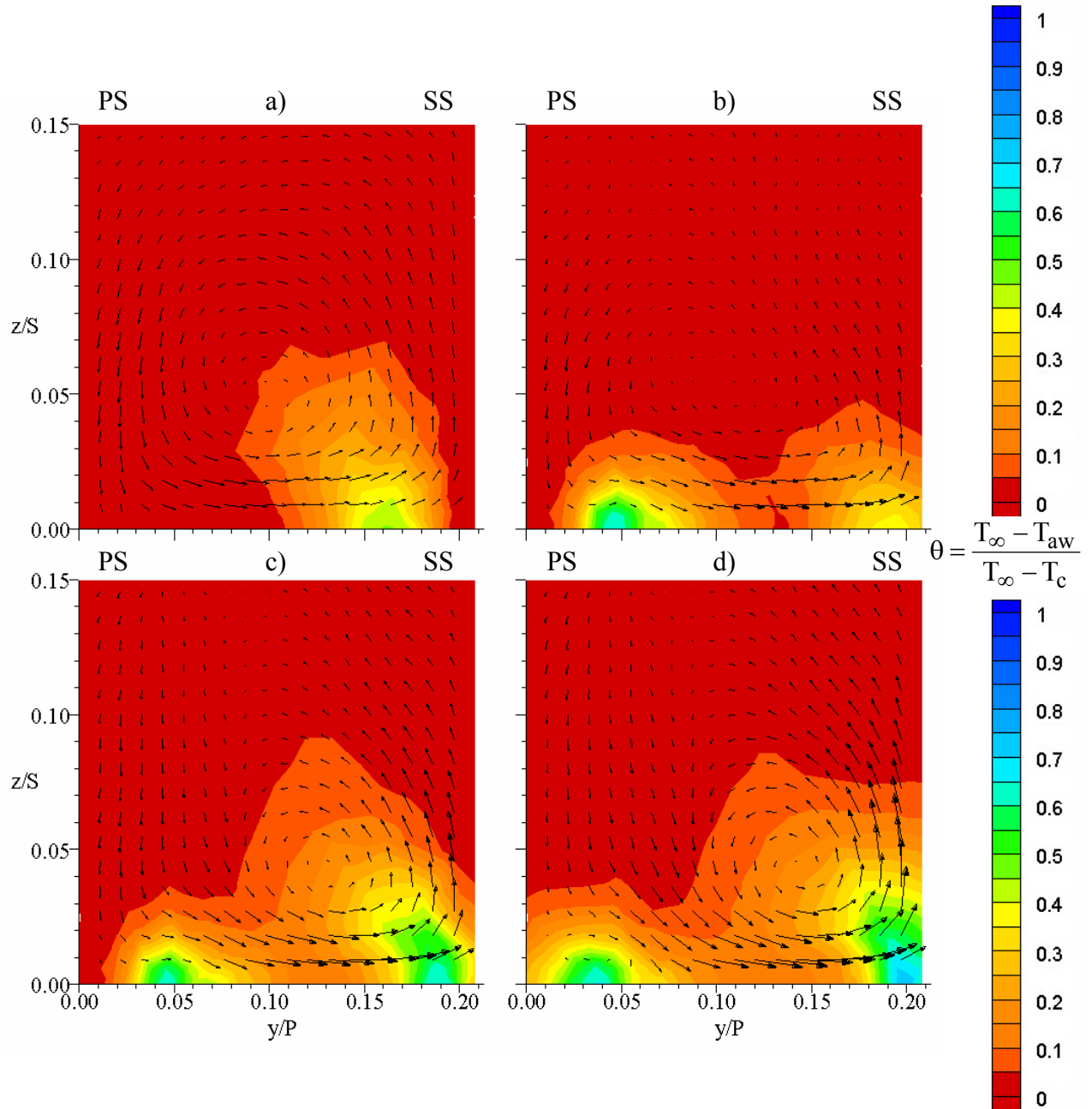


**Figure 6.10a-d** Secondary flow and thermal fields for the (a) slot cooling alone, case 1S0F0 (b) film-cooling alone, case 0S1F2 (c) combined slot flow-and low film flow rate, case 1S1F2 (d) combined film-cooling and slot flow at the higher film blowing ratio, case 1S2F2. Cooling hole pattern #2 was used for these results.

## Chapter 7

### Experimental Results

Experimental data provides the backbone for most research work. Before being implemented into production any product or design must be tested to validate the expected performance. An extensive test matrix of 17 experimental cases was developed to assess the impact of both slot cooling and film-cooling for the two different hole patterns. The test matrix, shown in Table 7.1, was designed to study the interaction of the slot and film-cooling holes as well as evaluate the impact of adjusting the coolant flow rates. Three different temperature profiles were studied. The inlet profiles are shown in Figure 7.1. An isothermal inlet temperature profile served as the baseline case and was tested at all coolant flow conditions. In addition, a near-wall peaked and center peaked profile were studied to evaluate the effects of a steep temperature gradient on endwall effectiveness levels and coolant trajectory. The adiabatic effectiveness contours were shown to be similar provided that the proper temperature, specifically the approaching near-wall temperature, was used in the normalization. A method was developed to identify areas of varying cooling needs and the spatial superposition method was evaluated to assess whether combined cooling cases could be accurately predicted from measurements of the individual cooling mechanisms. Finally, thermal field measurements were acquired for subsequent comparison with predictions.

Section 7.1 presents measurements of adiabatic effectiveness for all the various coolant flow rates and combinations with an isothermal inlet temperature profile. The effects of varying the momentum ratio of holes in the leading edge, upstream pressure side, and downstream pressure side regions are further discussed in Section 7.2. Jet separation as well as penetration to the vane is examined. Section 7.3 shows the effects of varying coolant between the slot and film-cooling holes by examining the area-averaged effectiveness levels. Section 7.4 evaluates the effects of a steep temperature gradient on endwall effectiveness levels and coolant trajectory. A method of identifying regions of varying cooling needs based upon deviation from the midspan streamlines is discussed in Section 7.5. The superposition method is evaluated in Section 7.6. The

intent is to determine if superposition can be used to accurately predict effectiveness levels and coolant trajectories for the combined slot and film-cooling cases. Section 7.7 briefly presents thermal field measurements for three cases, and finally, Section 7.8 provides a brief summary of the results.

### **7.1 Measurements of Adiabatic Effectiveness for an Isothermal Inlet Profile**

Three different inlet temperature profiles, shown in Figure 7.1, were tested. The isothermal profile served as the baseline. The temperature profiles were generated by three independently controlled heater banks upstream of the contraction in the wind tunnel. The temperature profiles have been normalized such that  $\theta = 0$  corresponds to the maximum temperature and  $\theta = 1$  corresponds to the coolant temperature in the plenum. The profiles were normalized in this manner to allow direct comparison to the measured adiabatic wall temperatures. The results of the different cooling mechanisms and flow rates with an isothermal inlet profile are discussed in the following sections.

#### *Slot Injection at the Combustor-Turbine Interface*

It is seen from Figures 7.2a-c that increasing the amount of slot flow has a dramatic effect on the endwall adiabatic effectiveness levels. At the low 0.5% slot flow rate shown in Figure 7.2a, the slot flow only exits in the middle of the passage with no coolant coming out upstream of the vane leading edge. When the slot flow is increased by 50% to 0.75% of the core flow, shown in Figure 7.2b, coolant exits across the entire width of the slot albeit still in a non-uniform manner. In both cases, though, a large uncooled region is left around the vane. This warm ring is especially evident in the stagnation region and along the pressure side. At the low slot flow rate the minimum effectiveness level is approximately 0.1 which corresponds to the near-wall dimensionless temperature shown in the uniform profile of Figure 7.1. This slight cooling effect of the near-wall fluid was due to the long 4m, (6.8C) unheated boundary between the heater bank used to condition the core flow and the test section. At the increased blowing rate, the coolant exiting across the entire width of the slot is thought to funnel the cooler near-wall fluid with the slot flow allowing the hotter mainstream gases

to convect down onto the surface leading to a measured adiabatic effectiveness level of zero.

When the slot flow is doubled from the baseline case to 1.0% of the core flow, as shown in Figure 7.2c, the coolant pattern is seen to be quite similar to the 0.75% case. The coolant, however, does slightly decrease the uncooled zone in the stagnation region, pushing the saddle point of the horseshoe vortex closer to the vane and slightly narrowing the hot ring along the pressure side. The coolant at the highest flow rate also appears to impact the vane suction side slightly further upstream than in the 0.75% case. In all cases the slot flow exits in a non-uniform manner and appears to be funneled between the legs of the horseshoe vortex towards the suction side.

Laterally-averaged adiabatic effectiveness levels for the three cases of slot flow without film-cooling are presented in Figure 7.3. Values are truncated at  $x/C_a = 0.8$  due to limited optical access beyond this point. Increasing the slot coolant by both 50% and 100% is seen to effectively double the cooling effectiveness levels at the slot exit with the highest slot flow rate performing only marginally better than the 0.75% flow rate throughout the passage. All three cases are seen to decay rapidly upstream of the vane and then decay more gradually through the passage with all three cases providing approximately the same cooling effectiveness levels near the trailing edge. This is the region where the coolant has narrowed to only a thin band in the contours.

#### *Film-Cooling without Slot Injection*

The baseline film-cooling cases without slot flow for each of the two patterns are shown in Figures 7.4a-d. The location of the slot, which was not simulated, is shown in black for reference. Each pattern was tested with a low and high film-cooling flow rate of 0.5% and 0.75% of the core flow respectively. The minimum effectiveness levels are shown to be  $\eta = 0.1$  for all cases corresponding to temperature of the slightly cooler boundary layer of the approaching fluid.

For pattern #1 at the low film flow rate, shown in Figure 7.4a, a fairly uniform coverage is seen across much of the passage. The leading row holes near the suction side inject as discrete jets in the direction of the streamlines despite being directed normal to the inlet direction (towards the top of the page). The leading row holes near the pressure

side inject in a more merged and directed pattern. The leading row holes just upstream of the leading edge, or the “leading edge blockers”, are quite ineffective at the low film blowing rate. The pressure side leading edge blockers appear to have virtually no coolant while the suction side leading edge blockers are quickly swept around the shoulder of the suction side leaving an uncooled region at the vane-endwall junction of the leading edge. The jets along the pressure side appear to inject in the streamwise direction and follow the contour of the vane, despite being directed axially downstream at the vane, leaving an uncooled region along the pressure side.

For the increased film-cooling case of pattern #1, shown in Figure 7.4b, several effects are seen from the heightened blowing. First the suction side jets of the leading row still inject as discrete jets, but lower adiabatic effectiveness values downstream of the holes indicate that the jets are lifting off of the surface. The pressure side leading row holes appear to be slightly more directed with coolant traces not appearing until downstream of the fourth hole from the pressure side as opposed to the third hole in the low blowing case. The upstream most row of three holes also exhibits lower  $\eta$  values and smaller affected areas in the high blowing case, once again exhibiting the characteristics of jet detachment. The leading edge blockers of pattern #1 at the 0.75% coolant flow rate are far more effective than at the 0.5% case. The suction side leading edge blockers appear highly effective at cooling the vane-endwall junction. The pressure side leading edge blockers appear to lift off at the injection location, impact the vane, and convect down the vane onto the endwall. This lift-off is evidenced by the coolant accumulating along the vane-endwall junction near the dynamic stagnation point on the pressure side. The pressure side holes within the passage penetrate approximately one hole diameter closer to the vane as compared with the 0.5% case thereby reducing, but not eliminating, the warm zone along the pressure side. This improved penetration is attributed to the increased momentum of the jets at the higher blowing ratio allowing the coolant to more closely approach the vane. Effects of increasing the momentum ratio are further discussed in section 7.2.

For pattern #2 at the low blowing rate, shown in Figure 7.4c, the most noticeable feature is the large hot streak through the center of the passage. This hot streak exists in the location where the gutter would be so including the gutter flow may tend to slightly

alleviate the problem. The effect of the gutter flow is expected to be minimal on most of the hot streak along the endwall, though. This is because, as shown in Figure 3.1b, the gutter runs along the downstream edge of the upstream rows of passage holes meaning that in a streamwise sense to any cross passage flows, which would distribute the coolant, the gutter would be downstream of the hot streak thereby providing little, if any, relief to the uncooled zone.

Once again the suction side leading row holes inject with the streamlines despite being directed towards the top of the page, although the local effectiveness levels are lower than in the corresponding case for pattern #1 indicating partial jet separation. The pressure side leading row holes inject in merged unison and are swept into the center of the passage providing a small measure of relief to the hot streak. The leading edge blockers of pattern #2 are far more effective than the leading edge blockers of pattern #1 at the same low 0.5% cumulative coolant flow rate. This is attributed to hole pattern #2 having only 78% of the cooling area of pattern #1 resulting in more available coolant per hole in pattern #2. The pressure side holes in the passage of pattern #2 also appear to reduce the uncooled zone along the vane-endwall junction when compared to pattern #1 once again because of the higher coolant per hole leading to a higher momentum flux at the pressure side holes.

The results of increasing the film-cooling flow rate, in pattern #2, to the high blowing rate are shown in Figure 7.4d. The jet detachment of the suction side, leading row holes appears to be exacerbated resulting in low effectiveness levels on the endwall. The coolant from the leading row holes just to the suction side of the gutter gap is initially more directed resulting in an impact of the upstream passage rows two holes upstream of the impact location at the low blowing rate. The coolant from the suction side, leading row holes also appears to be less effective at the high coolant flow rate and may suffer from blocking by the holes directionally downstream (bottom to top on the image) in the row causing the coolant to liftoff as it impacts coolant from the adjacent jet. The leading edge blockers appear to be largely unaffected although the coolant emerges as discrete jets just downstream of the holes and the local effectiveness levels are slightly lower. Within the passage, the pressure side jets appear well merged and penetrate to the vane-endwall junction eliminating the hot zone along the second half of the pressure side.

Local effectiveness levels are actually lower for these holes at the high blowing rate when compared to the results in Figure 7.4c, but effectiveness levels still appear to be more than adequate.

Laterally-averaged effectiveness data for the four cases without slot flow is presented in Figure 7.5. A spike is seen at  $x/C_a = -0.1$  where the leading row holes and leading edge blockers are encountered. Both patterns are seen to perform better in this region at the low blowing rate because separation of the leading row jets is induced at the high blowing rates. The average effectiveness levels for pattern #1 exceed those of pattern #2 for both flow rates. Pattern #2 has the large hot streak in the center of the passage which adversely affects the averaged levels. Pattern #2 shows slightly elevated cooling effectiveness levels at the higher blowing rate, while pattern #1 provides nearly identical results at either blowing rate.

#### *Slot Flow Combined with Film-Cooling for Pattern #1*

Moving along to the combined cooling mechanism cases, the adiabatic effectiveness levels for pattern #1 at each of the four low and high, slot and film-cooling combinations are shown in Figures 7.6a-d. For the low slot, low film case, shown in Figure 7.6a, the combined contours appear, at least physically, to be somewhat of a superposition of the cases of the film-cooling mechanisms alone. The minimum effectiveness level is  $\eta = 0.1$ . Once again, the slot flow does not emerge in the stagnation region and is funneled towards the suction side. The leading edge blockers are also quite ineffective leaving an uncooled area in the stagnation region. The pressure side jets in the passage inject in the stream-wise direction despite being aimed towards the vane leaving an uncooled zone along the pressure side.

When the film flow rate is increased to 0.75%, as shown in Figure 7.6b, the flow exiting the slot appears to be largely unaffected. The pressure side jets of the leading row are more directed and leave only low effectiveness coolant traces along the endwall surface indicating that a high momentum flux is inducing jet lift off. The same can be said for the upstream most row of three holes along the pressure side. The pressure side jets at the high film rate once again penetrate approximately one hole diameter closer to the vane slightly reducing the warm ring along the pressure side. The hot spot just

upstream of the second cross-passage row also appears to be enlarged at the increased blowing ratio as a result of the pressure side leading row jets pushing the slot flow closer to the suction side. This can be verified by counting that six film cooling holes in the upstream, cross-passage row are immersed in slot coolant at the low film flow rate as opposed to only five holes at the increased blowing rate. The minimum effectiveness level for this case is  $\eta = 0.5$ .

When the slot flow is increased to 0.75% of the core flow while the film-cooling is maintained at 0.5%, it is seen from Figure 7.6c that the slot coverage area is dramatically increased. Coolant exits across the entire width of the slot, but is still funneled towards the suction side. Adiabatic effectiveness levels across much of the upstream portion of the endwall are nearly unity indicating overcooling by the slot. The leading row holes in this area appear not to be necessary for endwall cooling. Therefore, the coolant emerging from these holes could be redistributed to more advantageous locations. As has consistently been the case, the leading edge blockers of pattern #1 at the low film-cooling rate appear to be quite ineffective leaving an uncooled zone at the leading edge as the coolant is immediately swept around the suction side. Also, the pressure side jets in the passage inject with the streamlines once again leaving an uncooled band along the pressure side. The minimum effectiveness level is  $h = 0$  corresponding to the temperature of the fluid just above the boundary layer which convects down as the boundary layer is swept with the slot coolant.

Finally, for pattern #1 at high slot and high film flow rates shown in Figure 7.6d, we see that the slot flow cools much of the endwall upstream of the vanes. Again, the pressure side leading row jets appear to constrict the slot flow pushing it further towards the suction side. These holes also separate and mix with the hot gases just above the endwall leading to minimum effectiveness levels of  $\eta = 0.1$ . The suction side leading edge blockers remain attached to the endwall providing coolant around the shoulder of the vane, while a small amount of coolant is also carried along the vane-endwall junction to the pressure side. The upstream rows of three holes along the pressure side exhibit the characteristics of jet lift-off with only low effectiveness levels downstream of the holes. Also the hole closest to the pressure side of each row in the passage appears to be more

directed at the hole exit opening a gap between the discrete jet and the other jets in the row before being swept downstream following the contour of the vane.

The laterally-averaged adiabatic effectiveness levels for the four combined slot and film-cooling cases for pattern #1 are shown in Figure 7.7. The average effectiveness levels immediately downstream of the slot are seen to be nearly 1 at the high slot flow rates when coolant exits across the entire slot. A spike at  $x/C_a = -0.1$  corresponds to the leading row and leading edge blockers. For both slot flow rates, the effectiveness levels are seen to be slightly higher at the low film-cooling rates in the region upstream of the vane. This is due to separation of the leading row jets and leading edge blockers as well as a constriction of the slot flow by the impinging pressure side, leading row jets. The effectiveness levels in the upstream half of the passage are also higher at the low blowing rates because of jet separation effects. The effectiveness levels of the two high slot flow cases are greater than those of the two low slot flow cases within the passage, because of the widened footprint of the slot coolant at the high flow rates. Beyond approximately  $x/C_a = 0.6$  all flow conditions yield approximately the same laterally averaged effectiveness levels.

#### *Slot Flow Combined with Film-Cooling for Pattern #2*

The contours of adiabatic effectiveness for pattern #2 at each of the four low and high, slot and film-cooling combinations are shown in Figures 7.8a-d. For the low slot and film-cooling case, shown in Figure 7.8a, the slot flow exits across only a portion of the slot. When compared to pattern #1 at the same flow rates, shown in Figure 7.6a, the exit location of the slot flow is seen to have migrated slightly toward the suction side of the vane relative to pattern #2 injecting from upstream of the leading edge blockers. This was not the case for pattern #1. The minimum effectiveness levels are approximately  $\eta = 0.1$  corresponding to the temperature of the approaching boundary layer. Also immediately noticeable is the large hot streak through the center of the passage that was also present without slot flow. The coolant from the pressure side leading row holes, which provided a small measure of relief to the hot streak without the presence of slot flow, appears drawn across the gap and merges with the slot coolant at the upstream rows of passage holes. The leading edge blockers are more effective at the same low film rate than they

were in pattern #1. Again, this is attributed to more available coolant per hole due to fewer holes in pattern #2. The coolant from the leading edge blockers fails to penetrate entirely to the vane, however, leaving a thin uncooled region at the vane endwall junction of the leading edge. The pressure side jets in the passage of pattern #2 at the low blowing ratio are seen to be more directed than their counterparts in pattern #1 because of the higher momentum due to fewer jets, but the coolant still fails to fully penetrate to the vane leaving a thin uncooled zone along the pressure side.

When the film-cooling is increased to 0.75% while maintaining the low 0.5% slot flow rate, the pressure side, leading row holes appear to constrict the slot coolant pressing it towards the suction side of the passage as shown in Figure 7.8b. This is seen in the slot coolant impacting the upstream row of holes further upstream than in the low blowing case resulting in a widening of the hot streak in the area between the upstream passage rows and the upstream most pressure side row of three holes. The passage pressure side jets also approach the vane providing coolant to most of the vane endwall junction along the pressure side. As with the low blowing rate the minimum adiabatic effectiveness levels are measured to be approximately  $\eta = 0.1$ .

For the high slot flow, low film flow case of pattern #2, shown in Figure 7.8c, the slot coolant exits across the entire span of the slot just as in the slot alone and pattern #1 high slot flow cases. A small area where  $\eta = 0$  is seen just upstream of the first row of three holes along the pressure side. This is thought to occur because of hot gases just above the boundary layer convecting down onto the endwall as the slot coolant sweeps the cooler boundary layer fluid towards the suction side. The slot flow appears to entrain the pressure side, leading row jets rather than the jets injecting downstream with the stream lines as was seen at the low slot flow conditions. The slot flow also appears to draw the upstream most jet of each of the pressure side rows across the passage while the jets closer to the pressure side follow the contour of the vane. This seems to illustrate the division between regions 2 and 3, as identified by Friedrichs (1998) and shown in Figure 2.1b, where the coolant in region 2 approximately follows the direction of the inviscid streamlines, and the coolant in region 3 is drawn across the passage by the strong endwall crossflows. The local effectiveness levels of the pressure side jets are slightly lower than

for the low film case with low slot flow shown in Figure 7.8a. The leading edge blockers perform similarly to the low slot and film-cooling case.

Finally, for pattern #2, the adiabatic effectiveness levels for the high 0.75% slot and 0.75% film-cooling cases are shown in Figure 7.8d. It is thought that the minimum effectiveness levels are slightly greater than zero because the pressure side, leading row jets separate and mix with the hot mainstream gases as they convect down onto the endwall surface. The increased momentum of the pressure side leading row jets constricts the slot flow pressing it towards the suction side as evidenced by the larger  $\eta = 0.5$  streak in the gap between the upstream and pressure side holes of the two cross-passage rows. The foot print of the coolant appears to be the same in this area but the distribution of the effectiveness levels has been altered from the high slot, low film flow case. In addition the upstream most jets in the pressure side rows appear more directed at the hole exits preventing the coolant from being immediately pulled out across the passage as was seen in Figure 7.8c. Once again the pressure side jets approach the vane eliminating much of the uncooled area at the vane-endwall junction along the pressure side. Also, the local effectiveness levels of the upstream most row of three holes appear lower than the corresponding holes at the low film flow rate indicating possible jet lift-off due to high momentum and jet blockage effects. The leading edge blockers of pattern #2 at the high film-cooling and high slot flow rates provide adequate cooling around the shoulder of the suction side while the pressure side leading edge blockers appear to separate and impact the vane before being washed down onto the endwall near the dynamic stagnation point. Separation is induced on the pressure side because of the stagnating flow in this area increasing the momentum ratio of the jets.

Laterally-averaged adiabatic effectiveness levels for the four combined slot and film-cooling cases for pattern #2 are presented in Figure 7.9. As was seen with pattern #1, increasing the slot coolant to 0.75% of the core flow dramatically increases the laterally averaged effectiveness levels at the slot exit. The effectiveness levels are also seen to be higher at the leading row holes and leading edge blockers because the width of the slot coverage area is greater. The performance is seen to be slightly worse at the low slot flow rate with increased blowing and slightly better at the high slot flow rate with increased blowing when compared to the low blowing cases. For the low slot flow rate,

local effectiveness levels along the pressure side were generally lower at the high film-cooling rate. At the high slot flow rate, however, local effectiveness levels for the holes along the pressure side were not significantly impacted by increasing the blowing. Because of the higher momentum jets, coolant from these holes was not drawn across the passage leading to a more coherent cooling zone along the pressure side. These effects along with the penetration to the vane-endwall junction led to improved average adiabatic effectiveness levels at the high blowing with high slot flow case. At approximately  $x/C_a = 0.45$ , the low slot, low film case is seen to be superior to the high slot low film case. This is because the higher slot flow draws the upstream most jets of the pressure side rows across the passage reducing their effectiveness. The low slot flow is not strong enough to adversely affect these jets.

## 7.2 Momentum Ratio at the Leading Edge and Along the Pressure Side

Jet separation and penetration to the vane as a result of increased jet momentum was discussed frequently in the preceding section. Three key areas: the leading edge, upstream pressure side, and downstream pressure side, were selected to examine the effects of varying the momentum ratio in more detail. Holes 1.1, 2.1, 1.3, 2.3, 1.6, and 2.6 as indicated in Figure 3.2a, were selected as representative holes because they lie in identical locations in each passage. Momentum ratios for each of these holes for the six cases involving low slot flow (three for each passage) are listed in increasing order in Table 7.2. The momentum ratios were calculated from predictions using:

$$I = \frac{\rho_j v_j^2}{\rho_\infty v_\infty^2} = \frac{\rho_j \left( \frac{\dot{m}_j}{\rho_j A_j} \right)^2}{2(p_{o,in} - p_{s,loc})} \quad 7.1$$

The momentum ratios for these holes are also plotted in Figures 7.10a-b along with subsets of the effectiveness contours for the representative hole and surrounding holes which should be subject to similar momentum flux ratios. The frames are depicted in the accompanying cartoon for reference. The corresponding case number and a dotted line indicating the particular hole are shown for each data point.

Holes 1.6 and 2.6 lie at the leading edge almost immediately upstream of the dynamic stagnation point. The blowing ratios for the leading edge holes are seen to be significantly higher than for the holes along the pressure side despite the velocity of these jets being lower. This occurs because of the stagnating core flow greatly reducing the kinetic energy of the mainstream. The lowest momentum flux ratios occur for pattern #1 with low slot and film-cooling flow and with only film-cooling. The jets are seen to barely emerge from the hole, if at all, for case 1S1F1. When  $I$  is increased slightly for case 0S1F1 the coolant is seen to emerge in the upstream direction. In both cases coolant from the leading edge blockers was swept around the suction side with no benefit to the pressure side. For pattern #2, the lowest momentum ratio was achieved for the case without slot injection where  $I = 1.843$ . Hole 2.6 was not captured in the image, but coolant from the leading edge blockers is noted accumulating at the vane-endwall junction while no coolant traces are seen from the hole immediately adjacent to hole 2.6. This indicates that complete jet separation has occurred at this momentum flux ratio. Adding slot leakage results in a slightly higher momentum flux ratio from hole 2.6. No coolant traces are seen downstream of the hole with coolant accumulation against the vane, once again indicative of complete jet separation. Holes immediately to the suction side of hole 2.6 are seen to be attached or only partially detached. The static pressure around the suction side is considerably lower leading to lower momentum flux ratios at the leading edge holes closer to the suction side. As the momentum flux ratio is increased at the leading edge by transitioning to the higher blowing rate for pattern #1, hole 1.6 appears fully detached. The holes to the suction side of hole 1.6 also exhibit lower effectiveness levels because of partial detachment. Coolant from these holes is thought to impact higher up on the vane and effectiveness levels at the vane-endwall junction are reduced as not enough coolant is available to wash down onto the endwall. At the highest case of  $I = 6.291$ , all holes at the leading edge are fully detached, but effectiveness levels along the vane-endwall junction are improved. This is because enough coolant exits the holes that when it impacts vane and is washed down a cooling benefit is still achieved.

The momentum flux data for the pressure side holes is presented in the zoomed frame of Figure 7.10b. At the upstream pressure side holes, represented by holes 1.1 and

2.1, the jets appear fully attached up to  $I = 0.462$ . At  $I = 0.553$  the effectiveness levels are not maintained as far downstream of the holes indicating partial or impending jet lift-off. Also, the upstream most hole for the cases 0S1F2 and 1S1F2, the two low blowing cases for pattern #2, are drawn away from the vane and towards the center of the passage. At the highest blowing ratio for hole 1.1 where  $I = 0.730$ , shown in case 1S2F1, The jet appears nearly fully detached. The same is true of hole 2.1 at the highest blowing rate. Also the upstream most hole for pattern #2, shown in case 1S2F2 remains coherent with its neighboring jets rather than being drawn into the passage. The upstream pressure side jets were not able to penetrate to vane before separation was induced.

The downstream pressure side jets, represented by holes 1.3 and 2.3, appear fully attached in all cases. A maximum momentum flux ratio of only  $I = 0.459$  was achieved because of the high mainstream velocities as the flow approaches the passage exit. As the momentum flux ratio was increased the downstream pressure side jets did penetrate closer to the vane finally impacting at the highest blowing ratio.

When comparing all holes, separation was induced in the range  $0.553 \leq I \leq 0.730$ . The upstream pressure side holes separated before impacting the vane while the downstream pressure side holes were able to penetrate completely to the vane. Complete detachment was noted to occur in the range  $1.255 \leq I \leq 1.843$ . Thole, Sinha, Bogard, and Crawford (1992) showed full detachment for  $I > 0.8$  for a hole with no compound angle on a flat plate. Holes on the endwall, however, are more analogous to compound angle holes.

### **7.3 Area-Averaged Effectiveness Levels**

The area-averaged adiabatic effectiveness level for each of the 15 experimental cases with an isothermal temperature profile is presented in Figure 7.11. The averages were computed from the axial location  $x/C_a = -0.24$ , corresponding to the location furthest upstream where the images covered the entire pitch for all cases, to  $x/C_a = 0.74$  where limited optical access prevented the entire width of the passage from being imaged. The various cases have been grouped by cumulative coolant flow rate to provide a quantification of the effects of distributing coolant between the slot and film-cooling holes.

It is seen that at the lowest coolant flow rate of 0.5%, the film-cooling holes provide a greater average cooling effectiveness than the slot flow alone. When the coolant and slot flow rates are increased to 0.75% of the core flow, the slot flow provides the highest average effectiveness level. This is somewhat misleading, though, because the slot average effectiveness levels have been artificially inflated by overcooling the large area in the upstream, center portion of the passage while providing no relief to the vane-endwall junction along both the leading edge and pressure side. Therefore, the most critical portion of the endwall experiences no cooling benefit. Also, one should notice that the average effectiveness level of pattern #1 is roughly the same as at the low flow case while pattern #2 actually performs worse at the increased blowing rate. This is due to jet separation which was noticed at many of the upstream holes and, in the case of pattern #2, the widening of the hot streak in the center of the passage.

For a cumulative flow rate of 1.0% of the core flow, both the slot only case and combined slot and film-cooling cases were tested. By including film-cooling with the slot flow, the average effectiveness levels were nearly matched while eliminating much of the uncooled ring along the pressure side. If the film-cooling holes were strategically placed so as to avoid holes in the area cooled by the slot, the average effectiveness levels of the combined cases would surely exceed that of the slot flow alone.

The 1.25% grouping consisted of four cases where the coolant was varied between slot and film-cooling holes. For pattern #1, a higher average effectiveness level was seen for the higher slot flow combined with low film-cooling. This combination produced the highest area-averaged effectiveness level of all conditions tested. The slot flow over cooled the upstream portion of the passage inflating the area-averaged effectiveness levels. No cooling was provided to the leading edge or along the pressure side. In addition the broad slot flow region blocked the slightly cooler near-wall fluid allowing the hotter mainstream gases just above to migrate down to the surface of the uncooled areas. The low slot, high film case also provided coolant to much of the endwall without wasting as much slot flow overcooling the upstream portion of the endwall. The iso-velocity design helped to prevent jet-liftoff in much of the passage, while the higher blowing rate provided enough momentum to the jets to cover the leading edge and penetrate near the airfoil, leaving very little of the endwall without any cooling.

Pattern #2 showed the same trend with the high slot, low film condition outperforming the low slot, high film cases, at least in the average sense. The higher film blowing rate narrowed the footprint of the slot flow and provided more direction to the pressure side jets widening the hot streak in the process. The upstream holes also exhibited characteristics of jet detachment, likely from interference by adjacent jets. The higher slot flow rate provided significantly more coolant to the broad uncooled area in the upstream portion of the passage. This combined with the less directed, stream-wise injection of the pressure side holes minimized the hot streak.

Finally, the high 0.75% slot flow rate combined with the high film-cooling rate for each pattern provided adequate effectiveness levels for both patterns. Pattern #1 showed a slight decline from the high slot, low film case because of lower local effectiveness levels due to jet lift-off. Pattern #2 exhibited a slightly higher average effectiveness level as the hot zone along the pressure surface was eliminated. The highest combined cooling cases indicate that the extra coolant is not justified as equal or higher effectiveness levels can be achieved with slightly less coolant. In all cases, hot spots, which are washed out in the averaging process, are still a concern and must be addressed.

#### **7.4 Effects of a Steep Temperature Gradient on Film-Cooling**

It was desired to determine if a strong temperature gradient would alter the coolant trajectories and effectiveness levels of the cooling mechanisms. Two inlet conditions, near-wall and center-peaked profiles, were considered to evaluate gradient effects. The profiles are shown in Figure 7.1.

Figures 7.12a and 7.12b provide the measured effectiveness levels for pattern #1 for the 0.5% slot and 0.5% film-cooling flow conditions. Figure 7.12a gives the effectiveness measurements for the near-wall (bottom peaked) temperature profile while Figure 7.12b gives the effectiveness measurements for the midspan peaked temperature profile. In both cases (Figures 7.12a and 7.12b), the normalizing temperature was that of the peak temperature whether it occurred near the wall or near the mid-span. While the coolant trajectories look quite similar the effectiveness levels are very different. For the midspan peaked temperature profile (Figure 7.12b) the range of effectiveness levels is

quite small given that the midspan to coolant temperature potential is large relative to what is being experienced in the near-wall region. The effectiveness levels for the near-wall peaked temperature case are nearly identical to that shown in Figure 7.6a. This illustrates that provided the representative temperature scaling is used, the effectiveness contours would be identical.

Figure 7.12c and 7.12d illustrate the effectiveness contours using the spatially averaged temperature for the bottom and midspan peaked temperature profiles shown in Figure 7.1. Because the near-wall peaked temperature is relatively small with regards to the entire cascade area, the effectiveness contours appear to be very much the same. To further illustrate the same phenomena is happening for all three temperature profiles, the adiabatic wall temperatures were further analyzed for the midspan peaked temperature profile in which the near-wall temperature (average temperature in the first 5% of the span) was used in the definition of effectiveness. Figure 7.12e illustrates that the contours are nearly identical to Figures 7.6a, 7.12a, and 7.12c. Based on these results it is clear that the endwall temperatures are dependent upon the temperatures leaving the combustor in the near-wall region and the local cooling.

### **7.5 Streamline Analysis of Film-Coolant Trajectory**

When placing film-cooling holes, a designer would like to predict film-coolant trajectory, which can be highly non-intuitive, in order to insure that the cooling needs of critical areas are met. A first approximation might be made using a 2-D inviscid prediction of the streamlines, which is often available, to predict the path of the coolant. In both the predictions and measurements presented in this study, the film-coolant has appeared to inject with the streamlines rather than in the direction of hole orientation lending credence to the streamline approach. Figures 7.13a-c illustrate contours of the predicted flow angle and streamlines at midspan, corresponding to the inviscid case, as well as at the 2% span location for both the low and high slot flow rates without film-cooling. Figure 7.13d shows the streamlines for all three cases superimposed. It can be seen from these figures that the midspan predictions are adequate at some locations, but the near-wall flow deviates considerably from the freestream in several key areas. These

differences indicate that the slot flow must be modeled to properly determine the coolant trajectory.

Around the leading edge strong flow turning is seen at the midspan which is expected. In the near-wall region, however, the flow turning is even more pronounced at the leading edge as well as along the upstream portion of the pressure side. The flow angle contours for the high slot flow rate, shown in Figure, 7.13c, indicate that the stagnation point has shifted slightly towards the suction side. In Figure 7.13d, the streamlines corresponding to near-wall locations with slot flow are seen to be drawn away from the vane and towards the middle of the passage. This is especially evident at the high slot flow case along the upstream portion of the pressure side. Upstream of the center of the passage, there appears to be little difference between the near-wall and the freestream and no difference between low and high slot flow. This occurs in the area where the slot coolant ejects at both the low and high slot flow rates. This low pressure area acts as a sink drawing all flow towards it. Both within and at the exit of the passage, the near-wall streamlines are seen to cross the inviscid streamlines indicating stronger cross flows along the wall which would be expected.

The 2% span streamlines for both the low and high slot flow cases are superimposed on the hole patterns in Figures 7.14a-b indicating the expected path traversed by jets emerging from the holes. It is seen that especially along the upstream portion of the pressure side, and the upstream portion along the suction side to a lesser extent, the coolant trajectory can be dramatically altered depending upon the slot flow rate. At a high slot flow rate, the coolant jets are drawn across the passage towards the slot flow, but at the low flow rate the slot coolant does not appear strong enough to entrain the jets along the pressure side. The cross flows at the exit of the passage are also shown to be slightly stronger at the high slot flow rate.

The streamlines presented in Figure 7.13d have been superimposed on measurements to determine if they are an accurate predictor of coolant trajectory in Figures 7.15a-d and 7.16a-d for low and high slot flows, respectively.

Predicted streamlines at 2% span for 0.5% slot flow without film-cooling are shown superimposed on measurements of the two patterns with 0.5% slot flow and 0.5% film flow in Figures 7.15a-b. For both patterns the film-coolant trajectories follow the

predicted streamlines quite well. The coolant from the leading edge holes is swept around the suction side and the jets along the pressure side follow the predictions. The slot coolant deviates from the predictions on the pressure side boundary due to impingement by the pressure side, leading row holes which were not included in the prediction. Also slightly stronger turning is seen in the measurements for pattern #1 near the trailing edge.

Predicted streamlines at the midspan are superimposed on the same two data sets in Figures 7.15c-d. The inviscid streamlines predict the coolant trajectories fairly well along the pressure surface in the downstream portion of the passage where only slightly stronger turning is shown in the measurements compared with the streamlines. At the leading edge and the upstream pressure side holes, however, the midspan computations under-predict the turning as the coolant traces are more directed towards the center of the passage. As with the near-wall predictions impingement by the pressure side, leading row holes on the slot coolant is not accounted for resulting in a misprediction of the shape of the slot coolant footprint along the pressure side boundary.

Predictions of the streamlines at 2% span for the highest 1% slot flow rate are superimposed on measurements of each pattern with 0.75% slot coolant and 0.5% film-cooling in Figures 7.16a-b. The case of 0.75% slot coolant without film-cooling was not computed, but because the 0.75% and 1% slot coolant cases were shown to be extremely similar in the measurements, the predicted streamlines for the higher slot flow case will still be used to illustrate the differences between predicting coolant trajectories based upon the inviscid streamlines versus near-wall predictions including slot flow. The near-wall streamlines again predict the coolant trajectories quite well. The leading edge holes follow the streamlines as do the pressure side holes both in the upstream and downstream regions. The small hot spot upstream of the first pressure side row for pattern #2 assumes the shape of the predicted streamlines. The slot coolant also conforms quite well to the predictions and is not influenced as strongly by the impinging pressure side, leading row jets.

In contrast, the midspan streamlines shown in Figures 7.16c-d do a relatively poor job of predicting the coolant trajectories. Turning is under predicted both at the leading edge and along the pressure side. This misprediction is most pronounced in the upstream,

pressure side rows which are drawn much more strongly towards the center of the passage. Stronger cross-passage flows are also seen in the hot spot of pattern #2 which does not conform well to the predicted streamlines. In addition the pressure side boundary of the slot coolant footprint is more strongly turned towards the center of the passage than the inviscid streamlines would predict. Turning near the trailing edge is also underpredicted.

Contour plots of the difference between the near-wall flow angles and the midspan flow angles, shown in Figures 7.17a-d, provide another method of viewing the flow angle information. At the low 0.5% slot flow rate, the near-wall flow angles deviate from the midspan by only about  $10^\circ$  except at the leading edge. This indicates that for low slot flow rates, the slot coolant exits only in the very low pressure region at the center of the passage where it is not strong enough to greatly influence the film-cooling jets along the pressure side. Conversely, at the higher 0.75% slot flow rate, where the coolant was shown to exit across the entire width of the slot, the cross flows induced by the larger slot flow are much stronger with a deviation of upwards of  $40^\circ$  from the midspan. This was noted particularly at the high slot, low film case of pattern #2, where the upstream most jets of the pressure side rows were drawn across the passage while the jets closer to the vane appeared to follow the inviscid streamlines. When examining the locations of the pressure side holes of pattern #2 in Figure 7.17d, the upstream most holes of the rows are seen to lie in an area with high deviations in flow angle from the midspan while the holes next to the vane are in areas of very little deviation from midspan. Consequently the coolant diverged appearing as discrete jets. When the film-cooling rate was increased, the jets had enough momentum to overcome the strong turning local to the hole and reach to the lower deviation zone before being swept downstream. This resulted in a coherent cool zone downstream of the jets. The misprediction of the coolant trajectories in the areas shown to have high deviations from the midspan was noted when examining the streamlines superimposed on the measurements.

The low pressure area in the middle of the passage acts as a sink drawing the slot flow in with little variation in streamlines from the midspan. Film-cooling holes in this area would be best used elsewhere as this area is naturally cooled by the flow field.

By examining contours of the difference between the near-wall and midspan streamlines, one is able to identify areas where the flow field is diverging by the strong gradients in the contours. This can aid a designer in identifying areas which will be harder to cool and help the designer assess the effects, from a coolant trajectory perspective, of slightly increasing or decreasing the film-cooling rate.

## 7.6 Spatial Superposition Analysis

A spatial superposition of results was performed to assess whether measurements of each cooling mechanism alone could be combined to accurately predict the results from the combined case. The method is illustrated in Figures 7.18a-c. The adiabatic effectiveness levels from the 0.5% slot flow alone and 0.5% film flow alone for pattern #2, shown in Figures 7.18a-b, are combined using the superposition equation developed by Sellers (1963):

$$\eta_{\text{sup}} = \eta_1 + \eta_2(1 - \eta_1) \quad (7.1)$$

to produce the combined case shown in Figure 7.18c. The superposition results are then compared to measurements of the combined case shown in Figure 7.18d.

For the low slot, low pattern #2 film-cooling case, shown in Figures 7.18c-d, the combined superposition-predicted effectiveness levels over predict the measured effectiveness levels by about 10% in many areas. The effectiveness levels of the uncooled areas are dictated by the near-wall fluid, as was shown in Section 7.4. If the temperature profile had been held perfectly isothermal ( $\theta = 0$ ) in the near-wall region then the uncooled areas would be accurately predicted, but because the effectiveness levels were slightly above zero in the individual measurements, the superposition magnified the cooling effects over predicting the effectiveness levels in the uncooled areas.

The effectiveness levels of the pressure side leading row holes are also over predicted as the cooling performance of these holes appears diminished when comparing the combined case measurements to those of the film only measurements and the superposition prediction. The slot flow appears to induce partial detachment of the pressure side leading row jets. When examining the flow angle deviation contours in Figure 7.17b, it is seen that coolant in this area is subject to slightly stronger cross flows

which would cause the jets to stack up lifting the coolant closest to the pressure side off of the surface.

When comparing the coolant trajectories between the superposition solution and the combined measurements, one will notice that the width of the slot exit area is mispredicted. For the combined case, slot flow exits upstream of the leading edge blockers allowing the slot flow to cover both rows of upstream passage holes. The superposition fails to accurately predict the coverage of both upstream passage rows. In addition, the pressure side leading row jets are shown to push the slot coolant slightly towards the suction side causing the coolant to cling to the downstream edge of the upstream rows of film-cooling holes. In contrast, the superposition solution shows coolant up to three hole diameters axially downstream of the holes thereby under predicting the width of the hot streak in the passage.

One will also notice that for the combined measurements, the leading edge blockers fail to fully penetrate to the vane-endwall junction. Once again when examining the flow angle deviation contours in 7.17b, the turning is seen to be stronger in this area when the slot flow is included, so the coolant is drawn towards the slot flow before it can reach the vane-endwall junction. When examining the pressure side jets, the superposition predicts the trajectories fairly accurately. This is because the low slot flow rate does not have the strength to impact cooling holes in this area.

The superposition predicted adiabatic effectiveness levels as well as the measurements of case 1S2F2 are shown in Figures 7.19a-b. Once again the uncooled areas are overpredicted as well as the local effectiveness levels of the pressure side leading row jets and the pressure side passage jets. The width of the slot flow exit area and the coverage of the upstream passage rows are under predicted. The impact of the pressure side leading row jets impacting the slot coolant and forcing it against the upstream passage rows is also not represented by the superposition solution.

Figures 7.20a-b present the superposition predicted and measured adiabatic effectiveness levels for the higher 0.75% slot flow rate combined with the low film-cooling flow rate for pattern #2. As was seen at the low slot flow rates, the superposition over predicts the effectiveness levels, but the misprediction seems to be more pronounced. We also see that the footprint of the slot flow is once again overpredicted

along with the penetration of the leading edge blockers. In addition, the superposition fails to predict the upstream most hole of each pressure side row being drawn across the passage. These results are not all too surprising, because as seen in Figure 7.17d, the higher slot flow rate tends to more dramatically alter the endwall cross flows.

Finally, Figures 7.21a-b present the predicted and measured adiabatic effectiveness levels for case 2S2F2, 0.75% slot flow and 0.75% film-cooling in pattern #2. As before, the effectiveness levels are somewhat over predicted, and the slot coverage area fails to include effects of the impinging film-cooling jets from the pressure side leading row. The trajectories and coverage area of the pressure side jets within the passage however, are predicted quite well. This is because at the high blowing rate, these holes are able to penetrate to the area of low deviation from the midspan where the slot coolant has little influence over the film-cooling.

## 7.7 Thermal Field Analysis

Thermal field measurements were taken for three cases to allow comparisons with predictions in the following chapter. The plane location and measurements are shown in Figures 7.22a-d and will be discussed briefly here. The plane is normal to the pressure side at  $s/C = -0.77$  and extends across the passage to the adjacent vane. The plane is viewed from downstream as indicated by the arrow so that the pressure side is on the left at  $y/P = 0$  and the suction side of the adjacent vane is on the right.

For the low slot flow case without film-cooling, shown in Figure 7.22b, the coolant is entrained in the passage vortex and transported across the passage to the suction side. The core of the coolant is located above the endwall at 2% span with a coolant foot extending down to the endwall. The peak endwall effectiveness is shown at  $y/P = 0.17$ .

The combined low slot and film case is shown in Figure 7.22c. Once again the core slot flow is entrained in the passage vortex and transported across the passage. A slightly cooler center is seen most likely from the cooling jets. The slot core is also lifted slightly and shifted further towards the suction side by the stronger secondary flows resulting from coolant injection. The pressure side jets are seen at approximately  $y/P =$

0.04. They adhere relatively well to the endwall surface. The hot streak in the center of the passage, which was shown in the adiabatic effectiveness contours, is clearly visible.

Finally, the increased blowing rate with the low slot flow for pattern #2 is shown in Figure 7.22d. The slot flow, as seen before, is entrained in the passage vortex and transported towards the suction side. The vortex is again strengthened, resulting in a more skewed shape, as a result of the increased blowing. A cool center from the endwall cooling jets clings to the endwall at  $y/P = 0.19$ . The slot and film-cooling along the suction surface is seen to climb the vane providing coolant below approximately  $z/S = 0.04$ . The pressure side jets also impact the vane climbing to  $z/S = 0.02$ . A cool center from the pressure side jets is maintained. The hot streak is visibly widened and the coolant concentrations spread apart as a result of the increased directionality of the cooling jets.

## 7.8 Summary

Measurements of endwall adiabatic effectiveness have been presented for an extensive test matrix combining both coolant from a flush slot and film-cooling from two distinct hole patterns. Slot flow without film-cooling was shown to adequately cool portions of the endwall while providing no benefit to the crucial vane-endwall junction both at the leading edge and along the pressure side. Film-cooling holes were shown to distribute coolant more evenly throughout the passage. Pattern #2, however, left a large uncooled streak down the center of the passage due to a provision for the gutter.

Film-cooling blowing ratio was shown to have a significant impact on cooling performance. The higher momentum flux associated with higher blowing allowed the coolant to penetrate to hard to cool areas at the leading edge and along the pressure side. Cooling jets in high pressure areas at the leading edge and along the upstream portion of the pressure side showed a tendency to separate before impacting the vane, while jets in the downstream region penetrated to the vane without separating. The higher momentum jets were also able to overcome the sink effect of the slot flow avoiding being drawn into the center of the passage.

Predicted streamlines at 2% span with included slot flow and at the midspan were compared and superimposed on measurements of film-cooling effectiveness. A

considerable deviation between the near-wall and midspan streamlines was observed and it was shown that slot flow rate and near-wall effects must be considered when predicting film-coolant trajectory based on streamlines. As the slot flow rate was increased the influence of the slot became greater making inclusion of the slot flow even more critical. A method of identifying cooling regions was developed by examining the differences in flow angles between the near-wall fluid and the midspan. Areas of large deviation proved challenging to cool while areas of small deviation acted as sinks drawing coolant in.

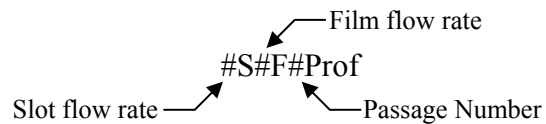
The spatial superposition method has been shown to over predict adiabatic effectiveness levels as well as mispredicting coolant trajectories in areas affected by the inclusion of slot flow as identified by the flow angle deviation method presented in Section 7.4. The superposition method may be a useful tool for designers wanting to gain an idea of the combined effects of two cooling mechanisms, however, as long as the designer identifies areas where the flow field is altered by interaction of the cooling mechanisms and applies a factor of safety to cooling effectiveness predictions.

Finally, thermal field measurements from three cases were presented. Coolant was shown to become entrained in the passage vortex and transported towards the suction side. Including film-cooling intensified the passage vortex and distorted the coolant structure. Increased jet momentum led to a widening of the jets between the pressure and suction side. The thermal fields will be compared to computational predictions in the following chapter.

**Table 7.1** Experimental Test Matrix

Case	Slot Flow %m <sub>in</sub>	Film Flow %m <sub>in</sub>	Inlet Temp Profile	Thermal Field
1S0F0	0.50	---	Flat	Y
2S0F0	0.75	---	Flat	N
3S0F0	1.00	---	Flat	N
0S1F1	---	0.50	Flat	N
0S1F2	---	0.50	Flat	N
0S2F1	---	0.75	Flat	N
0S2F2	---	0.75	Flat	N
1S1F1	0.50	0.50	Flat	N
1S1F2	0.50	0.50	Flat	Y
1S1F1Bot	0.50	0.50	Bot	N
1S1F1Mid	0.50	0.50	Mid	N
2S1F1	0.75	0.50	Flat	N
2S1F2	0.75	0.50	Flat	N
1S2F1	0.50	0.75	Flat	N
1S2F2	0.50	0.75	Flat	Y
2S2F1	0.75	0.75	Flat	N
2S2F2	0.75	0.75	Flat	N

Key:



Number	Passage Number	Flow Rate %m <sub>in</sub>
0	No Film-Cooling	No Cooling
1	1	0.50
2	2	0.75
3	---	1.00

**Table 7.2** Local Blowing and Momentum Ratio of Selected Holes for Various Cases

Hole	Region	M	I	Separated	Case
1.6	L.E.	0.469	0.241	N	1S1F1
1.6	L.E.	0.528	0.313	N	0S1F1
2.6	L.E.	1.295	1.843	Y	0S1F2
2.6	L.E.	1.377	2.112	Y	1S1F2
1.6	L.E.	1.722	3.265	Y	1S2F1
2.6	L.E.	2.409	6.291	Y	1S2F2
1.1	U.P.S.	0.465	0.219	N	0S1F1
1.1	U.P.S.	0.510	0.264	N	1S1F1
2.1	U.P.S.	0.675	0.462	N	0S1F2
2.1	U.P.S.	0.738	0.553	N	1S1F2
1.1	U.P.S.	0.848	0.730	Y	1S2F1
2.1	U.P.S.	1.113	1.255	Y	1S2F2
1.3	D.P.S.	0.487	0.238	N	0S1F1
2.3	D.P.S.	0.493	0.243	N	0S1F2
1.3	D.P.S.	0.560	0.314	N	1S1F1
2.3	D.P.S.	0.602	0.363	N	1S1F2
1.3	D.P.S.	0.611	0.374	N	1S2F1
2.3	D.P.S.	0.677	0.459	N	1S2F2

Region Key

L.E.	Leading Edge
U.P.S.	Upstream Pressure Side
D.P.S.	Downstream Pressure Side

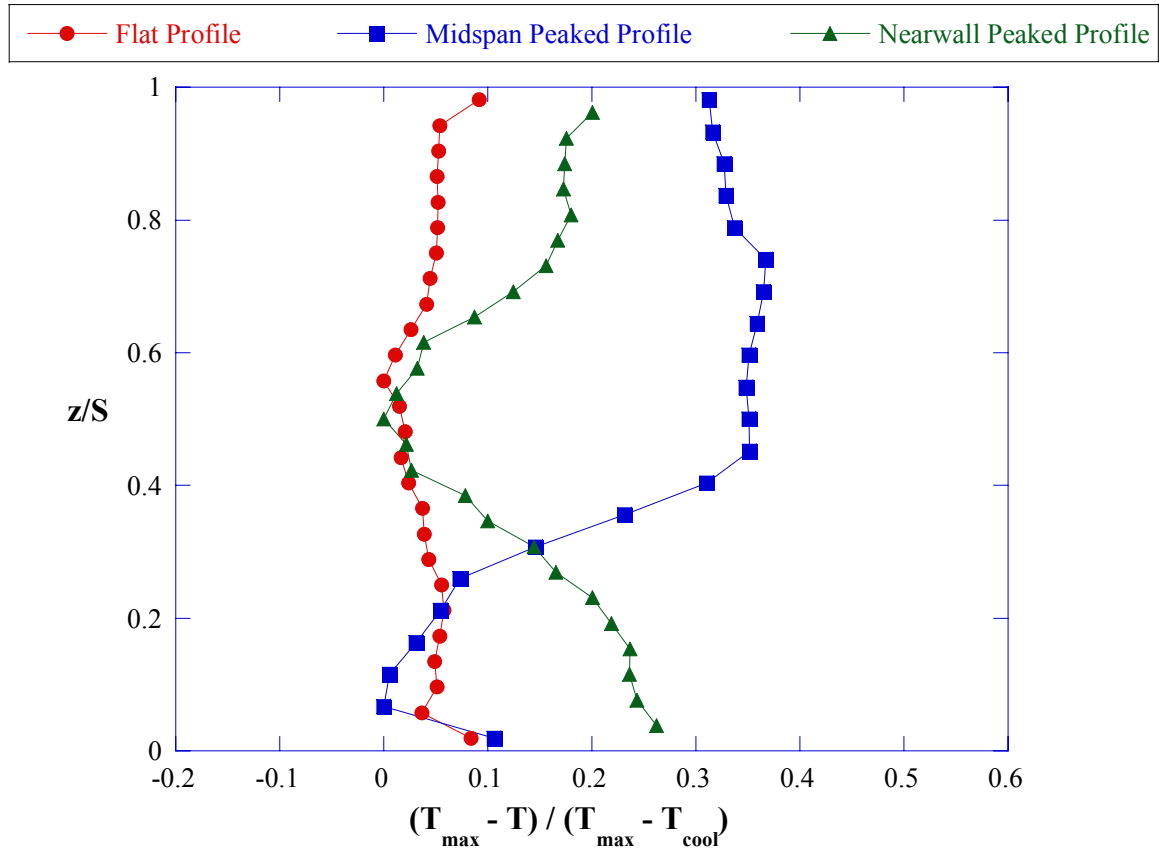


**Figure 7.1** Measured inlet temperature profiles for the cases investigated. These temperature profiles were measured just upstream of the contraction of the wind tunnel.

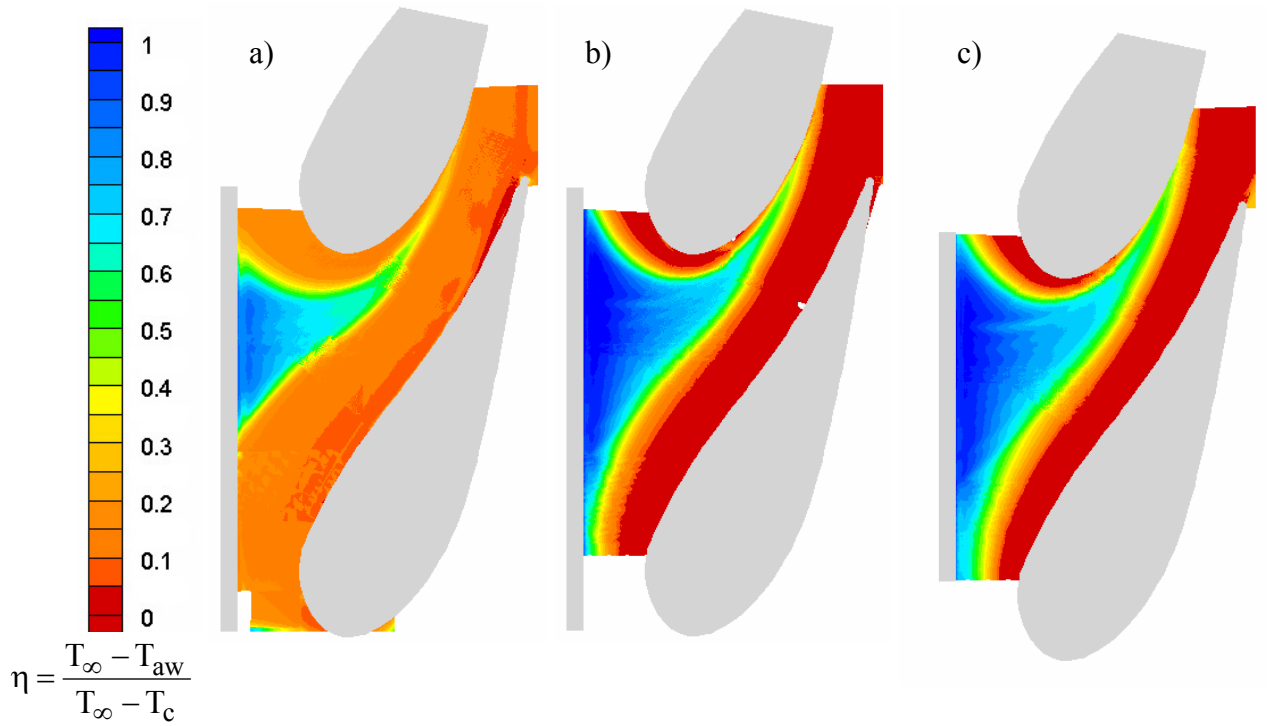


**Figure 7.2a-c** Contours of adiabatic effectiveness for the cases of slot flow without film-cooling (a) 0.5%, case 1SOF0, (b) 0.75%, case 2SOF0, and (c) 1.0% case 3SOF0.

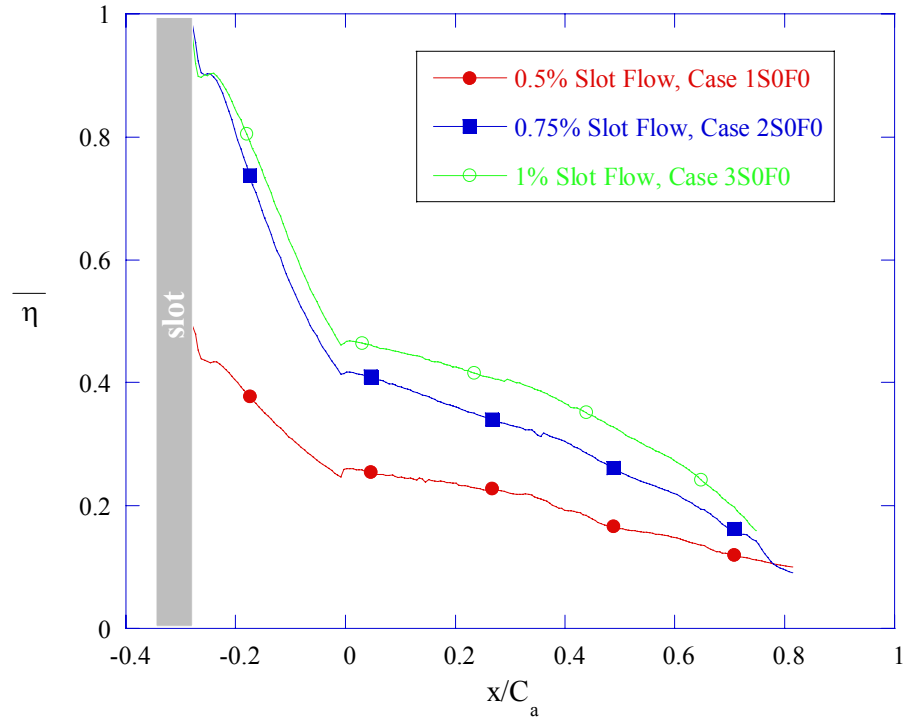


**Figure 7.3** Laterally averaged effectiveness levels for the three cases of slot flow injection without film-cooling.

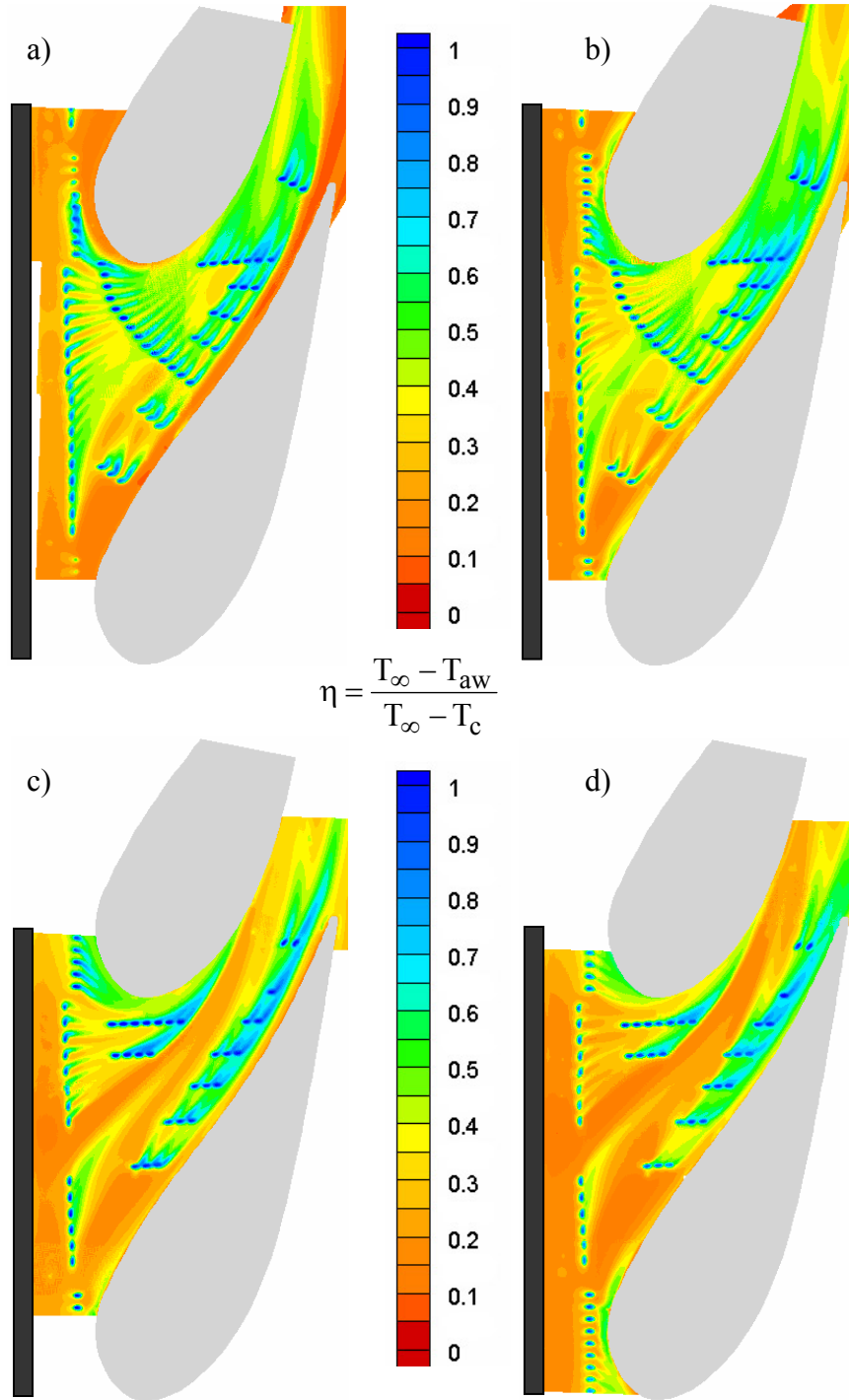


**Figure 7.4a-d** Contours of adiabatic effectiveness for the baseline film-cooling only cases: (a) pattern #1, 0.5% film, case 0S1F1, (b) pattern #1, 0.75% film, case 0S2F1, (c) pattern #2, 0.5% film, case 0S1F1, and (d) pattern #2, 0.75% film, case 0S2F2.

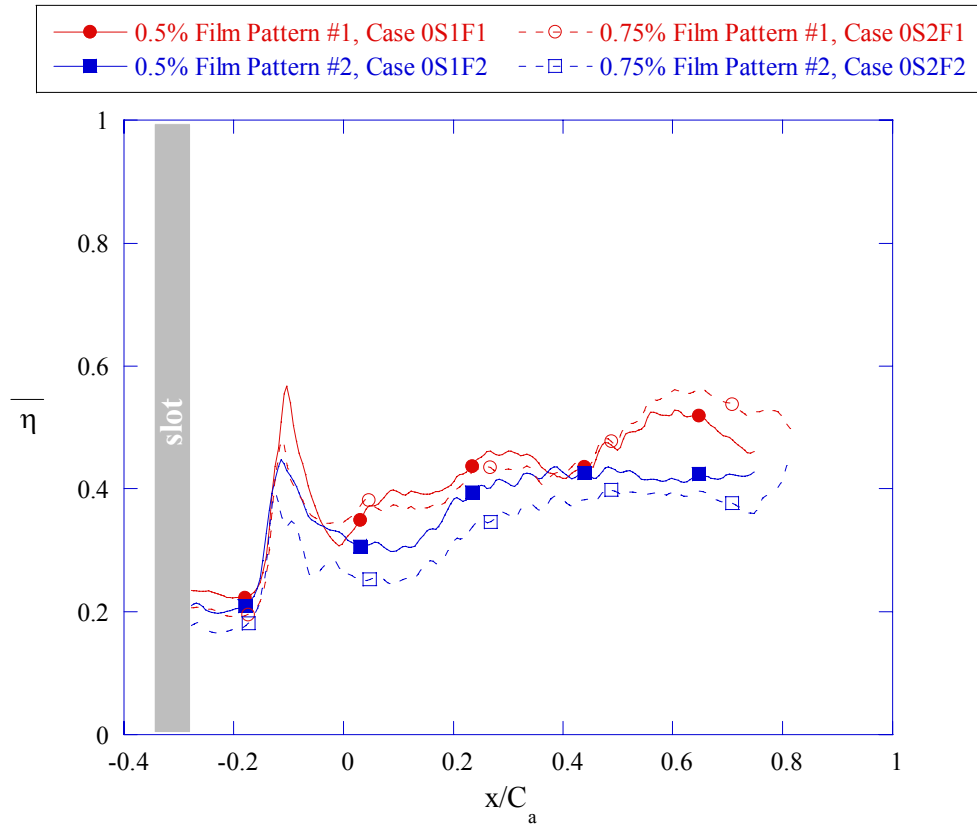


**Figure 7.5** Laterally averaged effectiveness levels for the four cases of film-cooling injection without slot injection.

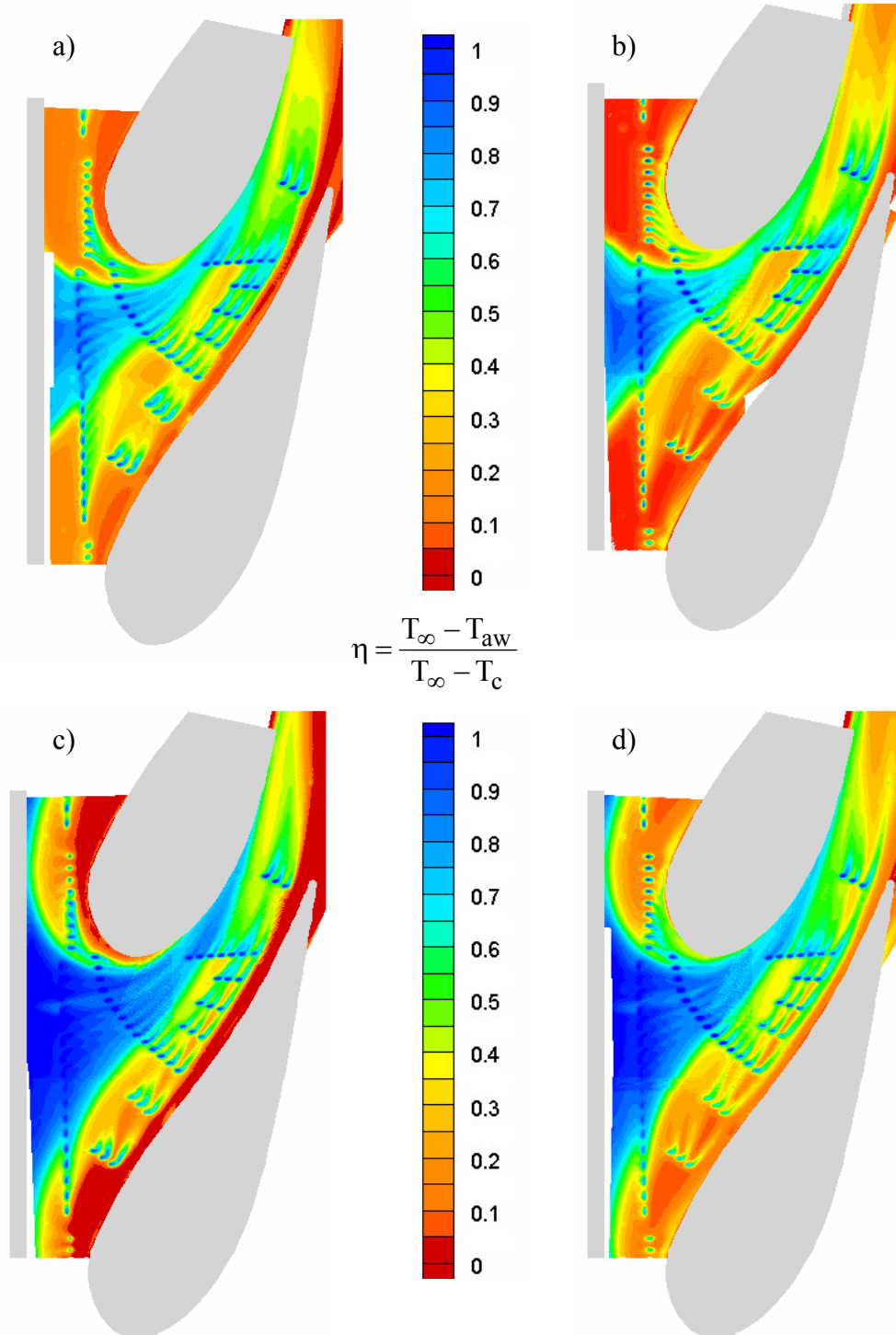


**Figure 7.6a-d** Contours of adiabatic effectiveness for pattern #1 at the various combined slot and film-cooling cases (a) 0.5% slot 0.5% film, case 1S1F1, (b) 0.5% slot 0.75% film, case 1S2F1, (c) 0.75% slot 0.5% film, case 2S1F1, and (d) 0.75% slot 0.75% film, case 2S2F1.

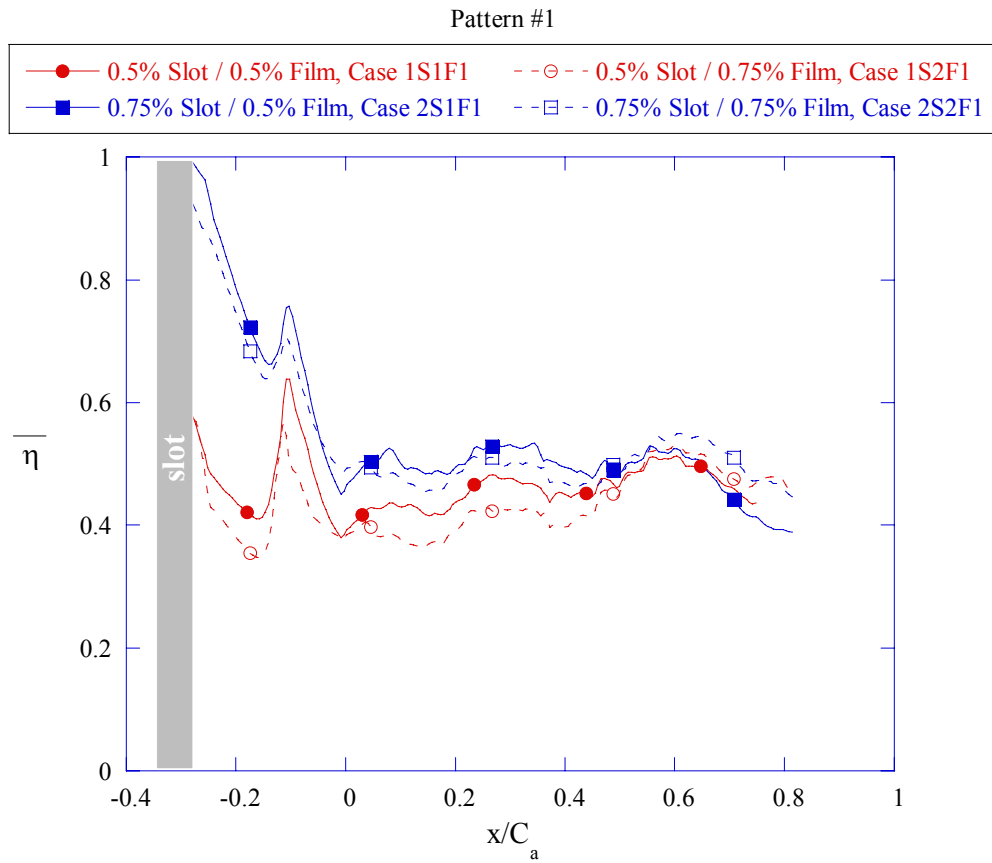


**Figure 7.7** Laterally averaged adiabatic effectiveness levels for pattern #1 at four cooling combinations of slot and film-coolant injection.

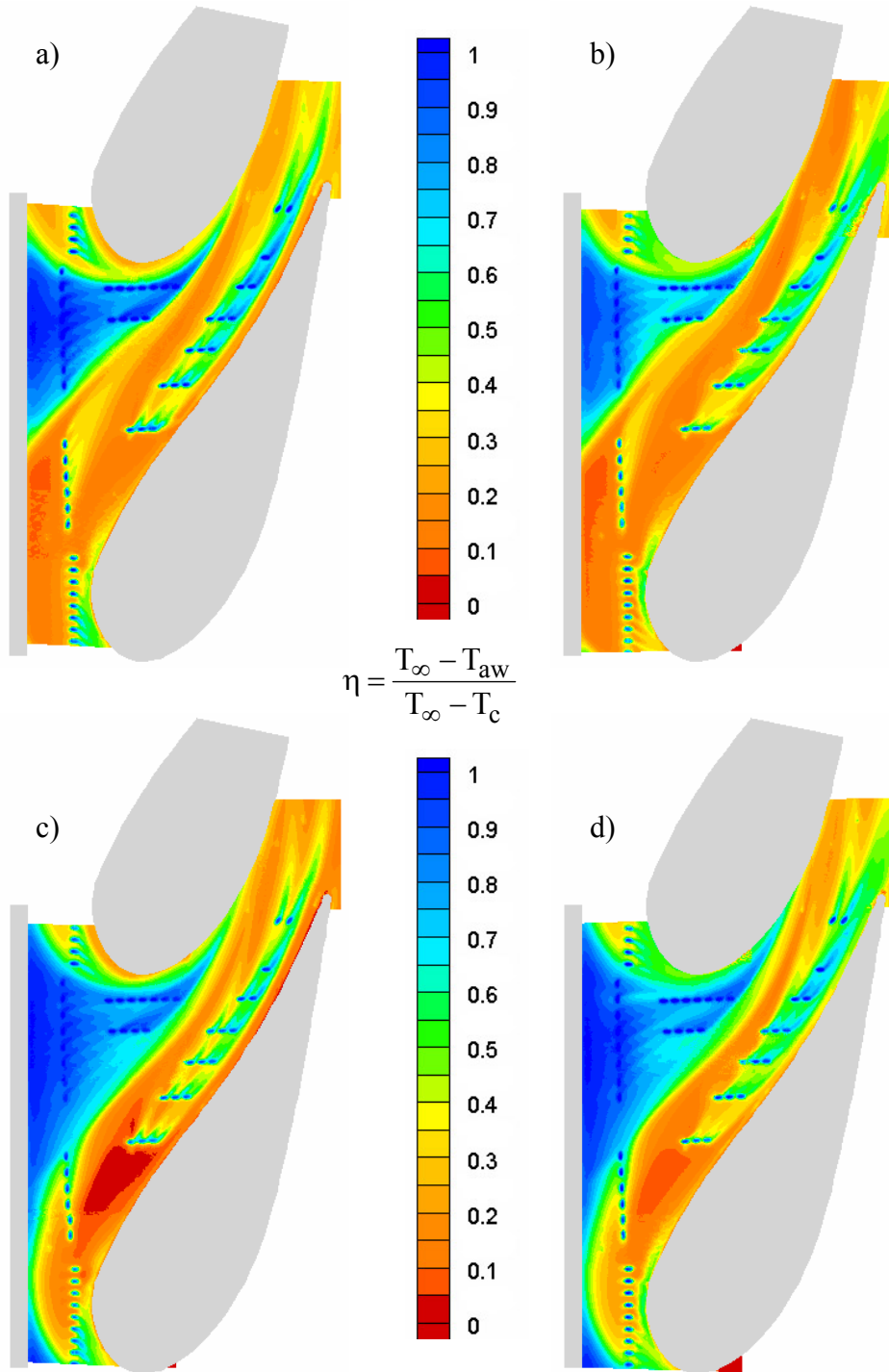


**Figure 7.8a-d** Contours of adiabatic effectiveness for pattern #2 at the various combined slot and film-cooling cases (a) 0.5% slot 0.5% film, case 1S1F2, (b) 0.5% slot 0.75% film, case 1S2F2, (c) 0.75% slot 0.5% film, case 2S1F2, and (d) 0.75% slot 0.75% film, case 2S2F2.

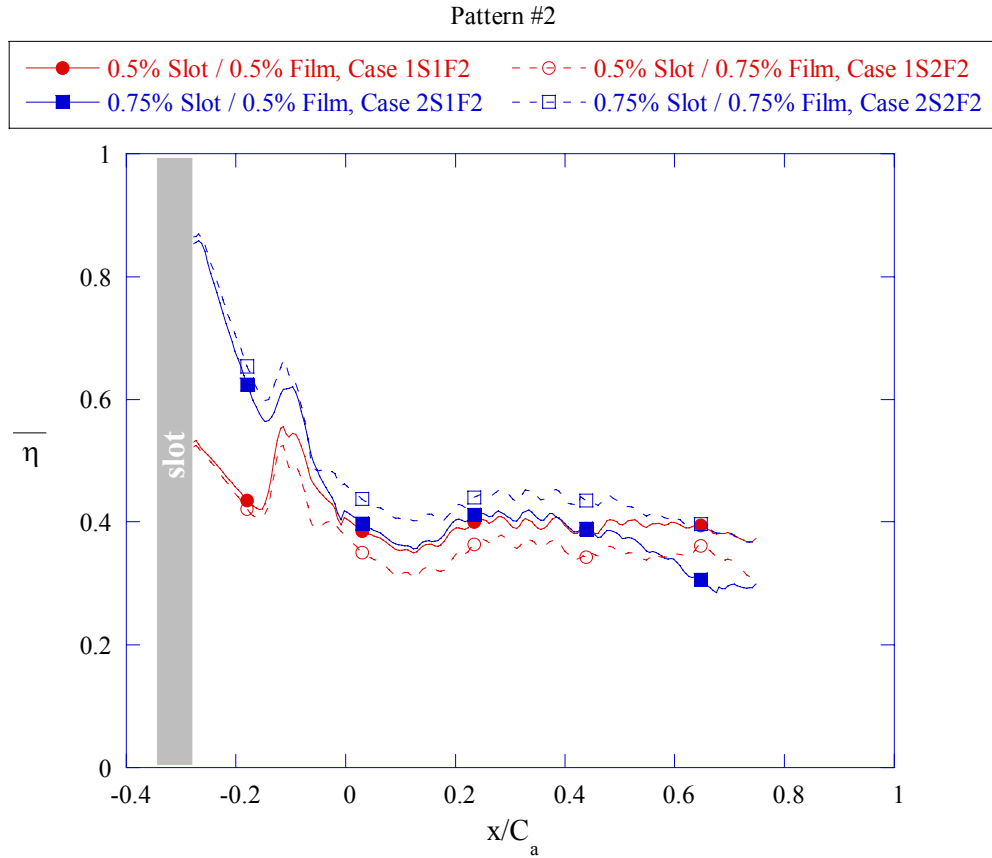


**Figure 7.9** Laterally averaged adiabatic effectiveness levels for pattern #2 at four cooling combinations of slot and film-coolant injection.

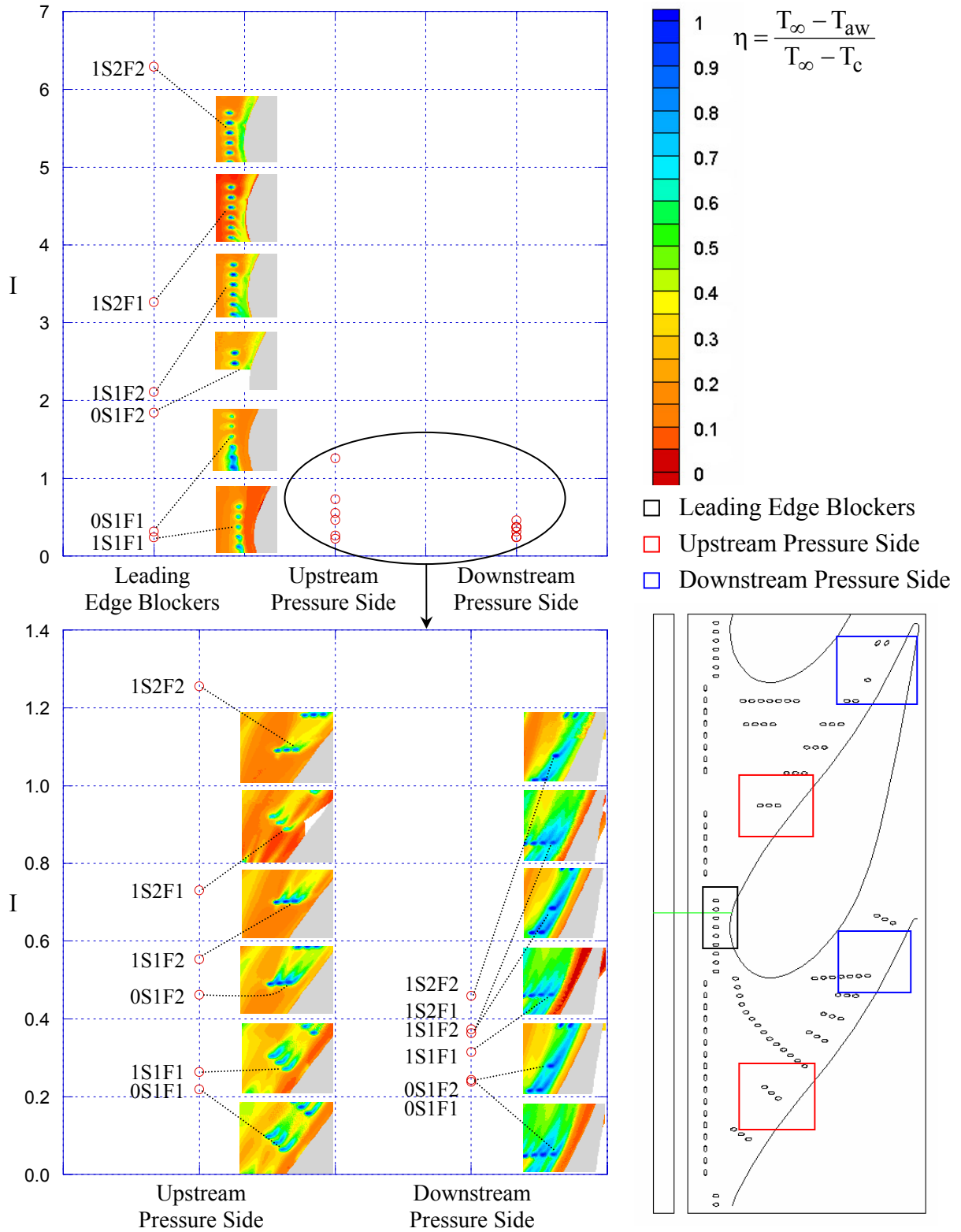


**Figure 7.10a-b** Momentum flux ratios for holes indicated by the dashed lines are shown in (a) the leading edge region and (b) the upstream and downstream pressure side regions. Adiabatic effectiveness levels of neighboring holes are also pictured for reference.

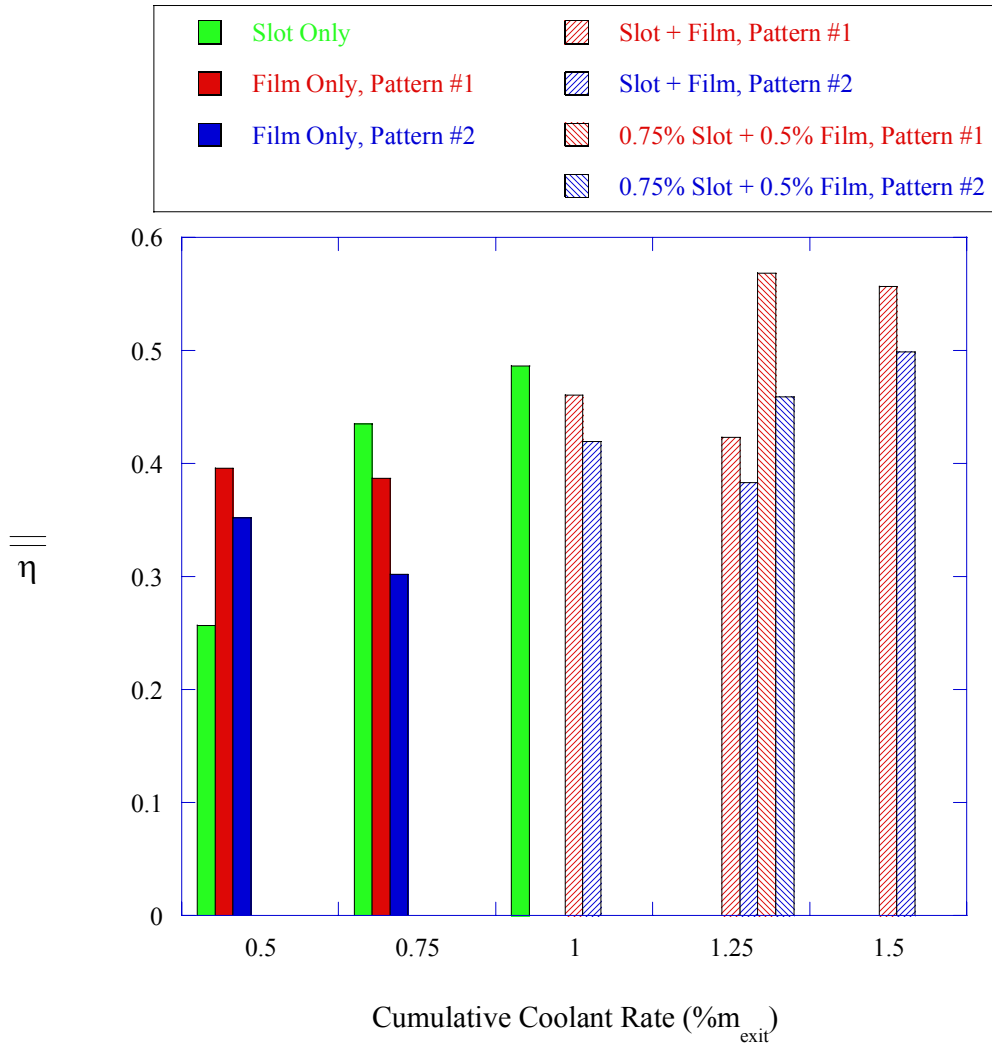


**Figure 7.11** Area-averaged effectiveness levels are shown for the 15 experimental cases with a uniform inlet profile. The cases are grouped by cumulative coolant flow rate providing a quantifiable method of assessing the effects of distributing coolant between the slot and film-cooling holes.

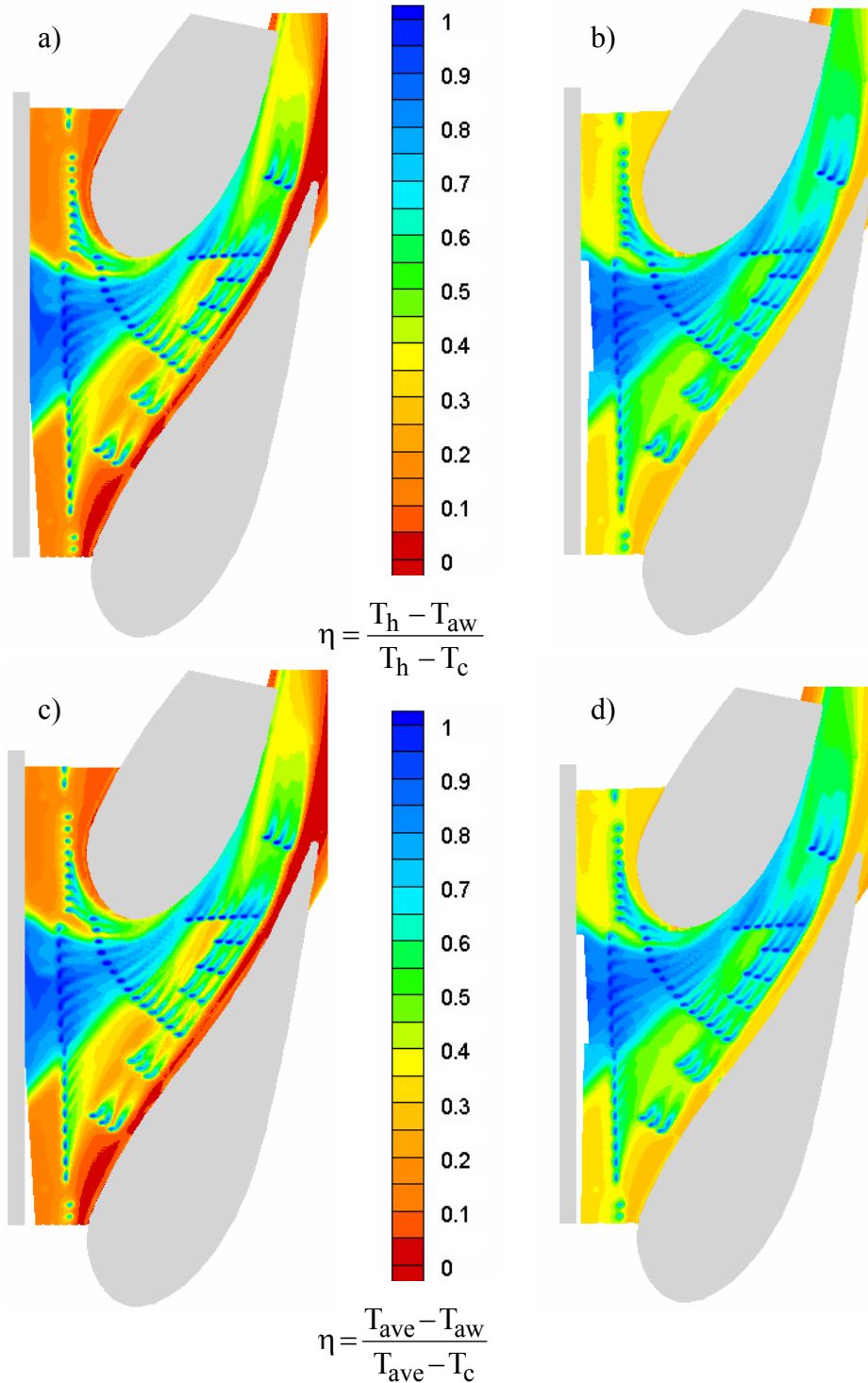


**Figure 7.12a-d** Adiabatic effectiveness contours are shown for case 1S1F2 with both an (a) endwall-peaked and (b) center-peaked inlet profile. Contours were normalized by the maximum temperature in the profile. The same cases are shown in (c) and (d) with the adiabatic wall temperature normalized by the spatially averaged temperature from the profile.

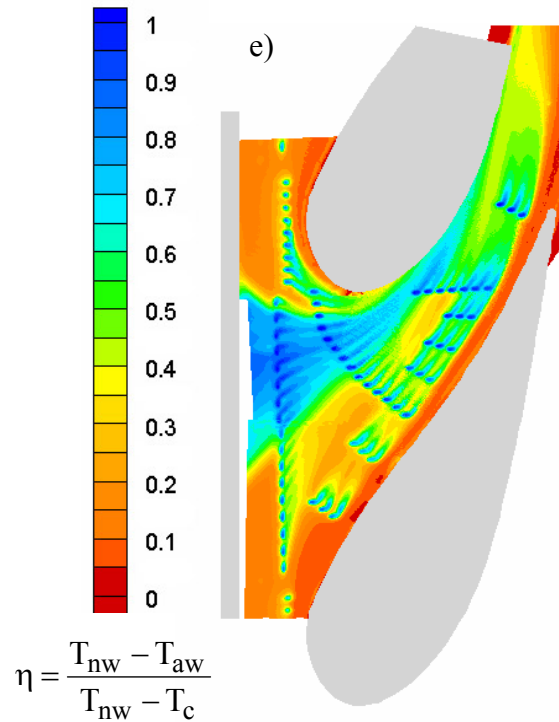


**Figure 7.12e** Adiabatic effectiveness contours are shown for case 1S1F2 with a near-wall peaked profile. The contours are normalized by the average near-wall temperature (0%-5% span) to illustrate that when properly scaled, the results from all three temperature profiles for case 1S1F2 appear the same.

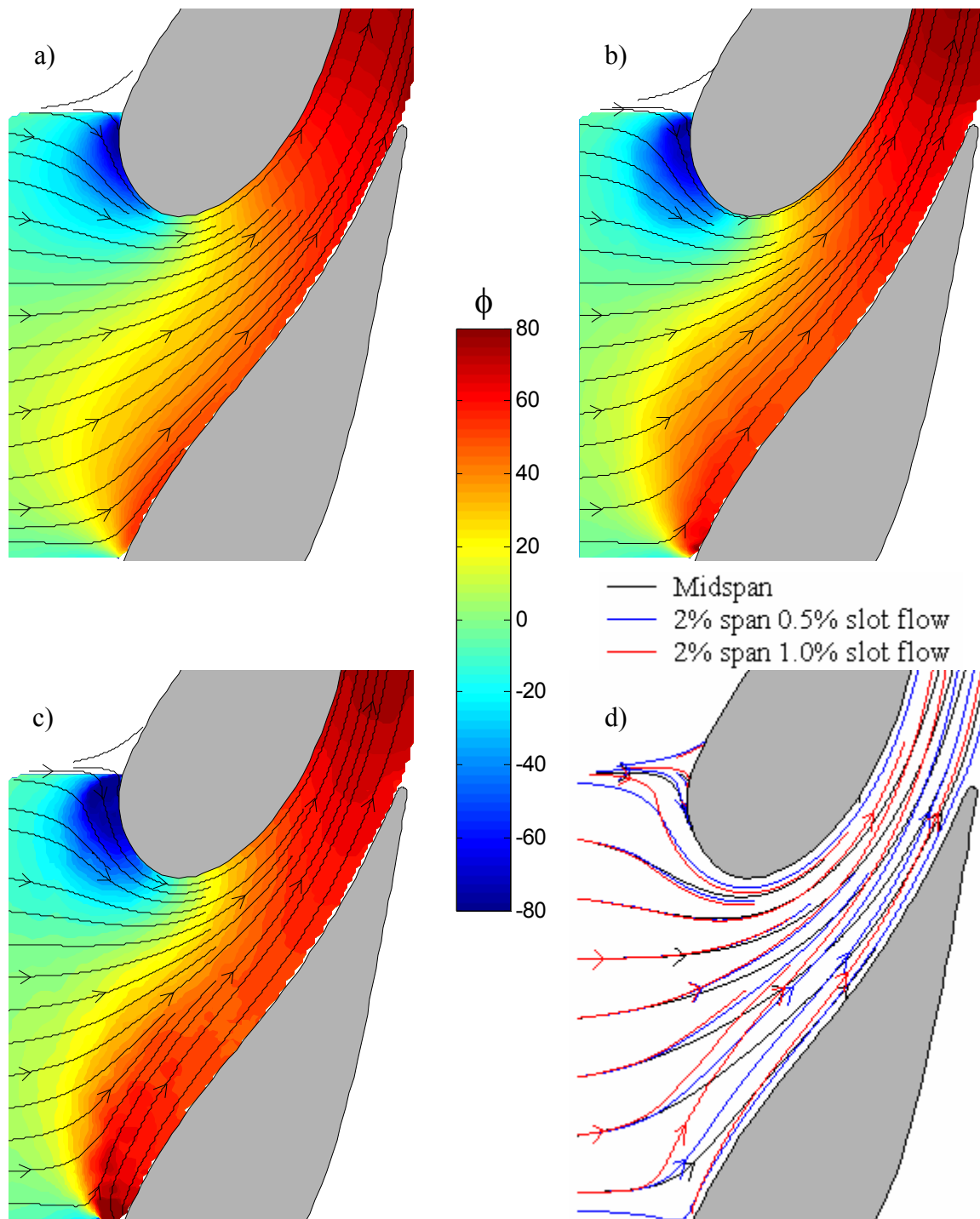


**Figure 7.13a-d** Contours of flow angle,  $\phi$ , measured in degrees as deviation from the downstream axial direction are shown along with streamlines for (a) the midspan corresponding to inviscid predictions (b) 2% span with a low 0.5% slot coolant flow rate and (c) 2% span with a high 0.75% slot coolant flow rate. The streamlines for all three cases are superimposed in (d) to illustrate the strengthened cross flow because of the slot.

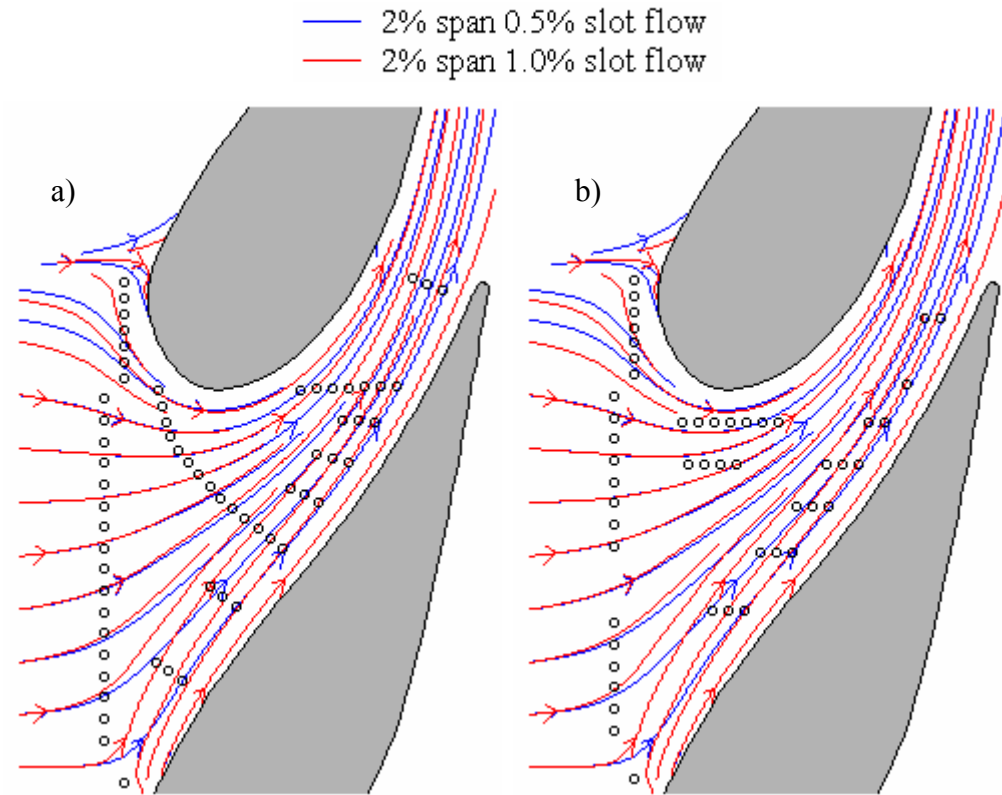


**Figure 7.14a-b** Predicted streamlines at 2% span for both the low and mid-level slot flow rates are presented with the hole locations of pattern #1 (a) and pattern #2 (b) shown for reference.

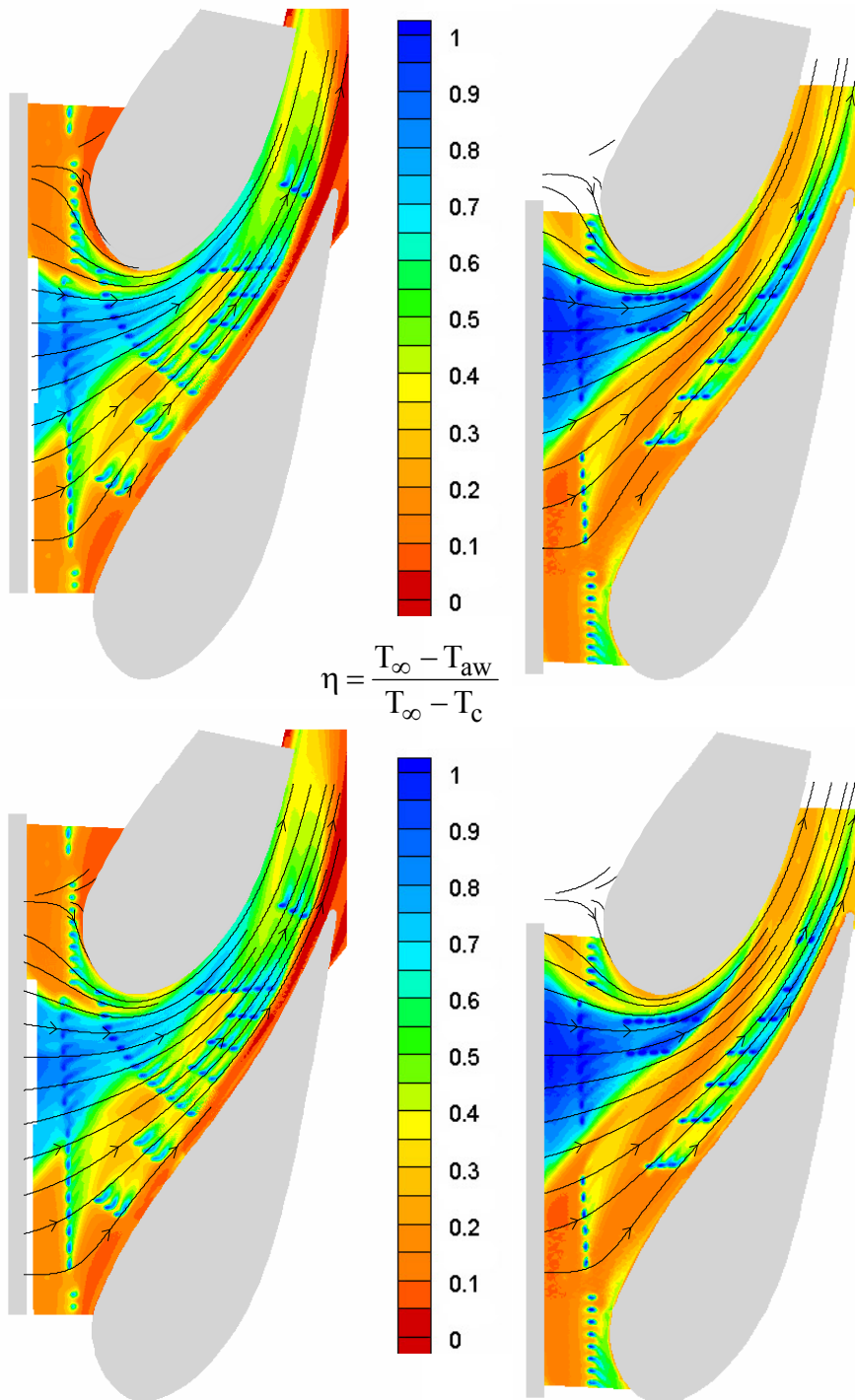


**Figure 7.15a-d** Predicted streamlines at 2% span for 0.5% slot flow without film-cooling are superimposed on (a) pattern #1 with 0.5% slot flow and 0.5% film-cooling and (b) pattern #2 with 0.5% slot flow and 0.5% film-cooling. The two cases are shown with predicted streamlines at the midspan superimposed in (c) and (d).

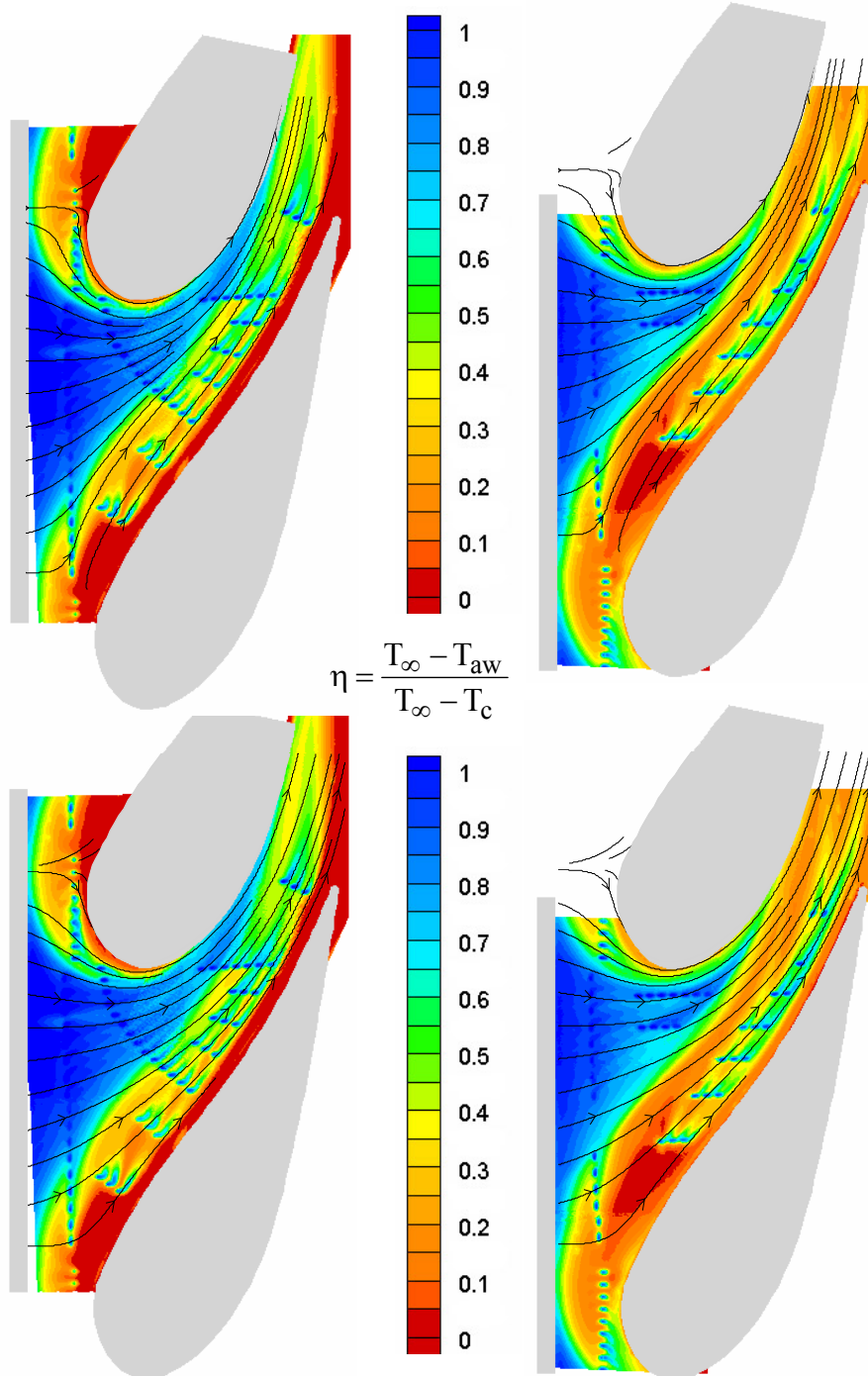


**Figure 7.16a-d** Predicted streamlines at 2% span for 1% slot flow without film-cooling are superimposed on (a) pattern #1 with 1% slot flow and 0.5% film-cooling and (b) pattern #2 with 1% slot flow and 0.5% film-cooling. The same two cases are shown with predicted streamlines at the midspan superimposed in (c) and (d).

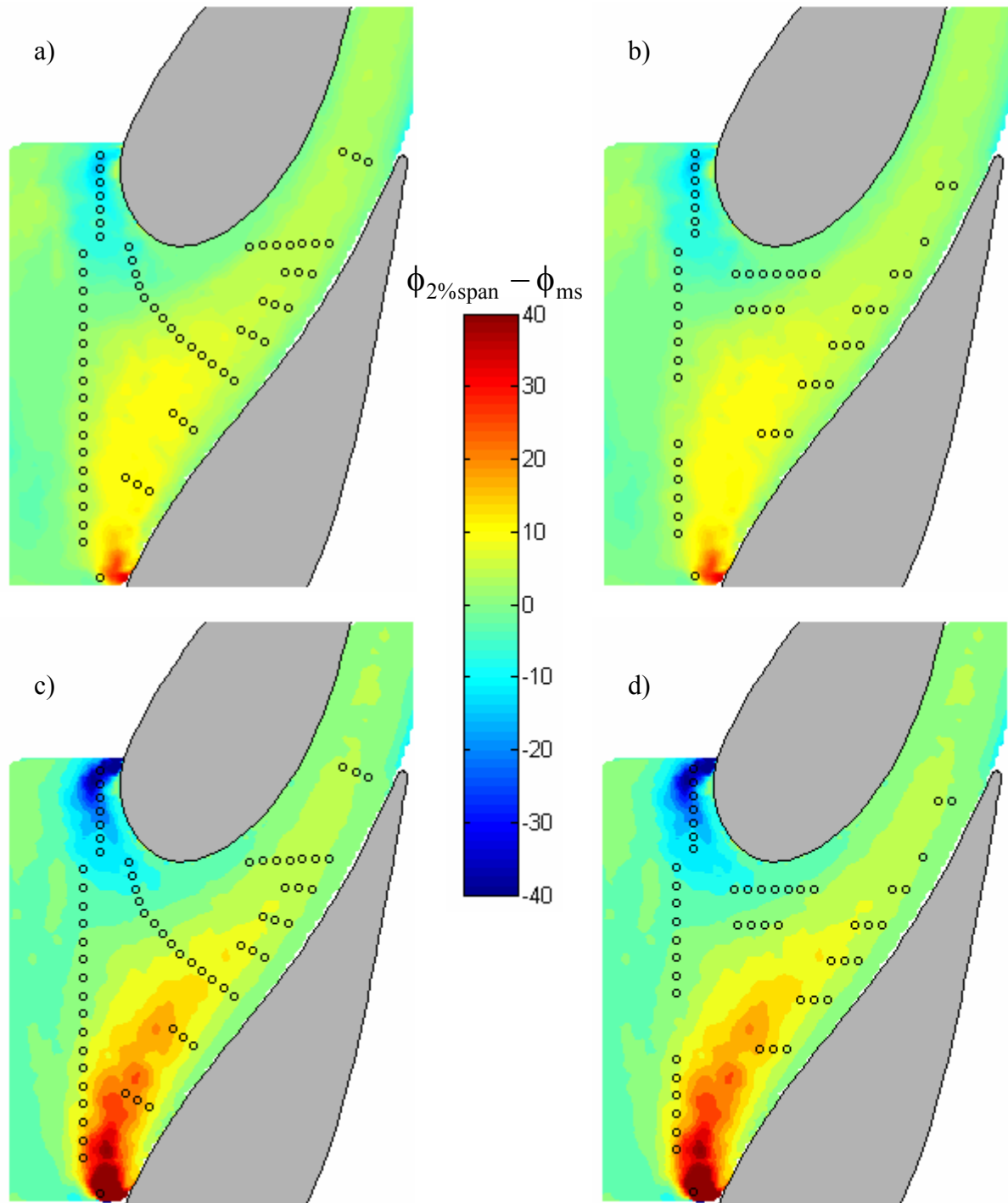


**Figure 7.17a-d** Contours of the difference between the predicted flow angles at 2% span and midspan are shown for the low 0.5% slot flow case (a) and (b) and the mid-level 0.75% slot flow case (c) and (d). The hole locations of pattern #1 and pattern #2 are shown for reference.

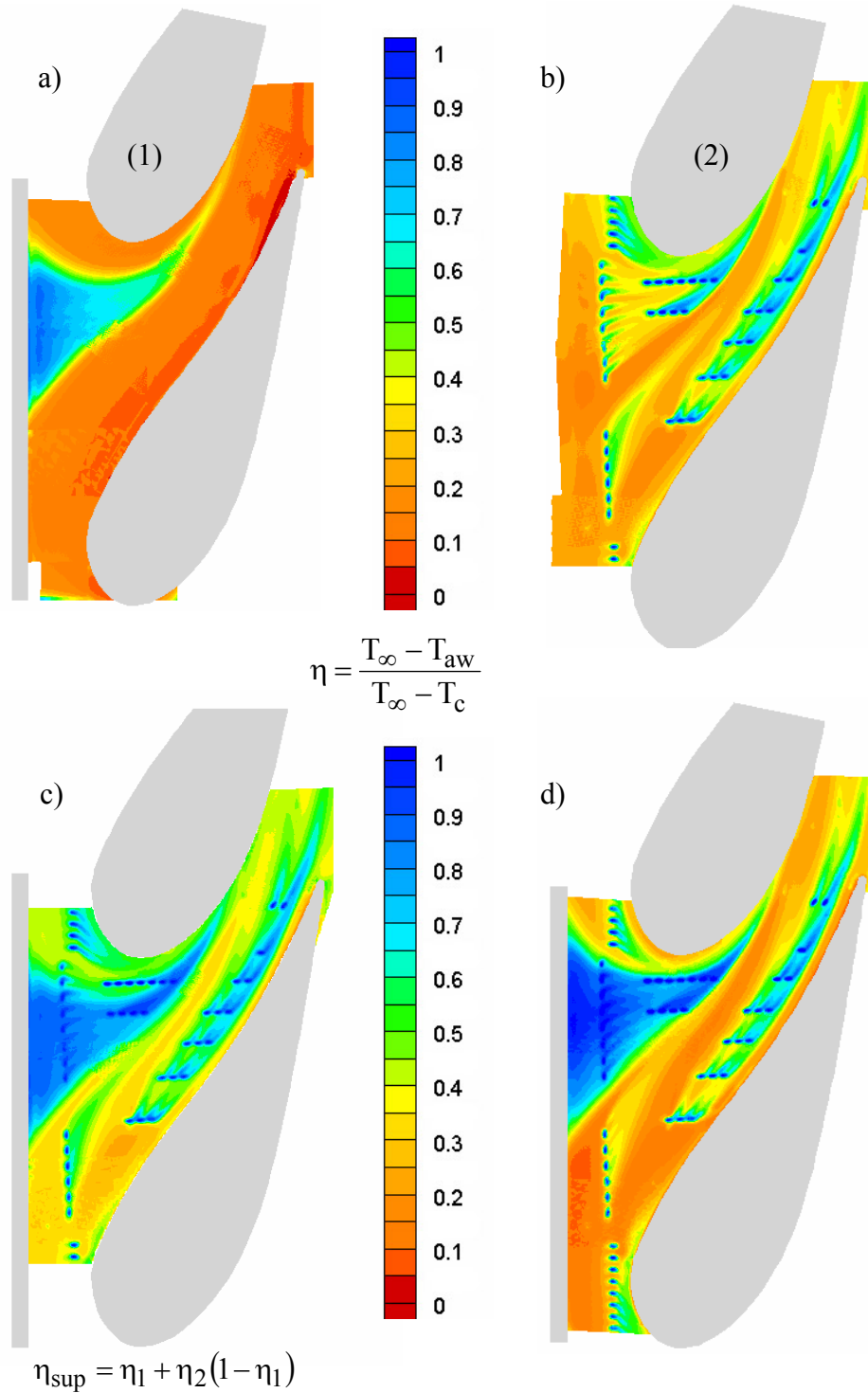


**Figure 7.18a-d** Contours of adiabatic effectiveness are shown for (a) case 1S0F0, 0.5% slot flow and (b) case 0S1F2, 0.75% film. Contours of adiabatic effectiveness for case 1S1F2, 0.5% slot 0.5% film, are shown from both (c) superposition and (d) measurements.

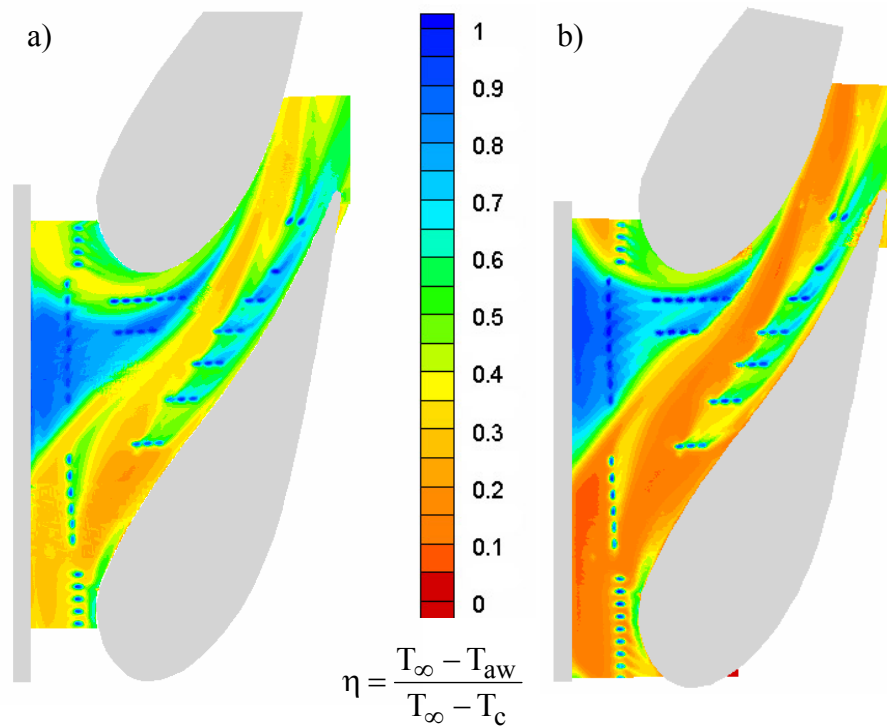


**Figure 7.19a-b** (a) Superposition predicted and (b) measured contours of adiabatic effectiveness are shown for case 1S2F2, 0.5% slot 0.75% film.

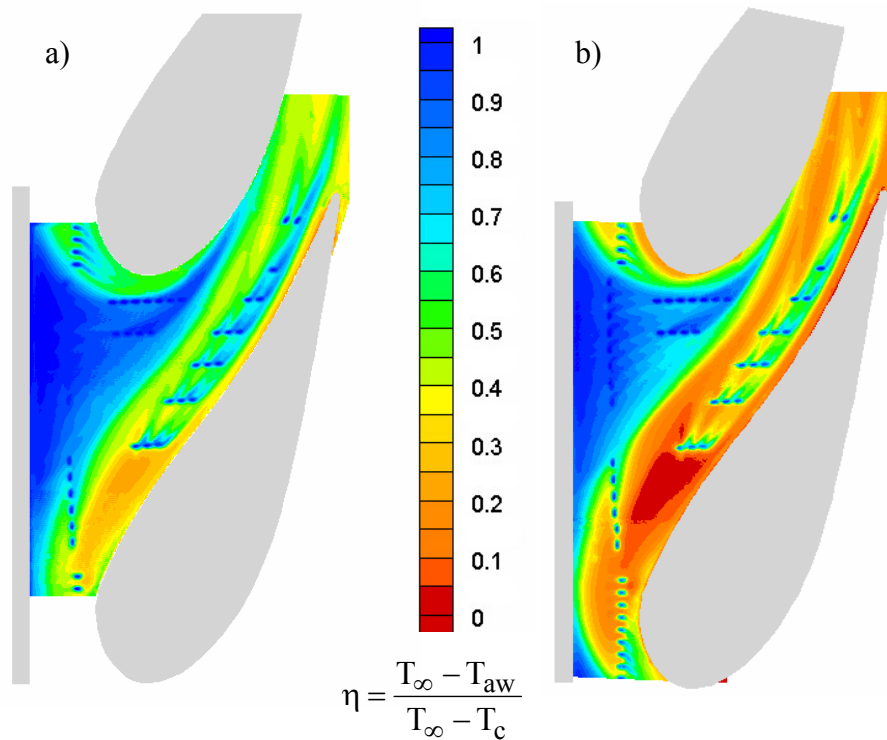


**Figure 7.20a-b** (a) Superposition predicted and (b) measured contours of adiabatic effectiveness are shown for case 2S1F2, 0.75% slot 0.5% film.

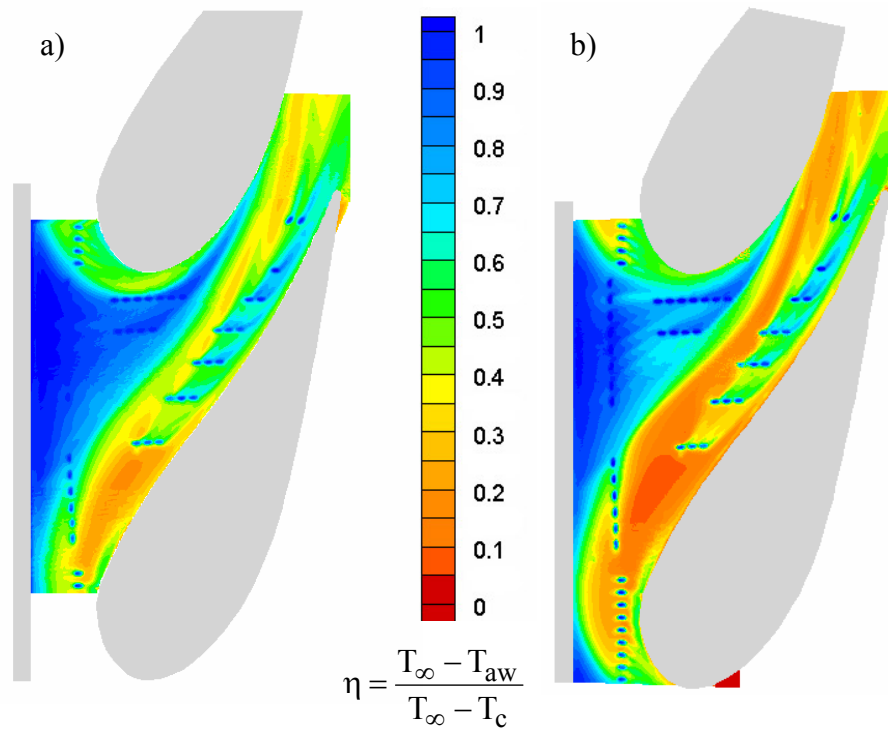


**Figure 7.21a-b** (a) Superposition predicted and (b) measured contours of adiabatic effectiveness are shown for case 2S2F2, 0.75% slot 0.75% film.

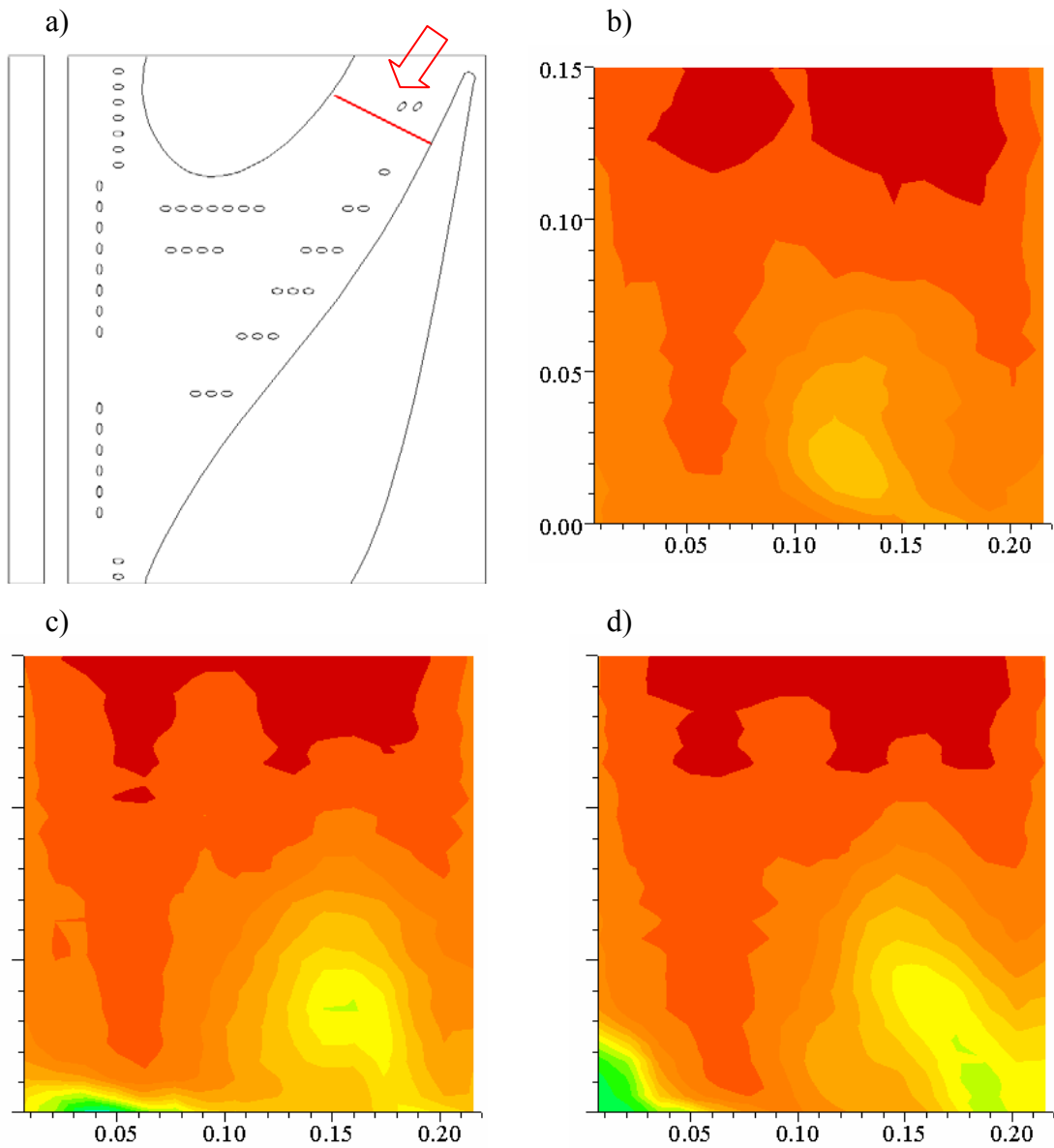


**Figure 7.22a-d** Thermal field data was acquired in (a) a plane normal to the pressure surface at  $x/C_a = -0.77$ . Contours of non-dimensional temperature are shown for (b) 0.5% slot flow without film-cooling, case 1S0F0, (c) 0.5% slot flow with 0.5% film-cooling, case 1S1F2, and (d) 0.5% slot flow with 0.75% film-cooling, case 1S2F2.

## Chapter 8

### Comparison of Predictions and Measurements

Computer simulation has become an integral part of the modern day engineering design process. Many different designs can be quickly generated and evaluated at relatively low expense. Computational simulation also lends itself to optimization studies so that the most critical design parameters can be identified and the impact of altering these parameters can be quantified. Before, a computational package can be relied upon in the design process, however, it must be compared to benchmark data to evaluate the validity and accuracy of solutions. This chapter provides a comparison of the computational results presented in chapter 6, with experimental results presented in chapter 7. The matrix of cases that were performed both computationally and experimentally is presented in Table 8.1.

Section 8.1 compares predicted and measured contours of adiabatic effectiveness for the eight cases. The contours are used to evaluate accuracy of coolant trajectory predictions as well as cooling effectiveness levels. The laterally-averaged adiabatic effectiveness levels are examined to evaluate trends in the cooling patterns between the predictions and measurements as well as between cases. Thermal field measurements are also presented for three cases to examine the migration of coolant once detached from the endwall. Section 8.2 compares the area-averaged adiabatic effectiveness levels between predictions and measurements and between cases. Trends produced by altering the coolant distribution between the cooling mechanisms are examined. Finally, Section 8.3 provides a brief summary of the comparisons.

#### 8.1 Adiabatic Effectiveness Contours

##### *Slot Flow Comparisons*

The most simplistic cooling case of a low, 0.5% slot flow without film-cooling was first computed. The prediction of endwall adiabatic effectiveness is shown in Figure 8.1a. The slot coolant is seen to exit in a non-uniform manner with no slot flow exiting upstream of the leading edge. The adiabatic effectiveness level rapidly decays at the slot

exit to approximately  $\eta = 0.5$ . The coolant is swept across the passage and exits along the suction side leaving an uncooled ring around the vane. The ring is particularly pronounced at the leading edge and along the pressure side. The adiabatic effectiveness levels in this area are  $\eta = 0$  corresponding to the temperature of the isothermal inlet flow.

Measurements of case 1S0F0 are shown in Figure 8.1b. Immediately noticeable, is that the lowest recorded adiabatic effectiveness levels are approximately  $\eta = 0.1$ . As was discussed in Section 7.1, this is a result of cooling of the near-wall fluid due to a long unheated section of the wind tunnel between the heater bank where the uniform temperature was generated and the test section. The adiabatic effectiveness levels in these areas correspond to the temperature of the approaching near-wall fluid and are not the result of any cooling benefit from the slot flow.

As was predicted, the slot coolant exits in a non-uniform manner with no coolant upstream of the leading edge and is swept towards the suction side. The width and exit location of the slot flow seems well predicted. The slightly cooled periphery of the slot flow prediction is not exhibited in the measurements, though, and the adiabatic effectiveness levels within the slot streak do not decay nearly as rapidly as was predicted. Also a slightly stronger turning of the pressure side edge of the coolant boundary towards the suction side is seen in the measurements just beyond the slot exit. Approximately half way through the passage in the measurements, the slot coolant is seen to taper to only a narrow area and is turned into the suction side. In contrast, the prediction shows a broader coolant band which extends through the passage and is not turned as sharply into the vane.

The thermal field was documented for case 1S0F0 in the plane indicated by the black line on Figures 8.1a-b. The plane is normal to pressure side at the surface location  $s/C = -0.77$  and extends across the passage to the suction side of the adjacent vane. The predictions and measurements are shown in Figures 8.2a and 8.2b respectively. The plane is viewed from downstream so that the pressure side is on the left and the suction side is on the right. The slot flow is predicted to be a coherent, well-defined structure, which is transported towards the suction side. A cool core is present at the endwall at the plane-width location  $0.15 \leq y/P \leq 0.18$ . Rings around the cool core lead to the slightly cooled gradients seen on the edges of the endwall slot flow pattern.

Measurements also show the slot coolant as a coherent structure that is transported towards the suction side. The dimensionless temperature at the endwall for much of the plane is the same as the inlet near-wall temperature indicating the presence of the upstream thermal boundary layer. The effects of the coolant are seen up to 7% span which is consistent with the prediction. The cool core of the slot flow is seen at  $y/P = 0.13$  and  $z/S = 0.02$ . The computation failed to predict the coolant core being lifted off of the endwall surface. In addition, the migration of the core towards the suction side was over-predicted. The measurements do, however, show a coolant foot at the plane width location  $0.15 \leq y/P \leq 0.18$  corresponding to the location of the coolant core in the prediction.

Predictions and measurements of endwall adiabatic effectiveness for case 3S0F0, 1.0% slot flow without film-cooling, are shown in Figures 8.3a-b. In both the prediction and measurements, the slot flow exits across the entire span of the slot. The coolant is convected towards the suction side leaving an uncooled perimeter around the vane. The footprint of the slot flow seems well predicted, but thermal spreading is under-predicted with a broader more gradual gradient around the periphery of the slot flow region than the measurements would suggest. In addition, the maximum cooling effectiveness levels are not sustained in as large an area as is shown at the slot exit of the measurements. Contrary to the low slot flow rate, the minimum effectiveness level was measured to be  $\eta = 0$ , matching the minimum predicted level. As was discussed in chapter 7, it is believed that the coolant exiting across the entire width of the slot tended to block the approaching near-wall fluid, which was slightly cooler, and funnel it along with the slot coolant into the center of the passage and towards the suction side. This drew the hotter gasses just above the boundary layer down onto the surface leading to a measured adiabatic effectiveness level of  $\eta = 0$ .

A comparison of the laterally-averaged adiabatic effectiveness levels from the predictions and measurements of both of the slot coolant rates is shown in Figure 8.4. Laterally-averaged effectiveness levels are often used to evaluate the performance of coolant as it progresses downstream. The average effectiveness levels are higher than predicted for both flow rates. At the low 0.5% flow rate the laterally-averaged effectiveness levels are higher than predicted both because the maximum effectiveness

levels are maintained over a larger area within the slot flow region and because the minimum effectiveness levels are higher than predicted because of the slightly cooler boundary layer. At the high, 1% slot flow rate, the measured values are higher than predicted because the maximum effectiveness levels are again maintained over a larger area than predicted and because the higher effectiveness levels extend closer to the coolant boundary rather than having a large, low gradient area around the periphery of the slot flow region. The trend of high effectiveness at the slot exit followed by a decaying adiabatic effectiveness was properly predicted through the passage. The measurements also tend to parallel the predicted values indicating that only the magnitudes of cooling effectiveness were significantly mispredicted.

#### *Endwall Film-Cooling Comparisons*

The film-cooling patterns were tested at the low 0.5% coolant flow rate without slot flow in order to gain a comparative baseline for the combined cooling mechanism cases. The predictions and measured contours of adiabatic effectiveness for pattern #1, the pattern based upon the iso-velocity line design, are shown in Figures 8.5a-b. Once again, the minimum measured effectiveness level corresponds to the temperature of the near-wall fluid rather than the slightly hotter midspan. The suction side leading row jets are predicted to inject as discrete jets along the incoming streamlines despite being directed normal to the inlet and in the direction of turning. The pressure side, leading row jets are also predicted to inject with the streamlines, but in a slightly less discrete fashion. The suction side, leading row jets were shown to inject with the streamlines as discrete jets in the measurements as well. The pressure side, leading row jets, however, were considerably more well directed than the predictions would suggest. This leads to a more contiguous cool zone just upstream of the first cross-passage row, but also supplies little, if any, coolant to the area just to the side of the two upstream, short rows. In addition, the cooling effectiveness of the leading row jets is predicted to decay more rapidly than the measurements indicate.

The performance of the leading edge blockers appears well predicted. The pressure side leading edge blockers provide no cooling relief, while the suction side leading edge blockers fail to penetrate to the vane-endwall junction and are swept around

the suction side. As with the leading row holes, the local effectiveness levels are somewhat under-predicted.

An uncooled streak along the pressure side was predicted and verified by the measurements. Coolant emerges from the downstream edge of the film-cooling holes in the measurements rather than from the side of the holes, as predicted, resulting in slightly narrower uncooled region. Cooling effectiveness levels along the pressure side, as well as throughout the passage, do not decay as rapidly as predicted.

A warm spot just upstream of the second cross-passage row is indicated in both the predictions and measurements, but the predicted adiabatic effectiveness level in this area is only  $\eta = 0.15$  where it was measured to be  $\eta = 0.3$ . In the exit region of the passage, as well as beyond the trailing edge, the coolant is turned more strongly towards the suction side than was predicted. In addition, thermal spreading within the passage seems under-predicted resulting in less uniform effectiveness levels than are shown by the measurements.

Predictions and measurements of adiabatic effectiveness for case 0S1F2, 0.5% film-cooling without slot flow for pattern #2, are shown in Figures 8.6a-b. As with the low slot flow alone and the film-cooling alone for pattern #1, the minimum effectiveness levels correspond to the temperature of the approaching near-wall fluid and effectiveness levels are generally under-predicted throughout the passage. A hot streak is both predicted and measured, although the width of the hot streak is under-predicted.

The leading row, suction side holes are predicted to inject in the streamwise direction with low effectiveness levels of approximately  $\eta = 0.35$ . These holes are shown to inject with the streamlines in the measurements as well, but the jets spread leaving less distinct traces. The local effectiveness levels were also measured to be higher than predicted at  $\eta = 0.5$ . The leading row, pressure side holes are predicted to inject downstream with the streamlines as well but in a less discrete fashion. The local effectiveness levels are again predicted to be  $\eta = 0.35$ , but they do not decay as rapidly as suction side leading row holes. Coolant from the suction side, leading row holes is carried downstream along the upstream edge of the pressure side rows. In contrast, coolant from these holes is seen to be more directed in the measurements. The coolant exits in a narrower more merged area and progresses downstream into the middle of the

hot streak. Coolant from the pressure side, leading row holes forces coolant from the suction side, leading row holes, as well as from the downstream holes of the two upstream passage rows, to adhere to the downstream edge of the two upstream passage rows. Coolant from these holes appears axially downstream of the upstream rows in the predictions. Local adiabatic effectiveness levels for the pressure side, leading row holes were measured to be approximately  $\eta = 0.5$ , consistent with local levels for the suction side, leading row holes, but as with predictions, the effectiveness levels do not decay as quickly downstream of the pressure side, leading row holes.

The leading edge blockers are well predicted on the suction side, except that the effectiveness levels are under-predicted. In both the predictions and measurements, the suction side leading edge blockers penetrate to the vane-endwall junction and provide coolant around the shoulder of the suction side. The pressure side leading edge blockers, however, are not as well predicted. This area is quite hard to predict because the stagnating flow requires very large cells in order to obtain the proper  $y^+$  values. If the cell size is increased, though, resolution is sacrificed. For the computations, smaller cells (lower  $y^+$ ) were used to avoid having a small section of cells which were much larger than other cells on the endwall. Coolant from the pressure side leading edge blockers is predicted to adhere to the endwall and be pulled away from the vane. The measurements indicate no cooling local to the hole. The jets appear to separate upon injection and impact the vane before being washed down into the vane-endwall junction along the pressure side near the stagnation point.

An uncooled area along the pressure side is both predicted and measured. Coolant from the pressure side jets penetrates slightly closer to the vane than predicted, just as was the case with pattern #1. Finally, the upstream most jet of each pressure side row appears to be drawn slightly more towards the center of the passage indicating stronger turning than predicted. This was also seen in the cases with slot flow alone.

A comparison of the laterally averaged effectiveness values for the two film-cooling patterns without slot flow for the predictions and measurements is shown in Figure 8.7. As with the cases with only slot flow, the average effectiveness levels are higher than predicted in large part due to cooling of the near-wall fluid before the test

section. This effect is easily seen from the predicted levels just downstream of the slot location, which are still upstream of the leading row of holes.

When examining the leading edge region where  $-0.2 \leq x/C_a \leq 0$ , two peaks are predicted corresponding to the spacing between the leading edge row holes oriented normal to the inlet flow and the leading edge blockers. This double peak is not seen in the measurements because the local effectiveness levels just downstream of the leading row holes are higher than predicted reducing the discrepancy in the average effectiveness levels at the axial locations just upstream and downstream of the leading edge blockers.

The trends through the passage are once again paralleled by the predictions with the average effectiveness levels rising until approximately  $x/C_a = 0.6$  where the levels slightly decay. When comparing the pattern #1 to pattern #2, pattern #1 is seen to be slightly more effective than predicted. From the computations, pattern #1 is slightly less effective in the leading edge region and does not outperform pattern #2 until approximately  $x/C_a = 0.5$ . Pattern #1 is then superior to pattern #2, in the laterally-averaged sense, throughout the exit of the passage. In contrast, the measurements show pattern #1 to be equal or superior to pattern #2 throughout the entire passage.

#### *Comparison of Slot Flow Combined with Film-Cooling for Pattern #1*

Moving along to the combined slot and film-cooling cases, the predictions and measurements of the low 0.5% slot flow combined with the low 0.5% film-cooling rate for pattern #1 are shown in Figures 8.8a-b. The width of the slot flow exit area is slightly over-predicted. The coolant is constricted between the leading row and the first cross-passage row, by the impinging pressure side, leading row jets in both the computations and measurements. Slightly stronger turning is also exhibited in the measurements resulting in the coolant impacting the suction side of the upper vane upstream of the impact location predicted by the computations.

The pressure side, leading row holes are shown to be more directed and merged in the measurements with a larger, contiguous affected zone and a higher adiabatic effectiveness level of  $\eta = 0.5$ , as compared to the predicted level of  $\eta = 0.35$ . The trajectory of the leading edge blockers is well predicted. Coolant exits and is swept around the suction side leaving an uncooled region at the leading edge. The coolant is

shown to impact the shoulder in the measurements, but is not predicted to impact the upper vane until near the trailing edge.

An uncooled region along the pressure side is also properly predicted. The upstream rows of three holes, however, are more directed in the measurements and decay less rapidly. Thermal spreading of the downstream jets along the pressure side and beyond the second cross-passage row also appears under-predicted resulting in more uniform adiabatic effectiveness levels in the measurements.

The results of increasing the film flow rate to 0.75% while maintaining the slot flow rate at 0.5% for pattern #1 are shown in Figures 8.9a-b. Again, the width of the slot exit region is slightly under-predicted, and a cool core is maintained just downstream of the leading row. The concentration of the highest effectiveness levels, forming the cool core, is not seen in the prediction. A constriction of the slot flow is exhibited in both the predictions and measurements as a result of impingement from the pressure side, leading row holes.

Increasing the coolant flow rate is predicted to improve the cooling performance of the pressure side, leading row holes, but it is seen from the measurements that increasing the cooling rate actually reduces the effectiveness of these holes. Also, the predicted adiabatic effectiveness levels of the pressure side, leading row holes are higher than the measured values. Both the over-prediction of the effectiveness levels and the misprediction of the trend are most likely due to jet separation which was either not captured or not as pronounced in the computations. The upstream rows of three holes along the pressure side also exhibit jet separation which was not fully captured by the computations. In addition, the hole closest to the pressure side in these two rows appears to follow the contour of the vane while the other two holes in the rows are drawn more towards the center of the passage. The computations predict that all three holes in these two rows will inject in the same direction leading to more uniform coverage of the areas just downstream of the rows. The uncooled area along the pressure side is well predicted and shows a reduction when compared to the low film-cooling rate for both the predictions and measurements.

The computations accurately predict the leading edge blockers on the suction side penetrating fully to the vane and providing coolant around the shoulder of the suction

side. As with the upstream pressure side holes, though, the effectiveness levels are over-predicted indicating that partial jet detachment is not properly captured. This problem seems exacerbated at the pressure side leading edge blockers. The predictions show coolant at the endwall between the holes and the stagnation point. The measurements indicate that the jets detach at the injection location and impact the vane before being washed down onto the vane endwall junction as evidenced by the coolant accumulation only along the junction at the pressure side.

Thermal spreading within the passage seems more accurately predicted with the varying effectiveness levels corresponding well although the warm spot upstream of the second cross-passage row is shown to be broader than predicted.

The predicted and measured laterally-averaged adiabatic effectiveness levels are compared for the two cases of combined slot and film-cooling for pattern #1 in Figure 8.10. At the low film-cooling flow rate, the trends throughout the passage are captured in the predictions, but, once again, the magnitudes are over-predicted by approximately  $\Delta\eta = 0.1$ . At the increased blowing rate, both the trends and magnitudes are quite well predicted. The average effectiveness levels are only slightly over-predicted in the upstream half of the passage where jet separation did not appear to be well captured.

#### *Comparison of Slot Flow Combined with Film-Cooling for Pattern #2*

The adiabatic effectiveness contours for pattern #2 with combined 0.5% slot and 0.5% film-cooling flow rates are shown in Figures 8.11a-b. The exit location of the slot flow is seen to be mispredicted with coolant exiting closer to the upper vane in the measurements. The large area where  $\eta = 0.5$  to the pressure side of the upstream passage rows is also not seen in the measurements and the maximum effectiveness level is maintained over a much larger area. Slot coolant is predicted to cover the gutter gap in the leading row of holes and be present axially downstream of the upstream passage rows, but the measurements show that the entire gutter gap is not covered and that the slot coolant adheres to the downstream edge of the upstream passage rows. Also, slightly stronger turning is seen near the flow plane indicated by the black line resulting in an impact location of the slot flow upstream of the predicted impact location.

The directionality of the pressure side, leading row holes is also under-predicted while the effectiveness of these holes is over-predicted. The measurements show low  $\eta = 0.35$  effectiveness levels indicating a potential jet separation. The coolant is also more merged and a thin, uncooled region between the slot flow and the coolant from the pressure side, leading row holes is evident. The predictions show higher  $\eta = 0.5$  effectiveness levels and cooling effects from the pressure side, leading row holes as far axially downstream as the upstream edge of the pressure side holes. Coolant from these holes is directed into the middle of the passage in the measurements. As a result of the higher directionality of the jets, the hot streak is shown to be broader in the measurements.

The local effectiveness levels of the leading edge blockers appear well predicted except the effectiveness levels do not decay as rapidly around the shoulder of the suction side. In addition, the coolant was predicted to travel to the vane-endwall junction, but the measurements show that the jets do not fully penetrate to the vane. The performance of the pressure side leading edge blockers, however, is especially mispredicted. Coolant is predicted to adhere to the endwall and be carried along the pressure side, but the jets are shown to be detached with coolant impacting the vane before washing down onto the junction in the measurements.

An uncooled region along the pressure side is shown in both the predictions and measurements. Both trajectories and local effectiveness levels of the pressure side jets are well predicted with the exception of the upstream most hole in each of the two upstream most rows of three holes. These two jets appear slightly more drawn towards the center of the passage resulting in a more discrete cooling pattern on the endwall.

Predictions and measurements of the thermal field taken in the plane indicated by the black line are presented in Figures 8.12a-b. In both the predictions and measurements, the hot streak in the center of the passage is clearly visible. The predictions indicate two areas of coolant concentration: one near the pressure side and one near the suction side. Both areas have a cool core of  $\theta = 0.65$  at the endwall. The minimum of the larger coolant zone, consisting of both slot and film-coolant, is shown at  $0.18 \leq y/P \leq 0.2$ . This coolest area is closer to the suction side than the center of the coolant mass which is seen above the endwall at  $z/S = 0.02$  and  $y/P = 0.17$ .

The measurements also show two areas of coolant concentration. The cool core of the slot and film coolant is shown off of the wall in the center of the coolant mass at  $z/S = 0.035$  and  $y/P = 0.16$ . This is quite different from the predictions of the coolant core on the endwall. The computations failed to predict that the coolant would be lifted off of the endwall and be entrained in the center of the passage vortex. A small coolant foot is maintained, however, at the endwall in the same location as the predicted coolant core. Both the predictions and measurements indicate a small measure of cooling effectiveness on the suction side of the vane below approximately  $z/S = 0.04$ . The film-cooling mass along the pressure side is seen to be much flatter and broader than predicted. A thin zone of maximum effectiveness  $\theta = 0.6$  is maintained at  $0.04 \leq y/P \leq 0.05$  which corresponds to the predicted maximum location.

Predictions and measurements of increasing the film-cooling to 0.75% of the core flow while maintaining the slot at 0.5% are shown in Figures 8.13a-b. As with the low film-cooling flow rate for pattern #2, the exit location of the slot flow is mispredicted with coolant exiting closer to the upper vane in the measurements. As a result, the entire width of the gutter gap in the leading row of holes is not cooled.

The directionality of the leading row, pressure side holes appears well predicted with the exception the slightly cooled region axially downstream of the leading row, pressure side holes. This is most likely cooling as a result of the mainstream mixing with the injecting jets, rather than the coolant jets convecting down through the center the passage in the hot streak region. The cooling effectiveness levels are over-predicted at  $\eta = 0.5$  while they were measured at only  $\eta = 0.35$ . The extremely low measured cooling effectiveness levels would seem to indicate jet separation which is not well captured by the predictions. In both the predictions and measurements, the slot flow is constricted by the pressure side, leading row holes impacting the upstream most hole of the upstream passage rows.

The leading edge blockers are predicted to inject in a discrete fashion indicating partial jet separation with maximum adiabatic effectiveness levels of  $\eta = 0.5$ . The measurements show the leading edge blockers being completely detached and impacting the vane before being washed down onto the vane-endwall junction. The maximum adiabatic effectiveness level in this region was also measured to be  $\eta = 0.5$ . Coolant

adheres to the pressure side in the vane-endwall junction just beyond the dynamic stagnation point in both the predictions and measurements.

Both predictions and measurements indicated only a thin uncooled region along the pressure side at the upstream rows of pressure side holes, while the cooling holes nearer to the exit penetrated to the vane endwall junction. The cooling effectiveness levels and direction of the pressure side jets are well predicted except that coolant from the upstream most hole of both the fourth pressure side row and the trailing edge row is drawn slightly more across the passage indicating stronger cross flow in the exit region than predicted.

The thermal fields in the indicated plane for case 1S2F2 are shown in Figures 8.14a-b. Both the predictions and the measurements show a widening of the hot streak between the two coolant zones when compared to the results of the low film flow case in Figures 8.11a-b. The larger coolant zone, consisting of slot and film coolant, is shifted closer to the suction side and appears more skewed indicating a stronger passage vortex for the higher film-cooling flow. A cool core is predicted and measured at the endwall and extends up to  $z/S = 0.02$ . The maximum dimensionless temperature, corresponding the minimum fluid temperature, is over-predicted at  $\theta = 0.7$  as compared to a measured value of  $\theta = 0.4$ . The plane width location is also slightly over-predicted at  $y/P = 0.2$ . Coolant is seen to accumulate against the suction side of the vane reaching a predicted height of  $z/S = 0.07$  and a measured height of  $z/S = 0.06$ .

The film-cooling zone along the pressure side has also moved closer to the vane with the predicted plane location from  $0.01 \leq y/P \leq 0.06$  and the measured range from  $0 \leq y/P \leq 0.06$ . The coolant is predicted in a semi-circular pattern with a cool core of  $\theta = 0.6$  at  $0.03 \leq y/P \leq 0.045$ . The measurements however show the coolant accumulating more against the vane rising up to  $z/S = 0.02$ . The maximum measured dimensionless temperature is  $\theta = 0.5$ .

A comparison of the predicted and measured laterally-averaged adiabatic effectiveness levels for slot flow combined with film-cooling pattern #2 is shown in Figure 8.15. For both cases the coolant was slightly more effective at the slot exit than predicted. As with pattern #1, at the low film-cooling rate, the measured effectiveness values exceed the predicted values throughout the entire passage. The deviation however

is only approximately  $\Delta\eta = 0.05$ . At the increased film-cooling flow rate, the predicted values exceed the measured average effectiveness level in the range  $0.4 \leq x/C_a \leq 0.6$  which is approximately where the gutter gap exists between the upstream passage rows and the pressure side holes. It is seen that the cool region from the slot flow and upstream passage rows is not as broad and less effective than predicted in this area and, the local effectiveness levels at the pressure side holes are slightly lower than predicted leading to the discrepancy.

## 8.2 Area-Averaged Adiabatic Effectiveness

Area-averaged effectiveness values provide a metric for comparing the effects of varying coolant distribution between the slot and film-cooling mechanisms. The area-averaged adiabatic effectiveness levels for to eight cases which were both computed and measured are shown in Figure 8.16. The cases are grouped by cumulative coolant flow rate. Area-averaged values were calculated from the axial location  $x/C_a = -0.235$  corresponding to the upstream most point where the measurements covered the full pitch of the cascade to  $x/C_a = 0.8$  where optical access to the passage was limited. The average effectiveness levels were consistently under-predicted because the endwall was artificially cooled by a slightly cooler approaching boundary layer than the predictions accounted for. As a result the measured adiabatic effectiveness levels in uncooled regions were often  $\eta = 0.1$  rather than  $\eta = 0$ . Also, thermal spreading was consistently under-predicted contributing to increased predicted endwall temperatures. At high blowing ratios, separation was induced in many of the upstream holes which was also not well captured. This led to closer agreement between the measurements and predictions, because local cooling was over-predicted offsetting the effects of the uncooled areas which were over-predicted because of the cooler near-wall fluid. This close agreement is seen in the 1.25% grouping.

The trends induced by changing the coolant distribution within the groups were well predicted. At 0.5% cumulative coolant flow, both the predictions and measurements indicate that the film-cooling holes alone provide superior cooling, in the area averaged sense, to the slot flow alone with pattern # 1 outperforming pattern #2. Within the 1% grouping, the slot flow was inaccurately predicted to provide the lowest area-averaged

effectiveness of the group when in fact it provided the highest area-averaged effectiveness. This case does not provide superior performance to the combined cases, though, because the area-averaged effectiveness levels have been inflated by large, overcooled slot area, while a warm uncooled ring was left around the vane. The film-cooling patterns offered similar average effectiveness levels without the large uncooled zones. Pattern #1 was accurately predicted to provide slightly better performance than pattern #2 at the 0.5% coolant flow rate when combined with 0.5% slot flow. In addition, all three cases with 1% cumulative coolant were shown both computationally and experimentally to provide improved area-averaged effectiveness levels over their corresponding 0.5% cumulative coolant flow cases. At 1.25% the best agreement was found between computations and experiments. The predicted trends from increasing the film blowing from 0.5% to 0.75% while maintaining the slot at 0.5% were not accurate. Film pattern #2 was predicted to yield equal performance, while film pattern #1 was predicted to provide improved performance, but measurements showed a decline in area-averaged effectiveness for both patterns. This was because the computations failed to accurately capture the separation of many of the upstream holes at the increased blowing rate.

### **8.3 Summary**

Contours of adiabatic effectiveness were compared for eight cases consisting of slot cooling alone, film-cooling alone for the two film-cooling hole patterns, and slot cooling combined with the film-cooling patterns. Computations were shown to be a valuable tool in aiding to locate film-cooling holes and predict coolant coverage. The coolant trajectories and footprint were generally well predicted while cooling effectiveness levels and thermal spreading were frequently under-predicted relative to the experiments. Minimum effectiveness levels were often lower than measured because the inlet profile was slightly cooler in the near-wall rather than having a perfectly uniform inlet profile as mandated by the computations. Large, uncooled rings around the vanes for the cases with only slot flow were properly predicted as well as uncooled areas along the pressure side, at the leading edge, and in the center of pattern #2 when film-cooling was included. The pressure side, leading row holes were frequently more directed than

predicted and stronger turning was seen along the upstream edge of the pressure side rows and in the exit region of the passage. Jet separation in the leading edge region and the upstream pressure side holes was also not well predicted.

**Table 8.1** Test Matrix of Cases with Both Predictions and Measurements

Case	Slot Flow %m <sub>in</sub>	Film Flow %m <sub>in</sub>	Inlet Temp Profile	Thermal Field
1S0F0	0.50	- - -	Isothermal	Y
3S0F0	1.00	- - -	Isothermal	N
0S1F1	- - -	0.50	Isothermal	N
0S1F2	- - -	0.50	Isothermal	N
1S1F1	0.50	0.50	Isothermal	N
1S1F2	0.50	0.50	Isothermal	Y
1S2F1	0.50	0.75	Isothermal	N
1S2F2	0.50	0.75	Isothermal	Y

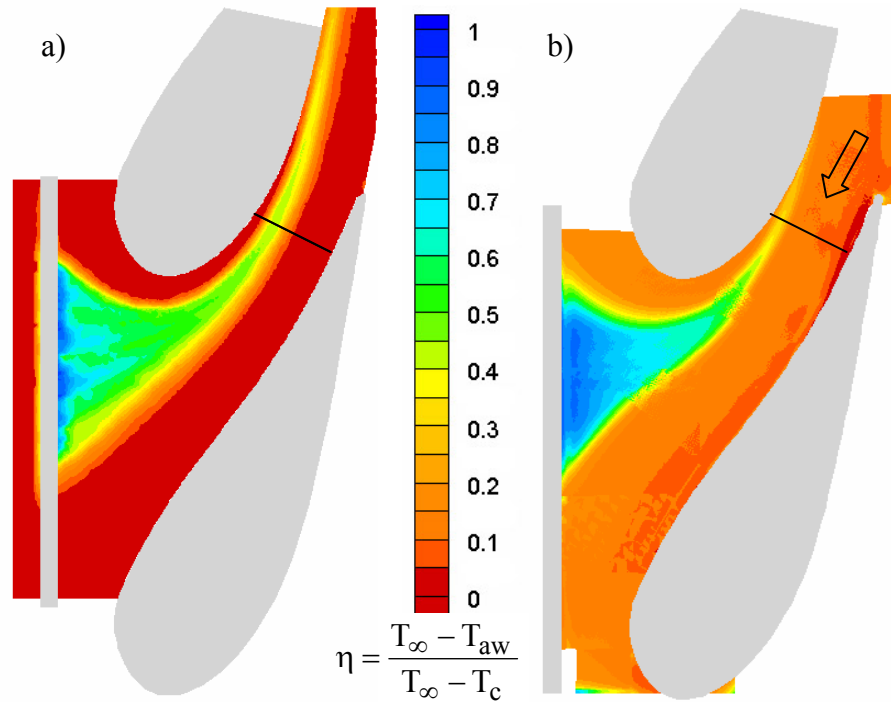


**Figure 8.1a-b** (a) Predictions and (b) measurements of adiabatic effectiveness are shown for the low 0.5% slot flow rate, case 1S0F0.

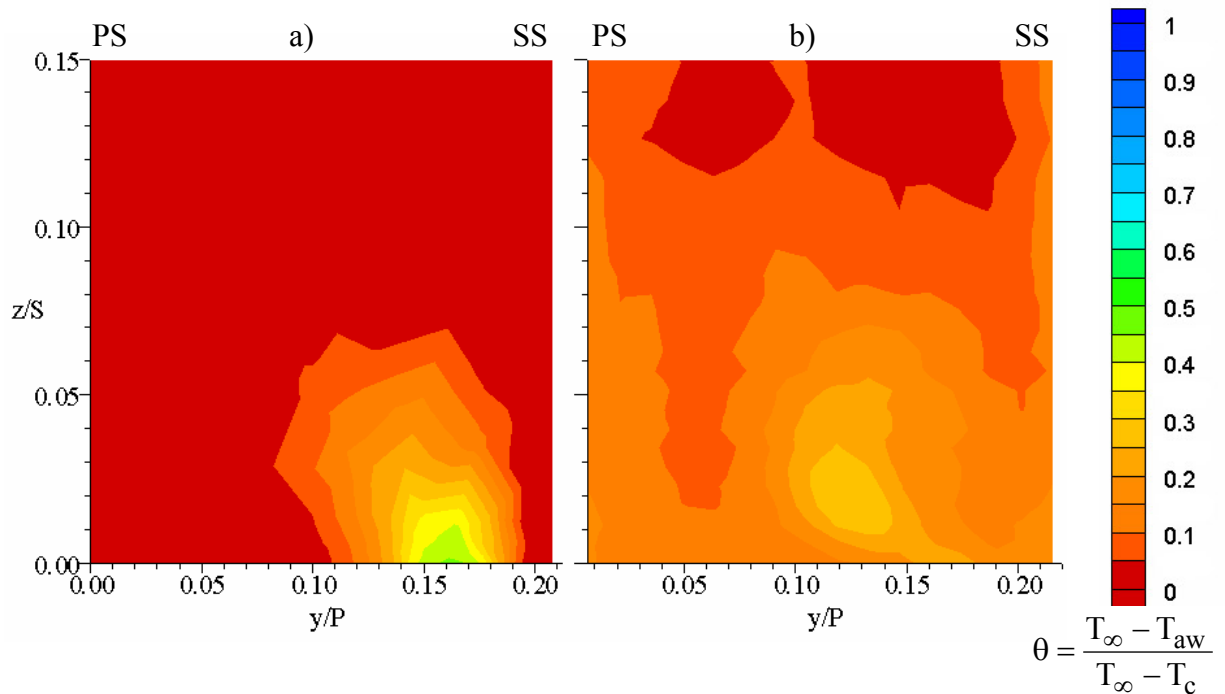


**Figure 8.2a-b** (a) Predictions and (b) measurements of the non-dimensional thermal field for case 1S0F0.

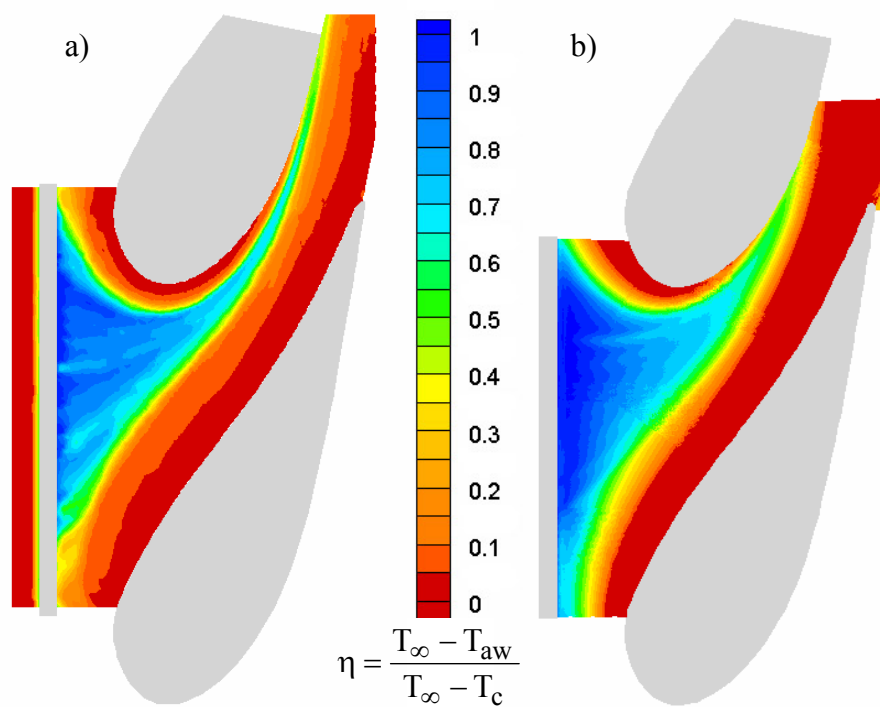


**Figure 8.3a-b** (a) Predictions and (b) measurements of adiabatic effectiveness are shown for the high 1.0% slot flow rate, case 3S0F0.

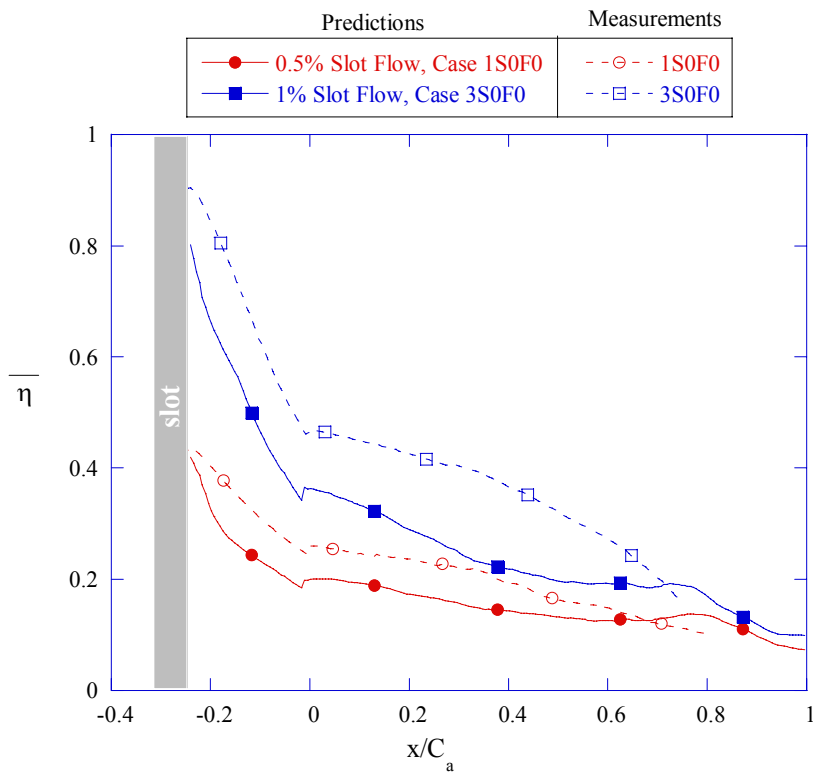


**Figure 8.4** Comparison of laterally-averaged adiabatic effectiveness for predicted and measured cases of slot flow alone.

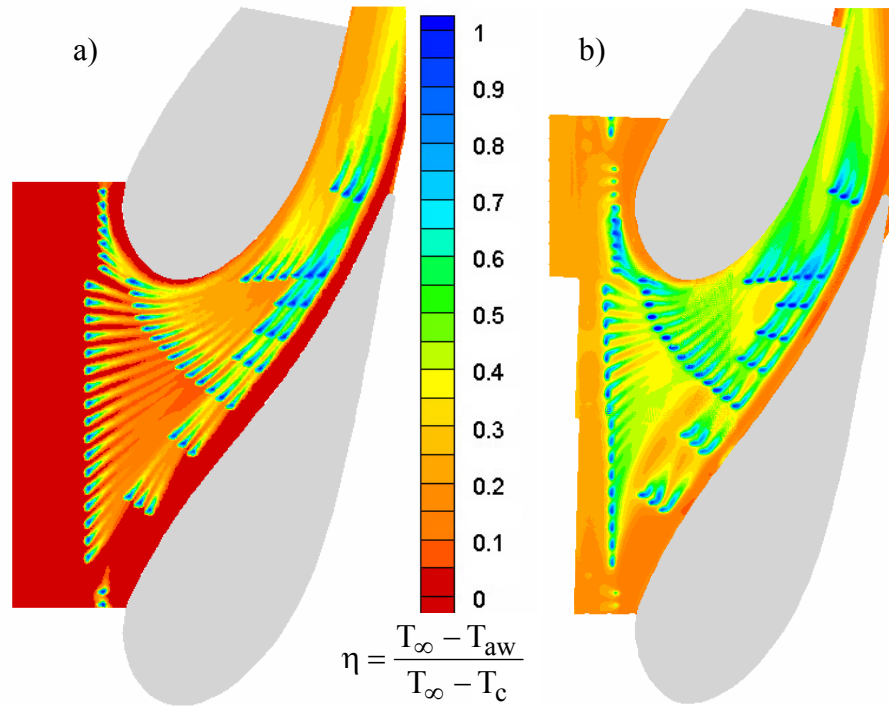


**Figure 8.5a-b** (a) Predictions and (b) measurements of adiabatic effectiveness for pattern #1 at 0.5% film-cooling without slot flow, case 0S1F1.

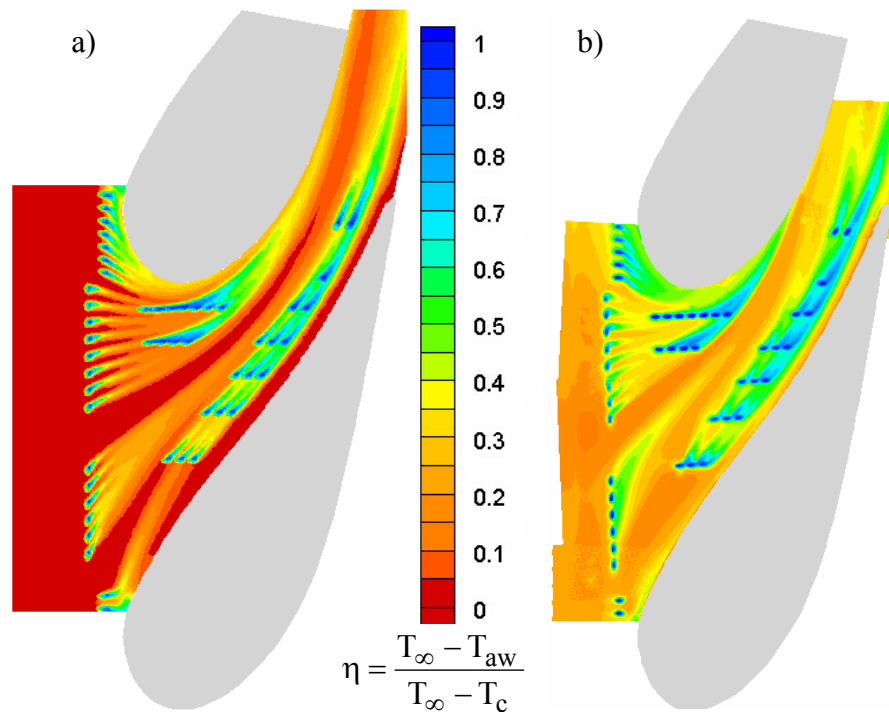


**Figure 8.6a-b** (a) Predictions and (b) measurements of adiabatic effectiveness for pattern #2 at 0.5% film-cooling without slot flow, case 0S1F2.

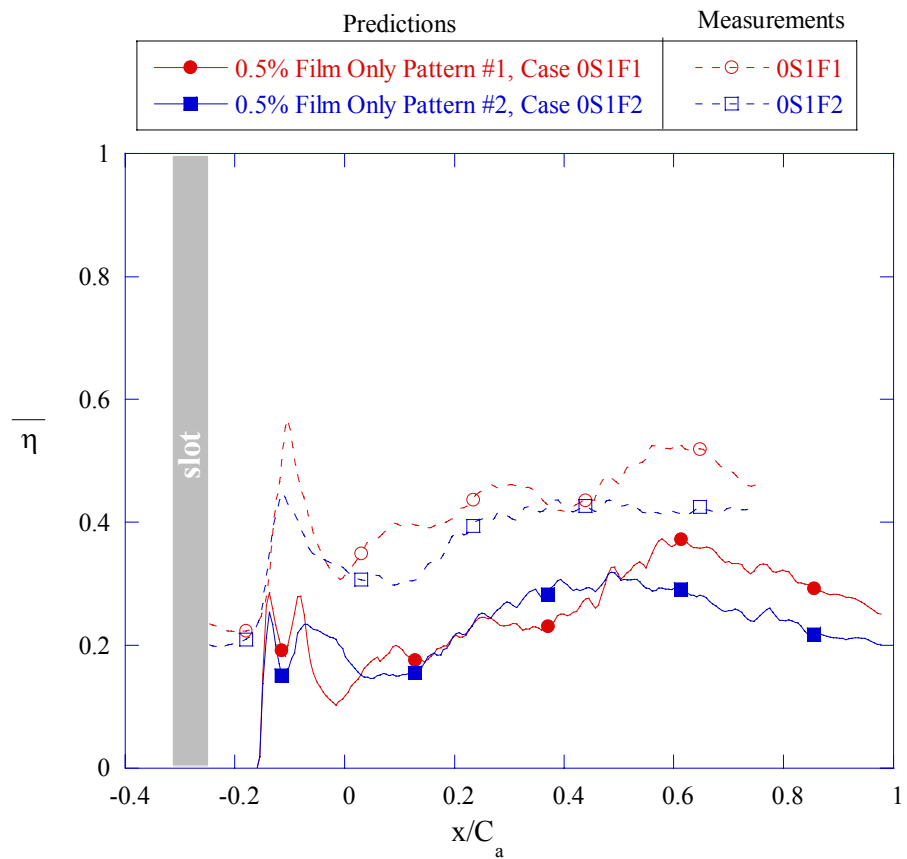


**Figure 8.7** Comparison of laterally-averaged adiabatic effectiveness for predicted and measured cases of film-cooling flow alone.

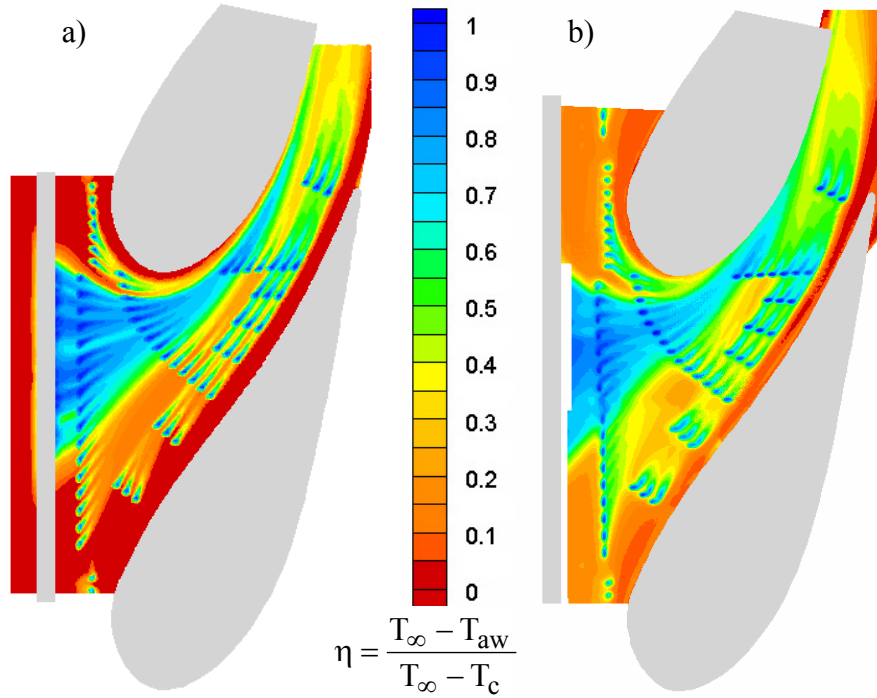


**Figure 8.8a-b** (a) Predictions and (b) measurements of adiabatic effectiveness for pattern #1 at 0.5% slot with the low 0.5% film-cooling flow rate, case 1S1F1.

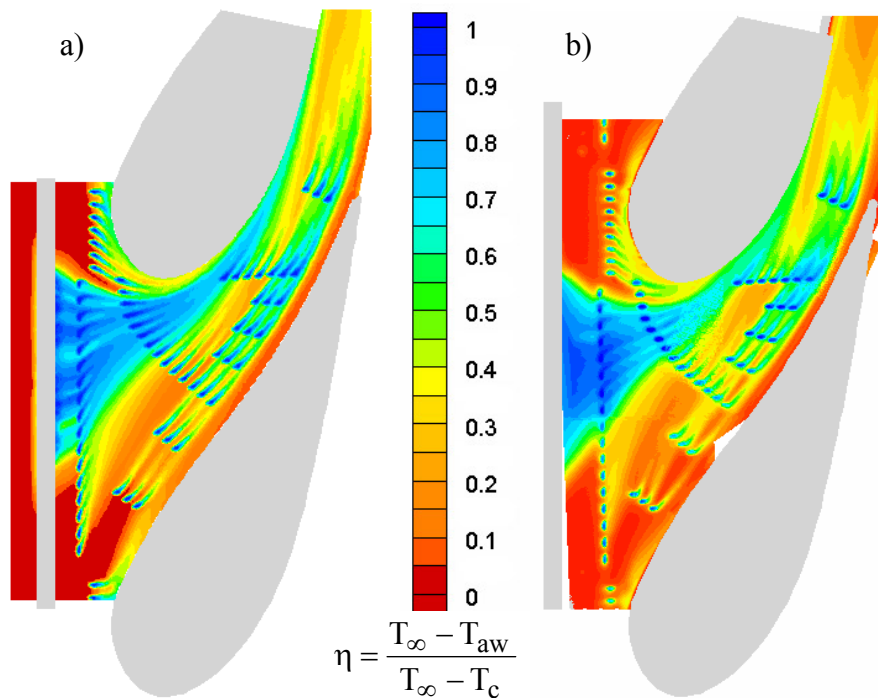


**Figure 8.9a-b** (a) Predictions and (b) measurements of adiabatic effectiveness for pattern #1 at 0.5% slot with the high 0.75% film-cooling flow rate, case 1S2F1.

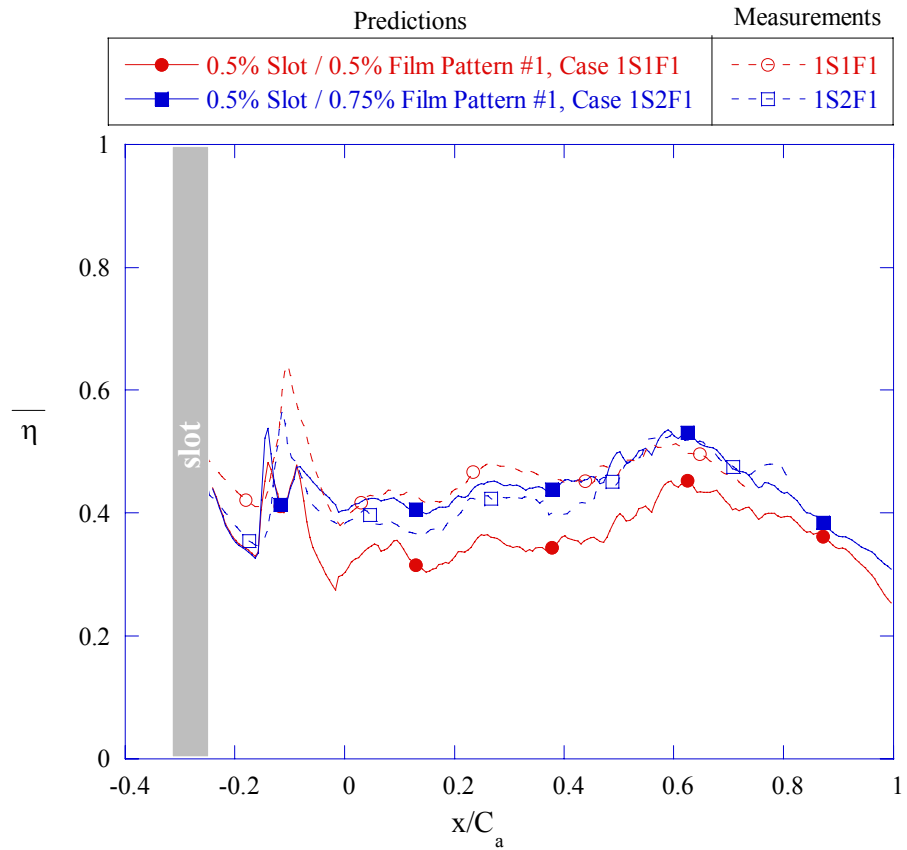


**Figure 8.10** Comparison of laterally-averaged adiabatic effectiveness from predictions and measurements for 0.5% slot flow with film cooling from pattern #1 at 0.5% and 0.75%.

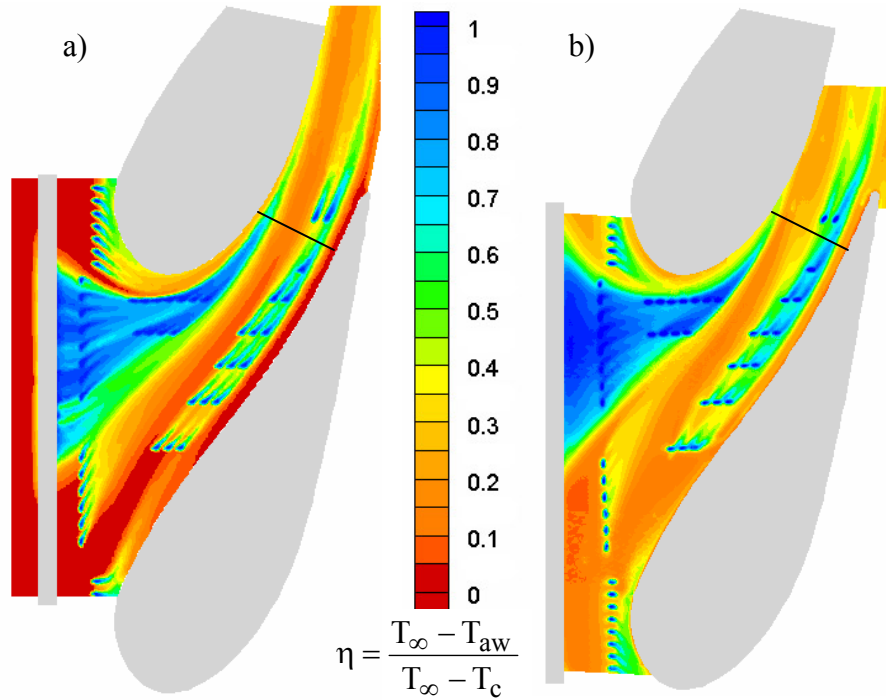


**Figure 8.11a-b** (a) Predictions and (b) measurements of adiabatic effectiveness for pattern #2 at 0.5% slot flow with the low 0.5% film-cooling flow rate, case 1S1F2.

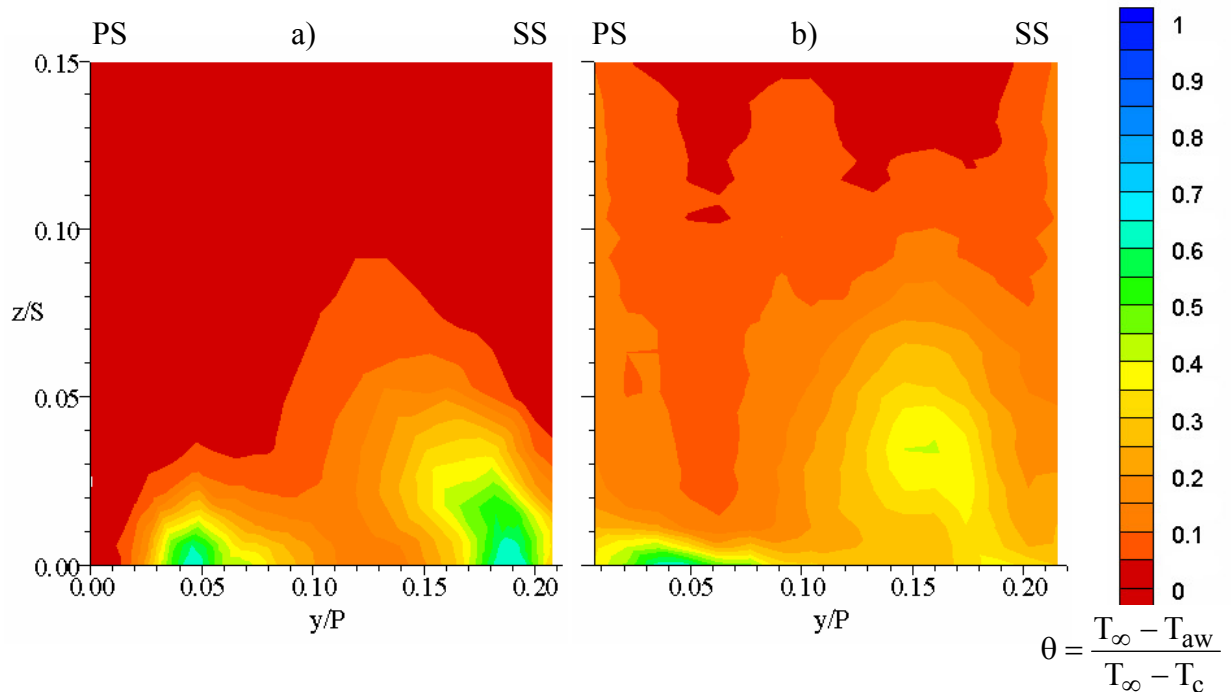


**Figure 8.12a-b** (a) Predictions and (b) measurements of the non-dimensional thermal field for case 1S1F2.

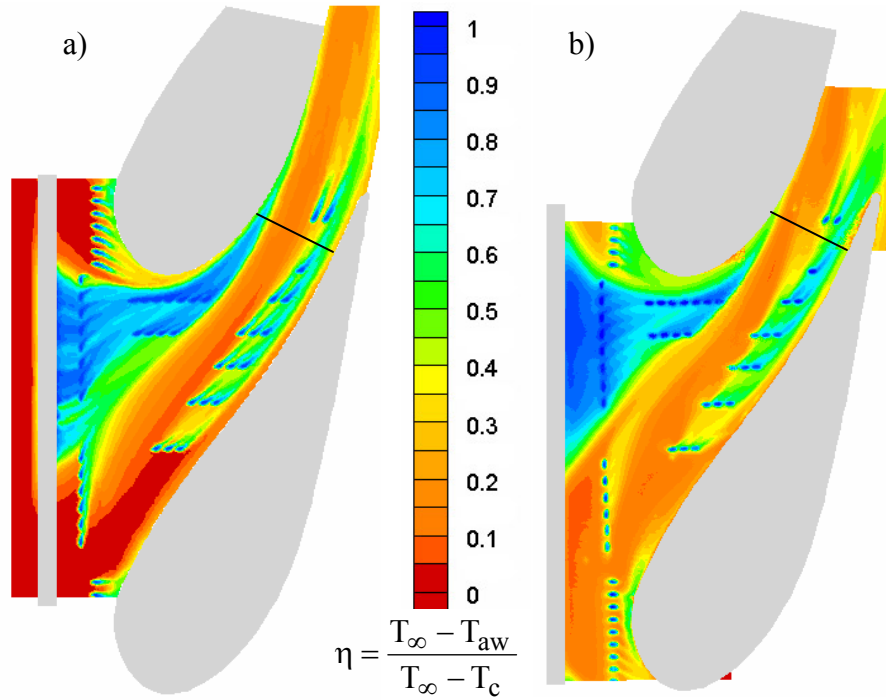


**Figure 8.13a-b** (a) Predictions and (b) measurements of adiabatic effectiveness for pattern #2 at 0.5% slot flow with the high 0.75% film-cooling flow rate, case 1S2F2.

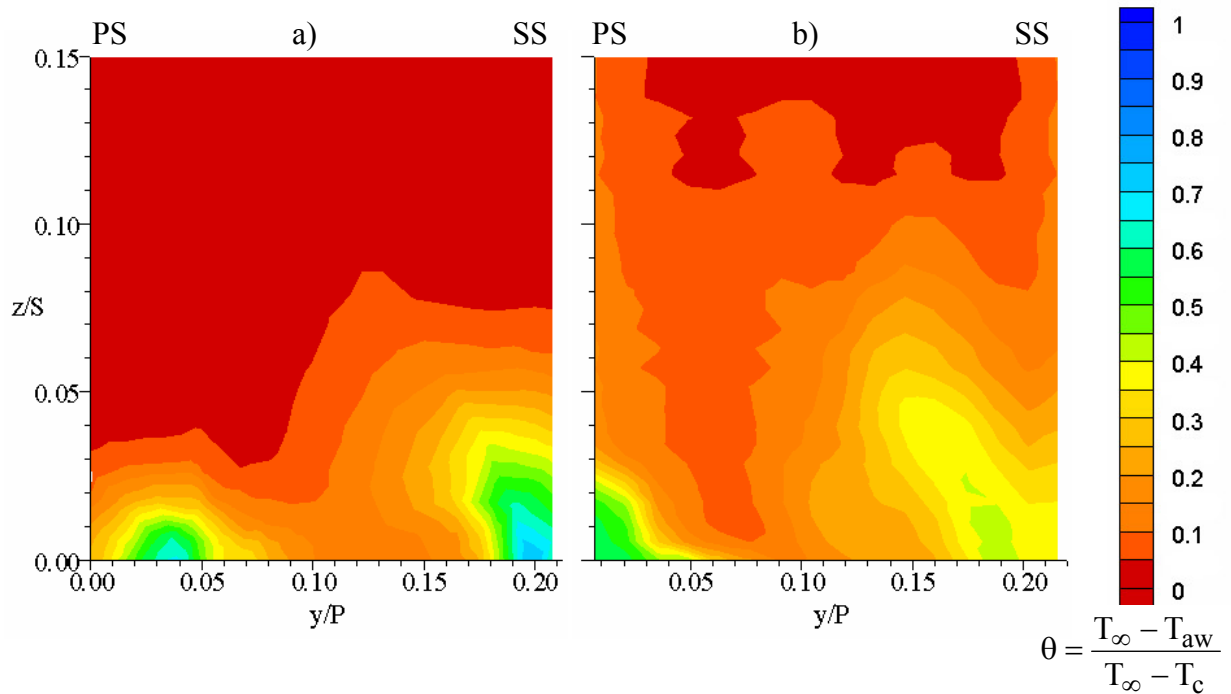


**Figure 8.14a-b** (a) Predictions and (b) measurements of the non-dimensional thermal field for case 1S2F2.

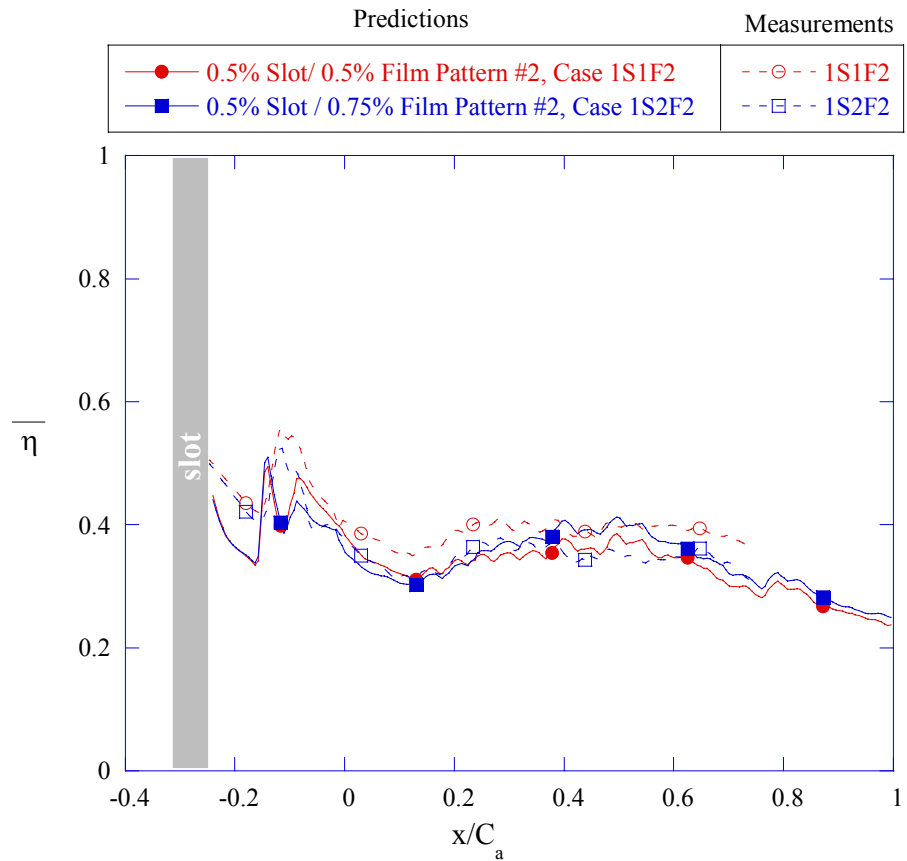


**Figure 8.15** Comparison of laterally-averaged adiabatic effectiveness from predictions and measurements for 0.5% slot flow with film cooling from pattern #2 at 0.5% and 0.75%.

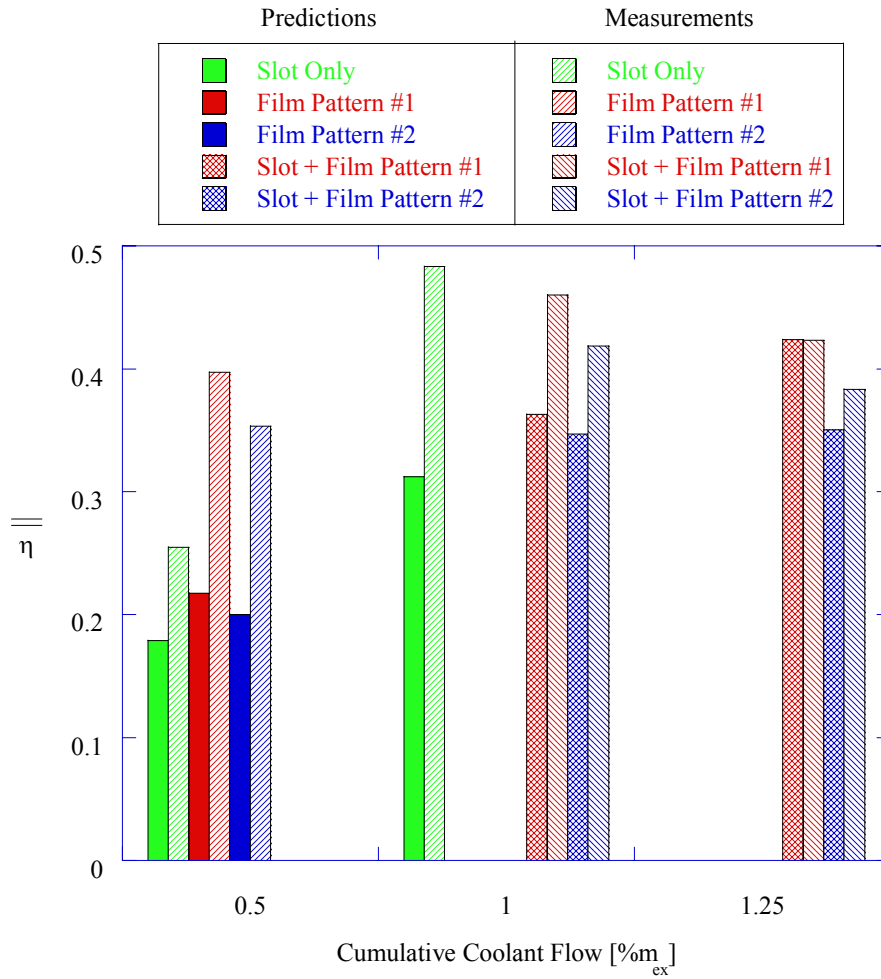


**Figure 8.16** Area-averaged adiabatic effectiveness levels from predictions and measurements grouped by cumulative coolant flow rate.

## Chapter 9

### Conclusions and Recommendations for Future Study

The goal of this research was to develop an understanding of the trajectory of slot and film-coolant as well as effectiveness levels achieved by each of these cooling methods. A test matrix was developed to evaluate the effectiveness and distribution of both slot flow and film-coolant from two original endwall film-cooling designs at various blowing and momentum flux ratios. The patterns were based on different design philosophies allowing a comparison of the design methods. Areas requiring special consideration were identified. The slot and film-cooling patterns were also combined to evaluate the influence that each cooling mechanism had on the other. The coolant distribution and effectiveness levels were both predicted using computational fluid dynamics (CFD) and measured in a large scale, low speed wind tunnel. The effects of coolant injection on the flow field and thermal field were also examined. The accuracy of the predictions was evaluated to determine if CFD was a viable tool to aid a designer in the development of a cooling scheme.

Section 9.1 provides a summary of the results obtained from the predictions. Section 9.2 recounts the findings from the measurements. The comparison of the predictions and measurements are outlined in section 9.3. Finally, section 9.4 offers suggestions for further investigation of this topic.

#### 9.1 Analysis of Predictions

Predictions were made of the effects of coolant injected from a two-dimensional slot at the combustor-turbine interface alone; endwall film-cooling alone; and combined slot and endwall film-cooling. The resulting endwall effectiveness from slot cooling alone showed a pattern that was quite non-uniform along the endwall with most of the coolant being swept toward the suction side of the vane. One could expect a burn-out near the vane-endwall juncture if only depending on the slot cooling from the combustor-turbine interface as a result of a warm ring extending most of the vane.

Placing film-cooling holes in the endwall is critical for increasing component life. The placement of these holes is difficult because the trajectory of the jets is not intuitive given the strong cross-flows that develop in the endwall region. The predictions showed that the jet trajectory is highly dependent on the local blowing ratio for the cooling holes. One of the most significant findings was a lack of endwall film-cooling along the region where two turbine vanes are mated. While this region typically has a gutter with some leakage flow, it is particularly important that there is cooler leakage flow present since it provides cooling to the regions where the endwall film-cooling does not.

Combining the slot and film-cooling flows provided the best overall coverage for the endwall, but the warm ring around the vane was still present until a higher flow rate through the film-cooling flows was introduced. The higher flow rate provided a higher momentum for the pressure side, film-cooling jets thereby allowing for a jet trajectory that approached the vane. One important finding was that there was a change in the secondary flows that developed for the combined film-cooling and slot flow studies as compared to the film-cooling alone and slot alone. This is important because this change in flow fields explained why the superposition method can not be used to predict the combined endwall film-cooling and slot cooling effectiveness levels. Moreover, using the superposition method resulted in an over-prediction of cooling results thereby over-predicting component life.

## **9.2 Analysis of Measurements**

Measurements of endwall adiabatic effectiveness were presented for an extensive test matrix combining both coolant from a flush slot and film-cooling from two distinct hole patterns. Slot flow without film-cooling was shown to adequately cool portions of the endwall while providing no benefit to the crucial vane-endwall junction both at the leading edge and along the pressure side. Film-cooling holes were shown to distribute coolant more evenly throughout the passage. Pattern #2, however, left a large uncooled streak down the center of the passage due to a provision for the gutter.

Film-cooling blowing ratio was shown to have a significant impact on cooling performance. The higher momentum flux associated with higher blowing allowed the coolant to penetrate to hard to cool areas at the leading edge and along the pressure side.

Cooling jets in high pressure areas at the leading edge and along the upstream portion of the pressure side showed a tendency to separate before impacting the vane, while jets in the downstream region penetrated to the vane without separation. The higher momentum jets were also able to overcome the sink effect of the slot flow avoiding being drawn into the center of the passage.

Predicted streamlines at 2% span with included slot flow and at the midspan were compared and superimposed on measurements of film-cooling effectiveness. A considerable deviation between the near-wall and midspan streamlines was observed and it was shown that the slot flow rate and near-wall effects must be considered when predicting film-coolant trajectory based on streamlines. As the slot flow rate was increased the influence of the slot became greater making inclusion of the slot flow even more critical. A method of identifying cooling regions was developed by examining the differences in flow angles between the near-wall fluid and the midspan. Areas of large deviation proved challenging to cool while areas of small deviation acted as sinks drawing coolant in.

The spatial superposition method was shown to over predict adiabatic effectiveness levels as well as mispredicting coolant trajectories in areas affected by the inclusion of slot flow as identified by the flow angle deviation method. The superposition method may be a useful tool for designers wanting to gain an idea of the combined effects of two cooling mechanisms, however, as long as the designer identifies areas where the flow field is altered by interaction of the cooling mechanisms and applies a factor of safety to cooling effectiveness predictions.

Finally, thermal field measurements from three cases were presented. Coolant was shown to become entrained in the passage vortex and transported towards the suction side. Including film-cooling intensified the passage vortex and distorted the coolant structure. Increased jet momentum led to a widening of the jets between the pressure and suction side.

### **9.3 Comparison of Predictions and Measurements**

Contours of adiabatic effectiveness were compared for eight cases consisting of slot cooling alone, film-cooling alone for the two film-cooling hole patterns, and slot

cooling combined with the film-cooling patterns. Computations were shown to be a valuable tool in aiding to locate film-cooling holes and predict coolant coverage. The coolant trajectories and footprint were generally well predicted while cooling effectiveness levels and thermal spreading were frequently under-predicted relative to the experiments. Minimum effectiveness levels were often lower than measured because the inlet profile was slightly cooler in the near-wall region rather than having a perfectly isothermal profile as mandated by the computations. Large, uncooled rings around the vanes for the cases with only slot flow were properly predicted as well as uncooled areas along the pressure side, at the leading edge, and in the center of pattern #2 when film-cooling was included. The pressure side, leading row holes were frequently more directed than predicted and stronger turning was seen along the upstream edge of the pressure side rows and in the exit region of the passage. Jet separation in the leading edge region and the upstream pressure side holes was also not well predicted.

#### **9.4 Recommendations for Future Study**

This study was performed to gain a greater understanding of slot and film-cooling trajectories and effectiveness and the interaction between the two cooling methods. Many possibilities exist for further study of these complex flows.

For this work traditional, round holes were used at a specific spacing with axial orientations. Fanned holes could be examined to lower the momentum of the jets and further diffuse the coolant. An optimization study could also be performed to determine optimal hole shape, number, spacing, injection angle, and compound angle.

In addition, two design philosophies were tested, one based on iso-velocity contours and the other on traditional axial rows. A new pattern could be designed based on streamline evaluation or other methods. Film-cooling holes could also be relocated or eliminated from the areas cooled by the slot flow.

Alternative slot configurations might also be evaluated. One potential configuration would be a partial slot only upstream of the vane leading edge. This may allow large, but imprecise, slot flow to cool the leading edge region while relying on discrete film holes to cool the specific trouble spots within the vane. Also, the film-coolant in this study was supplied from a common plenum, but a multiple plenum design

might be evaluated. This would allow more control over the quantity of coolant injected in specific areas which could lead to the prevention of jet separation in critical regions and the prevention of over-cooling in non-critical regions. In addition, this study was performed with a density near unity. During operation, a density ratio of 2:1 is not uncommon. The film-cooling effectiveness levels could be examined with the same mass flow rates, but the more realistic density ratio. This would alter the momentum flux ratios of the film-cooling jets.

Finally, the gutter flow effects should be considered. The gutter flow was not included in this study because the focus was on film-cooling, but the gutter flow is present in the engine and its cooling potential should be evaluated.

## References

- Barringer, M. D., Richard, O. T., Walter, J. P., Stitzel, S. M., and Thole, K. A., 2002, "Flow Field Simulations of a Gas Turbine Combustor," *Journal of Turbomachinery*, 124, pp. 508-516.
- Blair, M. F., 1974, "An Experimental Study of Heat Transfer and Film Cooling on Large-Scale Turbine Endwalls," *Journal of Heat Transfer*, pp. 524-529.
- Burd, S. W. and Simon, T. W., "Effects of Slot Bleed Injection over a Contoured Endwall on Nozzle Guide Vane Cooling Performance: Part I: Flow Field Measurements," 2000-GT-199.
- Burd, S. W., Satterness, C. J., and Simon, T. W., "Effects of Slot Bleed Injection over a Contoured Endwall on Nozzle Guide Vane Cooling Performance: Part II Thermal Measurements," 2000-GT-200.
- Cohen, H., Rogers, G.F.C., Saravanamuttoo, H.I.H, 2001, Gas Turbine Theory, Fifth Edition, Prentice Hall.
- Colban, W. F., Lethander, A. T., Thole, K. A., and Zess, G., 2002, "Combustor-Turbine Interface Studies: Part 2: Flow and Thermal Field Measurements," GT-2002-30527.
- Colban, W. F., Thole, K. A., and Zess, G., 2002, "Combustor-Turbine Interface Studies: Part 1: Endwall Measurements," GT-2002-30526.
- Fluent Inc., Version 6.0, 2002 (Fluent Inc: New Hampshire).
- Friedrichs, S., Hodson, H. P. and Dawes, W. N., 1996, "Distribution of Film-Cooling Effectiveness on a Turbine Endwall Measured Using the Ammonia and Diazo Technique," *Journal of Turbomachinery*, 118, pp. 613-621.
- Friedrichs, S., Hodson, H. P. and Dawes, W. N., 1997, "Aerodynamic Aspects of Endwall Film-Cooling," *Journal of Turbomachinery*, 119, pp. 786-793.
- Friedrichs, S., Hodson, H. P. and Dawes, W. N., 1999, "The Design of an Improved Endwall Film-Cooling Configuration," *Journal of Turbomachinery*, 121, pp. 772-780.
- Friedrichs, S., 1997, "Endwall Film-Cooling in Axial Flow Turbines," PhD Dissertation, Girton College.
- Granser, D. and Schulenberg, T., 1990, "Prediction and Measurement of Film Cooling Effectiveness for a First-Stage Turbine Vane Shroud," 90-GT-95.

Harasgama, S. P., and Burton, C. D., 1992, "Film Cooling Research on the Endwall of a Turbine Nozzle Guide Vane in a Short Duration Annular Cascade: Part 1—Experimental Technique and Results," *Journal of Turbomachinery*, 114, pp. 734-540.

Hermanson, K., and Thole, K.A., 2000, "Effect of Inlet Profiles on Endwall Secondary Flows," *Journal of Propulsion and Power*, 16, pp 286-296.

Hill, P., Peterson, C., 1992, Mechanics and Thermodynamics of Propulsion, Second Edition, Addison Wesley.

Hohlfeld, E.M., 2003, "Film Cooling Predictions Along the Tip and Platform of a Turbine Blade," Masters Thesis, Department of Mechanical Engineering, Virginia Polytechnic Institute and State University.

<http://www.aviation-history.com/engines/theory.htm>

[http://www.gepower.com/corporate/en\\_us/assets/gasturbines\\_heavy/prod/pdf/gasturbine\\_2002.pdf](http://www.gepower.com/corporate/en_us/assets/gasturbines_heavy/prod/pdf/gasturbine_2002.pdf)

Kang, M., Kohli, A., and Thole, K. A., 1999, "Heat Transfer And Flowfield Measurements In The Leading Edge Region of A Stator Vane Endwall," *Journal of Turbomachinery*, vol. 121, no. 3, pp. 558-568 (ASME Paper 98-GT-173).

Knost, D.K., Thole, K.A., "Computational Predictions of Endwall Film-Cooling for a First Stage Vane," GT-2003-38252.

Kost, F. and Nicklas, M., 2001, "Film-Cooled Turbine Endwall in a Transonic Flow Field: Part I – Aerodynamic Measurements," 2001-GT-0145.

Langston, L.S., 1980, "Crossflows in a Turbine Cascade Passage," *Journal of Engineering for Power*, vol. 102, pp. 866-874.

Mattingly, J.D., 1996, Elements of Gas Turbine Propulsion, McGraw Hill.

Moffat, R. J., 1988, "Describing the Uncertainties in Experimental Results," *Experimental Thermal and Fluid Science*, 1, pp. 3-17.

Nicklas, M., 2001, "Film-Cooled Turbine Endwall in a Transonic Flow Field: Part II – Heat Transfer and Film-Cooling Effectiveness Measurements," 2001-GT-0146.

Oke, R., Simon, T., Burd, S. W., Vahlberg, R., "Measurements in a Turbine Cascade Over a Contoured Endwall: Discrete Hole Injection of Bleed Flow," 2000-GT-214.

Oke, R., Simon, T., Shih, T. Zhu, B., Lin, Y. L., Chyu, M. "Measurements Over a Film-Cooled, Contoured Endwall with Various Coolant Injection Rates," 2001-GT-140.

Radomsky, R. W., and Thole, K. A., 2000, "Flowfield Measurements for a Highly Turbulent Flow in a Stator Vane Passage," *Journal of Turbomachinery*, 122, pp. 255-262.

Radomsky, R., and Thole, K. A., 2000, "High Freestream Turbulence Effects in the Endwall Leading Edge Region," *Journal of Turbomachinery*, vol. 122, pp. 699-708 (ASME Paper 2000-GT-201).

Radomsky, R.W., 2000, "High Freestream Turbulence Studies on a Scaled-Up Stator Vane," PhD Dissertation, Department of Mechanical Engineering, University of Wisconsin - Madison.

Roy, R. P., Squires, K. D., Gerendas, M., Song, S., Howe, W. J., and Ansari, A., "Flow and Heat Transfer at the Hub Endwall of Inlet Vane Passages-Experiments and Simulations," 2000-GT-198.

Sellers, J.P., 1963, "Gaseous Film Cooling with Multiple Injection Stations," *AIAA Journal*, vol. 1, pp. 2154-2156.

Thole, K.A., Sinha, A.K., Bogard, D.G., and Crawford, M.E., 1992, "Mean Temperature Measurements of Jets with a Crossflow for Gas Turbine Film Cooling Application," *Rotating Machinery Transport Phenomena*, J.H. Kim and W.J. Yang, ed., Hemisphere Pub. Corp., New York.

Vakil, S.S., 2002, "Flow and Thermal Field Measurements in a Combustor Simulator Relevant to a Gas Turbine Aero-Engine," Masters Thesis, Department of Mechanical Engineering, Virginia Polytechnic Institute and State University.

Zhang, L., Moon, H.K., "Turbine Nozzle Endwall Inlet Film Cooling – The Effect of a Back-Facing Step," GT-20030-38319.



**Table A.1 Steady State Check**

Time	3:39	3:48	4:05	4:23
Tinf	52.95	52.8	52.88	52.95
T1	45.92	45.87	45.98	45.97
T2	39.65	39.65	39.75	39.74
T4	42.03	42	42.16	42.08
T5	28.69	28.74	28.93	28.93
T9	36.72	36.82	37.01	36.82
TS5	37.23	37.19	37.3	37.2
THPM	14.15	14.13	14.12	14.09
TSPM	14.87	14.86	14.86	14.86
TempDiff	38.8	38.67	38.76	38.86

*Visual Basic Codes to Calculate Driving Pressure*

Option Explicit

---

```
Function fcnDeltaPCalc(PassNum As Double, Target As Double, PDynIn,
DensRatio As Double, AreaRatio As Double)
Dim Pdin As Double, Count As Double
Dim P1 As Double, P2 As Double, PSearch As Double
Dim Pa As Double, DeltaPa As Double, MIna As Double, Mdota As Double,
Cda As Double, Errora As Double
Dim Pb As Double, DeltaPb As Double, MInb As Double, Mdotb As Double,
Cdb As Double, Errorb As Double
Dim tol As Double, Delta As Double, Error As Double

Target = Target / 100
'Initialize Search Range
P1 = 0 'Lower Bound (Pa)
P2 = 250 'Upper Bound (Pa)

Delta = 0.001
tol = 0.000001
Count = 1
Do
    If Count > 1000 Then
        MsgBox ("Computation has exceeded maximum number of iterations")
        Exit Do
    End If
    PSearch = (P2 - P1) / 2 + P1
    ' Calculate for Value just below search Pt
    Pa = PSearch - Delta
    Cda = fcnCd(PassNum, Pa)
    ' DeltaPa = (Target / Cda) * (Target / Cda) * Pdin * DensRatio *
AreaRatio * AreaRatio
    MIna = Sqr(DensRatio * (Pa / PDynIn))
    Mdota = MIna * AreaRatio * Cda
```

```

Errora = Mdota - Target

' Calculate for Value just above search Pt
Pb = PSearch + Delta
Cdb = fcnCd(PassNum, Pb)
MInb = Sqr(DensRatio * (Pb / PDynIn))
Mdotb = MInb * AreaRatio * Cdb
Errorb = Mdotb - Target

' Determine Interval to Eliminate
If Abs(Errora) > Abs(Errorb) Then
    'Throw out the left half of the search range
    P1 = Pa
    Error = Errora
Else
    'Throw out the right half of the search range
    P2 = Pb
    Error = Errorb
End If
Count = Count + 1
Loop While Abs(Error) > tol
fcnDeltaPCalc = (Pb - Pa) / 2 + Pa
End Function

```

---

```

Function fcnCd(PassNum, DeltaP As Double)
If PassNum = 1 Then
    fcnCd = -0.058 * Sqr(DeltaP) + 1.363
Else
    fcnCd = -0.0174 * Sqr(DeltaP) + 0.9448
End If
End Function

```

---

```

Sub ClearPlenumData()
'
' ClearPlenumData Macro
' Macro recorded 1/30/2003 by dknostr
'
'
    Range("D114:F120").Select
    Selection.ClearContents
    Range("D114").Select
End Sub

```

## Appendix B: Code for Program Used to Align Images in Global Coordinates

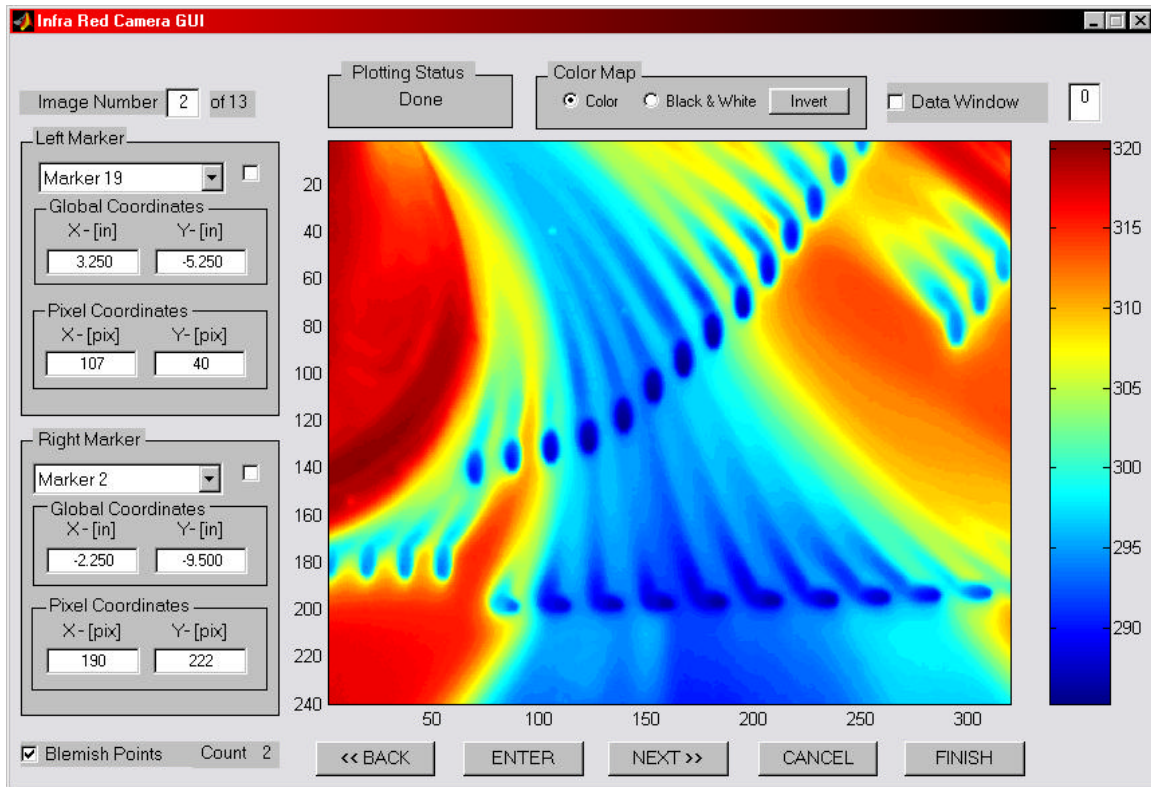


**Figure B.1** Graphical User Interface to Program for Image Alignment

```
% function IRLoad
% Calling Script for Image Processing Program
clear all
tic
close all
clc

% Input Dialog Box to gather image information
title = 'Image Data Input';
prompt = {'Number of Image Locations:', 'Number of Rows in
Image:', 'Number of Columns in Image:', ...
          'Number of Points to Skip when Sampling:', 'Masking Radius in
Pixels:', 'Smoothing Radius in Pixels'};
lines = 1;
default = {'13', '240', '320', '1', '3', '0.8'};
answers = inputdlg(prompt, title, lines, default);

if size(answers, 1) == 0
    clear all
    return
end

% Global variables to store X-loc, Y-loc, and Image Data
```

```

global AvgImage MarkerData Skip PixRad SmoothRad

NumPics = fix(str2num(answers{1}));
NumRows = fix(str2num(answers{2}));
NumCols = fix(str2num(answers{3}));
Skip = fix(str2num(answers{4}));
PixRad = fix(str2num(answers{5}));
SmoothRad = str2num(answers{6});
clear title prompt lines default answers

% Initialize Image Data cube
AvgImage = zeros(NumRows,NumCols,NumPics);

% Average images at each location and load into data cube
disp('Loading Images')
for i = 1:NumPics
    AvgImage(:, :, i) = ImageAverager(i);
end
clear i

% Initialize structure array to contain data about Markers and
Blemishes
[MarkerData(1:NumPics).LMlbl] = deal(1);
[MarkerData(1:NumPics).LMGlobX] = deal(0);
[MarkerData(1:NumPics).LMGlobY] = deal(0);
[MarkerData(1:NumPics).LMPixX] = deal(0);
[MarkerData(1:NumPics).LMPixY] = deal(0);
[MarkerData(1:NumPics).RMlbl] = deal(1);
[MarkerData(1:NumPics).RMGlobX] = deal(0);
[MarkerData(1:NumPics).RMGlobY] = deal(0);
[MarkerData(1:NumPics).RMPixX] = deal(0);
[MarkerData(1:NumPics).RMPixY] = deal(0);
[MarkerData(1:NumPics).BlemPixX] = deal([]);
[MarkerData(1:NumPics).BlemPixY] = deal([]);
[MarkerData(1:NumPics).Window] = deal([1 1;NumRows NumCols]);

% Run the GUI initialization program
disp('Loading GUI')
h_fig = IRGUI_3;
t = toc;
disp(['Time to initialize GUI: ', num2str(t), ' seconds'])
clear t NumPics

```

---

```

function AvgMat = ImageAverager(k)
% Function of load and average images

%===== Loop to load all pics =====%
for n=1:5
    FileLoad = ['load L',int2str(k),'_',int2str(n),''];
    eval(FileLoad)
    ARRAY = ['Mat(:, :, n) = L',int2str(k),'_',int2str(n),''];
    eval(ARRAY)

```

```

Clear = ['clear L',int2str(k),'_',int2str(n),'
L',int2str(k),'_',int2str(n),'_DateTime
L',int2str(k),'_',int2str(n),'_FrameInfo
L',int2str(k),'_',int2str(n),'_ObjectParam
L',int2str(k),'_',int2str(n),'_Scaling'];
    eval(Clear)
end

AvgMat = mean(Mat,3);

```

---

```

function varargout = IRGUI_3(varargin)
% IRGUI_3 Application M-file for IRGUI_3.fig
%   FIG = IRGUI_3 launch IRGUI_3 GUI.
%   IRGUI_3('callback_name', ...) invoke the named callback.

% Last Modified by GUIDE v2.0 06-Mar-2003 16:15:11

global AvgImage GlobMarkData

if nargin == 0 % LAUNCH GUI

    fig = openfig(mfilename,'reuse');

    % Generate a structure of handles to pass to callbacks, and store
it.
    handles = guihandles(fig);
    guidata(fig, handles);

    if nargout > 0
        varargout{1} = fig;
    end

%   MarkLbels = {'Other';'Marker 1';'Marker 2';'Marker 3';'Marker
4';'Marker 5';'Marker 6';'Marker 7';'Marker 8';'Marker 9';'Marker 10';
...
%               'Marker 11';'Marker 12';'Marker 13';'Marker 14';'Marker
15';'Marker 16';'Marker 17';'Marker 18';'Marker 19';'Marker 20'};
%   MarkXY = [[0:length(MarkLbels)-1]' [0:length(MarkLbels)-1]'];

    load DMarkerData
    MarkLbels = DMarkerData{1,1};
    MarkXY = DMarkerData{1,2};

    set([handles.cboLeftMark;handles.cboRightMark],'String',MarkLbels)
    set([handles.edLMGlobX;handles.edRMGlobX],'UserData',MarkXY(:,1))
    set([handles.edLMGlobY;handles.edRMGlobY],'UserData',MarkXY(:,2))
    set(handles.txtImageCount,'String',['of
',int2str(size(AvgImage,3))])

    % Contour plot the first Image
    m = jet(128);
    [C,h_con,Cf] = contourf(AvgImage(:,:,1),128);

```

```

set(h_con,'LineStyle','none')
set(gca,'YDir','reverse','DrawMode','fast')
colormap(m)
colorbar
drawnow
set(handles.txtStatus,'String','Done')

% Initialize Pixel clicking settings

set(gcf,'WindowButtonDownFcn','IRGUI_3(''Image_Click'',gcbo,[],guidata(
gcbo))')
set(gca,'UserData','Left') % Initialize Marker to left for image
clicking purposes
set(handles.chkLeftMark,'value',1)

elseif ischar(varargin{1}) % INVOKE NAMED SUBFUNCTION OR CALLBACK

    try
        [varargout{1:nargout}] = feval(varargin{:}); % FEVAL
switchyard
    catch
        disp(lasterr);
    end

end

%| ABOUT CALLBACKS:
%| GUIDE automatically appends subfunction prototypes to this file, and
%| sets objects' callback properties to call them through the FEVAL
%| switchyard above. This comment describes that mechanism.
%|
%| Each callback subfunction declaration has the following form:
%| <SUBFUNCTION_NAME>(H, EVENTDATA, HANDLES, VARARGIN)
%|
%| The subfunction name is composed using the object's Tag and the
%| callback type separated by '_', e.g. 'slider2_Callback',
%| 'figure1_CloseRequestFcn', 'axis1_ButtndownFcn'.
%|
%| H is the callback object's handle (obtained using GCBO).
%|
%| EVENTDATA is empty, but reserved for future use.
%|
%| HANDLES is a structure containing handles of components in GUI using
%| tags as fieldnames, e.g. handles.figure1, handles.slider2. This
%| structure is created at GUI startup using GUIHANDLES and stored in
%| the figure's application data using GUIDATA. A copy of the structure
%| is passed to each callback. You can store additional information in
%| this structure at GUI startup, and you can change the structure
%| during callbacks. Call guidata(h, handles) after changing your
%| copy to replace the stored original so that subsequent callbacks see
%| the updates. Type "help guihandles" and "help guidata" for more
%| information.

```

```

%|
%| VARARGIN contains any extra arguments you have passed to the
%| callback. Specify the extra arguments by editing the callback
%| property in the inspector. By default, GUIDE sets the property to:
%| <MFILENAME>(<SUBFUNCTION_NAME>', gcbo, [], guidata(gcbo))
%| Add any extra arguments after the last argument, before the final
%| closing parenthesis.

% -----
function varargout = Image_Click(h, eventdata, handles, varargin)
global AvgImage MarkerData
p = round(get(gca,'CurrentPoint'));
% Test to see if figure was clicked within axes
if p(1,1) >= 1 & p(1,1) <= size(AvgImage,2)
    if p(1,2) >= 1 & p(1,2) <= size(AvgImage,1)
        MarkerLoc = get(gca,'UserData');
        switch MarkerLoc
            case 'Left'
                set(handles.edLMPixX,'String',num2str(p(1,1)))
                set(handles.edLMPixY,'String',num2str(p(1,2)))
                % switch to Right Marker Pixel Data
                set(gca,'UserData','Right')
                off = [handles.chkLeftMark;handles.chkBlemish];
                mutual_exclude(off)
                set(handles.chkRightMark,'value',1)
            case 'Right'
                set(handles.edRMPixX,'String',num2str(p(1,1)))
                set(handles.edRMPixY,'String',num2str(p(1,2)))
                % switch to Blemish Pixel Data
                set(gca,'UserData','Blemish')
                off = [handles.chkRightMark;handles.chkLeftMark];
                mutual_exclude(off)
                set(handles.chkBlemish,'value',1)
            case 'Window'
                pt1 = p;
                rbbox;
                pt2 = round(get(gca,'CurrentPoint'));
                ImageNum = str2num(get(handles.edImageNum,'String'));
                MarkerData(ImageNum).Window = [pt1(1,2:-1:1);pt2(1,2:-
1:1)];
                otherwise % Blemish case
                    ImageNum = str2num(get(handles.edImageNum,'String'));
                    MarkerData(ImageNum).BlemPixX =
[MarkerData(ImageNum).BlemPixX p(1,1)];
                    MarkerData(ImageNum).BlemPixY =
[MarkerData(ImageNum).BlemPixY p(1,2)];
                    Count = str2num(get(handles.txtBlemCount,'string'));
                    set(handles.txtBlemCount,'String',int2str(Count+1))
                end
            end
        end
    end
end
end

```

```

% -----
function varargout = edImageNum_Callback(h, eventdata, handles,
varargin)
% Stub for Callback of the uicontrol handles.edImageNum.
global AvgImage MarkerData
ImageNum = str2num(get(handles.edImageNum,'String'));
if ImageNum < 1
    ImageNum = 1;
    set(h,'String',ImageNum)
elseif ImageNum > 14
    ImageNum = 14;
    set(h,'String',ImageNum)
end

set(handles.txtStatus,'String','Working ...')
% Contour Plot and turn off lines
[C,h_con,Cf] = contourf(AvgImage(:, :, ImageNum),128);
set(h_con,'LineStyle','none')
set(gca,'YDir','reverse','DrawMode','fast')

% Set Left Marker Data
set(handles.cboLeftMark,'Value',MarkerData(ImageNum).LMlbl)
set(handles.edLMGlobX,'String',num2str(MarkerData(ImageNum).LMGlobX,'%6
.3f'))
set(handles.edLMGlobY,'String',num2str(MarkerData(ImageNum).LMGlobY,'%6
.3f'))
set(handles.edLMPixX,'String',num2str(MarkerData(ImageNum).LMPixX))
set(handles.edLMPixY,'String',num2str(MarkerData(ImageNum).LMPixY))
% Set Right Marker Data
set(handles.cboRightMark,'Value',MarkerData(ImageNum).RMLbl)
set(handles.edRMGlobX,'String',num2str(MarkerData(ImageNum).RMGlobX,'%6
.3f'))
set(handles.edRMGlobY,'String',num2str(MarkerData(ImageNum).RMGlobY,'%6
.3f'))
set(handles.edRMPixX,'String',num2str(MarkerData(ImageNum).RMPixX))
set(handles.edRMPixY,'String',num2str(MarkerData(ImageNum).RMPixY))
% Set Blemish Counter
Count = size(MarkerData(ImageNum).BlemPixX,2);
set(handles.txtBlemCount,'String',int2str(Count))

colorbar
drawnow
set(handles.txtStatus,'String','Done')
set(gca,'UserData','Left')
IRGUI_3('chkLeftMark_Callback',gcbo,[],guidata(gcbo));

% -----
function varargout = cboLeftMark_Callback(h, eventdata, handles,
varargin)
% Stub for Callback of the uicontrol handles.cboLeftMark.
MarkNum = get(h,'Value');

```

```

MarkXY = [get(handles.edLMGglobX,'UserData')
get(handles.edLMGglobY,'UserData')];
set(handles.edLMGglobX,'String',num2str(MarkXY(MarkNum,1),'%6.3f'))
set(handles.edLMGglobY,'String',num2str(MarkXY(MarkNum,2),'%6.3f'))

% -----
function varargout = cboRightMark_Callback(h, eventdata, handles,
varargin)
% Stub for Callback of the uicontrol handles.cboLeftMark.
MarkNum = get(h,'Value');
MarkXY = [get(handles.edRMGglobX,'UserData')
get(handles.edRMGglobY,'UserData')];
set(handles.edRMGglobX,'String',num2str(MarkXY(MarkNum,1),'%6.3f'))
set(handles.edRMGglobY,'String',num2str(MarkXY(MarkNum,2),'%6.3f'))

% -----
function varargout = edLMGglobX_Callback(h, eventdata, handles,
varargin)
% Stub for Callback of the uicontrol handles.edLMGglobX.
disp('edLMGglobX Callback not implemented yet.')

% -----
function varargout = edLMGglobY_Callback(h, eventdata, handles,
varargin)
% Stub for Callback of the uicontrol handles.edLMGglobY.
disp('edLMGglobY Callback not implemented yet.')

% -----
function varargout = edLMPixX_Callback(h, eventdata, handles, varargin)
% Stub for Callback of the uicontrol handles.edLMPixX.
disp('edLMPixX Callback not implemented yet.')

% -----
function varargout = edLMPixY_Callback(h, eventdata, handles, varargin)
% Stub for Callback of the uicontrol handles.edLMPixY.
disp('edLMPixY Callback not implemented yet.')

% -----
function varargout = chkBlemish_Callback(h, eventdata, handles,
varargin)
% Stub for Callback of the uicontrol handles.chkBlemish.
off = [handles.chkRightMark;handles.chkLeftMark;handles.chkDataWindow];
mutual_exclude(off)
% if LeftMark check box was already on keep it marked
if get(h,'value') == 1
    set(gca,'UserData','Blemish')
else
    set(h,'value',1)

```

```

end

% -----
function mutual_exclude(off)
set(off, 'Value', 0)

% -----
function varargout = radiobutton_Color(h, eventdata, handles, varargin)
% Stub for Callback of the uicontrol handles.radiobutton1.
% h_rad = handles.radiobutton1
off = [handles.radBlackWhite];
mutual_exclude(off)
if get(h, 'value') == 1
    m = jet(32);
    % Check to see if colormap is inverted
    if get(handles.togInvert, 'Value') == 1
        m = flipud(m);
    end
    set(handles.txtStatus, 'String', 'Working ...')
    set(gcf, 'ColorMap', m);
    colorbar
    drawnow
    set(handles.txtStatus, 'String', 'Done')
else % if Radio button was already on keep it marked
    set(h, 'value', 1)
end

% -----
function varargout = radiobutton_BW(h, eventdata, handles, varargin)
% Stub for Callback of the uicontrol handles.radiobutton1.
% h_rad = handles.radiobutton1
off = [handles.radColor];
mutual_exclude(off)
if get(h, 'value') == 1
    m = bone(32);
    % Check to see if colormap is inverted
    if get(handles.togInvert, 'Value') == 1
        m = flipud(m);
    end
    set(handles.txtStatus, 'String', 'Working ...')
    set(gcf, 'ColorMap', m);
    colorbar
    drawnow
    set(handles.txtStatus, 'String', 'Done')
else % if Radio button was already on keep it marked
    set(h, 'value', 1)
end

% -----
function varargout = togInvert_Callback(h, eventdata, handles,
varargout)

```

```

% Stub for Callback of the uicontrol handles.togInvert.
m = flipud(get(gcf,'ColorMap'));
set(handles.txtStatus,'String','Working ...')
set(gcf,'ColorMap',m);
colorbar
drawnow
set(handles.txtStatus,'String','Done')

% -----
function varargout = cmdBack_Callback(h, eventdata, handles, varargin)
% Stub for Callback of the uicontrol handles.cmbBack.
ImageNum = str2num(get(handles.edImageNum,'String'));
Write_Marker_Data(ImageNum, guidata(gcbo))

% Proceed to previous image
BackNum = ImageNum - 1;
if BackNum >= 1
    set(handles.edImageNum,'String',BackNum)
    IRGUI_3('edImageNum_Callback',gcbo,[],guidata(gcbo));
    set(gca,'UserData','Left')
end

% -----
function varargout = cmdNext_Callback(h, eventdata, handles, varargin)
% Stub for Callback of the uicontrol handles.cmdNext.
ImageNum = str2num(get(handles.edImageNum,'String'));
Write_Marker_Data(ImageNum, guidata(gcbo))

% Proceed to next Image
NextNum = ImageNum + 1;
if NextNum <= 14
    set(handles.edImageNum,'String',NextNum)
    IRGUI_3('edImageNum_Callback',gcbo,[],guidata(gcbo));
    set(gca,'UserData','Left')
end

% -----
function varargout = cmdEnter_Callback(h, eventdata, handles, varargin)
% Stub for Callback of the uicontrol handles.cmbBack.
ImageNum = str2num(get(handles.edImageNum,'String'));
Write_Marker_Data(ImageNum, guidata(gcbo))

% -----
function varargout = cmdCancel_Callback(h, eventdata, handles,
varargin)
% Stub for Callback of the uicontrol handles.cmdCancel.
close 'Infra Red Camera GUI'

```

```

% -----
function varargout = cmdFinish_Callback(h, eventdata, handles,
varargin)
% Stub for Callback of the uicontrol handles.cmdFinish.
ImageNum = str2num(get(handles.edImageNum, 'String'));
Write_Marker_Data(ImageNum, guidata(gcbo))
Pass = get(handles.edPassage, 'String');
MarkerLocs = [get(handles.edLMGlobX, 'UserData')
get(handles.edLMGlobY, 'UserData')];
close 'Infra Red Camera GUI'
IRCalc(MarkerLocs, Pass)

% -----
function varargout = Write_Marker_Data(ImageNum, handles)
global MarkerData
% Write Left Marker Data to Matrix
MarkerData(ImageNum).LMlbl = get(handles.cboLeftMark, 'Value');
MarkerData(ImageNum).LMGlobX =
str2num(get(handles.edLMGlobX, 'String'));
MarkerData(ImageNum).LMGlobY =
str2num(get(handles.edLMGlobY, 'String'));
MarkerData(ImageNum).LMPixX =
round(str2num(get(handles.edLMPixX, 'String')));
MarkerData(ImageNum).LMPixY =
round(str2num(get(handles.edLMPixY, 'String')));

% Write Right Marker Data to Matrix
MarkerData(ImageNum).RMlbl = get(handles.cboRightMark, 'Value');
MarkerData(ImageNum).RMGlobX =
str2num(get(handles.edRMGlobX, 'String'));
MarkerData(ImageNum).RMGlobY =
str2num(get(handles.edRMGlobY, 'String'));
MarkerData(ImageNum).RMPixX =
round(str2num(get(handles.edRMPixX, 'String')));
MarkerData(ImageNum).RMPixY =
round(str2num(get(handles.edRMPixY, 'String')));

% -----
function varargout = chkLeftMark_Callback(h, eventdata, handles,
varargin)
% Stub for Callback of the uicontrol handles.chkLeftMark.
off = [handles.chkRightMark; handles.chkBlemish; handles.chkDataWindow];
h_chk = handles.chkLeftMark;
mutual_exclude(off)
% if LeftMark check box was already on keep it marked
if get(h_chk, 'value') == 1
    set(gca, 'UserData', 'Left')
else
    set(h_chk, 'value', 1)
end

```

```

% -----
function varargout = chkRightMark_Callback(h, eventdata, handles,
varargin)
% Stub for Callback of the uicontrol handles.chkRightMark.
off = [handles.chkLeftMark;handles.chkBlemish;handles.chkDataWindow];
h_chk = handles.chkRightMark;
mutual_exclude(off)
% if RightMark check box was already on keep it marked
if get(h_chk,'value') == 1
    set(gca,'UserData','Right')
else
    set(h_chk,'value',1)
end

% -----
function varargout = chkDataWindow_Callback(h, eventdata, handles,
varargin)
off = [handles.chkLeftMark;handles.chkRightMark;handles.chkBlemish];
mutual_exclude(off)
% if LeftMark check box was already on keep it marked
if get(h,'value') == 1
    set(gca,'UserData','Window')
else
    set(h,'value',1)
end

% -----
function varargout = edPassage_Callback(h, eventdata, handles,
varargin)
% Stub for Callback of the uicontrol handles.edit10.
disp('edit10 Callback not implemented yet.')


---



function IRCalc(MarkerLocs, Pass)
% Calling Function for Calculation and Plotting Routines
global AvgImage MarkerData Skip PixRad
[Data,MarkCheck,Scale] = IRImageOrient(MarkerLocs, Pass);

SmoothData = IRSmooth(Data,Scale);

if nargin == 1
    Pass = '0';
end

tic
disp('Writing Data Files ...')
switch Pass
case {'1','2'}

```

```

        save PassIRImageData
        save('PassSmoothData.dat','SmoothData','-ASCII','-DOUBLE','-TABS')
    otherwise
        save IRImageData
        save('SmoothData.dat','SmoothData','-ASCII','-DOUBLE','-TABS')
    end
    t = toc;
    disp(['Time to write data: ',num2str(t),' seconds'])

    ContourAndPatch(SmoothData);

```

---

```

function [Data,MarkCheck,Scale] = IRImageOrient(MarkerLocs, Pass)
% Function to perform image transformations with transition matrix
tic
disp('Performing Image Transformations...')
global AvgImage MarkerData Skip PixRad
s = size(AvgImage);
% Generate X and Y matrices. Y is reversed in order to increase with
% the global Y axis. All images are intially assumed to be aligned
% with the bottom edge along the global X axis and left edge along
% the global Y axis
[X Y Z] = meshgrid(1:s(2),s(1):-1:1,1:s(3));
Z = 0*Z;
% Delete the "other" marker location row
MarkerLocs(1,:) = [];

% Initialize X, Y, and Z Global Matrices and Blemish Pt Matrix
XG = zeros(size(AvgImage)); YG = zeros(size(AvgImage)); ZG =
zeros(size(AvgImage));
BlemPts = []; Data = [];
% for i = 1:s(3)

switch Pass
case '1'
    Images = [1 2 3 10 11 12 13];
case '2'
    Images = 3:8;
otherwise
    Images = 1:s(3);
end

for i = Images
    % Vectors containing x and y data for Left(1) and Right(2) Marker
    Glob1 = [MarkerData(i).LMGlobX MarkerData(i).LMGlobY]';
    Glob2 = [MarkerData(i).RMGlobX MarkerData(i).RMGlobY]';
    Pix1 = [MarkerData(i).LMPixX MarkerData(i).LMPixY]';
    Pix2 = [MarkerData(i).RMPixX MarkerData(i).RMPixY]';

    % Pixel location
    BlemPix = [MarkerData(i).BlemPixX' MarkerData(i).BlemPixY'];

    % Calculate local reference distances and scaling

```

```

RefPix = sqrt((Pix2(1)-Pix1(1))^2 + (Pix2(2)-Pix1(2))^2);
DeltaX = Glob2(1) - Glob1(1);
DeltaY = Glob2(2) - Glob1(2);
RefDist = sqrt((Glob2(1)-Glob1(1))^2 + (Glob2(2)-Glob1(2))^2);
Scale(i) = RefDist/RefPix; % inches/pixel

% Shift Pixel indices so that 0,0 is at Marker 1
X(:, :, i) = X(:, :, i) - X(1, Pix1(1), i);
Y(:, :, i) = Y(:, :, i) - Y(Pix1(2), 1, i);

% Scale Local coordinates from Pixels to inches
X(:, :, i) = X(:, :, i)*Scale(i);
Y(:, :, i) = Y(:, :, i)*Scale(i);

% Develop transformation Matrix to go from rotated local
coordinates to system aligned with picture
% 1 - Coordinate System aligned with image
% 2 - Coordinate System in image with x aligned along Markers
% G - Global Coordinate System

% Vector from Left Marker to Right marker
Vector_L = [X(Pix2(2), Pix2(1), i) Y(Pix2(2), Pix2(1), i) 0]' -
[X(Pix1(2), Pix1(1), i) Y(Pix1(2), Pix1(1), i) 0]';
% Normalize to unit vector
x_2 = Vector_L/sqrt(sum(Vector_L.^2));
z_2 = [0 0 1]';
% Unit y vector in image coordinates where x lies along line
between markers
y_2 = cross(z_2, x_2);

% Transformation matrix from 1 to 2 is the inverse of T from 2 to 1
which is
% the transpose for a rotation matrix
T1_2 = inv([x_2 y_2 z_2]);

% Vectors in the Global coordinate system from origin to Marker
locations
M1_G = [Glob1(1) Glob1(2) 0]';
M2_G = [Glob2(1) Glob2(2) 0]';
% Vector from Left to Right Marker expressed in Global Units
Vector_G = M2_G - M1_G;
% Normalize to unit vector
x_G = Vector_G/sqrt(sum(Vector_G.^2));
z_G = [0 0 1]';
% Unit y vector in global coordinates
y_G = cross(z_G, x_G);
T2_G = [x_G y_G z_G];
T1_G = T2_G*T1_2;

% Rotate the Coordinates Matrices and offset
XG(:, :, i) = T1_G(1,1)*X(:, :, i) + T1_G(1,2)*Y(:, :, i) +
T1_G(1,3)*Z(:, :, i) + Glob1(1);
YG(:, :, i) = T1_G(2,1)*X(:, :, i) + T1_G(2,2)*Y(:, :, i) +

```

```

T1_G(2,3)*Z(:, :, i) + Glob1(2);
    ZG(:, :, i) = T1_G(3,1)*X(:, :, i) + T1_G(3,2)*Y(:, :, i) +
T1_G(3,3)*Z(:, :, i) + 0;

    % Vector of marker locations after rotation and translation
    MarkCheck(:, :, i) = [XG(Pix1(2),Pix1(1),i) YG(Pix1(2),Pix1(1),i)
ZG(Pix1(2),Pix1(1),i); ...
    XG(Pix2(2),Pix2(1),i) YG(Pix2(2),Pix2(1),i)
ZG(Pix2(2),Pix2(1),i)];
    j = 1;

    % Sample Image
    Rows = MarkerData(i).Window(:,1);
    Cols = MarkerData(i).Window(:,2);
    Xpts = XG(Rows(1):Skip:Rows(2),Cols(1):Skip:Cols(2),i);
    Ypts = YG(Rows(1):Skip:Rows(2),Cols(1):Skip:Cols(2),i);
    Tpts = AvgImage(Rows(1):Skip:Rows(2),Cols(1):Skip:Cols(2),i);
    ImageData = [Xpts(:) Ypts(:) Tpts(:)];
    Data = [Data;ImageData];
    while j <= size(BlemPix,1)
        BlemPts = [BlemPts;XG(BlemPix(j,2),BlemPix(j,1),i)'
YG(BlemPix(j,2),BlemPix(j,1),i)'];
        j = j + 1;
    end
end
clear X Y Z i j BlemPix DeltaPixX DeltaPixY DeltaX DeltaY Glob1 Glob2
M1_G M2_G Pix1 Pix2 RefDist RefPix ...
    ScaleX ScaleY T1_2 T2_G T1_G Vector_G Vector_L s x_2 x_G y_2
y_G z_2 z_G

MaskPts = [MarkerLocs;BlemPts];
% Convert blemish radius from pixels to inches and delete all chosen
points within the Blemish radius
Radius = PixRad*mean(Scale);
for i = 1:size(MaskPts,1);
    Dist = sqrt((Data(:,1)-MaskPts(i,1)).^2 + (Data(:,2)-
MaskPts(i,2)).^2);
    Ind = find(Dist <= Radius);
    Data(Ind,:) = [];
end
t = toc;
disp(['Time to compute image transformations: ',num2str(t),'
seconds']);

```

---

```

function SmoothData = IRSmooth(Data,Scale)
% This function is only used to convert to metric units
% Loop through pts and average all points that fall with in search
radius of each point
tic
global SmoothRad
% Smooth loop turned off because of time. Smoothing performed by
griddata

```

```

% Radius = SmoothRad*mean(Scale);
% j = 1; k = 0; SmoothData = [];
% disp('Beginning smoothing process')
% for i = 1:size(Data,1);
%     CurrentPt = Data(i,:);
%     Dist = sqrt((Data(:,1)-CurrentPt(1)).^2 + (Data(:,2)-
CurrentPt(2)).^2);
%     Ind = find(Dist <= Radius);
%     if length(Ind) > 1 % One pt will be the current point
%         Avg = mean(Data(Ind,3));
%         SmoothData(j,:) = [CurrentPt(1:2) Avg];
%         k = k + 1;
%     else
%         SmoothData(j,:) = [CurrentPt];
%     end
%     j = j + 1;
% end
SmoothData = Data;
t = toc;
% disp([int2str(k),' of ',int2str(size(Data,1)),' points were smoothed
in ',num2str(t),' seconds.'])
SmoothData(:,1:2) = SmoothData(:,1:2)*0.0254;
% Plot Data Pt locations
plot(SmoothData(:,1),SmoothData(:,2),'.'); axis equal

```

---

```

function ContourAndPatch(SmoothData)
% Function to contour temperature data and see if images are in place
tic
% sample data for faster plotting
SubData = SmoothData(1:7:end,:);
xv = linspace(min(SubData(:,1)),max(SubData(:,1)),250);
yv = linspace(min(SubData(:,2)),max(SubData(:,2)),1000);
disp('Mapping Data...')
[XG,YG,TG] = griddata(SubData(:,1),SubData(:,2),SubData(:,3),xv,yv');
disp('Contouring Data...')
figure
[Cf,h,C] = contourf(XG,YG,TG,20); axis equal tight
set(h,'LineStyle','none')
m = jet(20);
colormap(m)
load VaneXY
load SlotXY
h(1) = patch(VaneXY(:,1),VaneXY(:,2),[0.7 0.7 0.7]);
h(2) = patch(VaneXY(:,1),VaneXY(:,2)+0.457,[0.7 0.7 0.7]);
h(3) = patch(VaneXY(:,1),VaneXY(:,2)-0.457,[0.7 0.7 0.7]);
h(4) = patch(SlotXY(:,1),SlotXY(:,2), [0.7 0.7 0.7]);
set(h,'LineStyle','none')
t = toc;
disp(['Time to grid and contour data: ',num2str(t),' seconds'])

```

## Appendix C: Visual Basic Code for Secondary Flow Calculations

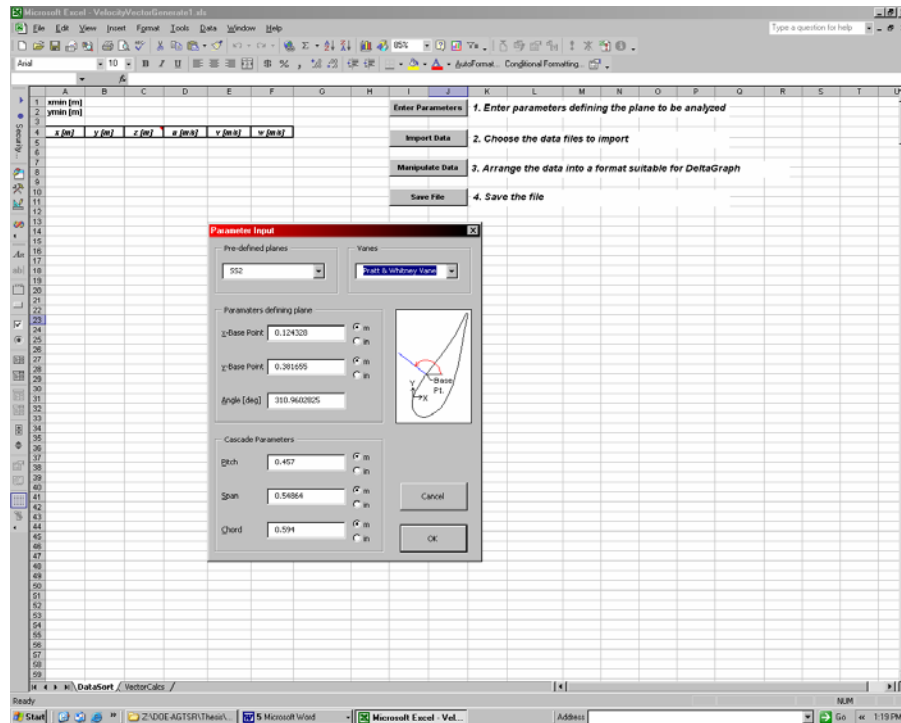


Figure C.1 The “Enter Parameters” button opens a GUI to input plane data to the spreadsheet.

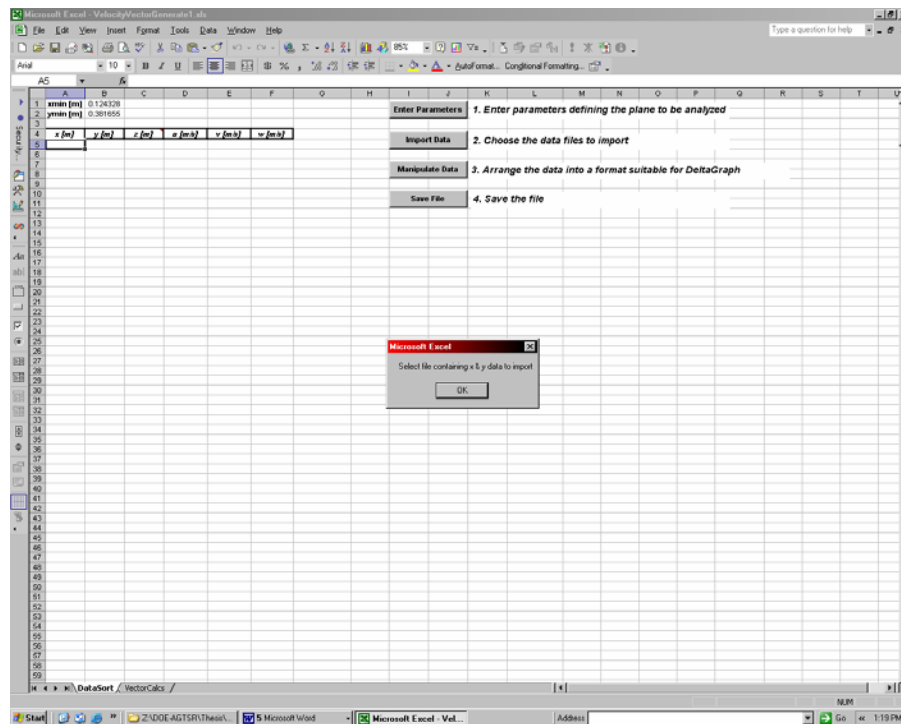


Figure C.2 The “Import Data” button runs the Text File Import Wizard.

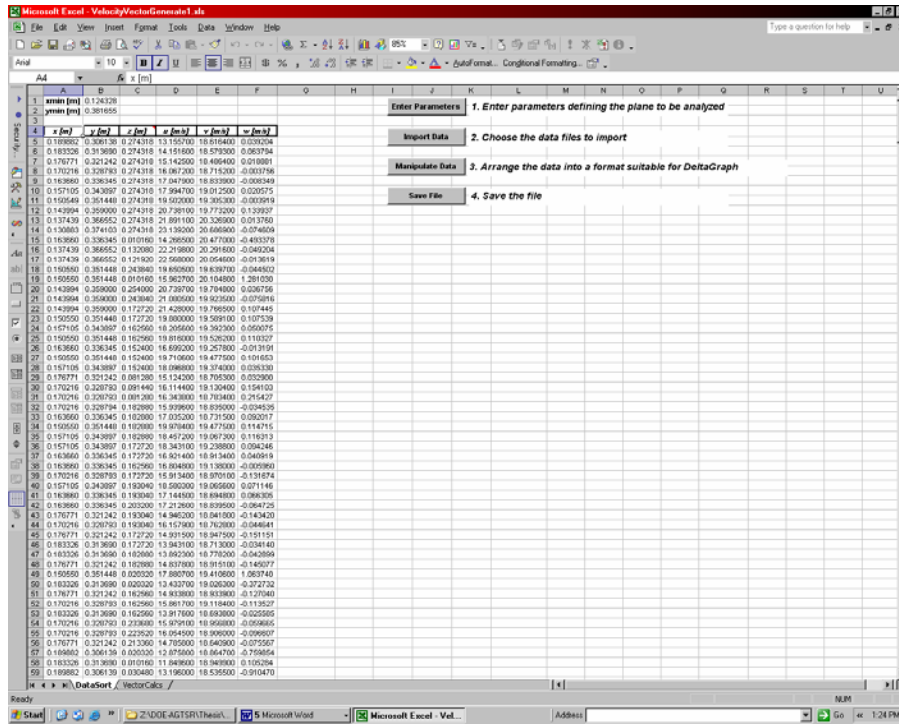


Figure C.3 After importing the data all rows with text are deleted.

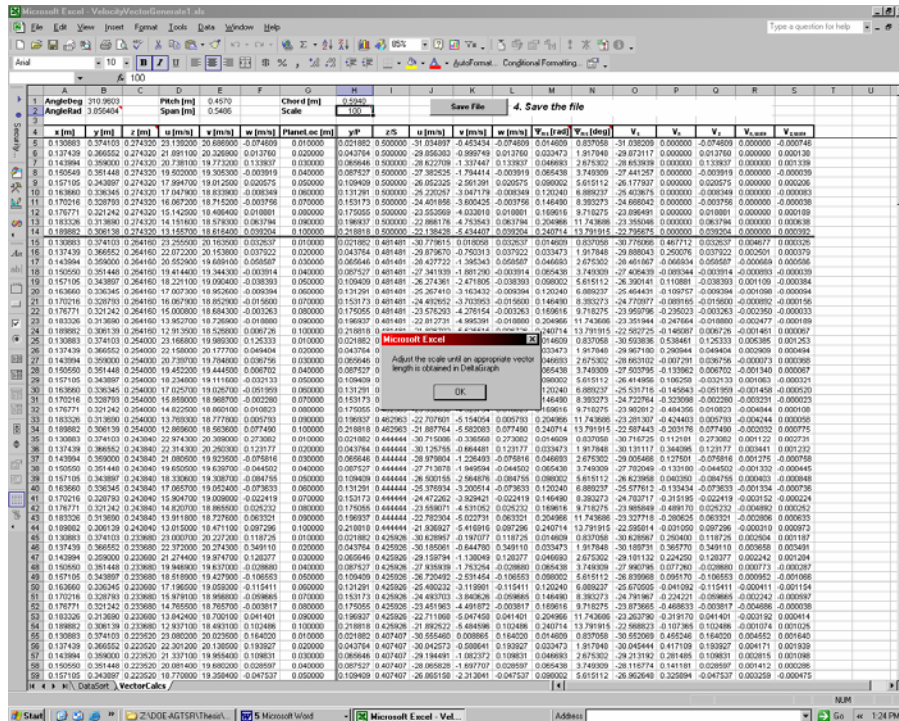


Figure C.4 The “Manipulate Data” button sorts the data, performs the flow plane calculations, and formats the output.

### *Enter Parameters Button Module*

```
Option Explicit
'=====
'
'
' This module contains functions for calling custom dialog Boxes
'
'=====

Sub ShowParametersForm()
    frmParameters.Show
End Sub

Sub ShowAnalysisPlanesForm()
    frmAnalysisPlane.Show
End Sub
```

---

### *Parameter Input GUI*

```
Option Explicit
Const Pi = 3.14159265358979

Private Sub cmbPlanes_Click()
    Select Case cmbPlanes.ListIndex
    Case 0
        txtXbase.Text = ""
        txtYBase.Text = ""
        txtAngle.Text = ""
    Case 1
        txtXbase.Text = "-0.000305"
        txtYBase.Text = "0.455970"
        txtAngle.Text = "180"
    Case 2
        txtXbase.Text = "0.124328"
        txtYBase.Text = "0.381655"
        txtAngle.Text = "310.9602825"
    Case 3
        txtXbase.Text = "0.249921"
        txtYBase.Text = "0.379524"
        txtAngle.Text = "153.576204"
    End Select
End Sub

Private Sub cmbVanes_Click()
    Select Case cmbVanes.ListIndex
    Case 0
        txtPitch.Text = ""
        txtSpan.Text = ""
        txtChord.Text = ""
    Case 1
```

```

        txtPitch.Text = "0.457"
        txtSpan.Text = "0.54864"
        txtChord.Text = "0.594"
    End Select
End Sub

Private Sub cmdCancel_Click()
    Unload frmParameters
End Sub

Private Sub cmdOK_Click()
    Dim Msg As String    'Prompt
    Dim Config As Long   'Button Configuration
    Dim Title As String  'Title
    Dim Ans As Long      'MsgBox response

    ' Activate the propersheet
    If IsNumeric(txtXbase.Text) And IsNumeric(txtYBase.Text) And _
        IsNumeric(txtAngle.Text) And IsNumeric(txtPitch.Text) And _
        IsNumeric(txtSpan.Text) And IsNumeric(txtChord) Then

Workbooks("VelocityVectorGeneratel.xls").Sheets("DataSort").Activate
    If optIn1.Value = True Then
        Range("xBase").Value = Val(txtXbase.Text) * 0.0254
    Else
        Range("xBase").Value = Val(txtXbase.Text)
    End If

    If optIn2.Value = True Then
        Range("yBase").Value = Val(txtYBase.Text) * 0.0254
    Else
        Range("yBase").Value = Val(txtYBase.Text)
    End If

    Sheets("VectorCalcs").Activate

    Range("AngleDeg").Value = Val(txtAngle.Text)
    Range("AngleRad").Value = (Range("AngleDeg").Value-90)* Pi/180

    If optIn3.Value = True Then
        Range("pitch").Value = Val(txtPitch.Text) * 0.0254
    Else
        Range("pitch").Value = Val(txtPitch.Text)
    End If

    If optIn4.Value = True Then
        Range("span").Value = Val(txtSpan.Text) * 0.0254
    Else
        Range("span").Value = Val(txtSpan.Text)
    End If

    If optIn5.Value = True Then

```

```

        Range("chord").Value = Val(txtChord.Text) * 0.0254
    Else
        Range("chord").Value = Val(txtChord.Text)
    End If

Unload frmParameters

' Format the data entries
Sheets("DataSort").Select
Range("xBase:yBase").Select
With Selection
    .NumberFormat = "0.000000"
    .HorizontalAlignment = xlCenter
End With

Sheets("VectorCalcs").Select
Range("AngleDeg,pitch:span,chord").Select
With Selection
    .NumberFormat = "0.0000"
    .HorizontalAlignment = xlCenter
End With
Range("A5").Activate

Sheets("DataSort").Select
Range("A5").Activate

Else
    Msg = "You must enter a number for each parameter." & vbCrLf
    Msg = Msg & "Would you like to try again"
    Config = vbYesNo + vbExclamation
    Title = "Error!"
' Ask user to try again
    Ans = MsgBox(Msg, Config, Title)
    Select Case Ans
        Case vbYes
            Exit Sub
        Case Else
            Unload frmParameters
    End Select
End If
End Sub

Private Sub UserForm_Initialize()
    cmbPlanes.AddItem ""
    cmbPlanes.AddItem "Stagnation Plane"
    cmbPlanes.AddItem "SS2"
    cmbPlanes.AddItem "DPS1"
    cmbPlanes.ListIndex = 0

    cmbVanes.AddItem ""
    cmbVanes.AddItem "Pratt & Whitney Vane"
    cmbVanes.ListIndex = 0

```

End Sub

---

### *Data Import Button Module*

Option Explicit

```
Sub DataImport()  
    Dim ErrMsg  
    Dim Msg As String, DataFile As String, Title As String  
    Dim Count As Integer  
  
    Sheets("DataSort").Activate  
  
    On Error GoTo ErrorMessage  
  
    For Count = 1 To 3  
        Msg = "Select file containing "  
        Select Case Count  
            Case 1  
                Range("A5").Activate  
                DataFile = "x & y data to import"  
                Msg = Msg & DataFile  
                MsgBox Msg  
                Application.Dialogs(xlDialogImportTextFile).Show  
            Case 2  
                Range("C5").Activate  
                DataFile = "z & u data to import"  
                Msg = Msg & DataFile  
                MsgBox Msg  
                Application.Dialogs(xlDialogImportTextFile).Show  
            Case 3  
                Range("E5").Activate  
                DataFile = "v & w data to import"  
                Msg = Msg & DataFile  
                MsgBox Msg  
                Application.Dialogs(xlDialogImportTextFile).Show  
        End Select  
    Next Count  
  
    NonDataDelete  
    Columns("A:G").Select  
    Selection.Columns.AutoFit  
    Range("A4").Select  
  
    Exit Sub  
  
ErrorMessage:  
    If DataFile <> "" Then  
        MsgBox "You have generated an error while selecting " &  
DataFile  
    Else
```

```

        ErrMsg = Error(Err)
        MsgBox "ERROR: " & ErrMsg
    End If
End Sub

Sub NonDataDelete()
    Dim Msg As String, DataType
    Dim BlankCount As Integer, Row As Integer
    Dim TextCells, Cell As Object

    Application.ScreenUpdating = False
    Range("A5").Activate

    BlankCount = 0
    Do Until BlankCount > 10
        Select Case ActiveCell
            Case Empty
                Row = ActiveCell.Row
                Rows(Row).Delete
                BlankCount = BlankCount + 1
            Case Else
                Select Case IsNumeric(ActiveCell)
                    Case True
                        ActiveCell.Offset(1, 0).Activate
                        BlankCount = 0
                    Case Else
                        Row = ActiveCell.Row
                        Rows(Row).Delete
                End Select
            End Select
        End Select
    Loop
End Sub

```

---

### *Manipulate Data Button Module*

```

Option Explicit
Const Pi = 3.14159265358979
'=====
'
'
'This module contains functions for analyzing ss2 and stag plane
'
'=====
Sub PlaneDetermine()
    Application.ScreenUpdating = False
    Workbooks("VelocityVectorGeneratel.xls").Activate
    Sheets("VectorCalcs").Select
    Select Case Range("AngleDeg").Value
        Case ""
            MsgBox "You must define the plane first"
            Sheets("DataSort").Select
    End Select
End Sub

```

```

        Exit Sub
    Case 180
        Call StagnationDataArrange
    Case Else
        Call DataArrange
    End Select
End Sub

Sub StagnationDataArrange()
    Workbooks("VelocityVectorGenerate.xls").Activate
    Sheets("DataSort").Activate
    Range("A5").Activate

    Dim NumRows As Integer, NumCols As Integer

    Application.ScreenUpdating = False

    NumRows = Range(ActiveCell, ActiveCell.End(xlDown)).Count
    NumCols = Range(ActiveCell, ActiveCell.End(xlToRight)).Count

    Call CopyZ
    Call RoundZ(NumRows)
    Call SecondThirdQuadDataSort
    Call PlaneLoc(NumRows)
    Call PlaneLocCheck(NumRows)
    Call VectorCalcsPaste
    Call EdgeFormat
    Call xC(NumRows)
    Call zS(NumRows)
    Call StagVnScale(NumRows)
    Call StagVzScale(NumRows)
    Call StagVectorCalcsFormat
End Sub

Sub DataArrange()

    Workbooks("VelocityVectorGeneratel.xls").Activate
    Sheets("DataSort").Activate
    Range("A5").Activate

    Dim NumRows As Integer, NumCols As Integer

    Application.ScreenUpdating = False

    NumRows = Range(ActiveCell, ActiveCell.End(xlDown)).Count
    NumCols = Range(ActiveCell, ActiveCell.End(xlToRight)).Count

    ' Call SubRoutines
    Call CopyZ
    Call RoundZ(NumRows)

```

```

Call DataSort
Call PlaneLoc(NumRows)
Call PlaneLocCheck(NumRows)
Call VectorCalcsPaste
Call EdgeFormat
Call yP(NumRows)
Call zS(NumRows)
Call uCalc(NumRows)
Call vCalc(NumRows)
Call zCopy(NumRows)
Call PsiRad(NumRows)
Call PsiDeg(NumRows)
Call VsCalc(NumRows)
Call VnCalc(NumRows)
Call VzCalc(NumRows)
Call VnScale(NumRows)
Call VzScale(NumRows)
Call VectorCalcsFormat

End Sub

Sub CopyZ()

    ' Copy contents of "Z" to another row
    Range("C5").Activate
    Range(ActiveCell, ActiveCell.End(xlDown)).Copy Range("H5")
    Application.CutCopyMode = False

End Sub

Sub RoundZ(NumRows As Integer)
    Dim Cell As Object
    Dim Row As Integer
    Range(ActiveCell, ActiveCell.End(xlDown)).ClearContents

    ' Use ROUND to eliminate truncation error
    Row = ActiveCell.Row
    Range(ActiveCell, ActiveCell.Offset(NumRows - 1, 0)).Select
    For Each Cell In Selection
        ActiveCell.Value = Round(ActiveCell.Offset(0, 5).Value, 5)
        ActiveCell.Offset(0, 5).ClearContents
        ActiveCell.Offset(1, 0).Activate
    Next Cell
End Sub

Sub DataSort()
    ' Sort the Data
    Range("A5").CurrentRegion.Select
    Selection.Sort Key1:=Range("C5"), Order1:=xlDescending,
Key2:=Range("A5") _
    , Order2:=xlAscending

    ' Format Data

```

```

    With Selection
        .NumberFormat = "0.000000"
        .HorizontalAlignment = xlCenter
    End With
End Sub

Sub SecondThirdQuadDataSort()
    ' Sort the Data
    Range("A5").CurrentRegion.Select
    Selection.Sort Key1:=Range("C5"), Order1:=xlDescending,
Key2:=Range("A5") _
        , Order2:=xlDescending

    ' Format Data
    With Selection
        .NumberFormat = "0.000000"
        .HorizontalAlignment = xlCenter
    End With
End Sub

Sub PlaneLoc(NumRows As Integer)
    Dim Row As Double, Col As Double
    Dim xVal, yVal
    Dim xLength As Single, yLength As Double
    Dim Count As Integer

    Range("G4").Activate
    ActiveCell.Select
    ActiveCell.FormulaR1C1 = "PlaneLoc [m]"
    With Selection
        .HorizontalAlignment = xlCenter
        .Font.Bold = True
        With .Borders(xlEdgeLeft)
            .LineStyle = xlContinuous
            .Weight = xlMedium
        End With
        With .Borders(xlEdgeTop)
            .LineStyle = xlContinuous
            .Weight = xlMedium
        End With
        With .Borders(xlEdgeBottom)
            .LineStyle = xlContinuous
            .Weight = xlMedium
        End With
        With .Borders(xlEdgeRight)
            .LineStyle = xlContinuous
            .Weight = xlMedium
        End With
    End With

    Row = 0
    For Count = 1 To NumRows
        'Row = Row + 1
    
```

```

        ActiveCell.Offset(1, 0).Activate
        Row = ActiveCell.Row
        Col = ActiveCell.Column
        xLength = Cells(Row, 1).Value - Range("xBase").Value
        yLength = Cells(Row, 2).Value - Range("yBase").Value
        ActiveCell.Value = Sqr(xLength * xLength + yLength * yLength)
    Next Count

    ' Copy contents of "PlaneLoc" to another row
    Range("G5").Activate
    Range(ActiveCell, ActiveCell.End(xlDown)).Copy Range("I5")
    Application.CutCopyMode = False

    Dim Cell As Object
    Range(ActiveCell, ActiveCell.End(xlDown)).ClearContents

    ' Use ROUND to eliminate truncation error
    Row = ActiveCell.Row
    Range(ActiveCell, ActiveCell.Offset(NumRows - 1, 0)).Select
    For Each Cell In Selection
        ActiveCell.Value = Round(ActiveCell.Offset(0, 2).Value, 4)
        ActiveCell.Offset(0, 2).ClearContents
        ActiveCell.Offset(1, 0).Activate
    Next Cell

    With Selection
        .NumberFormat = "0.0000"
        .Font.Bold = False
        .HorizontalAlignment = xlCenter
    End With

    Columns("L:L").EntireColumn.AutoFit
End Sub

Sub PlaneLocCheck(NumRows As Integer)
    Dim Row As Integer, Col As Integer
    Dim RowCount As Integer, ActiveRow As Integer
    Dim i, Diff
    Dim Msg As String

    Range("G6").Activate
    Row = ActiveCell.Row
    Col = ActiveCell.Column

    ' Count Number of cells which have already been read
    RowCount = 1
    ' Find the first repeating row
    Do Until ActiveCell.Value < Cells(Row - 1, Col).Value
        ActiveCell.Offset(1, 0).Activate
        Row = ActiveCell.Row
        RowCount = RowCount + 1
    Loop

```

```

Msg = "There is a problem in cell(s)" & vbCrLf & vbCrLf

' Test to see if points are properly stagered
For i = 1 To NumRows - (RowCount + 1)
    ActiveRow = ActiveCell.Row
    Diff = ActiveCell.Value - Cells(ActiveRow - RowCount, Col).Value
    Diff = Round(Diff, 4)

    If Diff <> 0 Then
        Msg = Msg & ActiveCell.Address & vbCrLf
        ActiveCell.Interior.Color = vbRed
    End If
    ActiveCell.Offset(1, 0).Activate
Next i

If Msg <> "There is a problem in cell(s)" & vbCrLf & vbCrLf Then
    MsgBox Msg & vbCrLf & "Please examine these cells"
    Exit Sub
End If
End Sub

Sub VectorCalcsPaste()
    Range("A4").CurrentRegion.Copy Worksheets("VectorCalcs").Range("A4")
End Sub

Sub EdgeFormat()
    Sheets("VectorCalcs").Select
    Range("G4").Activate
    Range(ActiveCell, ActiveCell.End(xlDown)).Select
    With Selection.Borders(xlEdgeRight)
        .LineStyle = xlDouble
        .Weight = xlThick
        .ColorIndex = xlAutomatic
    End With
End Sub

Sub yP(NumRows As Integer)
    Dim Count As Integer, Row As Integer
    Range("H4").Activate
    ActiveCell.Value = "y/P"
    ActiveCell.Offset(1, 0).Activate

    For Count = 1 To NumRows
        Row = ActiveCell.Row
        ActiveCell.Value = Cells(Row, 7).Value / Range("pitch").Value
        ActiveCell.Offset(1, 0).Activate
    Next Count
End Sub

Sub xC(NumRows As Integer)
    Dim Count As Integer, Row As Integer

```

```

Range("H4").Activate
ActiveCell.Value = "x/C"
ActiveCell.Offset(1, 0).Activate

For Count = 1 To NumRows
    Row = ActiveCell.Row
    ActiveCell.Value = -Cells(Row, 7).Value / Range("chord").Value
    ActiveCell.Offset(1, 0).Activate
Next Count
End Sub

Sub zS(NumRows As Integer)
Dim Count As Integer, Row As Integer
Range("I4").Activate
ActiveCell.Value = "z/S"
ActiveCell.Offset(1, 0).Activate

For Count = 1 To NumRows
    Row = ActiveCell.Row
    ActiveCell.Value = Cells(Row, 3).Value / Range("span").Value
    ActiveCell.Offset(1, 0).Activate
Next Count
End Sub

Sub uCalc(NumRows As Integer)
Dim Count As Integer, Row As Integer
Dim AngleRad As Double
Range("J5").Activate

AngleRad = Range("AngleRad").Value

For Count = 1 To NumRows
    Row = ActiveCell.Row
    ActiveCell.Value = Cells(Row, 4).Value * Cos(AngleRad) +
Cells(Row, 5).Value * Sin(AngleRad)
    ActiveCell.Offset(1, 0).Activate
Next Count
End Sub

Sub vCalc(NumRows As Integer)
Dim Count As Integer, Row As Integer
Dim AngleRad As Double
Range("K5").Activate

AngleRad = Range("AngleRad").Value

For Count = 1 To NumRows
    Row = ActiveCell.Row
    ActiveCell.Value = Cells(Row, 5).Value * Cos(AngleRad) -
Cells(Row, 4).Value * Sin(AngleRad)
    ActiveCell.Offset(1, 0).Activate
Next Count
End Sub

```

```

Sub zCopy(NumRows As Integer)
  Dim Count As Integer, Row As Integer
  Range("L5").Activate

  For Count = 1 To NumRows
    Row = ActiveCell.Row
    ActiveCell.Value = Cells(Row, 6).Value
    ActiveCell.Offset(1, 0).Activate
  Next Count
End Sub

Sub PsiRad(NumRows As Integer)
  Dim i As Integer, Row As Integer, Col As Integer
  Dim Count As Integer, RowRepeat As Integer, NewRows As Integer
  Dim PlaneLocation As Double, RowSearch As Double, ColSearch As
  Double, PsiRef As Double

  Range("M5").Activate
  Row = ActiveCell.Row
  Col = ActiveCell.Column
  i = 1

  ' Calculate values in first two cells
  For i = 1 To 2
    ActiveCell.Value = Atn(Cells(Row, Col - 2).Value / Cells(Row,
Col - 3).Value)
    ActiveCell.Offset(1, 0).Activate
    Row = ActiveCell.Row
  Next i

  ' Calculate value of Psi at the midspan and search for the point
  where midspan data ends
  Do Until Cells(Row, Col - 4) <> Cells(Row - 1, Col - 4).Value
    ActiveCell.Value = Atn(Cells(Row, Col - 2).Value / Cells(Row,
Col - 3).Value)
    ActiveCell.Offset(1, 0).Activate
    Row = ActiveCell.Row
  Loop

  ' Adjust the number of rows that need to be calculated
  ' 4 compensates for cells above and including label, 1 includes
  active cell
  RowRepeat = Row - (4 + 1)
  NewRows = NumRows - RowRepeat

  For Count = 1 To NewRows
    PlaneLocation = Cells(Row, Col - 6).Value
    Range("G5").Activate
    RowSearch = ActiveCell.Row
    ColSearch = ActiveCell.Column
    Do Until ActiveCell.Value = PlaneLocation
      ActiveCell.Offset(1, 0).Activate
    Loop
  Next Count
End Sub

```

```

        RowSearch = ActiveCell.Row
    Loop
    PsiRef = Cells(RowSearch, Col).Value
    Cells(Row, Col).Activate
    ActiveCell.Value = PsiRef
    ActiveCell.Offset(1, 0).Activate
    Row = ActiveCell.Row
Next Count

End Sub

Sub PsiDeg(NumRows As Integer)
    Dim Count As Integer, Row As Integer, Col As Integer

    Range("N5").Activate
    Row = ActiveCell.Row
    Col = ActiveCell.Column
    For Count = 1 To NumRows
        ActiveCell.Value = Cells(Row, Col - 1).Value * 180 / Pi
        ActiveCell.Offset(1, 0).Activate
        Row = ActiveCell.Row
    Next Count
End Sub

Sub VsCalc(NumRows As Integer)
    Dim Count As Integer, Row As Integer, Col As Integer

    Range("O5").Activate
    Col = ActiveCell.Column

    For Count = 1 To NumRows
        Row = ActiveCell.Row
        ActiveCell.Value = Cells(Row, Col - 5).Value * Cos(Cells(Row,
Col - 2)) + _
            Cells(Row, Col - 4).Value * Sin(Cells(Row,
Col - 2))
        ActiveCell.Offset(1, 0).Activate
    Next Count
End Sub

Sub VnCalc(NumRows As Integer)
    Dim Count As Integer, Row As Integer, Col As Integer

    Range("P5").Activate
    Col = ActiveCell.Column

    For Count = 1 To NumRows
        Row = ActiveCell.Row
        ActiveCell.Value = Cells(Row, Col - 5).Value * Cos(Cells(Row,
Col - 3)) - _
            Cells(Row, Col - 6).Value * Sin(Cells(Row,
Col - 3))
    Next Count
End Sub

```

```

        ActiveCell.Offset(1, 0).Activate
    Next Count
End Sub

Sub VzCalc(NumRows As Integer)
    Dim Count As Integer, Row As Integer, Col As Integer

    Range("Q5").Activate
    Col = ActiveCell.Column

    For Count = 1 To NumRows
        Row = ActiveCell.Row
        ActiveCell.Value = Cells(Row, 6).Value
        ActiveCell.Offset(1, 0).Activate
    Next Count
End Sub

Sub VnScale(NumRows As Integer)
    Dim Count As Integer, Row As Integer, Col As Integer

    Range("R5").Activate
    Row = ActiveCell.Row
    Col = ActiveCell.Column

    For Count = 1 To NumRows
        ActiveCell.Formula = "=" & Cells(Row, Col - 2).Address &
"/scale"
        ActiveCell.Offset(1, 0).Activate
        Row = ActiveCell.Row
    Next Count
End Sub

Sub StagVnScale(NumRows As Integer)
    Dim Count As Integer, Row As Integer, Col As Integer

    Range("R5").Activate
    Row = ActiveCell.Row
    Col = 4

    For Count = 1 To NumRows
        ActiveCell.Formula = "=" & Cells(Row, Col).Address & "/scale"
        ActiveCell.Offset(1, 0).Activate
        Row = ActiveCell.Row
    Next Count
End Sub

Sub VzScale(NumRows As Integer)
    Dim Count As Integer, Row As Integer, Col As Integer

    Range("S5").Activate
    Row = ActiveCell.Row
    Col = ActiveCell.Column

```

```

    For Count = 1 To NumRows
        ActiveCell.Formula = "=" & Cells(Row, Col - 2).Address &
"/scale"
        ActiveCell.Offset(1, 0).Activate
        Row = ActiveCell.Row
    Next Count
End Sub

Sub StagVzScale(NumRows As Integer)
    Dim Count As Integer, Row As Integer, Col As Integer

    Range("S5").Activate
    Row = ActiveCell.Row
    Col = 6

    For Count = 1 To NumRows
        ActiveCell.Formula = "=" & Cells(Row, Col).Address & "/scale"
        ActiveCell.Offset(1, 0).Activate
        Row = ActiveCell.Row
    Next Count
End Sub

Sub VectorCalcsFormat()
    Dim Row As Integer, Col As Integer
    Dim Msg As String

    Range("G6").Activate
    Row = ActiveCell.Row
    Col = ActiveCell.Column

    Do Until ActiveCell.Value < Cells(Row - 1, Col).Value
        ActiveCell.Offset(1, 0).Activate
        Row = ActiveCell.Row
    Loop

    Cells(Row, 1).Activate
    Range(ActiveCell, ActiveCell.End(xlToRight)).Select
    With Selection.Borders(xlEdgeTop)
        .LineStyle = xlContinuous
        .Weight = xlMedium
        .ColorIndex = xlAutomatic
    End With

    Range("H5").Select
    Range(Selection, Selection.End(xlDown)).Select
    Range(Selection, Selection.End(xlToRight)).Select
    With Selection
        .NumberFormat = "0.000000"
        .Font.Bold = False
        .Font.Italic = False
        .HorizontalAlignment = xlCenter
    End With

```

```

Range("A4").Select
Range(Selection, Selection.End(xlToRight)).Select
With Selection
    .Font.Bold = True
    .Font.Italic = False
    .HorizontalAlignment = xlCenter
End With

Columns("A:S").Select
Selection.Columns.AutoFit

Application.ScreenUpdating = True

Range("scale").Select
Msg = "Adjust the scale until an appropriate vector" & vbCrLf
Msg = Msg & "length is obtained in DeltaGraph"
MsgBox Msg
End Sub

Sub StagVectorCalcsFormat()
Dim Row As Integer, Col As Integer
Dim Msg As String

Range("G6").Activate
Row = ActiveCell.Row
Col = ActiveCell.Column

Do Until ActiveCell.Value < Cells(Row - 1, Col).Value
    ActiveCell.Offset(1, 0).Activate
    Row = ActiveCell.Row
Loop

Cells(Row, 1).Activate
Range(ActiveCell, ActiveCell.End(xlToRight)).Select
With Selection.Borders(xlEdgeTop)
    .LineStyle = xlContinuous
    .Weight = xlMedium
    .ColorIndex = xlAutomatic
End With

Cells(Row, 18).Activate
Range(ActiveCell, ActiveCell.End(xlToRight)).Select
With Selection.Borders(xlEdgeTop)
    .LineStyle = xlContinuous
    .Weight = xlMedium
    .ColorIndex = xlAutomatic
End With

Range("H5").Select
Range(Selection, Selection.End(xlDown)).Select
Range(Selection, Selection.End(xlToRight)).Select
With Selection
    .NumberFormat = "0.000000"

```

```

        .Font.Bold = False
        .Font.Italic = False
        .HorizontalAlignment = xlCenter
    End With

    Range("R5").Select
    Range(Selection, Selection.End(xlDown)).Select
    Range(Selection, Selection.End(xlToRight)).Select
    With Selection
        .NumberFormat = "0.000000"
        .Font.Bold = False
        .Font.Italic = False
        .HorizontalAlignment = xlCenter
    End With

    Range("A4").Select
    Range(Selection, Selection.End(xlToRight)).Select
    With Selection
        .Font.Bold = True
        .Font.Italic = False
        .HorizontalAlignment = xlCenter
    End With

    Columns("A:I").Select
    Selection.Columns.AutoFit

    Columns("R:S").Select
    Selection.Columns.AutoFit

    Application.ScreenUpdating = True

    Range("scale").Select
    Msg = "Adjust the scale until an appropriate vector" & vbCrLf
    Msg = Msg & "length is obtained in DeltaGraph"
    MsgBox Msg
End Sub

```

---

### *Save File Button Module*

```

Option Explicit
Option Private Module
Public NewFileName As Variant
Public CallSave As Boolean
Public NoSave As Boolean

Sub SaveButton()
    Dim InitialFilename As String, FileFilter As String
    Dim FilterIndex As String, Title As String

    InitialFilename = "VelocityVectors1.xls"
    FileFilter = "Microsoft Excel Workbook (*.xls),*.xls," & _
        "Web Page (*.htm;*.html),*.htm;*.html," & _

```

```

        "Web Archive (*.mht;*.mhtml),*.mht;*.mhtml," & _
        "XML Spreadsheet (*.xml),*.xml," & _
        "Template (*.xlt),*.xlt," & _
        "Text (Tab delimited) (*.txt),*.txt"
    FilterIndex = 1
    Title = "Save As"

    ' Show SaveAs dialogbox
    NewFileName = Application.GetSaveAsFilename(InitialFilename,
FileFilter, FilterIndex, Title)

    ' Test to see a filename was chosen or the dialog was cancelled
    If NewFileName = False Then

        ' Cancel the variable indicating that a call has been made to
save the file
        CallSave = False

        ' Variable to indicate that the user has declined to save the
file
        NoSave = True
        Exit Sub
    Else
        ' Set flag so that BeforeSaveMethod recognizes that SaveAs
dialog was displayed
        CallSave = True
        ActiveWorkbook.SaveAs FileName:=NewFileName
    End If
End Sub

```

## Vita

Daniel G. Knost was born on December 21, 1978 to Jack and Susan Knost in Charlotte, North Carolina. For 13 years Daniel attended Providence Day School in Charlotte graduating in 1997. While at Providence Day, Daniel earned four varsity letters in tennis and three in football. During his senior seasons he was selected as homecoming captain for the football team and was team captain and #1 singles and doubles player for the tennis team. In August, 1997 Daniel enrolled at North Carolina State University. At N.C. State, Daniel participated in the University Scholars Program and played one year on the club tennis team at #1 singles. Daniel graduated Magna Cum Laude in May of 2001 with a B.S. in mechanical engineering. He came to Virginia Tech in June of 2001 and began work on his M.S. Daniel currently plans to pursue a PhD in mechanical engineering at Virginia Tech. He would also like to hold an engineering position in motorsports and obtain his P.E. license upon completion of his schooling. In his free time Daniel enjoys watching and attending sporting events, especially for the Wolfpack, playing tennis, visiting his family, and spending time with his girlfriend Nicole and beagle Katie.

A few of Daniel's favorite things are:

College Team :	N.C. State Wolfpack
Professional Team:	Carolina Panthers
Tennis Player:	Andre Agassi / Steffi Graf
Tennis Tournament :	U.S. Open
Racecar Driver:	Dale Earnhardt / Dale Earnhardt Jr.
Trucks:	Chevrolet
Movie :	Top Gun / Days of Thunder / Crocodile Dundee
City:	Chicago
Food:	Cheeseburgers / Pork Bar-B-Que
Soda:	Cheerwine / Pepsi